Technische Universität Dresden

Modeling and Simulation of Components and Circuits with Intrinsically Active Polymers

Dipl.-Ing.

Philipp Jan Mehner

der Fakultät Elektrotechnik und Informationstechnik der Technische Universität Dresden

zur Erlangung des akademischen Grades

Doktoringenieur

(Dr.-Ing.)

genehmigte Dissertation

Vorsitzender	Prof. Dr.-Ing. habil. Hagen Malberg
Gutachter	Prof. Dr.-Ing. Andreas Richter
Gutachter	Prof. Dr.-Ing. habil. Thomas Wallmersperger

Tag der Einreichung: 02.11.2020
Tag der Verteidigung: 04.02.2021

Acknowledgment

I am deeply indebted to a great many people who have supported me throughout my time writing this dissertation and throughout my academic career more generally. My greatest debt is to my doctoral supervisor Prof. Dr.-Ing. Andreas Richter. His novel and interdisciplinary research direction allowed me to develop new modeling strategies. He supported my research not only materially, but above all through deep, fruitful, and professional insights into the behavior of the hydrogel material and the design of active microfluidic systems.

In addition, I would like to thank Prof. Dr.-Ing. habil. Uwe Marschner for the constant support with modeling and simulation challanges, especially for the efficient design of network models and model reduction approaches. His support ranges from my first lecture in my studies to the completion of this dissertation. Also, the continuous feedback from Prof. Dr. habil. Thomas Wallmersperger in modeling hydrogel behaviors with FEM pushed this work significantly.

Then, I would like to thank all of my colleagues from various chairs who have all contributed to this work, with special thanks to M.Sc. A. Beck, Dr. S. Häfner and Dr. P. Frank for the development and fabrication of the test samples. Also, Dr. A. Voigt has always supported me with very helpful simulation advices.

A special thanks go to the relentless students B. Xu, Dipl.-Ing. D. Zhongke, D. Hong, F. Stolba, M.Sc. J. Tang, Y. Gao, M. Reim, M. Li, and A. Gubsch, who have all contributed in the areas of experiments, characterization, FEM and layout synthesis.

Furthermore, I would like to thank Prof. Bethanie Stadler from the University of Minnesota, who very generously hosted me and enabled me to investigate a promising research idea. When I was still a student, I had my first encounter with polymers in the lab of Prof. Carol Livermore from the Northeastern University in Boston. I am very grateful for the opportunities and I will never forget these stays.

Vital support came as well from the German Science Foundation who, over the RTG 1865 hydrogel-based microsystems, gathered a unique and interdisciplinary team, over multiple excellent chairs, which all gave significant insights and feedback with broad directions and interests. This collaborative environment was excellently managed by Prof. Dr.-Ing. habil. Gerald Gerlach.

Lastly, my most humble and biggest thank you goes to my family, whose eternal love, care and insight never ceased. A special thanks is needed to my father, who deeply followed my model ideas and to my mother, who always motivated me to pursue my dreams.

Dedication

My Family

Abstract

Lab-on-chip systems are becoming increasingly important for medical diagnostics and drug discovery. Large laboratory equipment for the analysis and synthesis of substances are miniaturized on a microfluidic chip attached to a portable device. It offers a high throughput and samples can be assessed on site at low cost. Microfluidics are the key technology for lab-on-chip systems and fluidic logic circuits, which evaluate and classify achieved results. Microfluidic systems consist of channels, pumps, mixers, reactors, microvalves and other parts. At the TU Dresden, an autonomous microvalve based on hydrogel actuation has been developed in a miniaturizable scale. It enables complex large-scale microfluidic systems which need to be analyzed with sophisticated design methods and algorithms to accurately predict the behavior on the computer before starting a time-consuming manufacturing process of prototypes.

In this work, a design platform for the modeling, simulation and optimization of fluidic components and their interactions in larger systems is developed. A hydrogel-based stimulus-sensitive microvalve is the core element of the microfluidic toolbox. Essential material properties as swelling-stimuli functions and the cooperative diffusion are extracted from measurements. The results provide necessary input data for finite element simulations in order to extract characteristic properties of the mechanical and fluid domains. Finally, the behavior of the microvalve and other fluidic library elements is implemented in Matlab Simscape for component and system simulations. Case studies and design optimization can be realized in a very short time with high accuracy. The toolbox is suitable for research and development and as software for academic education. The library elements are evaluated for a chemofluidic NAND gate, a chemofluidic decoder and a chemofluidic oscillator.

Zusammenfassung

Lab-on-Chip-Systeme sind für die medizinische Diagnostik und die Wirkstoffforschung von Interesse. Laborgeräte für die Analyse und Synthese von Substanzen werden auf einem Chip integriert. Sie bieten einen hohen Durchsatz und analysieren Proben vor Ort mit geringen Kosten. Die Mikrofluidik ist eine Schlüsseltechnologie für Lab-on-Chip-Systeme und für nachfolgende fluidische Schaltungen zur Bewertung und Klassifizierung der Ergebnisse. Diese Systeme bestehen unter anderem aus Kanälen, Pumpen, Mischern, Reaktoren und Mikroventilen. Ein autonomes und miniaturisierbares Ventil auf der Basis von Hydrogelaktuatoren wurde an der TU Dresden entwickelt und in fluidische Systeme integriert. Für den Entwurf sind moderne Simulationsmethoden und -algorithmen notwendig, um das Verhalten am Computer zu bewerten bevor ein zeit- und kostenintensiver Herstellungsprozess von Prototypen gestartet wird.

In dieser Arbeit wird eine Entwurfsplattform für die Modellierung, Simulation und Optimierung von fluidischen Komponenten und deren Wechselwirkungen in größeren Systemen entwickelt. Ein Mikroventil auf der Basis von stimulussensitiven Hydrogelen ist das Kernelement des Entwurfstools. Wesentliche Materialeigenschaften wie das Quellverhalten und der kooperative Diffusionskoeffizient werden zu Beginn mit Messungen ermittelt. Mit Finite-Elemente-Simulationen werden aus diesen Daten charakteristische Kennwerte für das mechanische und fluidische Verhalten bestimmt. Sie bilden die Basis für komplexe Systemmodelle in Matlab Simscape, welche das Mikroventil und weitere fluidische Grundelemente in ihrem Zusammenwirken beschreiben. Verschiedene Konzepte können in kurzer Zeit und mit hoher Genauigkeit analysiert, optimiert und verglichen werden. Die Toolbox eignet sich für die Forschung und Entwicklung sowie als Software für die akademische Ausbildung. Sie wurde für den Entwurf eines chemofluidischen NAND-Gatters, für einen chemofluidischen Decoder und für einen chemofluidischen Oszillator eingesetzt.

Table of Contents

List of Abbreviations

1D . . . . . one-dimensional
2D . . . . . two-dimensional
3D . . . . . three-dimensional
AE . . . . . algebraic equation
AFM . . . . . atomic force microscope
APDL . . . . . ANSYS parametric design language
BEM . . . . . boundary element method
CAD . . . . . computer-aided design
CCCS . . . . . current-controlled current source
CCVS . . . . . current-controlled voltage source
CE . . . . . capillary electrophoresis
CFD . . . . . computational fluid dynamic
CVPT . . . . . chemical volume phase-transition transistor
DAE . . . . . differential algebraic equation
DOF . . . . . degree of freedom
FDM . . . . . finite difference method
FE . . . . . finite element
FEM . . . . . finite element method
FSI . . . . . fluid structure interaction
FTIR . . . . . Fourier-transformation infrared spectroscopy
FVM . . . . . finite volume method
GUI . . . . . graphical user interface
HPLC . . . . . high-performance liquid chromatography
IC . . . . . integrated circuit
ICTE . . . . . instantaneous coefficient of thermal expansion
IOT . . . . . Internet of Things
LCST . . . . . lower critical solution temperature
LED . . . . . light-emitting diode
MDA . . . . . Microfluidic Design automation
MEMS . . . . . micro-electro-mechnical-systems
MFX . . . . . multi field solver
MOR . . . . . model order reduction
ODE . . . . . ordinary differential equation
PCR . . . . . polymerase chain reactions
PDE . . . . . partial differential equation

PEB . . . . . post-exposure baked
pH . . . . . potential of hydrogen
PID . . . . . proportional-integral–derivative controller
RGB . . . . . red, green and blue
ROM . . . . . reduced order model
SB . . . . . soft-baked
SCTE . . . . . secant coefficient of thermal expansion
UCST . . . . . upper critical solution temperature
UV . . . . . ultraviolet
VCCS . . . . . voltage-controlled current source
VCVS . . . . . voltage-controlled voltage source
VSM . . . . . vibrating-sample magnetometer

List of Chemicals

NIPAAm . . . . . *N*-isopropylacrylamid
PNIPAAm . . . . Poly(*N*-isopropylacrylamide)
P(NIPAAm-co-SA) Poly(*N*-isopropylacrylamide-co-sodium acrylate)
SA . . . . . Sodium Acrylate
PI . . . . . 2-Hydroxy-4'-(2-hydroxyethoxy)-2-methylpropiophenone
Ordyl SY355 . . . dry film resist
ITO . . . . . Indium-Titan-Oxid
BIS . . . . . *N*,*N*'-Methylene-bis(acrylamide)
PDMS . . . . . Polydimethylsiloxane

List of Symbols

Symbol	Unit	Description
A	m^2	area
C	-	concentration
C_{10}, C_{01}	Pa	Mooney-Rivlin parameters for deviatoric deformation
D	m^2/s	diffusion coefficient
DD	Pa	Mooney-Rivlin parameter for incompressibility
D_{fac}	s	damping factor
E	Pa	Young's modulus
F	N	force
F_{ij}	-	defomration gradient
G	Pa	shear relaxation modul
G	$\mathrm{m}^3/(\mathrm{s}\,\mathrm{Pa})$	fluidic conductivity
G'	Pa	shear storage modul
G''	Pa	shear loss modul
I	A	current
J	$\mathrm{mol}/(\mathrm{m}^2\,\mathrm{s})$	diffusion flux
K	N/m	mechanical stiffness
L	N, W	Lagrangian multiplier
PF	-	penalty factor
Q	-	volume swelling degree
R	$\mathrm{s}\,\mathrm{Pa}/\mathrm{m}^3$	fluidic resistance
ST	°C, K, %	stimulus variable
T	°C, K	temperature
U	V	voltage
V	m^3	volume
$\Delta\mu$	$\mathrm{m}^3\,\mathrm{Pa}$	chemical potential
Λ	-	stretch ratio
Ψ	V	electrical potential
α	$1/$°C, $1/\mathrm{K}$	thermal expansion coeefficient
β	-	material parameter, Monney-Rivlin solid
χ	-	Flory polymer-solvent interaction parameter
χ_2	-	Flory non-linearity factor
δh	J/mol	interaction enthalpy change
δs	J/mol	interaction entropy change
$\dot{V}$	m^3/s	volume flow rate
$\dot{m}$	kg/s	mass flow
η	$\mathrm{Pa}\,\mathrm{s}$	dynamic viscosity
κ_0	$\mathrm{m}/(\mathrm{s}\,\mathrm{Pa})$	polymer permeability
λ	$\mathrm{W}/(\mathrm{m}\,\mathrm{K})$	thermal conductivity
$\mathscr{A}$	J/m^3	free energy density
$\mathscr{F}$	J	Helmholtz free energy

Symbol	Unit	Description
$\mathcal{G}$	Pa	shear modulus
$\mathcal{K}$	Pa	bulk modulus, osmotic modulus
$\mathbb{Q}$	W	heat flow rate
$\mathcal{R}$	$\mathrm{J/(K\,mol)}$	universal gas constant
$\mathcal{k}$	-	geometry factor
$\mathcal{m}$	$\mathrm{kg/mol}$	molar weight
$\mathcal{r}$	-	ratio parameter
ν	-	Poisson's ratio
ϕ	-	inverse swelling degree
σ	Pa	mechanical stress
τ	s	rise time
ε	-	strain
φ	$^\circ$	angle
ϱ	$\mathrm{kg/m^3}$	mass density
ζ	-	coefficient of friction
b,a	-	time adaption factor
c	F, $\mathrm{J/(kg\,K)}$	electric capacitance
h	m	height
hys_{hyst}	-	hysteresis tollerance factor
k	-	curvature factor
k_B	$\mathrm{m^2\,kg/(s^2\,K)}$	Boltzmann constant
l	m	length
n	-	power factor
n_S	mol	solvent amount
n_{avrg}	-	spatial parameter
n_{sgn}	-	sign value parameter
p, P	Pa	pressure
r	m	radius
t	s	time
u	m	displacement
v	$\mathrm{m/s}$	velocity, speed
w	m	width
x,y,z	m	coordinate variables

Chapter 1

Introduction to Microfluidic Systems

content of chapter

Microfluidics focuses on the development of regulated, intelligent microsystems that are able to handle, dose, measure and analyze small amounts of liquids or gases in a confined space, typically in the sub-millimeter range. It plays an important role in the development of miniaturized analysis systems, e.g. Lab-on-a-Chip for medical technology and biotechnology, but also can include process technology, sensor technology and consumer goods [1]. Microfluidics can therefore be a key to challenge the spread of Covid-19 and are an essential building block for IOT in health care [2].

Especially microfluidic systems for diagnostics are usually arranged in a polymer chip and consist of multiple components such as pumps, channels, junctions, mixers, switches and reaction chambers. These chips have a wide variety of applications, ranging from chemical processing such as mixing multi-phase flows with high-precision [3], enzyme cascade microreactions [4]–[6] to the generation of material samples in the micrometer and nanometer range, which is often impractical with conventional macroscopic technologies [7].

One of the most prominent application for microfluidic devices are Lab-on-a-Chip systems. These microfluidic chips often emulate a very complex environment to enable cell metabolism and growth. For example, when examining lung cells, they not only have to be in an environment with adequate nutrition, but also the stretching movement of the lungs must be stimulated for optimal adaptations [8], [9]. For body cells, in-vivo cell systems must replicate further conditions such as gravity, pressure, shear stress and other physical or chemical parameters to mimic their place of origin. Once the artificial environment has been adapted, reliable cell studies [10]–[12] are possible. As an example, the cell responses to viruses and the corresponding medications can now be examined and enable specialized point of care diagnostics [13], [14]. It is even envisioned to replicate entire organ reactions (organ-on-a-chip) [8], [15] and body metabolism (human-on-a-chip) [9] in order to test the effectiveness and its doses of the medication preclinically. These systems actually use human cells to avoid expensive and ethically contentious animal experiments which are known to not adequately replicate the human organism or its metabolic mechanisms [12].

Microfluidic systems are also required in a new area of biological tissue engineering. There the goal is to assemble cells into living biological tissue that structurally and morphologically represent the same targeted biological functions. The microfluidic systems must be able to provide nutrition and chemical substances to the cells and must simultaneously allow for sensing and analyzing the cell response by different measurement technologies [16]–[18]. The

challenge is that, in contrast to classic polymer lab-on-chip systems, 3D tissues have to be assembled with high precision and all chemical and nutrient gradients have to be adequately taken into account. This poses many challenges in terms of material, technology and design, but could potentially save many lives if, for example, the entire organic system can be manufactured ex vivo and without animal support [19].

1.1 Chemofludic Enables Scalable and Logical Microfluidics

Since the 1990s, Lab-on-a-Chip systems have regularly shown great potential for the integration of fluidic circuits and promise to revolutionize complex laboratory processes with high palatalization capabilities [12], [20]–[22]. However, during the Covid-19 pandemic, when millions of the same tests were taking place, no Lab-on-Chip system could be considered for the required detection. Instead, comparable labor-intensive methods are used to extract the RNA by pipetting and perform real-time PCR [23]. The reason is most likely that classic Lab-on-Chip systems mainly consist of passive elements and are often only controlled by external devices. There is a lack of real autonomous processing with active components such as a microfluidic transistor, which hinders the use of microfluidic systems for real applications. Many different concepts have been proposed for the development of microfluidic valves, which are often used either electromagnetically [24] or electrostatically [25], piezoelectric [26] or pneumatically [27].

It is postulated that microfluidic devices can only be used successfully if real logical microfluidic systems are developed [28]. Most of the work is focused on micropneumatics where a gas pressure can squeeze an adjacent membrane-insulated channel and thus control the fluid flow. This intuitively leads to controllable microfluidic designs, and similar to microelectronics, many combinatoric circuits [29], [30], flip-flops, a four-bit processors [31] or a 12-bit counters [32] could be implemented.

In general, micropneumatic devices scale through the application of micro-technologies, but the increase in chip functionality is proportional to the required external devices such as electromagnetic valves and pumps that must be handled by a computer-controlled system. A solution to this scaling problem could be a microfluidic platform based on hydrogel, which was first introduced in [33]–[35]. There a hydrogel is used to control the flow of fluids based on the environmental stimuli. Hydrogel-based microvalves have a transistor-like behavior and can be compared to transistors in microelectronics. It is noteworthy that thermally controlled hydrogel-based microvalves require an additional electronic layer, which is why only chemically powered microfluidics can really scale without external devices. Chemofluidic logic circuits such as AND, OR, NAND and NOR [6], [36], a chemofluidic oscillator [37] and an analog-digital decoder have already been demonstrated and are modeled in **Section 7.3**. In chemofluidics, non-electronic and autonomous preprogrammed circuits can be developed that are used for diagnostic assays such as drug and cell studies in high throughput screening applications [38]–[40].

These IC demonstrate the flexibility of chemofluidic systems, and the independent function can now be scaled down to the minimal volume requirements. MEMS-compatible methods that are comparable to microelectronics are used to produce these microfluidic circuits.

Now a scaling law like Moore's law could be derived. To ensure the potential success of the hydrogel based chemofluidic platform, three cornerstones must be fully mastered:

1. **Material**
2. **Technology**
3. **Design Automation**

Due to the photo patterning of hydrogels with a reversible volume phase transition, they can be integrated into the MEMS concept [35], [41], [42]. With the help of soft lithography [43] and further developments in the 2.5-dimensional process [44], competitive manufacturing as known from microelectronics can be established for scalable volume-dependent microfluidic circuits. Compared to microelectronics, however, design automation in microfluidics is critically underdeveloped. Simulation tools for the flow behavior in microfluidics are known [45], but in particular there is no transistor-based platform with bidirectional chemofluidics. A possible **MDA** concept must offer an **IC platform** for microfluidics which captures the pressure-flow-relationship and the stimulus transport simultaneously. The library elements must be comprehensive, adaptable and user-friendly to model various applications without long training periods. The aim of this work is therefore to provide essential design strategies for the initiation of these tools.

1.2 Focus of this Work

Challenging in modeling of active polymeric systems are the complex and nonlinear interactions of different physical domains. It is not just the nonlinear hyperelastic material law, which is often represented by Mooney-Rivilin solids in computational mechanics. Difficulties arise in modeling of stimulus dependent swelling functions for hydrogels which show saturation effects and hysteresis depending on the signal history. The static and dynamic swelling response must be described accurately in order to analyze the volume phase-transition and the related fluid flow through the micro-valves. The synthesis process of hydrogels affects all these nonlinear material properties. Even in the same batch, strongly different properties could be observed.

For the resulting chemofluidic component description, versatile and complex nonlinear behavior need to be implemented, which is conceptually flexible for an entire range of hydrogel-based chemofluidic circuits. In the proposed chemofluidic toolbox, governing equations are described by material, physical and dimensional parameters which have to be adapted to the material composition of the hydrogel and the current layout of the functional elements. The component behavior is either defined by analytical equations derived from the theory, extracted from finite element simulations results or taken from measurements. A sophisticated computer-aided design process is vital to develop advanced systems in shortest time.

Several modeling approaches for microfluidic systems have been published recently [45], [46]. They are focused on a special application and model components by analytical terms. For instance, the Hagen-Poiseuille equation defines the fluidic resistance in microchannels and microvalves. Those models are appropriate for conceptual design but cannot provide the accuracy which is needed for the final stage of product development. In this work, it will be

shown, that the flow channel in hydrogel-based microvalves is a complex three-dimensional structure and requires CFD simulations to determine the true volume flow rate for given stimuli signals.

The goal of this thesis is to develop an automated modeling and simulation approach for microfluidic systems with a special focus on hydrogel-based microvalves:

- The proposed model generation process should be easy to use and allow great flexibility in designing a variety of systems for microfluidic applications. Frequently used core elements are implemented in a library of the microfluidic toolbox. The elements can then be placed as a custom library element in a user defined model and parameters are set or modified through a mask in a GUI. The interface ports operate bidirectionally for both, the fluid flow and the stimulus transport which reduces the wiring effort of microfluidic circuits [47].
- The implemented models support fast and accurate transient simulations. Many specific functional details have been assigned to the library elements to improve the performance. For instance, the hydrogel-based microvalve allows for arbitrary swelling functions, considers static and transient hysteresis effects in the hydrogel, models the transient response based on the cooperative diffusion coefficient and evaluates the fluidic resistance from data obtained by CFD simulations.
- Characteristic material parameters for new hydrogel compositions can be automatically extracted by experimental characterization for modeling and simulation. A computer-controlled test stage measures the swelling response at different stimuli by optical inspection. The area change of the hydrogel is determined by an image recognition procedure and provides necessary data for the volume swelling degree in subsequent simulation models.
- A one-way fluid-structure interaction (1-FSI) routine in the finite element program ANSYS-CFX has been developed to extract fluidic resistance functions for new microvalve designs. The routine models swelling of hydrogels by a thermo-mechanical analogy relationship whereby the coefficient of the instantaneous thermal expansion is adapted to the measured swelling response. It provides 3D models of the hydrogel at different swelling states which are transferred by moving wall boundary conditions to the fluidic domain. Transient CFD-simulations extract data for fluidic resistances which are utilized in the system model library elements.
- The microfluidic toolbox should be implemented in a software environment which is widely used in academic education and industrial research. The software should be suitable for microfluidic designs and provide interfaces for other system components. Matlab supports signal flow graphs and generalized Kirchhoffian networks in one model at the same time. It offers toolboxes for function fit procedure, symbolic mathematics, image recognition routines and signal processing. Not only the simulations but also the preparation of new library elements and the evaluation of simulation results (post-processing) can be realized in the same modeling environment.
- A layout synthesis concept is envisioned for the future. The concept is shortly introduced at the end of this work. The layout synthesis is an optimization routine, which modifies design and layout parameters, places the element to certain positions and connects the

fluid channels automatically to the interface ports. At the end of the layout synthesis, the tool creates the mask layout and provides characteristic data for the microfabrication of prototypes.

This work is structured into 8 chapters with additional information in the appendix. As shown in **Figure 1.1**, each chapter is organized sequentially, whereby the most important results are required as inputs for the topics covered in the next chapters.

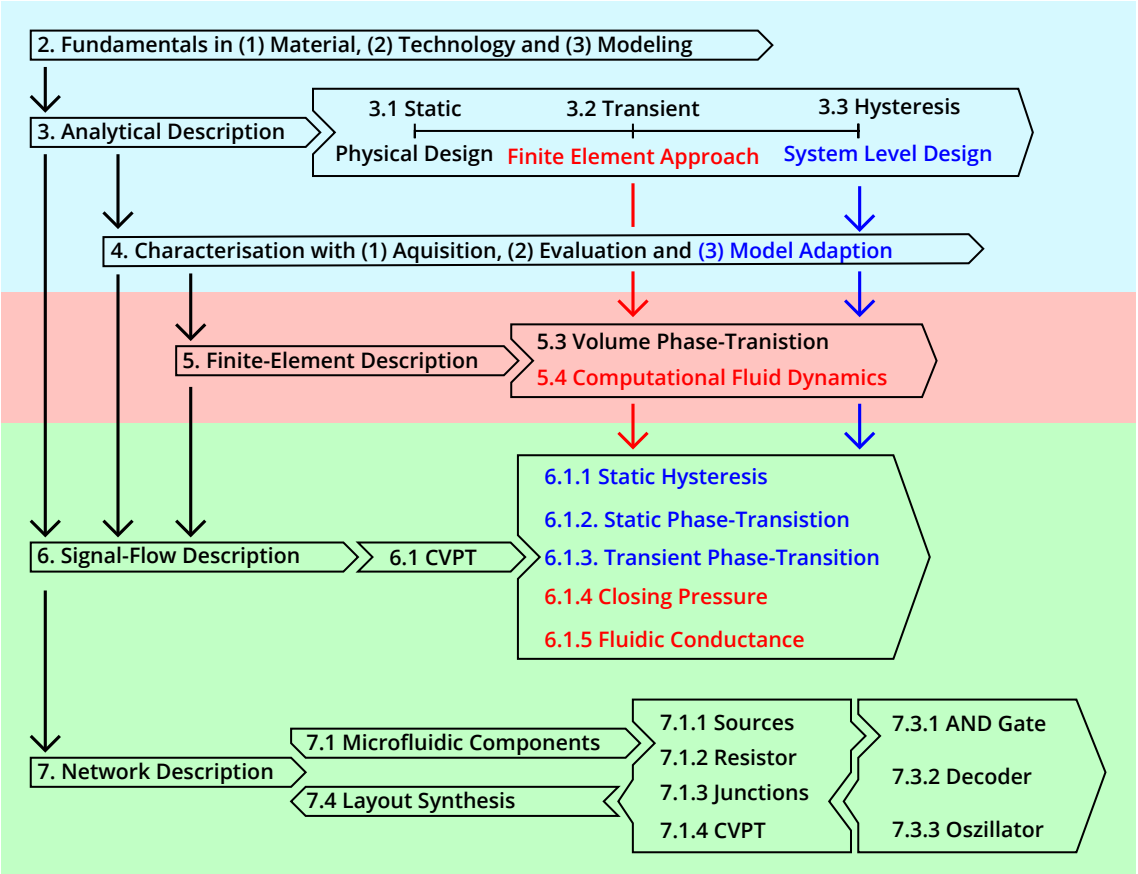

Figure 1.1: Overview of the chapters and its dependencies.

Chapter 1 begins with an introduction to the work. It illuminates the latest developments in the field of microfluidics and focuses in particular on chemofluidic logic circuits. Chemofluidic logic circuits enable autonomously working lab-on-chip systems for medical, chemical and biological applications. Chemofluidic logic circuits require special design tools that record stimulus-dependent flow rates in microfluidic systems. Such software does not yet exist. Requirements and key elements for a sophisticated Microfluidic Design automation (MDA) toolbox are explained in detail.

Chapter 2 introduces hydrogel as a functional material, its synthesis, the fabrication process of a microfluidic chip and general design methodologies for microfluidic components and systems. The chapter defines essential parameters and physical properties, which describe hydrogels as an active and smart material in microfluidic applications. It follows a summary of modeling and simulation techniques and the computer-aided design processes, which are used to describe active microfluidic systems.

Chapter 3 focuses on the theoretical background and related analytical and numerical methods for describing the swelling behavior of hydrogels. It starts with the quasi-static response, which can be used for slowly varying processes. It provides the theoretical basis for the volume phase-transition, which is represented by sigmoidal functions in subsequent simulation routines. Transient effects are based on the theory of Tanaka and Doi. The rise time can be estimated analytically for basic shape elements such as rods or spherical hydrogels. Finite element routines provide access to any structure, with the swelling reaction being modeled by thermal expansion. The final part is the theoretical background for modeling static and dynamic hysteresis effects in system-level simulations.

Chapter 4 deals with the development of a computer-aided measurement routine for the transient swelling response of hydrogels with the aim of reducing manual labor, increasing throughput and improving accuracy and repeatability. The measurement setup and the evaluation software enable the bulk characterization of individual hydrogel samples in order to record statistical properties and estimate optimal parameters for a minimal loss of yield. The data acquisition routine is based on LabVIEW and records the behavior with up to $10\,\mathrm{Hz}$. The following image processing routines in Matlab evaluate the characterization results in parallel. A fully integrated, GUI-based design and measurement process was implemented, which is intuitive to use and predicts the experimental results for further use in component and system models.

Chapter 5 is focused on finite element modeling of microfluidic components. Analytical descriptions exist only for simple shape elements such as straight channels or ideal junctions. Hydrogel based micro-valves are three-dimensional components and its behavior can hardly be approximated by analytical terms. Three-dimensional finite elements simulations are necessary to determine the swelling response of hydrogels and the related change of the fluidic resistance in the flow channel. The hydrogel swelling is modeled by thermomechanical expansion whereby the related material parameters have been adapted to measurement results obtained in the previous chapter. Furthermore, the fluidic resistances are simulated for different swelling states in ANSYS-CFX. Moving wall boundary conditions are implemented in the FSI) routine to capture the changed channel topology during transient simulation steps. Finite element results are utilized in further system simulation models by fit functions or lookup tables.

The most complex and essential component in chemofluidics is the microvalve. In **Chapter 6**, a detailed signal flow graph is developed to model the stimulus dependent fluid flow through the micro-valve. Hysteresis effects, the quasi-static and transient volume phase-transition, the elastic compression of the hydrogel on the walls, the associated closing pressure and leakage rate as well as the fluid flow behavior are implemented and tested in Matlab/Simulink library elements. It was shown that the physical behavior and the interactions of fluid and stimulus domains can be simulated precisely and efficiently. Difficulties arise from algebraic loops in larger models.

A current limitation in Matlab/Simulink is that cascading signal flow models and network models are not supported. Therefore, the previously discussed signal flow models are revised and implemented in Matlab/Simscape. **Chapter 7** discusses the final modeling approach, in which microfluidic library elements are represented by a combination of signal flow models and network model components. It could be shown that the volume phase-transition can be

efficiently described by signal flow graphs and the bidirectional pressure-flow relationship by generalized Kirchhoffian network elements. The implemented library elements were used to model a chemofluidic NAND gate, an analog-digital decoder and a chemofluidic oscillator. Finally, a 2D layout synthesis routine is envisioned, which extracts the mask layout for certain design and process settings.

Chapter 8 summarizes the previous chapters and highlights most important results and their implications. Based on the achieved results, a short overview of possible next steps is given to further improve the simulation capabilities for scalable integrated chemofluidic circuits.

Chapter 2

Fundamentals for Hydrogel-based Lab-on-Chip Systems

content of chapter

This chapter introduces hydrogels as a functional material, its synthesis and the used fabrication process of chemofluidic chips with hydrogel components. Based on these materials and behaviors, the general design methodologies are derived which are used in this work to describe active microfluidic components and integrated circuits.

This thesis is focused on modeling, simulation and characterization of microfluidic devices. However, design and characterization of new products require fundamental knowledge of manufacturing technologies and physical effects of involved components and materials. The first section of this chapter defines essential parameters and physical properties which describe a hydrogel as an active and *smart material* in microfluidic applications. The next section gives a brief overview of the synthesis and the used microfabrication process of the hydrogel-based chemofluidic circuits. Finally, the third section introduces modeling and simulation techniques and the computer-aided design process which are used to describe active microfluidic systems.

2.1 Basic Hydrogel Material Behavior

Hydrogels are functional materials which consist of a water volume (hydro-) and a polymer network volume (-gel). The amount of solvent which is stored in the gel can be controlled by different stimuli. It leads to dimensional changes known as swelling. This change in volume and shape can be utilized for several sensor and actuator applications. A stimuli-driven, hydrogel-based transistor for chemofluidic logic circuits will be discussed and is the main focus in this work.

Since hydrogel was first reported in 1948 [48], numerous papers and reviews on the capabilities of hydrogels, its material properties and the general physical and chemical behavior have been published [49]–[51]. Those material data provide valuable information for modeling and simulation of hydrogels in fluidic devices. However, if the composition of the hydrogel or the process conditions are changed, the resulting material properties often vary significantly. For this reason it is recommended to measure the basic parameters for every synthesized hydrogel, categorize them and according to the design specification select the

proper materials, to reliably manufacture chemofluidic devices. Through automated characterization and system-oriented descriptions it does not necessarily result into an increase in labor. Since component and systems models in this work are based on phenomenological quantities, they can be easily measured and adapted to other materials properties and geometric layouts for any given design task.

2.1.1 Basic Swelling Behavior

One of the most investigated hydrogels is Poly(*N*-isopropylacrylamide) (PNIPAAm), which is sensitive to many stimuli such as temperature [52], chemical concentration levels (e. g. ethanol in water) [53], [54], bio-molecules [55], [56], electric fields [57] or the pH values [58]. It makes hydrogel very attractive for sensor and actuator applications, but the variety of stimuli causes cross-talk when different signals are overlaid at the same time. In most articles, the temperature stimulus has been investigated and exploited for practical applications.

Thermoresponsive hydrogels show a typical swelling behavior especially around a so called lower critical solution temperature (LCST). When the ambient temperature is increased, the polymeric chains are more attracted to each other and start to entangle. Thereby, these chains reduces the hydrophilicity and squeezes the solvent out of the gel. The hydrogel shrinks to the collapsed state. When the ambient temperature is decreased, the polymeric chains disentangle whereby the hydrophilicity increases and ambient solvent is absorbed by the material. The hydrogel swells and the material changes to the swollen state. A third state is the dried state, in which there is no solvent in the gel and only the polymer network remains. Then, the hydrogel has its smallest size. It is a possible reference level, but it can not be used for the targeted microfluidic applications [59].

2.1.2 General Properties of Hydrogels

The practical operating range of hydrogels for chemofluidic systems is between the collapsed and the swollen state. Changes in size during the swelling process are described by a characteristic length $l(T)$ which might be the thickness of thin gels or the radius of spherical gels. It is a dimensional parameter of the hydrogel which is relevant for modeling of microfluidic devices and effects the functional behavior. In the collapsed state, the characteristic length has its minimal value defined by l_0. In the swollen state, the characteristic length has its maximum value defined by l_1. The swelling ability is described by the total length change $\Delta l = l_1 - l_0$ which is calculated from the upper and lower bounds of the characteristic length in the operating range.

Since most hydrogels swell isotropic, the characteristic length $l(T)$ can be converted into other dimensional parameters or functions which describe the surface or the volume of the hydrogel with regard to the stimulus. For modeling and simulation, it is convenient to define material parameters which do not depend on the size of the specimen. For this reason, swelling-stimulus functions are defined by ratios where the characteristic length $l(T)$ or the volume of the gels $V(T)$ are divided by reference values which are usually taken from the collapsed state (e.g. l_0, V_0). The relative volume change is known as volume swelling degree

$Q(T) = \frac{V(T)}{V_0}$ and its inverse is referred as polymer volume fraction $\phi(T) = \frac{1}{Q(T)}$. Both functions describe the quasi-static swelling behavior of hydrogels.

Another important parameter is the threshold temperature at which the hydrogels transitions from the swollen to the collapsed state. For the case of PNIPAAm, this temperature is called lower critical solution temperature (LCST). If the hydrogel can only transition once, then the process is called volume phase-change. If the this transition is fully reversible, then the process is called volume phase-transition. This volume phase-transition is not a sudden change at the threshold temperature, rather the hydrogel change the swelling state smoothly in a certain temperature range. Especially for continuous systems, volume phase-transition hydrogels are utilize in applications like microfluidic transistors [36], [38], [60], [61] or chemical sensors [62]–[64]. For one-time processes, which are common in e.g. diagnostic, volume phase-change hydrogels can be used. This work will focus on reversible phase-transition hydrogel behaviors, because a reversible phase-transition description can also describe phase-change behaviors with only minimal adaptions. In this work, the phase-transition is described by a sigmoidal function either as a characteristic length $l(T)$ or the volume swelling degree $Q(T)$ with regard to the stimulus as a temperature T or a concentration C.

For the transition temperature a characteristic property of the hydrogel is the ratio of hydrophilic and hydrophobic polymeric components within the macro-molecular structure of the copolymer [65], [66]. Thermoresponsive hydrogels are divided into two categories. The first category shows a phase separation at increasing temperatures and the transition point is referred LCST. Hydrogels of this type shrink at increasing temperatures and a more extensive discussion with the focus on the thermodynamic phenomenon will be given in **Section 3.1.1**. The other category shows a phase separation for decreasing temperatures and the transition point is referred UCST. Hydrogels of this type swell with increasing temperatures. The physical background and the synthesis of both hydrogel types are discussed in [67].

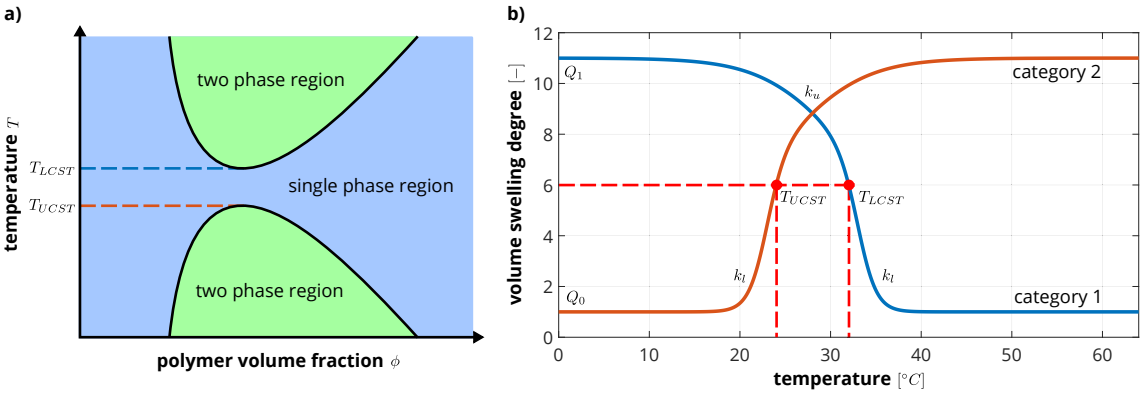

Figure 2.1: LCST values extracted from the polymer-solvent mixture plot and from the volume-phase transition curve.

The terms LCST and UCST are related to the phase transition of polymers in a solution [68]. Below of the LCST value, hydrogels of the first category are in a hydrated state and become soluble for all compositions expressed by the polymer volume fraction ϕ in **Figure 2.1 a)**. Accordingly, the hydrogels swell under the critical temperature and collapse above it. The lower critical temperature of the hydrogel can also be extracted from the

volume phase-transition curve $Q(T)$ or from the characteristic length $l(T)$ as shown in **Figure 2.1 b)**. The LCST value is commonly defined as the temperature where the function value of $Q(T)$ or $l(T)$ are in the center between the upper and lower bounds. Since the volume swelling degree depends with the power of three on the characteristic length, it shifts the slopes of the curves and the resulting extracted LCST values from both curves are not identical. Another measure could be the turning point of the curve or measuring the translucency change of the gel. In general, there is no strict rule on how exactly to calculate the transition temperature, but all measures give similar results for the LCST value.

An actoric design parameters of hydrogels is the stiffness in the collapsed state and the stiffness change depending on the volume swelling degree. Hydrogels are incompressible hyperelastic materials. Stiffness data are necessary to describe elastic deformations caused by mechanical or fluidic loads and displacement constraints in the assembly. The fluidic pressure can cause leakage rates of microvalves due to local deformations in narrow gaps. For uniaxial tension and compression, the stiffness can be defined by the Young's modulus as a function of the volume swelling degree $E(Q)$. It will be shown that swollen hydrogels are softer as gels in the collapsed state.

Dynamic properties are necessary to characterize the transient response of hydrogels, which are one of the most essential parameters for hydrogel-based transistors. Often only the cooperative diffusion coefficient D_{coop} is described but for component-oriented design simulation, a time constant τ for swelling and shrinking processes are needed. This time constant depend on the geometry and the applied stimulus boundaries. In this work, it will be demonstrated with experimental references, that through numerical simulations, these values can be exactly predicted for arbitrary structures and a size-dependent time function will be formulated for subsequent component and system models.

2.2 Overview of the used Microtechnology

The fabrication of active chemofluidic systems highly depends on the design and the intended applications. In this section, the standard operation procedure, which is used in this work to synthesize and microfabricate hydrogel-based microfluidic chips is introduced. These processes are mainly developed by Dr.-Ing. Philipp Frank, Dr.-Ing. Sebastian Häfner and M.Sc. Anthony Beck of the TU Dresden. Based on their processes the characterization and modeling strategies are derived.

2.2.1 Synthesis of P(NIPAAm-co-SA)

In this work, Poly(*N*-isopropylacrylamide) (PNIPAAm) is copolymerized with Sodium Acrylate (SA) to improve the swelling behavior of the material. Therefor, P(NIPAAm-co-SA) is the material of choice and here the synonym "hydrogel" is related to PNIPAAm with 2.5% SA.

Material: For starting material *N*-isopropylacrylamid (NIPAAm, Sigma-Aldrich, St. Louis, MO; USA), n-hexane (VWR, International GmbH), Sodium Acrylate (SA, Sigma-Aldrich, St. Louis, MO; USA), *N*,*N*'-Methylene-bis(acrylamide) (BIS, Sigma-Aldrich, St. Louis, MO; USA) and 2-Hydroxy-4'-(2-hydroxyethoxy)-2-methylpropiophenone (PI, Irgacure 2959, Sigma-Aldrich, St. Louis, MO; USA) are used as received.

Synthesis of the Prepolymers: As a first step, NIPAAm is recrystallized with n-hexane for purification purposes. Then, NIPAAm ($2.069\ g$), SA ($0.044\ g$), BIS ($0.043\ g$), de-ionized water ($15\ g$) and PI ($0.043\ g$) are weighed in a round bottom flask and sealed with a septum. The mixture is stirred under an argon flow for 30 minutes in order to create an inert solution. Finally, the flask is covered with a tin foil to protect the mixture from UV-light and the pre-polymer solution is stored in a refrigerator at $7°C$ [69].

Photo-structuring: Figure 2.2 shows the process flow for photo-structuring of hydrogels. Thereby a glass slide and a spacer form a cavity (1), which is filled with the pre-polymer solution (2). This cavity is then covered with a glass photo-mask (3) and is subsequently UV-exposed for 15 seconds with a 365 nm wavelength (i-line) light-emitting diode (LED) array (4). After the exposure, the glass mask is removed and the substrate is rinsed (5). Finally, the spacer is detached (6) and the patterned hydrogels can be used for the microfluidic chip (7) [70].

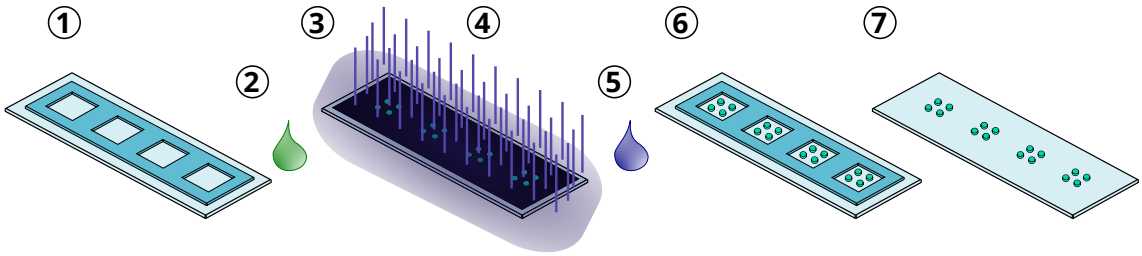

Figure 2.2: Photo-structuring process of PNIPAAm hydrogels.

Chemical Reaction: The photo-initiator (PI) disintegrates during UV radiation and free radicals are formed. These radicals break the double bond of the monomers in NIPAAm, SA and BIS, which immediately causes a chain reaction and polymer chains are formed. These chains interconnect to each other and when, for example, NIPAAm and SA are bonded, a copolymer is obtained. Together with BIS, a three-dimensional polymer network matrix leads to a solid material. The applied process causes the compounds to be shaped randomly known as random radical polymerization. FTIR can be used to monitor the absorption of light for certain binding structures, which generates a unique fingerprint for each hydrogel. The chemical equations for the process are summarized in **Figure 2.3**.

The radical polymerization is ended by switching off the UV light. The remaining open bonds of the polymer either react with other open bonds of a polymer or with other radicals to close the chains. In addition, the free radical can also react with one another to neutralize the polymerization activity.

The radicals in the pre-polymer solution also react with oxygen, which forms oxygen radicals. Oxygen radicals are known to be much less effective, which is why they are often used as inhibitors [71]. The hydrogels should be synthesized in a glove box with an inert gas to avoid oxygen contaminations and drying of the pre-polymer solution. Hydrogels with different compound compositions, the use of various tools for the synthesis as well as their effects on the reaction kinetics are further discussed in [72].

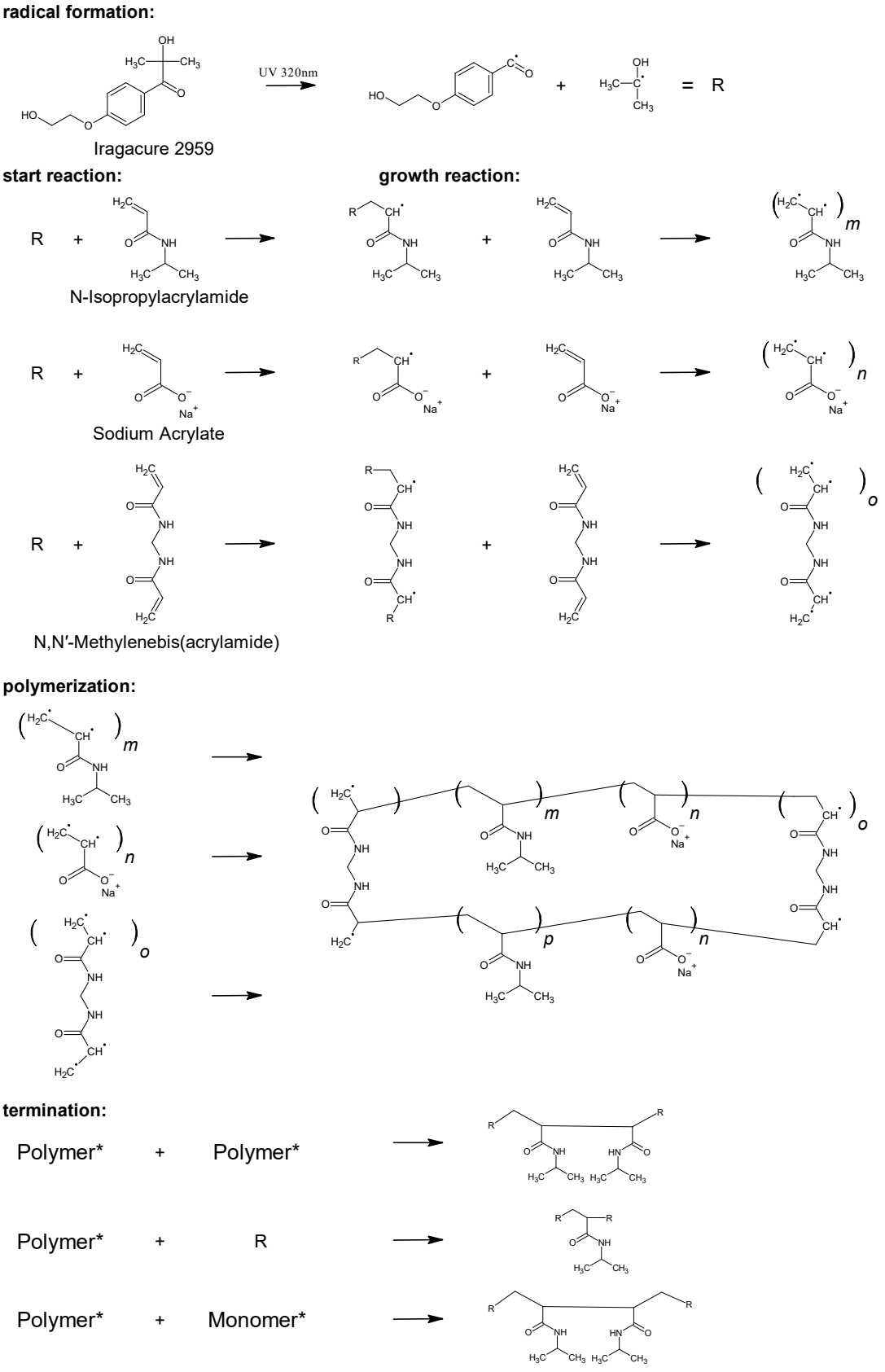

Figure 2.3: Radical Polymerization of NIPAAm and SA with BIS under UV-light.

2.2.2 Microfabrication of a Microfluidic Chip

The common design process of a microfluidic chip begins often with a 3D model of the intended device, which is created in a CAD software such as "Autodesk Inventor" without system analysis. The parametric 3D model is then converted with "LinkCAD" into a 2D mask layout, which is written in a standard "Gerber" format. The layout data are transferred to a photo-structured resist from which a master for a subsequent molding process is obtained. Several PDMS mold samples can then be copied from the master which are bonded on a substrate as basic components for the microfluidic chips.

The master can be either fabricated on a glass substrate (Borofloat 33, Schott AG, Mainz, Germany) or on a microscope slide. It starts with an intensive cleaning process using de-ionized water, followed by isopropanol and finally a nitrogen treatment in order to eliminated all contaminations from the substrate. A dehydration bake at $150°C$ for 20 minutes is recommended to evaporate any remaining liquids from the surface.

As a next step, the microfluidic layout is transferred to the master. The fluid flow domain, which is the cavity in the microfluidic chip, must be filled with a solid material for the subsequent molding process. The solid material is obtained from a photo-structured dry film resist (Ordyl SY355, Elga Europe, Nerviano, Italy), which is laminated on the substrate and SB at $85°C$ for 3 minutes. After aligning a photo-mask, the photo-resist is exposed to UV-light for about 300 seconds and then it is PEB at $85°C$ for 30 minutes. After baking, the dry film resist is structured with Ordyl developer for about 3 minutes and is terminated with Ordyl rinser. The quality of the photo-structuring process can be inspected optically with a microscope. At the end, the master is hard baked at $120°C$ for 1.5 hours.

The next step is the molding process. A PDMS mixture (RTV 615, MG Chemicals, New Mills, UK) with a ratio of 10:1 is poured into a beaker, is carefully stirred and then degassed under vacuum. The previously manufactured master substrate is then placed into a petri-dish and covered with the PDMS mixture. The mold is cured at $60°C$ for 3 hours, which forms solid PDMS samples. The samples is peeled the master and can be treated with a petroleum-ether mixture for 12 hours to remove residual monomers in the PDMS [73], [74].

Now the microfluidic chip is assembled: In a first step, contact holes are punched through the PDMS mold for the inlet and outlet openings. Then the hydrogel actuators are placed in the valve cambers and the PDMS chip with the hydrogel is bonded on the substrate. After the bonding process, tips of syringe needles are pressed into the punched holes. The needle tips act as adapters for the tubes in order to connect pressure or flow pumps. Finally, heating structures and sensors might be integrated for stimuli and flow control. Then the equipment is connected to a computer system to perform automated measurement procedures.

In general, the design of the chip, the fabrication of the photo-mask, the synthesis of the hydrogel actuators, the master fabrication, the microfluidic mold, the assembly, chip contacting and the wiring of the entire measurement setup is quite labor intensive. If an efficient process flow is established and depending on the complexity of the chip, from design to evaluating the results, at least two weeks are needed, which only increases with increasing chip complexity. If the result suggests a design change, then the process starts from the beginning, making the development of novel microfluidic devices very time consuming and often tedious.

2.3 Introduction to Modeling and Simulation Techniques

There are several sophisticated design tools on the market, which allows for modeling and simulation of fluidic systems. Most commonly CFD tools like ANSYS Fluent are used to describe 3D fluidic behavior. Further more specialized tools for microfluidic chips are often tailored to very specific microfluidic applications and describe mostly the resistive behavior analytically. Also an important part is the layout synthesis microfluidic, which does exist for pneumatic microfluidic circuits [45]. However a comprehensive active chemofluidic platform, which includes a chemical and heat transport layer is missing. Microfluidic network models are in development [46], [75] but either they lack of a flexible active micro-valve environment or a flexible bidirectional transport layer, allowing a multi-directional flow regime.

Chemofluidic devices are a very complex multi-domain systems and it is very challenging to create a behavioral model of a temperature or chemical triggered hydrogel-based microvalve. In this particular example, the temperature distribution (thermal domain) changes the size of the hydrogel in the mechanical domain, which affects the conductivity in the fluidic domain. To this bidirectional multi-domain coupling, the phase-transition in the static domain and dynamic properties need to be solvable in the same model. In the transient domain, the volume dependent rise and fall time for opening and closing the valve are of specific interest.

Beside to the microvalve, there are other components such us pumps, flow channels, junctions, and mixers in larger microfluidic systems, which have to be integrated in the same model. All those components interact with each other and a bi-directional fluid-flow and stimulus transport has to be analyzed precisely and efficiently. It needs a computer aided-design process that is focused on the specific requirements for this type of application. Therefore, the goal of this thesis is to develop a component description, which can be used by every microfluidic designer. For each component the goal is to develop a flexible and intuitive interfaces, which are adaptable for specific needs and still predict accurately and efficiently hydrogel-based, active chemofluidic circuits.

2.3.1 Computer-aided Design Methodologies

Most microfluidic research projects plan multiple iteration cycles in advance, consisting of design, prototyping, testing, and improvements, redesign, to eventually create a new device. An accurate and reliable virtual design process will significantly shorten the development cycle, reduce costs and could improve the performance and reliability [76] (pp. 7).

The design process can be classified into two strategies. A **top-down approach** starts from the system requirements and its algorithmic description. It creates subsystems with individual tasks and interactions to each other. Microfluidic subsystems would be, for example, channels, junctions or the valve, which are described by general physical parameters. Each subsystem is then refined into smaller shape elements, which receive a very detailed description based on dimensional parameters. Finally, it leads to the mask layout and theoretically to a working prototype.

The **bottom-up approach** starts from the most detailed description. There, the layout defines the simulation strategies, which predict the behavior of the component [77] (pp. 256). The bottom-up approach is supported by many simulation tools. In a first step, the mask

layout is extruded to a 3D solid model in a CAD system, which is then transferred to a FE tool and the FE-simulation results provide input parameters for system simulations or the electronic circuit design. *The approach is very suitable to analyze existing ideas but new devices can only be developed, if the desired function drives the layout (top-down) and not the layout drives the intended function (bottom-up).*

A combination of the top-down and bottom-up approach is referred **V-model**. In **Figure 2.4** shows a general recommendation for a systematic design methodology of mechatronic systems, which is published in [78].

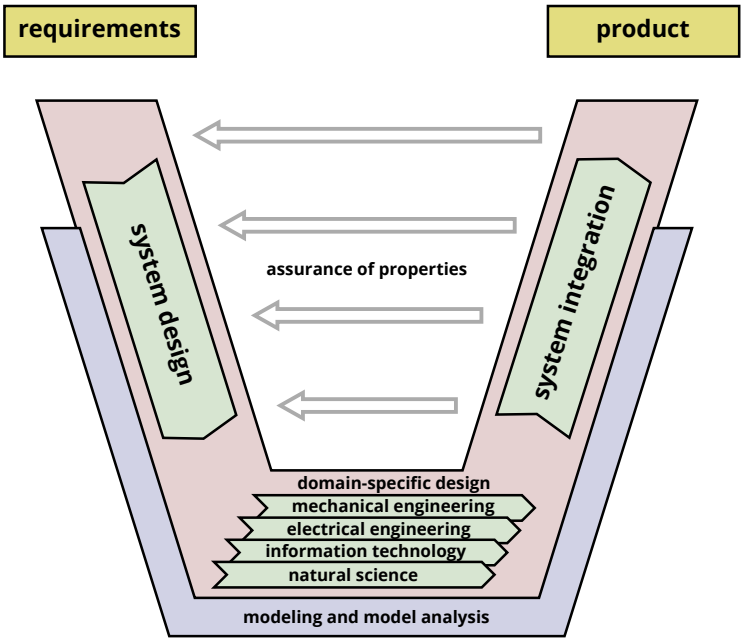

Figure 2.4: V-model for mechatronic design [78].

For the case of microfluidic applications, the V-Model is adapted in **Figure 2.5**. Their, the top-down part starts with clarifying system specifications and the partitioning into subsystems. It is followed by a conceptual design phase, which provides general physical and dimensional parameters based on simplified models. The third step is the component design phase where essential model parameters are verified and improved by, for example, finite element simulations. At the end of the top-down procedure, a mask layout can be generated.

The bottom-up part integrates all component models into a system description. Often, the component models can not directly be connected to each other because system models use a very specific language or modeling strategy. Component models must be translated into the preferred system design environment and the models have to be reduced in their complexity to get an acceptable simulation time. After the virtual computer models fulfill are requirements, real-world prototypes are manufactured and the obtained behavior is verified with the product specifications.

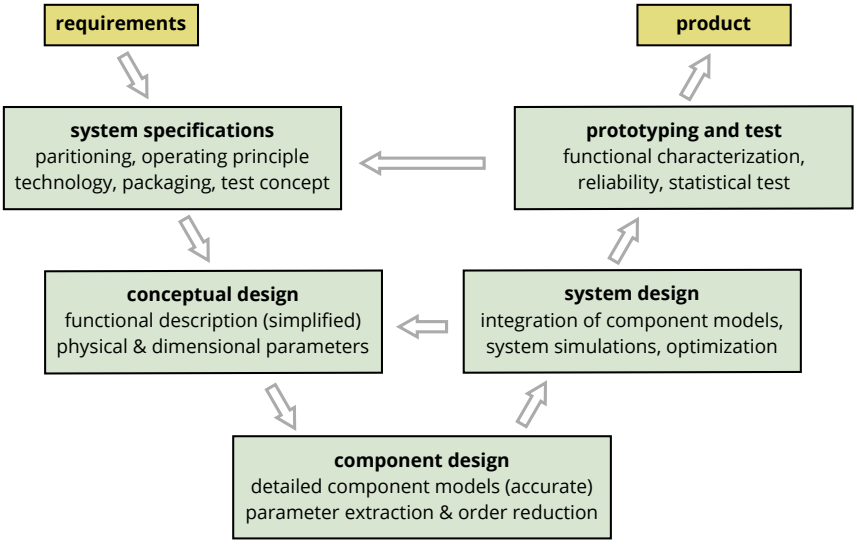

Figure 2.5: Combining top-down and bottom-up for microfluidic design.

2.3.2 Model Abstraction Levels for Computer-Aided Design

Engineering applications and in particular microfluidic devices can be described by various models at different levels of abstraction. All three design phases shown in the V-model of **Figure 2.4** have specific requirements and restrictions on modeling and simulation methods.

The primary goal of the **conceptual design phase** is selecting proper element definitions and to estimate physical parameters and geometrical dimensions for the target application. During conceptual design, the models are usually based on analytical descriptions, which provide the input-output relationship of the target element and its dependency on design parameters by simple mathematical functions. For new design elements, the governing equations are derived manually from the underlaying engineering theory but can then be implemented in a library for repeated use in different applications what will be shown in **Chapter 6** and **7**. The biggest advantage of analytical descriptions is that the relationship between input data, design parameters and the output data are given by mathematical functions. It is easy to calculate function values and derivatives, which are necessary for optimization routines and sensitivity analyses. Likewise, parameters can simply be used in ordinary differential equations to estimate the transient and harmonic response. Simulations are very fast what is the reason that new design ideas can by analyzed, optimized and compared against each other in shortest time. Analytical models can be implemented in mathematical software tools as Matlab, MathCad or Mathematica.

It follows the **component design phase** where parameters and results of the conceptual design are verified and, if necessary, the accuracy is improved. Component models are solved by using FEM where complicated three-dimensional shape elements can be analyzed for arbitrary load situations and boundary conditions. The biggest advantage is the accuracy, but there are also some drawbacks. Finite element simulations are very time consuming, especially for transient simulations with a large number of time steps. The next disadvantage is that finite element simulations just provide result data but no relationship to design parameters. For instance, ANSYS-CFX calculates the fluidic resistance of arbitrary flow channels. The

influence of dimensional parameters such as length, width or thickness on the flow resistance can only be calculated indirectly through data sampling and function fit procedures. Therefore, FEM is seldom used for design optimization and sensitivity analyses. Typical FEM tools are ANSYS, ABACUS or COMSOL.

The final step is the **system design phase** where different analytical and numerical component models are integrated to a comprehensive system description. System simulations analyze the cooperative interplay of different physical components with each other, to electronic circuits and controller units. Often several thousand times steps have to be analyzed to evaluate the performance of microfluidic systems. Finite element model components must be reduced in their complexity prior the integration into the system model environment. It can be realized by data sampling and function fit procedures or lookup tables where the FE-results are represented by a simple input-output relationship. System models are usually based on signal flow graphs or Kirchhoffian networks, which can be implemented in Matlab Simulink/Simscape, Cadance or LTSpice.

Modeling is strongly related to an experimental characterization. Experimental data obtained from earlier designs or data, which are extracted from test structures provide valuable information for models at all three levels of abstraction. Valuable input data are, for instance, the elastic material properties, swelling-stimulus functions or dynamic properties such as the time constant of a step response.

2.3.3 Modeling Techniques for Microvalves in a Fluidic System

The temperature triggered hydrogel-based microvalve is the core element for microfluidic systems in **Chapter 7**. The input-output relationship is schematically shown in **Figure 2.6**. The actuating mechanism is based on a hydrogel, which changes its size due to a stimulus signal. The swelling modifies the cross-sectional area of a fluid channel, which finally affects the fluid flow. The functional behavior can be analyzed by the following steps:

1. The stimulus temperature T changes a characteristic length $l(T)$ of the hydrogel, for instance the thickness at the center. The quasi-static response is directly related to the volume swelling degree $Q(T)$, which is represented by a sigmoidal function in the simulation model. The stimulus dependent quasi-static length is referred equilibrium length $l_{eq}(T)$.

2. The cooperative diffusion coefficient D_{coop} and the size of the hydrogel determine the time constant τ of the valve. The transient response is described by a first-order differential equation, which leads to a stimulus and time dependent characteristic length, which is referred kinematic length $l_{kin}(T, t)$.

3. Hydrogel is an incompressible material and uniform surface loads do not cause elastic deformations. However, pressure gradients Δp and displacement constraints affect the swelling state and a leakage flow can appear. The characteristic length, which includes elastic deformations is referred compressed length $l_c(T, t, \Delta p)$.

4. The fluid conductance is directly related to the cross-sectional area of the valve. For conceptual design, the fluidic conductance can be approximated by the Hagen-Poiseuille

equation. For more accurate component models, the true three-dimensional shape of the fluid channel requires finite element simulations to extract the relationship between the fluidic resistance and the characteristic length of the hydrogel. The fluid domain simulation results at different swelling states are mapped to a fit function $G(l_c)$, which is used for system design.

5. The volume flow rate $\dot{V}(G, \Delta p)$ depends of the fluidic resistance and the pressure difference Δp across the microvalve. It is the output signal of the valve.

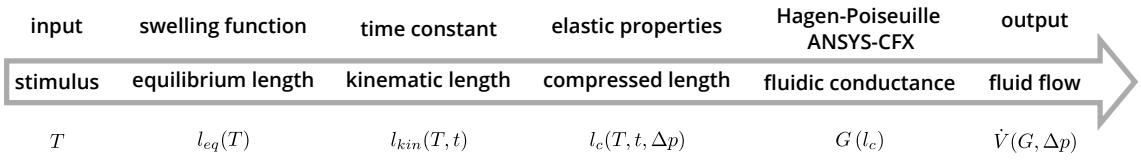

Figure 2.6: Signal flow chart of the temperature stimulated hydrogel-based microvalve.

In practice, the hydrogel's behavior is not simply described by a unidirectional signal flow from the input to the output. For chemical stimuli, the concentration level at the input is directly coupled with the results of the fluid flow at the output and forms a feedback loop. In particular, the chemical stimulus level at the input of the valve depends on the fluid velocity and the flow direction. In fact, the fluid flow and the stimulus transport are usually in the same channels. Consequently, the physical behavior must be described by three quantities, which are the pressure and the volume flow rate in the fluid domain and the chemical stimulus level in the fluid, which is modeled in the transport domain.

Both, fluid and transport domain quantities are coupled what makes modeling and simulation challenging. The theory of Kirchhoffian networks, which relates flow and across quantities could be applied to the pressure-flow relationship but the third quantity, which is the temperature or the chemical stimulus level in the transport domain needs special considerations.

The general design concept of microfluidic system is shown in **Figure 2.7**. It starts with the application concept, which has been explained for a microfluid NAND gate, a microfluidic decoder and a chemo-fluidic oscillator in **Section 7.3**. A first design step is the partitioning into subsystems, which are pressure pumps, flow pumps, channels, junctions, stimulus triggered microvalves and the flow outlets. Each element is described by analytical functions, which take physical, material and dimensional parameters into account. Additionally, the microvalve behavior is based on finite element simulation results for the hydrogel's swelling response, the time constant for the cooperative diffusion process and the fluidic conductance as a function of the characteristic length.

Different methods for modeling and simulation have been implemented and tested. It starts with a pure signal flow description of the microvalve in Matlab Simulink discussed in **Chapter 6**. The model works stable and accurate for individual components but the interconnection to other library elements causes numerical problems with algebraic loops. The microfluidic system has then been reworked and implemented by a combination of generalized Kirchhoffian networks and signal flow graphs in Matlab Simscape. Multiple elements can now be intuitively connected to each other at the interface ports to a model larger microfluidic

system without any numerical issues.

The model generation procedure starts from simple lumped element models, which have been improved in their complexity during the design process. For example, the fluid channel was first represented by a single fluidic resistor and has then been enhanced to a complex delay line consisting of a series of ten active low pass filters. The simulation results are verified with experimental results or data from scientific reports of the devices under test. The presented design methodology has been proven on several examples and can be applied to further microfluidic applications.

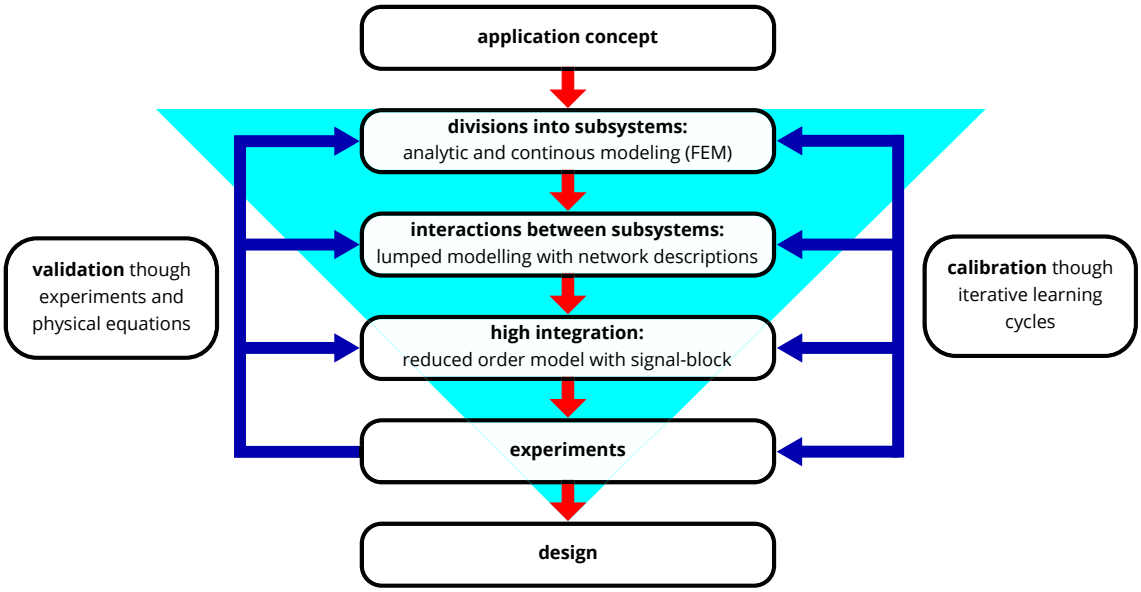

Figure 2.7: Recommended simulation approach starting from a first application idea to modeling a complex geometry with for example finite elements.

Chapter 3

Analytical Descriptions of Swelling

content of chapter

Hydrogels are inherently able to change dimensions and shapes in response to a stimulus. This behavior, known as swelling, offers many possibilities for technical applications in microfluidics, such as hydrogel-based microvalves, which are the focus of this work. Precise and efficient models to describe the static and dynamic behavior of hydrogels are essential to design new devices with optimized performance. The theoretical background on a physical abstraction level and related modeling techniques, which are utilized for component and system design will be discussed in this chapter.

The swelling behavior of hydrogels is described by a thermodynamic energy formulation known as Helmholtz free energy [79]. The Helmholtz function is a thermodynamic potential that measures the energy, which is necessary to transfer a closed system from one stimulus level, in particular a temperature, to another one. To formulate the “closed system” for this conceptual model, not only the polymeric volume of the hydrogel needs to be considered but also the ambient solvent content to accurately predict the swelling effect [80]. The Helmholtz free energy can then be defined as a function of the stimulus and the volume swelling degree. In equilibrium, the Helmholtz free energy function is minimal and the derivative with regard to the swelling degree is therefore zero. For the quasi-static case, the volume swelling degree can be calculated for any given stimulus as demonstrated in **Section 3.1**.

The solution of the Helmholtz equation describes the swelling behavior of the hydrogel without constraints. It provides the fundamental basis for further simulation techniques, which are necessary to model the influence of loads and boundary conditions in a valve chamber and to consider the true shape of hydrogels for practical applications. However, the swelling behavior can also be measured on test specimens, which will be discussed in **Chapter 4**. Measurements are important because the physical models contain empirical terms and their validity should at least be verified on the synthesized hydrogels.

The swelling behavior is analogous to the thermal expansion behavior in structural mechanics. Physically however, they differ. During the swelling process, the stimulus diffuses through the material, cause a change in solvent attraction and then the solvent diffuses into the material, creating the volume expansion. For the thermal expansion behavior, there the temperature distribution affects the atom oscillation in the solid material, which changes the density and ultimately the size of the material. Compared to swelling with molecular interaction, the thermal expansion with atomic interaction is an instant reaction. Never the less,

the differential equation describing the volume change for swelling or the volume change through thermal expansion, are equal and will be further discussed in **Section 5.1**.

The thermal expansion coefficient describes the length change and consequently the volume change of a solid model as a function of the temperature as shown in **Section 3.1.2**. Using analogy relationships, the temperature corresponds to the stimulus and the coefficient of thermal expansion must be adapted to the swelling behavior, which is either obtained from physical models or measurements. In practice, the coefficient of thermal expansion becomes a function of the stimulus and can precisely map arbitrary phase-transition behaviors for modeling and simulation of hydrogels.

In simplest case, the hydrogel can be considered as a single DOF system where a characteristic length is affected by the swelling process depending on the applied stimulus. In such a single DOF model, the characteristic length defines entirely the functional behavior of a microfluidic system. It may seem simplistic, but it gives valuable information about the general behavior and the influence of design parameters for the conceptual phase in prototyping. For detailed investigations, the models are improved in their complexity whereby finite element models are utilized in the final stage of design as shown in **Chapter 5**.

A hydrogel-based microvalve will be discussed in the following sections of this work. In this device, the change in length of the hydrogel opens and closes a small gap in a microfluidic channel and controls the fluidic resistance and consequently the fluid flow through the valve. The 3D swelling behavior can be simulated by finite element models, which take the true shape of the hydrogel and the previously discussed thermal expansion relationship into account.

In addition to the stimulus-dependent swelling, further parameters are required to describe the static and transient response. The swelling process of hydrogels is affected by external mechanical loads and displacement constraints. For the microvalves example, the hydrogel is surrounded by liquids, which are pumped through the valve. This flow causes a pressure gradient on the surface of the hydrogel. Further loads occur at the closed state of the valve, in which the hydrogel is pressed onto the solid walls of the valve chamber. Mechanical loads and displacement constraints initiate elastic deformations, which are described by various stiffness terms in structural mechanics. For uniaxial loads, it is usually the Young's modulus and the Poisson's ratio. For hyperelastic materials, the Mooney-Rivlin model can be used will be shown in **Chapter 5**.

In continuum mechanics, the transient behavior is influenced by inertial and damping forces, which affect the settling time and the rise time of the system. However, the transient swelling response in hydrogels is mainly defined by the solvent diffusion into the gel matrix. This process is referred swelling kinetics in literature [81]–[84]. It has been shown that the solvent penetration is much slower than the stimulus diffusion into the hydrogel and inertial effects can be ignored [85]. Consequently, the transient response is defined by a first-order differential equation whereby the characteristic time constant is defined by the slowest process, which is the solvent penetration. The transient behavior will be discussed in **Section 3.2**.

Finally, hydrogels show a hysteresis effect [86], [87]. Hysteresis is defined by the swelling history and needs to be analyzed in order to predict the current model parameters. Hysteresis can be observed if the swelling and shrinking response to a stimulus change are not identical.

It is hypothesized that the attraction of the solvent caused by the hydrophilicity change of the material [88] could explain this irregularity, which can be observed by slowly varying stimulus signals. In **Section 3.3.1**, the process is referred as static hysteresis and is described by a hysteresis offset parameter, which shifts the phase-transition curves to the right or to the left.

A second type of hysteresis is referred as diffusion-based hysteresis and can be observed for fast varying processes in the time domain. It is a transient effect and depends on the characteristic time constant of the first-order differential equation and the stimulus frequency. The characteristic time constant in the model is similar to a damping coefficient in a spring-mass-damper system and causes energy dissipation in each stimulus cycle. It can be observed by hysteresis loops, which widens with higher frequencies and larger time constants. Diffusion based hysteresis will be discussed in **Section 3.3.2**.

3.1 Quasi-Static Description

The quasi-static swelling describes the dependency of the volume swelling degree Q or its inverse, the polymer volume fraction ϕ with regard to the stimulus temperature T. It is a nonlinear relationship and requires an iterative solution procedure in numerical simulation tools. Time-dependent effects caused by the diffusion process are described in **Section 3.2**.

In **Section 3.1.1**, the quasi-static swelling behavior is derived from the chemo-thermodynamic energy formulation on the physical level of abstraction. In the next chapter, the swelling behavior and the elasticity of the hydrogel are represented by a thermo-mechanical analogy relationship. The hydrogel behavior will be described by analytical terms, which are expanded to a matrix method for uniaxial swelling. The matrix methods are utilized in finite element tools for 1D truss elements and illustrate the general modeling approach of thermo-mechanical interactions in simulation tools. 2D shell elements and three-dimensional (3D) solid elements for advanced finite element simulations are derived from the one-dimensional (1D) case. Finally in **Section 3.1.3**, the swelling behavior is described by sigmoidal functions, which are widely used in numerical models to represent phase-transition processes with saturation effects. The proposed sigmoidal functions can be adapted easily to various input functions and can be efficiently evaluated in the system-level modeling process.

3.1.1 Physical Static Chemo-Thermal Description

The quasi-static swelling behavior of hydrogels is based on molecular interactions (chemical properties) and chain-solvent interactions (physical properties). A comprehensive physico-chemical description was first developed by Huggins [89], [90], Flory [91]–[93] and Rehner [94], [95]. It defines the static equilibrium of the volume change as a function of the applied temperature and the molar chain weight of the polymer. The theory presented in this chapter is based on [80].

The hydrogel consists of a polymeric volume V_p in the dried state and a solvent volume V_s, which penetrates into the hydrogel during the swelling process. The total volume of the hydrogel in a swollen state is defined by $V_{HG} = V_p + V_s$. In the following model, the swelling

behavior is either described by the volume swelling degree Q or by its inverse, the polymer volume fraction $\phi = \frac{1}{Q}$. The volume swelling degree Q is the ratio of the volume in the swollen state V_{HG} and the volume in the dry state V_p.

The swelling behavior of hydrogels is analyzed by the Helmholtz free energy equation $\mathscr{F}(T, \phi)$, which can be expressed as a function of the temperature T and the polymer volume fraction ϕ. The model is solved for a constant volume of the polymer $V_p = const$, which is immersed in a finite volume of solvent in order to form a closed system. In the dry state, there is no solvent within the hydrogel. It defines a reference energy at the temperature T with $\mathscr{F}_0(T) = \mathscr{F}(T, \phi = 1)$. In the swollen state, parts if the solvent V_s penetrate into the hydrogel and the energy is then defined by $\mathscr{F}(T, \phi)$. The energy difference $\Delta\mathscr{F}(T, \phi)$ between the swollen and the dry state is:

$$\Delta\mathscr{F}(T, \phi) = \mathscr{F}(T, \phi) - \mathscr{F}_0(T, \phi = 1). \tag{3.1}$$

Equation 3.1 describes the energy, which is necessary to transform the hydrogel from the dried state to the swollen state. The swelling equilibrium $\phi(T)$ occurs if the change of the energy difference $\Delta\mathscr{F}(T, \phi)$ is zero for an infinitesimal small change of the polymer volume fraction ϕ, which is here a local minimum of the energy equation.

The free energy change contributes from a mixing part of the polymer-solvent molecules $\Delta\mathscr{F}_{mix}$ and the elasticity part of the polymer network $\Delta\mathscr{F}_{elast}$:

$$\Delta\mathscr{F} = \Delta\mathscr{F}_{mix} + \Delta\mathscr{F}_{elast}. \tag{3.2}$$

Furthermore, the energy change from polymer-solvent mixing is separated by an entropic part $\Delta\mathscr{F}_{entr}$ following Flory [91] and Hirotsu [96] and an interaction part $\Delta\mathscr{F}_{inter}$:

$$\Delta\mathscr{F}_{mix} = \Delta\mathscr{F}_{entr} + \Delta\mathscr{F}_{inter}. \tag{3.3}$$

The entropic part contributes from the number of statistical arrangements of polymer chains and solvent molecules in the hydrogel volume:

$$\Delta\mathscr{F}_{entr} = \mathscr{R}Tn_s \ln(1-\phi) = \mathscr{R}T\frac{V_p}{\bar{V}_s} \cdot \left(\frac{1}{\phi} - 1\right) \ln(1-\phi). \tag{3.4}$$

The entropic part of the Helmholtz free energy depends on the universal gas constant $\mathscr{R}$, the applied temperature T, the number of solvent molecules n_s in the gel (in mol) and the polymer volume fraction ϕ. The number of solvent molecules n_s can be replaced by:

$$n_s = \frac{V_s}{\bar{V}_s} = \frac{V_p}{\bar{V}_s} \cdot \left(\frac{1}{\phi} - 1\right), \tag{3.5}$$

where V_s is the volume of the solvent in the gel, $\bar{V}_s$ is the molar volume of the solvent and V_p the volume of the polymer. The interaction part contributes from polymer and solvent interaction energies [80] and is defined by:

$$\Delta\mathscr{F}_{inter} = \mathscr{R}Tn_s\chi\phi = \mathscr{R}T\frac{V_p}{\bar{V}_s} \cdot \left(\frac{1}{\phi} - 1\right)\chi\phi, \tag{3.6}$$

where χ is the Flory polymer-solvent interaction parameter. The original Flory theory showed

deviations to measurements on real hydrogels. Hirotsu [96] introduced empiric values for χ, which depend on the polymer volume fraction ϕ and the temperature T. The interaction parameter is now described by the interaction enthalpy change δh, the interaction entropy change δs (hydrophobic interaction), the Boltzmann constant k_B and a non-linearity factor χ_2, which is here a constant:

$$\chi(T,\phi) = \chi_1(T) + \chi_2 \cdot \phi \tag{3.7}$$

$$\chi_1(T) = \frac{\delta h}{k_B \cdot T} - \frac{\delta s}{k_B}. \tag{3.8}$$

The elastic contribution is defined by the energy, which is required to stretch the polymer chains during the swelling process:

$$\Delta \mathscr{F}_{elast} = \frac{3}{2}\mathscr{R}T\frac{V_p}{\bar{V}_s}r \cdot \left(\phi^{-\frac{2}{3}} - 1 + \frac{1}{3}\ln\phi\right). \tag{3.9}$$

The elastic contribution is derived for free swelling conditions in all three spatial directions. There are no external forces or displacement constraints that affect the swelling process of the gel. The ratio parameter r is defined by the molar chain weight of the polymer m_p, the molar weight of the solvent m_s and their respective densities ϱ_p and ϱ_s:

$$r(m_p) = \frac{\bar{V}_s}{\bar{V}_p} = \frac{m_s}{\varrho_s} \cdot \frac{\varrho_p}{m_p}. \tag{3.10}$$

In equilibrium, the derivative of the Helmholtz free energy change with regard to the polymeric volume fraction must be zero:

$$0 = \frac{\partial \Delta \mathscr{F}(T,\phi)}{\partial \phi} = \frac{\partial \Delta \mathscr{F}_{mix}(T,\phi)}{\partial \phi} + \frac{\partial \Delta \mathscr{F}_{elast}(T,\phi)}{\partial \phi}. \tag{3.11}$$

The mixing and the elastic terms in **Equation 3.11** can be considered as competitive effects, which want to increase and decrease the volume of the hydrogel. An increase of the elastic term reduces the volume swelling degree similar to a stiffness parameter in solid mechanics. According to [80], the Helmholtz free energy change $\Delta\mathscr{F}(T,\phi)$ can also be used to compute the osmotic pressure and the chemical potential for arbitrary T and ϕ values. Likewise, both derivatives become zero in the equilibrium state and lead to identical results for the quasi-static swelling behavior. From the physical point of view, the derivatives of the free energy change relationship are different measures for the driving forces, which change the volume of the hydrogel until the equilibrium position is reached. Solving **Equations 3.11** leads to the following implicit formulation:

$$\frac{\partial \Delta \mathscr{F}}{\partial \phi} = 0 = -\frac{\mathscr{R}V_pT}{\bar{V}_s\phi^2} \cdot \left[\ln(1-\phi) + r \cdot \phi^{\frac{1}{3}} + \left(1 - \frac{r}{2}\right)\phi + \left(\frac{\delta h}{Tk_B} - \frac{\delta s}{k_B} + \chi_2\right)\phi^2 + 2\chi_2\phi^3\right], \tag{3.12}$$

which can be transformed to a temperature function $T(\phi, m_p)$, which depends on the polymer swelling fraction ϕ and the molar chain weight m_p of the polymer:

$$T(\phi, m_p) = \frac{-\frac{\delta h}{k_B} \cdot \phi^2}{\ln(1-\phi) + r(m_p) \cdot \phi^{\frac{1}{3}} + \left(1 - \frac{r(m_p)}{2}\right) \cdot \phi - \left(\frac{\delta s}{k_B} + \chi_2\right) \cdot \phi^2 + 2\chi_2 \cdot \phi^3}. \tag{3.13}$$

Table 3.1 lists the parameters of **Equation 3.13**, which have been used to calculate the quasi-static swelling response of PNIPAAm polymers in [80], [97].

Table 3.1: List of parameters used to calculate the static swelling behavior of PNIPAAm.

parameter	Symbol	Value	Unit
universal gas constant	$\mathcal{R}$	8.314459848	$\mathrm{J/(mol\,K)}$
Boltzmann constant	k_B	$1.380649 \cdot 10^{-23}$	$\mathrm{J/K}$
interaction enthalpy	δh	$-11.5 \cdot 10^{-21}$	$\mathrm{J/mol}$
interaction entropy	δs	$-4.7 \cdot 10^{-23}$	$\mathrm{J/mol}$
non-linearity factor	χ_2	0.25	-
molar mass of water	m_s	18	$\mathrm{g/mol}$
density of water	ϱ_s	1000	$\mathrm{kg/m^3}$
molar mass of PNIPAAm	m_p	$[2.000, 50.000]$	$\mathrm{g/mol}$
density of PNIPAAm	ϱ_p	1100	$\mathrm{kg/m^3}$
temperature	T	$[0, 60]$	°C

In **Figure 3.1**, the volume swelling degree Q is plotted with regard to the stimulus temperature T and the molar chain weight m_p of the polymer. The Matlab source code and the derivations in Mathcad are provided in **Appendix E.1**. Swelling measurements on hydrogels with chemical stimuli have been published in [98]. The response surfaces are comparable to the data obtained from thermal stimuli.

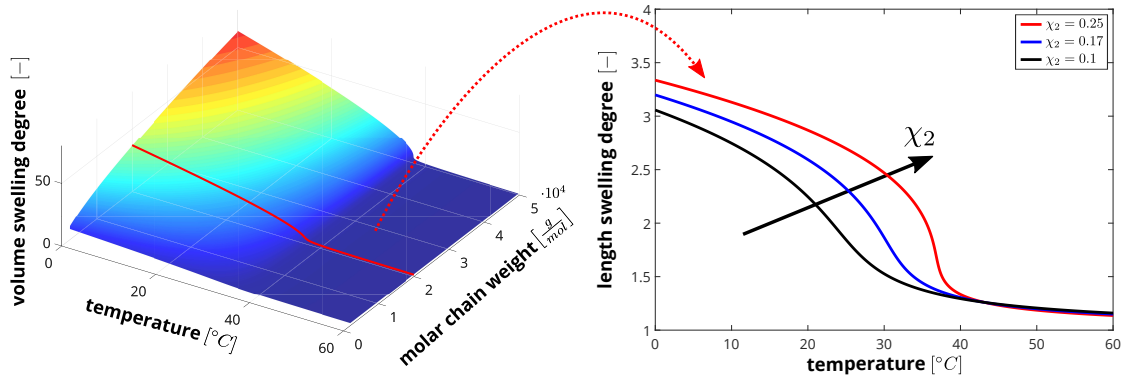

Figure 3.1: Analytic swelling behavior for the static domain depending on the temperature T and the molar chain weight m_p.

The hydrogel swelling results of **Equation 3.13** are very sensitive to the empiric Flory polymer-solvent interaction parameter χ. Different curves are shown exemplarily in the right plot of **Figure 3.1**. The non-linearity factor χ_2 changes the curvature and the function values of the swelling response. Furthermore, increasing values of the interaction enthalpy δh move the curve to the right what leads to larger swelling values and a higher threshold defined by the lower critical solution temperature T_{LCST}. The interaction entropy δs acts in the opposite way. Changes of $1\,\%$ in the χ_1 parameters move the T_{LCST} threshold about $3\,°\mathrm{C}$. For this rea-

son, swelling measurements on hydrogels are recommended to verify the theoretical data for subsequent modeling and simulation procedures.

3.1.2 Finite Element Routine for Static Thermo-Elastic Expansion

Swelling of hydrogels can be modeled by thermal expansion in different numerical simulation tools. It is a convenient way because most design software programs support thermal-mechanical simulations at various levels of abstraction. In this chapter, the fundamental background will be discussed for a 1D-*truss* (sometimes also referred as *spar*) element, which can be used for modeling of uniaxial tension and compression. 1D-*truss* elements can also be applied for 2D and 3D models where several 1D elements are linked together with a certain angle to simulate the swelling in horizontal and vertical directions.

In numerical simulation tools, thermal expansion is either described by a load vector or a matrix coupling. Load vector coupling is preferred if the mechanical behavior has to be analyzed for a given temperature profile. A matrix coupling is preferred for systems where both, the mechanical and the thermal behavior has to be analyzed simultaneously. The theoretical background of a two-dimensional 8-node quadrilateral finite element, which allows for coupled thermo-mechanical simulations is summarized in **Appendix A**. The source code for linear static simulations has been implemented in Matlab and is tested on several examples. It gives identical results to the *PLANE223* coupled-field element of the finite element program ANSYS.

The aim of this chapter is to summarize numerical methods for modeling and simulation of swelling effects in hydrogels. In real applications, swelling leads to large deformations and non-linear effects must be considered. 3D finite element simulations are discussed in **Chapter 5** and results are utilized for system simulations in **Chapter 6** and **7**.

In numerical simulation tools, the length and volume change of solid models is described by the thermal expansion coefficient α. The thermal strain ε_{th} is defined by:

$$\varepsilon_{th} = \alpha^{se}(T) \cdot (T - T_{ref}) = \int_{T_{ref}}^{T} \alpha^{in}(T')\, dT', \tag{3.14}$$

where α^{se} is the secant coefficient of thermal expansion, α^{in} is the instantaneous coefficient of thermal expansion (elaborated in **Appendix B**), T is the current stimulus temperature and T_{ref} the reference temperature of the hydrogel, here in the collapsed state.

The total strain ε_t is the sum of mechanical strain ε_m caused by external forces or displacement constraints and the thermal strain ε_{th} induced by a temperature change:

$$\varepsilon_t = \frac{\Delta l}{l_0} = \varepsilon_m + \varepsilon_{th}. \tag{3.15}$$

In a linear model, the total strain is equal to the ratio of the length change Δl with regard to the reference length l_0 in the dry state. For uniaxial extensions, the stress-strain relationship is defined by Hook's law whereby only mechanical strain causes stress. Mechanical stress σ is defined by:

$$\sigma = \frac{F_m}{A_0} = E \cdot \left(\frac{\Delta l}{l_0} - \alpha(T) \cdot (T - T_{ref}) \right), \tag{3.16}$$

where E is the Young's modulus, A_0 is the initial cross-sectional area of the body and F_m are mechanical forces. In the following notation, the coefficient of thermal expansion and the Young's modulus are assumed to be constant. However, both parameters are functions and depend either on the stimulus (for example a temperature), on the volume swelling degree or the polymer volume fraction in the following chapters of this work.

A mechanical single degree of freedom (DOF) system is defined by spring forces ($(F) = [K] \cdot (u)$) which are in equilibrium with external forces F_{ext}. The thermal expansion is represented by equivalent forces that cause the same stretch. They are added to the mechanical forces F_m as defined by:

$$\frac{E \cdot A_0}{l_0} \cdot u = F_m + E \cdot A_0 \cdot \alpha \cdot (T - T_{ref}). \tag{3.17}$$

A 1D-*truss* element with nodes i and j can be described by the following matrix notation:

$$\begin{bmatrix} \frac{EA}{l_0} & -\frac{EA}{l_0} \\ -\frac{EA}{l_0} & \frac{EA}{l_0} \end{bmatrix} \cdot \begin{pmatrix} u_i \\ u_j \end{pmatrix} = \begin{pmatrix} F_i \\ F_j \end{pmatrix} + \begin{pmatrix} -E \cdot A_0 \cdot \alpha \cdot (T - T_{ref}) \\ +E \cdot A_0 \cdot \alpha \cdot (T - T_{ref}) \end{pmatrix}, \tag{3.18}$$

where the first term on the right is the mechanical load vector and the second term is the thermal load vector. A pre-defined element temperature change $(T - T_{ref})$ can be considered directly for mechanical domain simulations referred as **load vector coupling**. Discretization into a series of elements allows for non-uniform temperature profiles in models based on the FEM. The signs of the load vector elements in **Equation 3.18** results from the sign rule of mechanical and thermal elements explained in **Figure 3.2**.

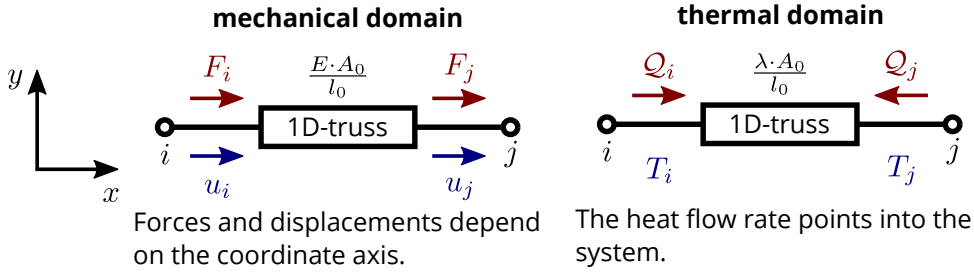

Forces and displacements depend on the coordinate axis.

The heat flow rate points into the system.

Figure 3.2: Sign rules for 1D-*truss* elements in the mechanical and thermal domain.

A **matrix coupling** is implemented for systems where the mechanical and the thermal domain are analyzed simultaneously. Each finite element node has one (u) or more (u_x, u_y, u_z) mechanical degrees of freedom which describe the force-displacement relationship in spatial directions and a thermal degree of freedom that describes the heat flow rate $\mathbb{Q}$ with regard to the nodal temperatures. In case of uniaxial heat flow, the thermal conduction is described through:

$$\mathbb{Q} = \frac{\lambda \cdot A_0}{l_0} \cdot (T_i - T_j), \tag{3.19}$$

where λ is the thermal conductivity and T_i and T_j are the temperatures at the interfaces of the

truss element. The heat flow is independent on the reference temperature T_{ref}. A 1D-coupled domain element can be described by:

$$\begin{bmatrix} \frac{E\cdot A_0}{l_0} & -\frac{E\cdot A_0}{l_0} & \frac{E\cdot A_0\cdot\alpha}{2} & \frac{E\cdot A_0\cdot\alpha}{2} \\ -\frac{E\cdot A_0}{l_0} & \frac{E\cdot A_0}{l_0} & -\frac{E\cdot A_0\cdot\alpha}{2} & -\frac{E\cdot A_0\cdot\alpha}{2} \\ 0 & 0 & \frac{\lambda\cdot A_0}{l_0} & -\frac{\lambda\cdot A_0}{l_0} \\ 0 & 0 & -\frac{\lambda\cdot A_0}{l_0} & \frac{\lambda\cdot A_0}{l_0} \end{bmatrix} \cdot \begin{pmatrix} u_i \\ u_j \\ T_i \\ T_j \end{pmatrix} = \begin{pmatrix} F_i \\ F_j \\ \mathbb{Q}_i \\ \mathbb{Q}_j \end{pmatrix} + \begin{pmatrix} E\cdot A_0\cdot\alpha\cdot T_{ref} \\ -E\cdot A_0\cdot\alpha\cdot T_{ref} \\ 0 \\ 0 \end{pmatrix}. \tag{3.20}$$

For numerical simulations, either loads (forces or heat flow rates) or constraints (displacements and temperatures) can be applied to the finite element nodes. In the models, at least one node for each degree of freedom must be constrained to reference values, which are commonly the clamps and the ambient temperature. It can be realized by the penalty method or the Lagrangian multiplier method [99] (pp. 145). The Lagrangian method is numerically more stable and will be briefly illustrated in the following example.

Zero displacement constraints are assigned to node i, which is defined by the 5^{th} line in **Equation 3.21**. The temperature at node i will be set to $50\,^{\circ}\mathrm{C}$ defined in line number 6. The reference temperature is set to $20\,^{\circ}\mathrm{C}$. Finally, a mechanical load F_x is applied to node j and a heat flow rate $\mathbb{Q}$ is coupled into the system at node j for demonstration. The finite element matrix system becomes:

$$\begin{bmatrix} \frac{E\cdot A_0}{l_0} & -\frac{E\cdot A_0}{l_0} & \frac{E\cdot A_0\cdot\alpha}{2} & \frac{E\cdot A_0\cdot\alpha}{2} & 1 & 0 \\ -\frac{E\cdot A_0}{l_0} & \frac{E\cdot A_0}{l_0} & -\frac{E\cdot A_0\cdot\alpha}{2} & -\frac{E\cdot A_0\cdot\alpha}{2} & 0 & 0 \\ 0 & 0 & \frac{\lambda\cdot A_0}{l_0} & -\frac{\lambda\cdot A_0}{l_0} & 0 & 1 \\ 0 & 0 & -\frac{\lambda\cdot A_0}{l_0} & \frac{\lambda\cdot A_0}{l_0} & 0 & 0 \\ 1 & 0 & 0 & 0 & 0 & 0 \\ 0 & 0 & 1 & 0 & 0 & 0 \end{bmatrix} \cdot \begin{pmatrix} u_i \\ u_j \\ T_i \\ T_j \\ L_1 \\ L_2 \end{pmatrix} = \begin{pmatrix} 0 \\ F_x \\ 0 \\ \mathbb{Q} \\ 0 \\ 50\,^{\circ}\mathrm{C} \end{pmatrix} + \begin{pmatrix} E\cdot A_0\cdot\alpha\cdot 20\,^{\circ}\mathrm{C} \\ -E\cdot A_0\cdot\alpha\cdot 20\,^{\circ}\mathrm{C} \\ 0 \\ 0 \\ 0 \\ 0 \end{pmatrix}. \tag{3.21}$$

The Lagrangian multipliers L_1 and L_2 represent the reacting force and the heat flow rate at node i in the given example. The system can easily be solved by the following matrix vector product:

$$\{u\} = [K]^{-1} \cdot (\{F_m\} + \{F_{th}\}), \tag{3.22}$$

where $[K]^{-1}$ is the inverse stiffness matrix, $\{F_m\}$ and $\{F_{th}\}$ are the load vectors and the vector $\{u\}$ provides the result data of the model.

2D and 3D finite element models utilize shape functions to interpolate nodal properties at internal Gaussian points in order to extract the finite element equations in matrix notation. The approach is described for 8-node quadrilateral elements in **Appendix A**. The system matrices are assembled by a superposition of element matrices, which leads to the following general form in finite element tools:

$$\begin{pmatrix} [K_{uu}] & [K_{uT}] \\ 0 & [K_{TT}] \end{pmatrix} \cdot \begin{pmatrix} \{u\} \\ \{T\} \end{pmatrix} = \begin{pmatrix} \{F_m\} + \{F_{th}\}\cdot T_{ref} \\ \{\mathbb{Q}\} \end{pmatrix}, \tag{3.23}$$

where $[K_{uu}]$ is the elastic stiffness matrix, $[K_{TT}]$ is the thermal conductivity matrix and $[K_{uT}]$

the thermoelastic stiffness matrix. For linear systems, a unidirectional coupling from the thermal domain to the mechanical domain requires no equilibrium iterations.

For hydrogel simulations, the Young's modulus and the coefficient of thermal expansion changes as a function of the stimulus and the volume swelling degree. Consequently, the coefficients of the stiffness matrix and the load vector depend on the simulation results what leads to a non-linear system and requires iterative solution procedures. Finite element tools such as ANSYS or system simulators as Matlab offer various modifications of the Newton-Raphson procedure [99] (pp. 496) to calculate the equilibrium state.

The Newton-Raphson procedures require derivatives of all system matrix and load vector coefficients with regard to the unknown displacement and temperature degrees of freedom to formulate the Jacobian matrix (also known as tangential stiffness matrix). Matrix coefficients with user defined settings for the Young's modulus and the coefficient of thermal expansion are defined by a series of discrete sample points, which are linearly interpolated in ANSYS as discussed in **Chapter 5**.

In microfluidic systems, 3D finite element simulations are necessary to model the swelling state of the hydrogel at different stimulus concentrations. The outer faces of the swollen gel are transferred by moving wall boundary conditions to the fluid domain in order to compute the fluidic resistances for subsequent system simulations in **Chapter 6** and **7**.

Existing finite element tools such as ANSYS do not support special simulation routines for chemo-thermo-mechanical interactions in hydrogels. It is still challenging and a fundamental research topic. Trendsetting principles and algorithms have been published by Wallmersperger *et al.* [100] and Ballhause *et al.* [101]. In those articles, the change of the chemical concentrations, the electrical potential and the mechanical displacements are investigated for varying ambient conditions. A fully coupled bi-directional finite element model has been developed and implemented, which considers the ion exchange, the domain formation and the change of bound charges [102]–[105].

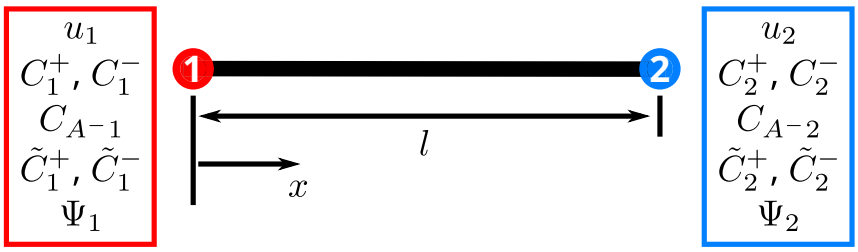

Figure 3.3: Two-node link element formulation for the hydrogel swelling behavior depending on its respective concentrations.

The developed two-node 1D element shown in **Figure 3.3** has seven degrees of freedom for each node, which are the mechanical displacement u, the concentrations of the mobile cations C^+ and anions C^-, the concentration of bound anionic charges C_{A^-}, the reference concentrations ($\tilde{C}^+$, $\tilde{C}^-$) and the electrical potential Ψ. The elements are aligned in a row through the solvent and the gel. They have been used to simulate concentration distributions, the osmotic pressure that deforms the gel and the electric potential influenced by the electrical field of mobile ions, bound charges and voltages at electrodes. The implemented finite element equations have the following form [100]:

$$\begin{bmatrix} K_{uu} & 0 & 0 & 0 & K_{u\tilde{C}^+} & K_{u\tilde{C}^-} & 0 \\ 0 & K_{C^+C^+} & 0 & 0 & 0 & 0 & K_{C^+\Psi} \\ 0 & 0 & K_{C^-C^-} & 0 & 0 & 0 & K_{C^-\Psi} \\ K_{C_{A^-}u} & 0 & 0 & 0 & 0 & 0 & K_{C_{A^-}\Psi} \\ 0 & 0 & 0 & 0 & K_{\tilde{C}^+\tilde{C}^+} & 0 & 0 \\ 0 & 0 & 0 & 0 & 0 & K_{\tilde{C}^-\tilde{C}^-} & 0 \\ 0 & K_{\Psi C^+} & K_{\Psi C^-} & K_{\Psi C_{A^-}} & 0 & 0 & K_{\Psi\Psi} \end{bmatrix} \cdot \begin{pmatrix} u \\ C^+ \\ C^- \\ C_{A^-} \\ \tilde{C}^+ \\ \tilde{C}^- \\ \Psi \end{pmatrix} = \begin{pmatrix} F_u \\ F_{C^+} \\ F_{C^-} \\ F_{C_{A^-}} \\ F_{\tilde{C}^+} \\ F_{\tilde{C}^-} \\ F_\Psi \end{pmatrix}. \quad (3.24)$$

3.1.3 Static System Level Design for Hydrogel Swelling

Swelling-stimulus functions can either be calculated analytically based on the Helmholtz free energy or the swelling response is measured on prototypes. It is demonstrated that analytical models based on the physical level of abstraction are very sensitive to empiric parameter variations. Furthermore, the behavior and interactions of internal physical properties is very complex and leads to time and resource consuming simulation models. It is vital to understand the physical nature, but engineering devices and systems are often described on a higher level of abstraction.

This work focuses on the implementation of properties in system models, which can be observed by measurements and characterize the macroscopic behavior by phenomenological properties. Typical properties are the volume swelling degree Q which can be detected by optical inspection, the stiffness which can be measured by indentation and dynamic properties discussed in **Section 3.2.3**.

In the following, the quasi-static swelling is described by the volume swelling degree Q as a function of the applied temperature T. Other stimulus sources can be considered in a similar way. The volumetric swelling is usually defined by the lower and upper volume bounds, which are measured in the dry and in the swollen state. It leads to the minimum swelling degree Q_0 and the maximum swelling degree Q_1. In between, the swelling-stimulus functions follow a smooth monotonically decreasing or increasing behavior with saturations in the dry and swollen state. It is a typical S-shaped curve, which can be described by a *sigmoidal function* [106], [107] or a *logistic function* [108] (pp. 50-56):

$$f(x) = \frac{a_1 - a_0}{1 + e^{-k \cdot (x - x_0)}} + a_0, \quad (3.25)$$

where x_0 is the sigmoidal midpoint on the x-axis, a_1 is the maximum, a_0 the minimal function value and k is the sigmoidal growth rate of the curve. The midpoint x_0 is the x-value, at which the function value $f(x)$ is in the middle between the maximum and the minimum. For static hydrogel swelling applications, this point is referred as lower critical solution temperature T_{LCST} and can be considered as a transition point where the stimulus changes the swelling states “collapsed” and “swollen” for logic applications with binary states. In reality, it is a smooth transition whereby the slope of the curve is described by the k parameter.

Equation 3.25 is adapted to a function, which starts from Q_1, ends at Q_0 and uses the transition point T_{LCST} with a growth rate k. It leads to the following equation:

$$Q(T) = \frac{Q_1 - Q_0}{1 + e^{-k \cdot (T - T_{LCST})}} + Q_0. \tag{3.26}$$

Equation 3.26 is referred as a 4-parameter sigmoidal function. The sigmoidal function plotted in **Figure 3.4** can directly be used to extract Q_1, Q_0 and T_{LCST} from the diagram. The growth parameter k is approximated by the $\Delta T'$ parameter according to **Equation 3.27**. The value $\Delta T'$ is similar to the rise time of an exponential functions and defines the temperature change from the LCST that is necessary to reach the maximum or minimum volume swelling degree within a certain tolerance band. The factor 5 is related to an accuracy of $99.3\,\%$ and a factor of 3 can be used for a $95\,\%$ accuracy:

$$k = -\frac{5}{\Delta T'}. \tag{3.27}$$

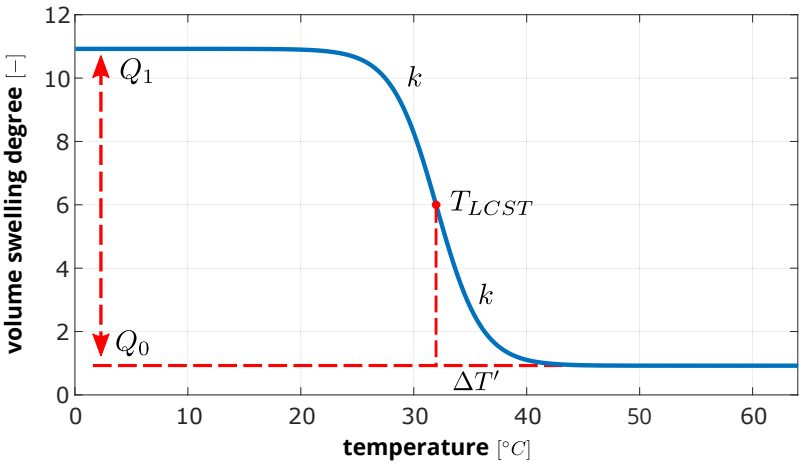

Figure 3.4: 4-point sigmoid function based on the parameters Q_1, Q_0, T_{LCST} and k.

Experimental results have shown that the curvatures below and above the LCST are not identical. A 5-parameter sigmoidal function has been developed to better approximate the asymmetric response. Likewise, the upper curvature k_u and the lower curvature k_l parameter can be extracted from the temperature distances $\Delta T'_u$ and $\Delta T'_l$, which are necessary to reach the tolerance band:

$$Q(T) = \frac{Q_1 - Q_0}{1 + \frac{1}{1 + e^{k_u \cdot (T - T_{LCST})}} + 0.5 \cdot e^{-k_l \cdot (T - T_{LCST})}} + Q_0. \tag{3.28}$$

Figure 3.5 illustrates a typical example and **Table 3.2** lists the extracted parameters. It could be shown that the parameters of sigmoidal functions can be easily adjusted to measurement data. Sigmoidal functions usually provide satisfying results for an analytical description of the swelling response at arbitrary stimuli signals. **Equation 3.28** will be utilized for modeling and simulation of swelling processes of hydrogels in microfluidic devices. The function values and their derivatives can efficiently be calculated in each time step of transient simulations.

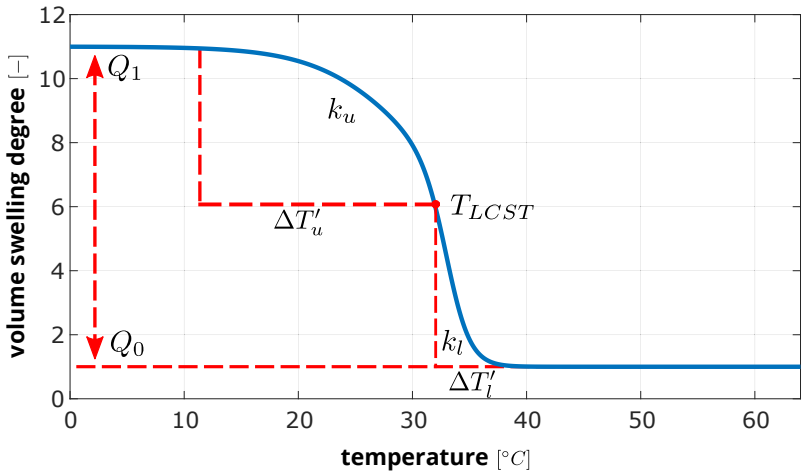

Figure 3.5: 5-parameter sigmoid function based on the parameters Q_1, Q_0, T_{LCST}, $\Delta T'_u$ and $\Delta T'_l$.

Noteworthy is, that the characterization of hydrogels always depend on the targeted description and always causes different absolute values. For the example of T_{LCST}, also optical refraction phase-transition points are used characterization [109] or depending on the analytic function, the turning point of the slope can be defined. In this work T_{LCST} is always the mid point of the sigmoidal function, which is also always the turning point of the slope.

Table 3.2: List of parameters used to draw the 5-parameter sigmoid function of **Figure 3.5**.

parameter	Symbol	Value	Unit
maximum swelling degree	Q_1	11	-
minimum swelling degree	Q_0	1	-
lower critical solution temperature	T_{LCST}	32	°C
temperature distance for upper curvature	$\Delta T'_u$	20	°C
temperature distance for lower curvature	$\Delta T'_l$	5	°C

3.2 Transient Description

The transient behavior is observed by a step change of the ambient stimulus. Thereby the diffusion of the stimulus varies between the heat transfer coefficient in the order of $D_{th} = 10^{-3}\,\mathrm{cm}^2/\mathrm{s}$ and a diffusion of solvent with $D_{solu} = 10^{-5}\,\mathrm{cm}^2/\mathrm{s}$. In case of a step change of the ambient stimulus, the current equilibrium will shift to a new equilibrium state, in which the hydrogel is now desired to swell. The process to the new swelling state is a time dependent process, where the hydrogel changes in size until the new equilibrium is reached. This resulting volume change is also called cooperative diffusion coefficient and is in the order of $D_V = D_{coop} = 10^{-7}\,\mathrm{cm}^2/\mathrm{s}$ [85]. For the description of a thermal induced swelling behavior, the heat transfer and the resulting volume change diffusion differ by the order of $\frac{D_{th}}{D_{coop}} = 10^4$. Therefore, only the slowest process has to be implemented in transient simulations and the thermal transfer can be considered as an instant quasi-static process.

3.2.1 Physical Dynamic Chemo-Thermal Description

A first comprehensive analytical description of the swelling kinetics was published by Tanaka and Fillmore in [110], [111] and a summary can be found in [80].

The **Tanaka-Fillmore theory** is based on fundamental principles of continuum mechanics. A displacement vector as a function of a position and time $u(r,t)$ has been used to calculate the components of the stress tensor σ_{ik} [112] (pp. 1-37). The indices of σ_{ik} refer to forces along the k-axis, which act on a unit plane perpendicular to the i-axis. The stress-displacement relationship is defined by:

$$\sigma_{ik} = \mathcal{K}(\nabla \cdot \boldsymbol{u})\delta_{ik} + 2\mathcal{G} \cdot \left(u_{ik} - \frac{1}{3} (\nabla \cdot \boldsymbol{u})\, \delta_{ik} \right), \tag{3.29}$$

where **Equation 3.29** is a PDE consisting of the nabla operator ∇, the Kronecker delta δ_{ik}, the bulk modulus $\mathcal{K}$, the shear modulus G and a displacement vector field $\boldsymbol{u}$ of each point within the hydrogel. The first term of **Equation 3.29** describes the stress caused by a volume change and the second term the stress resulting from shear deformations. As a next step, Newton's equation of motion is used to describe the dynamic response by:

$$\varrho \frac{\partial^2 \boldsymbol{u}}{\partial t^2} = \nabla \cdot \boldsymbol{\sigma} - \zeta \frac{\partial \boldsymbol{u}}{\partial t}, \tag{3.30}$$

where ζ is the coefficient of friction and ϱ the density of the hydrogel. The left side of **Equation 3.30** represents inertial forces and the right side the elastic forces and friction forces, which result from the relative motion between the solvent and the gel network. For high polymer-solvent frictions, inertia effects are neglected $\varrho \frac{\partial^2 \boldsymbol{u}}{\partial t^2} = 0$, which eliminates the second time derivatives:

$$\frac{\partial \boldsymbol{u}}{\partial t} = \frac{\nabla \cdot \boldsymbol{\sigma}}{\zeta}. \tag{3.31}$$

Combining **Equation 3.29** and **3.31** leads to:

$$\frac{\partial \boldsymbol{u}}{\partial t} = \frac{\mathcal{K} + \frac{\mathcal{G}}{3}}{\zeta} \nabla (\nabla \cdot \boldsymbol{u}) + \left(\frac{\mathcal{G}}{\zeta} \right) \Delta \boldsymbol{u}, \tag{3.32}$$

where Δ is the Laplace operator. **Equation 3.32** can be solved analytically for simple shape elements. Tanaka investigated spherical hydrogels where the displacement vector $\boldsymbol{u}$ can be represented by a single component, which are displacements in radial direction $\boldsymbol{r}$. Here, $\boldsymbol{r}$ is the radial vector and r represents the scalar amplitude. Together they can form the unit vector $\vec{e}_r$ with:

$$\boldsymbol{u}(\boldsymbol{r}) = u(r) \cdot \frac{\boldsymbol{r}}{r} = u(r) \cdot \vec{e}_r. \tag{3.33}$$

Now the displacement field is only a function of the radius. If a one-dimensional system is considered, the displacement field $\boldsymbol{u}(\boldsymbol{r})$ is transformed to a scalar displacement $u(r)$ forming **Equation 3.32** to a scalar description:

$$\frac{\partial u}{\partial t} = D_{coop} \frac{\partial}{\partial r} \left(\frac{1}{r^2} \left[\frac{\partial}{\partial r} (r^2 u) \right] \right). \tag{3.34}$$

In **Equation 3.34**, the cooperative diffusion coefficient D_{coop} is introduced as a function of the bulk modulus $\mathscr{K}$, the shear modulus $\mathscr{G}$ and the friction coefficient ζ. Tanaka quantified the diffusion coefficients from pure mechanical properties, which are measured on specimens:

$$D_{coop} = \frac{\mathscr{K} + \frac{4}{3}\mathscr{G}}{\zeta}. \tag{3.35}$$

Equation 3.34 has been solved for given initial displacement conditions and zero stress boundary conditions at the outer faces of the sphere with a radius r_0. A superposition of eigenfunctions $f_n(x)$ leads to the following displacement-time relationship:

$$u\left(r,t\right) = \sum_n f_n(x) e^{-n^2 \frac{D_{coop} \cdot \pi^2}{r_0^2} t}. \tag{3.36}$$

Equation 3.36 is the analytical solution for a step change of the stimulus at the outer faces. The first eigenmode has usually the largest magnitude and contributes most to the transient response. The time constant τ, which is related to the first eigenmode can directly be extracted from the exponent term with $n = 1$:

$$\tau = \frac{r_0^2}{\pi^2 \cdot D_{coop}}. \tag{3.37}$$

Tanaka developed a first comprehensive theory, which explains the time dependent swelling behavior of hydrogels. The approach of Tanaka is more of a heuristic nature and therefore more advanced thermodynamic descriptions are later developed.

The **Doi theory** [81], is also based on principles of continuum mechanics but the stress-displacement relationship is directly extracted from the thermodynamic free energy equation discussed in **Section 3.1.1**. Doi uses the free energy density as a function of the deformation gradient F_{ij} to formulate the stress-displacement relationship. The free energy density $\mathscr{A}\left(F_{ij}, T\right)$ contributes from the mixing part and the elastic part:

$$\mathscr{A}\left(F_{ij}, T\right) = \mathscr{A}_{mix}\left(F_{ij}, T\right) + \mathscr{A}_{elast}\left(F_{ij}, T\right). \tag{3.38}$$

F_{ij} is referred deformation gradient $F_{ij} = \partial r_i' / \partial r_j$ and is calculated from the derivatives of the position vectors in the initial and deformed state. The position vector describes the location of arbitrary points in the hydrogel, whereby r is the initial position and r' is the deformed position. The deformation gradient is a tensor of the second order, which can be used to separate normal strain (stretch, compression), shear strain and rigid body rotations of an infinitesimal small reference volume. The stress tensor in the hydrogel is defined by [80]:

$$\sigma_{ij}\left(\boldsymbol{r}'\right) = \frac{\partial A}{\partial F_{ik}} \cdot F_{jk}\left(\boldsymbol{r}'\right). \tag{3.39}$$

In addition to the polymer deformation, the time dependent polymer velocity field v_p, the solvent flow field v_s and the solvent pressure field p must also be taken into account. The final differential equation of motion is based on the following four assumptions:

1) The solvent pressure p is equal to the stress $\boldsymbol{\sigma}$ on the surface of thy hydrogel:

$$\nabla \left(\boldsymbol{\sigma} - p\boldsymbol{I} \right) = 0. \tag{3.40}$$

2) With Darcy's law of porous media [113], the solvent permeation speed is proportional to the pressure gradient v_p and the polymer permeability κ_0. The solvent permeation is the velocity of the solvent v_s relative to the polymer network v_p:

$$\boldsymbol{v_s} - \boldsymbol{v_p} = \kappa_0(\phi) \cdot \nabla p. \tag{3.41}$$

3) The polymer volume fraction ϕ is defined by the mass conservation law:

$$\frac{\partial \phi}{\partial t} = -\nabla \cdot \left(\phi \boldsymbol{v_p} \right). \tag{3.42}$$

4) Finally, the incompressibility condition leads to:

$$\nabla \left[\phi \boldsymbol{v_p} + (1 - \phi)\, \boldsymbol{v_s} \right] = 0. \tag{3.43}$$

Equation 3.40 - 3.43 can be summarized to the following nonlinear partial differential equation of motion, which is linearized at the initial state ϕ_0:

$$\left(\mathscr{K} + \frac{\mathscr{G}}{3} \right) \nabla \nabla \cdot \boldsymbol{u} + \mathscr{G} \nabla^2 \boldsymbol{u} = \nabla p. \tag{3.44}$$

Hereby is $\mathscr{K}$ the osmotic modulus and $\mathscr{G}$ the shear modulus. The osmotic modulus describes restoring forces for the swelling deformation and can be calculated from the second derivatives of the free energy density $\mathscr{A}(\phi)$ with regard to the polymer volume fraction ϕ:

$$\mathscr{K} = \phi_0^2 \cdot \left(\frac{\partial^2}{\partial \phi^2} \left(\frac{\mathscr{A}(\phi)}{\phi} \right) \Big|_{\phi = \phi_0} \right). \tag{3.45}$$

The shear modulus $\mathscr{G}$ is calculated from the second derivative of the free energy density with regard to the engineering strain $\varepsilon = \frac{u}{l}$:

$$\mathscr{G} = \frac{\partial^2}{\partial \varepsilon^2} \mathscr{A} \left(\phi(\varepsilon) \right). \tag{3.46}$$

In order to calculated derivatives with regard to engineering strain, the polymer volume fraction ϕ must be replaced in the energy formulation by the stretch ratios $\Lambda = \frac{l}{l_0}$ in spatial directions and finally by the engineering strain:

$$\phi(\varepsilon) = \frac{1}{Q} = \frac{1}{\Lambda_1 \cdot \Lambda_2 \cdot \Lambda_3} = \frac{1}{(1 + \varepsilon) \cdot \left(1 - \frac{\varepsilon}{2}\right)^2}. \tag{3.47}$$

A compressibility is only achieved if a solvent moves in or out of the gel, which causes swelling. With Darcy's law in **Equation 3.41** and the incompressibility condition in **Equation 3.43**, the pressure-displacement relationship is formulated by:

$$\nabla \dot{\boldsymbol{u}} = (1 - \phi_0) \cdot \kappa_0 \nabla^2 p. \tag{3.48}$$

Equation 3.44 and **3.48** describe the linearized form of the displacement field $\boldsymbol{u}$ and the pressure field p as a function of the time t. The Tanaka-Fillmore **Equation 3.35** can be ob-

tained under the assumption that the polymer velocity field and solvent velocity field are opposite for the entire hydrogel space [80]. The cooperative diffusion coefficient can then be described by:

$$D = \left(\mathscr{K} + \frac{4}{3}\mathscr{G}\right) \cdot (1 - \phi_0) \cdot \kappa_0, \tag{3.49}$$

which is used to calculate the time constant τ for simple shape elements analytically. Doi investigated swelling of thin hexahedral, of cylindrical and of spherical hydrogels. Similar to Tanaka, the time constants depend on physical hydrogel properties, which are the osmotic modulus $\mathscr{K}$, the shear modulus $\mathscr{G}$ and the polymer permeability χ.

For small deformations, the polymer permeability χ is the inverse of the polymer friction coefficient ζ of the Tanaka theory and **Equation 3.49** and **3.35** are identical [81] (eq. 71). Different is just the way, how the $\mathscr{K}$ and $\mathscr{G}$ material parameters are determined. Tanaka used pure mechanical properties, which have been measured by light scattering spectroscopy, macroscopic swelling experiment and other mechanical rheology tests [110], [111]. Doi extracted the data theoretically from the Helmholtz free energy equation without measurements.

An **alternative description of the cooperative diffusion coefficient** is provided in [114]. There, the cooperative diffusion coefficient is expressed as a function of the volume swelling degree $D \sim Q^{-n}$, for which the power variable n is set to $n = 0.75$. To resolve the proportionality, a base diffusion coefficient D_0 is introduced:

$$D_{coop} = D_0 \cdot Q^{-n}. \tag{3.50}$$

Thereby, the **Einstein–Smoluchowski equation** is used for the base diffusion coefficient D_0 of the gel. This base diffusion depends on the dynamic viscosity η_s, the hydrodynamic radius r_h of a single polymer chain, the Boltzmann constant k_B and the temperature T [115] (pp. 319):

$$D_0 = \frac{k_B T}{6\pi\eta_s r_h}. \tag{3.51}$$

3.2.2 Finite Element Routine for Dynamic Thermo-Elastic Expansion

Transient finite element simulations provide information about the swelling response for time-dependent stimuli signals. A step signal is usually applied to calculate the rise time of a system. The time-dependent behavior of thermo-mechanical systems is described by the mass and damping matrices and the static behavior is solely defined by the stiffness matrix. The stiffness matrix includes the expansion behavior and elastic deformations as discussed in **Section 3.1.2**. The mass and damping matrices define eigenfrequencies, inertial effects and energy loss mechanisms.

For the example of a coupled thermo-mechanical solid element, **Equation 3.23** is now expanded by a mass matrix $[M]$, the mechanical damping matrix $[C]$, the specific heat matrix $[C_t]$ and the thermoelastic damping matrix $[C_{tu}]$ [116] (pp. 299):

$$\begin{pmatrix} [M] & [0] \\ [0] & [0] \end{pmatrix} \begin{pmatrix} \{\ddot{u}\} \\ \{\ddot{T}\} \end{pmatrix} + \begin{pmatrix} [C] & [0] \\ [C_{tu}] & [C_t] \end{pmatrix} \begin{pmatrix} \{\dot{u}\} \\ \{\dot{T}\} \end{pmatrix} + \begin{pmatrix} [K_{uu}] & [K_{uT}] \\ [0] & [K_{TT}] \end{pmatrix} \begin{pmatrix} \{u\} \\ \{T\} \end{pmatrix} = \begin{pmatrix} \{F\} \\ \{Q\} \end{pmatrix}. \quad (3.52)$$

The elastic stiffness matrix $[K_{uu}]$, the thermal conductivity matrix $[K_{TT}]$ and the thermoelastic stiffness matrix $[K_{uT}]$ are already introduced in chapter 3.1.2.

For hydrogel-based applications, the specific heat matrix is most important to approximate the transient responses. Inertial effects caused by the mass matrix, by mechanical damping or by thermoelastic damping can be ignored. The specific heat matrix in combination with the thermal conductivity matrix define how fast the temperature penetrates into the hydrogel. Thereby, the resulting heat transfer coefficient is defined by the thermal conductivity λ, the material density ϱ and the specific heat capacity c_{th}, which are adapted to the cooperative diffusion constant in **Section 5.2.4**:

$$D_{th} = \frac{\lambda}{\varrho \cdot c_{th}}. \quad (3.53)$$

For simple structures, the heat transfer coefficient can be used to calculate the time constant τ analytically. The time constant is a characteristic quantity, which characterizes the step response of a linear first-order differential equation. After $t = 1\tau$, $t = 3\tau$ and $t = 5\tau$ time duration, the step response reaches $63.2\,\%$, $95\,\%$ and $99.3\,\%$ respectively.

The time constant of any diffusion process is derived from the mean square displacements [117] and is commonly demonstrated for the random walk theory example [118], [115] (pp. 319, 329):

$$\tau = \frac{l_c^2}{2 \cdot n \cdot D_{th}}, \quad (3.54)$$

where D_{th} is the diffusion coefficient, n is the spatial dimension of the problem and l_c is a characteristic length.

For spherical hydrogels where the solvent penetrates from all directions into the gel, the parameter n must be set to 3 and the characteristic length is the radius of the sphere. Hydrogels are often flat structures, which are fixed at the bottom face. Here, the solvent penetrates mainly from the top face into the hydrogel. For those models, the parameter n becomes 1 and l_c is the thickness. In **Equation 3.54**, the time constant τ is related to diffusion results measured at a specific point with a distance l_c to the outer faces. It is the center point for spheres or the bottom face of a flat hydrogel with large lateral dimensions. Numerical finite element simulations are utilized to calculate the time constant for other points or structures where the distance l_c to the point of interest is not constant. For a cube, n must be set to 2.13 and l_c is the half edge length as shown in **Figure 3.6**.

In practice, the time constant should be related to an average swelling degree of the hydrogel volume and not on the center point. Average swelling over time is usually measured by experimental characterization or has to be analyzed in modeling and simulation of microfluidic components and systems. Average swelling is faster as local swelling at the center point. Finite element simulations have shown, that the time constant for spherical hydrogels is about three times lower and n must be set to 9 in **Equation 3.54**. Further values for typical

structures are listed in **Figure 3.6**.

Transient finite element simulations provide local and average time constants for arbitrary shapes and stimulus functions. Further details will be discussed in **Chapter 5**. Transient simulations in finite element tools are usually based on the Newmark-time integration schema [99] (pp. 777). It is an implicit numerical solver for ODE systems of second order and considers a constant or a linear acceleration in each time step.

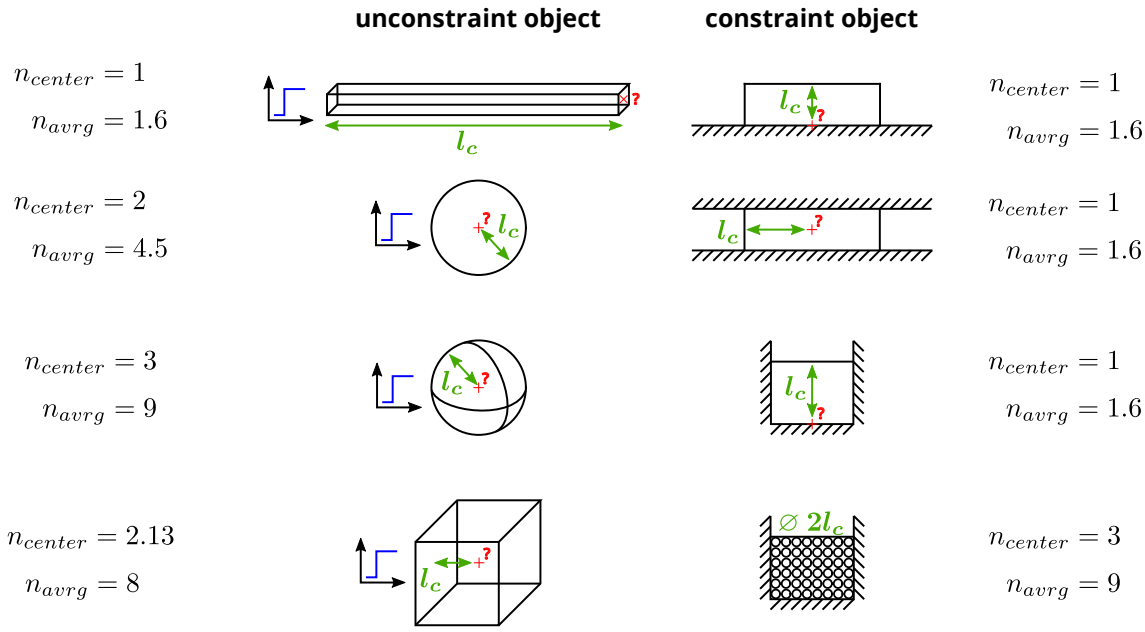

Figure 3.6: Common unconstrained and constrained hydrogels with the numerically determined spatial parameter n focusing either on the center point of the system or the average temperature distribution.

3.2.3 Transient System Level Design for Hydrogel Swelling

Following the modeling concept for the static behavior presented in **Section 3.1.3**, the dynamic response in system level design is described by the time dependent length or volume change of the hydrogel, which is primarily depending on the time constant τ. Length and volume parameters are easier to obtain by measurements as internal physical quantities such as the bulk modulus $\mathcal{K}$, the shear modulus $\mathcal{G}$ or the friction coefficient ζ, which are utilized by Tanaka and Doi to describe the swelling kinetics.

In system models, the dynamic behavior of hydrogels is usually described by a single degree of freedom, which is a characteristic length parameter or by a few DOF, which are dimensional parameters in different spatial directions. The transient response can be efficiently analyzed in a two-step procedure. It starts with a static simulation step, which computes a stimulus dependent length. The stimulus dependent target length is referred equilibrium length $l_{eq}(T)$. It follows a transient simulation step, which calculates the time-dependent kinematic length $l(t)$ of the hydrogel. The relationship between equilibrium length and kinematic length is defined by:

$$d(l) \cdot \dot{l}(t) + l(t) = l_{eq}(T). \tag{3.55}$$

Thereby is $d(l)$ the damping coefficient, $l(t)$ the kinematic length and $l_{eq}(T)$ the equilibrium length of the first-order differential equation. The damping coefficient is equal to the time constant τ because the stiffness term must be set to one in order to obtain the same static and transient response at constant stimulus signals:

$$d(l) = \tau(l). \tag{3.56}$$

The time constant of hydrogels is a function of the kinematic length, the cooperative diffusion and a constant scale factor d_{fac}, which depends on the shape of the hydrogel:

$$\tau(l) = d_{fac} \cdot \frac{l(t)^2}{D_{coop}(l)}. \tag{3.57}$$

According to **Equation 3.50**, the cooperative diffusion D_{coop} is a function of a base diffusion D_0, the volume swelling degree $Q(l)$ and a power factor, which is $n = -0.75$:

$$D_{coop}(l) = D_0 \cdot Q(l)^n. \tag{3.58}$$

The base diffusion D_0 is usually measured by fitting experimental response functions. The volume swelling degree $Q(l)$ is defined by:

$$Q(l) = \frac{l(t)^3}{l_0^3}, \tag{3.59}$$

where $l(t)$ is the kinematic length and l_0 is the unswollen length. **Equation 3.59** is applicable for hexahedral and spherical hydrogels since the swelling degree in spatial directions is identical. Finally, the damping coefficient of **Equation 3.55** can be described by:

$$d(l) = d_{fac} \cdot \frac{l(t)^{2-3n} \cdot l_0^{3n}}{D_0}. \tag{3.60}$$

It is known that swelling processes of hydrogels are faster than shrinking processes. In system models, it is easy to distinguish swelling and shrinking by the first time derivative of the stimulus signal. The parameter d_{fac} introduced in **Equation 3.57** scales the time constant τ. An if-condition can be implemented in system simulators to change the value of the parameter d_{fac} depending on the slope of the length-time function $l(t)$. The value of the parameter d_{fac} is usually considered in the value of the base diffusion D_0 for increasing stimuli functions what keeps the parameter d_{fac} just for decreasing stimuli in the following equation:

$$d(l) = \begin{cases} \frac{l(t)^{2-3n} \cdot l_0^{3n}}{D_0} & \frac{dl(t)}{dt} \geq 0 \\ d_{fac} \cdot \frac{l(t)^{2-3n} \cdot l_0^{3n}}{D_0} & \frac{dl(t)}{dt} < 0 \end{cases}. \tag{3.61}$$

Experimental results have shown that the time constants of swelling and shrinking processes differ strongly especially for concentration triggered PNIPAAm. **Figure 3.7** visualizes the static and transient response of a typical example simulated in Matlab Simulink.

Figure 3.7 shows the equilibrium length and the kinematic length of the hydrogel for an applied stimulus pulse function. The blue line is the equilibrium length $l_{eq}(T)$, which jumps

from $500\ \mu m$ to $600\ \mu m$ and follows the idealized stimulus pulse instantaneously. The length change depends on the implemented quasi-static swelling behavior in the system model. The red curve is the kinematic length $l(t)$, which describes the true time-dependent length or swelling behavior of the hydrogel. The red curve would be an exponential function for constant damping terms. In **Equation 3.61**, the damping coefficient depends on the kinematic length and leads to a non-linear first-order differential equation. The red curve is distorted and differs to the linear response.

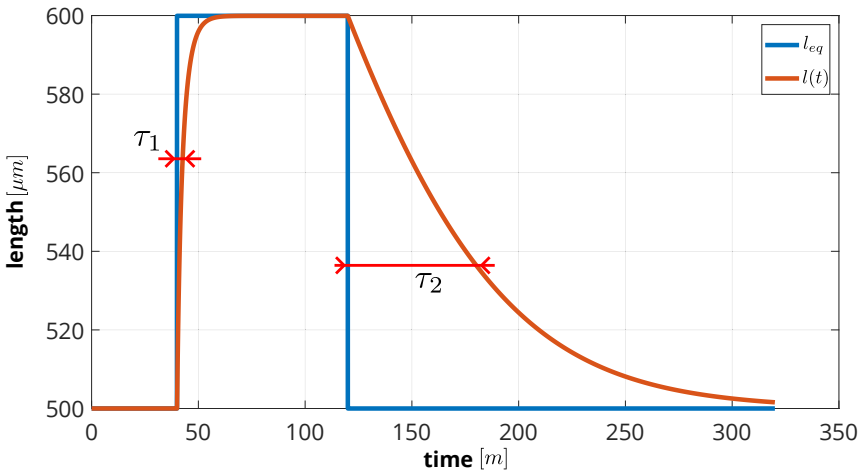

Figure 3.7: Equilibrium and kinematic length of the hydrogel at a stimulus pulse function.

3.3 Swelling Hysteresis Effect

Hysteresis is a system behavior, in which the change in an effect occurs with a time delay compared to the cause. In systems with hysteresis, the output quantity does not only depend on the input signal but also on its history. Hysteresis occurs in many natural and technical processes, especially in the magnetization of a permanent magnet, in control engineering, in biology and economics. It is known that hydrogels also have hysteresis effects [86], [87] and one of the earliest experimental investigations have been done at the TU Dresden [59], [119]. Hysteresis effects can be quantified by a sinusoidal stimulus function, which covers the entire operating range of the hydrogel. The related length or volume change is plotted on the y-coordinate. Hysteresis occurs if swelling and shrinking curves are not identical. The area in between indicates hysteresis and describes an energy loss in physics. It can be distinguished between a rate-dependent and a rate-independent hysteresis. Rate-dependent hysteresis is an effect, which depends on the rate (first time derivative) or the frequency of the stimulus signal. It is a transient or dynamic effect. A rate-independent hysteresis does not depend on the frequency and occurs also for quasi-static stimulus changes. During the experimental review, the frequency must be changed to decide whether there is quasi-static or dynamic hysteresis.

Transient hysteresis is determined by the damping element in a first-order differential equation. In **Section 3.2.3**, it could be demonstrated that the damping coefficient depends on the cooperative diffusion parameter of the hydrogel. Therefore, transient hysteresis is also referred diffusion-based hysteresis. Damping effects are proportional to both, the coefficient of the damper element and the first time derivative of the kinematic length according to **Equation 3.55**. Diffusion-based hysteresis is discussed in **Section 3.3.2**.

Quasi-static hysteresis occurs also for slowly varying stimulus functions. There can be several physical reasons. It is hypothesized that the attraction of the solvent caused by the hydrophilicity change of the material [88] causes this irregularity, which can be observed by slowly varying stimulus signals. Another reason can be the non-linearity parameter χ_2 of the energy function in **Section 3.1.1**. Large values cause a bifurcation as shown in **Figure 3.8**, which leads to an inherent hysteresis with jumps in the swelling and shrinking path. Ideal jumps of the hydrogel length are impossible and the swelling and shrinking behavior undergoes there a smooth transition with shifted phase-transitioning curves, which is shown in **Figure 3.8**.

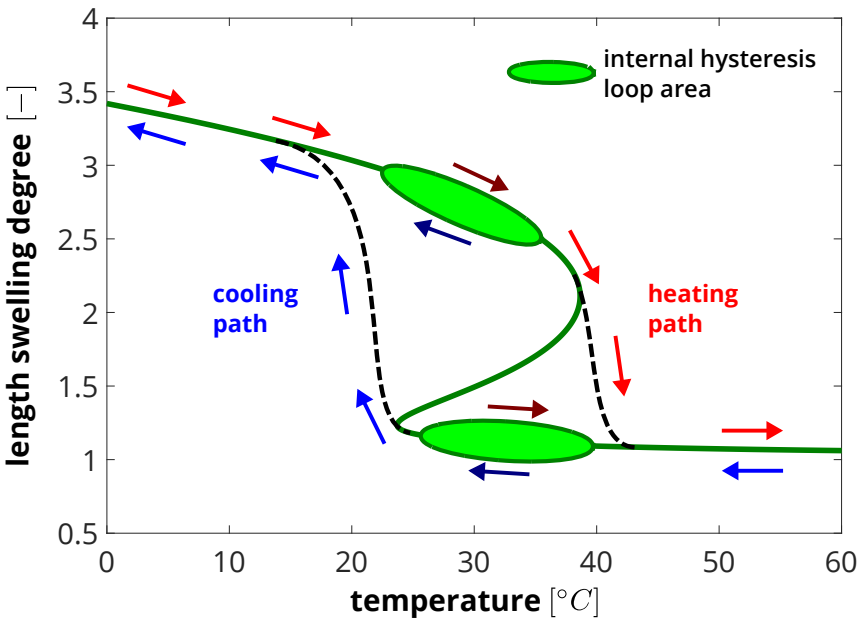

Figure 3.8: Quasi-static hysteresis caused by a bifurcation of the swelling response function.

Most likely, both effects can cause hysteresis, with one or the other dominating. A depleting sinusoidal stimulus function can be applied to indicate, which effect is dominant. According to the first hypothesis, internal hysteresis loops can end in the inner area or at the center of the hysteresis area. Internal hysteresis loops of the bifurcation model would either end at the upper or lower branch of the blue curve as shown in **Figure 3.8**.

3.3.1 Quasi-static Hysteresis

Quasi-static hysteresis models consist of outer and inner hysteresis loops. Outer loops become visible if the stimulus change covers the entire operation range from the left to the right saturation point. Internal loops appear for depleting stimulus functions, which oscillate

with decreasing amplitudes around the lower critical solution temperature T_{LCST}.

The left hysteresis hull curve is utilized for decreasing stimuli and describes the swelling behavior. The right hull curve is used for increasing stimuli and describes the shrinking part. The original swelling response curve without hysteresis goes through the T_{LCST} point. The outer hysteresis hull curves are shifted horizontally to the right or to the left as shown in **Figure 3.9**.

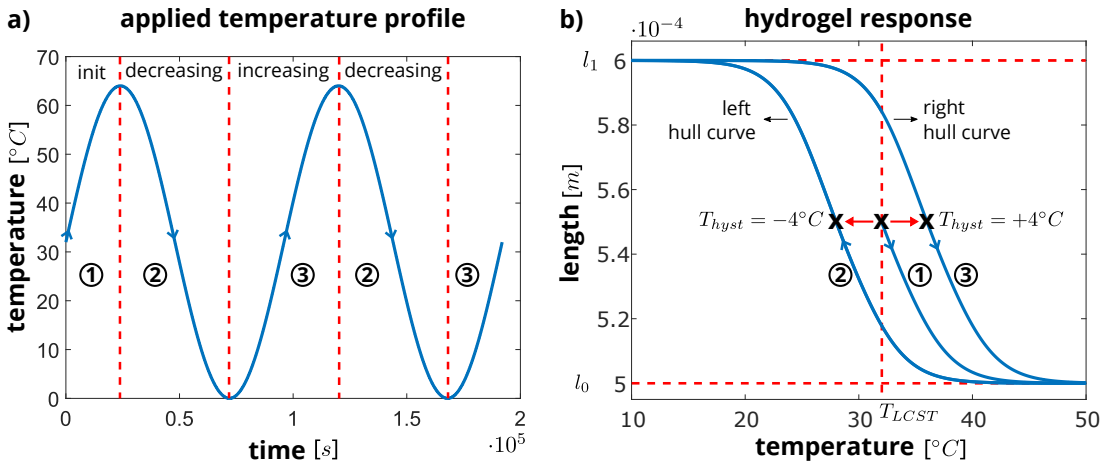

Figure 3.9: Hull curves showing the equilibrium length of the hydrogel at sinusoidal temperature profiles.

It can be realized by adding a hysteresis offset parameter T_{hyst} into the sigmoidal function of **Equation 3.62**. A positive value shifts the curve to the right, which happens for decreasing stimuli and a negative value to the left. The T_{hyst} value can be changed by if-conditions during transient simulations. The change of the hysteresis offset parameter will be triggered by a sign change of the stimulus derivative in system models presented in **Section 6.1.1**:

$$Q(T) = \frac{Q_1 - Q_0}{1 + \frac{1}{1+e^{k_u \cdot \left(T - T_{LCST} - T_{hyst}\right)}} + 0.5 \cdot e^{-k_l \cdot (T - T_{LCST} - T_{hyst})}} + Q_0. \tag{3.62}$$

Modeling and simulation of internal hysteresis loops will be explained at the swelling results for a depleting stimulus function shown in **Figure 3.10**. The hysteresis model is initialized in the center of the volume phase-transition process. Thereby the hydrogel length is in the center between the upper and lower bound and the stimulus temperature is equal to the lower critical solution temperature T_{LCST} as shown in point (1). By increasing the ambient temperature, it follows the regular 5-parameters sigmoidal function until point (2) is reached. Now, a decreasing temperature is detected and a hysteresis offset temperature of $T_{hyst} = -2\,°\mathrm{C}$ is applied in **Equation 3.62**. When point (3) is reached, the temperature increases and the hysteresis offset is changed to $T_{hyst} = +2\,°\mathrm{C}$. Reaching point (4) another sign change of the stimulus derivative is detected. The sign change happens outside of the lower saturation range l_0 and special calculations must be activated to model internal hysteresis loops, which start from there. The swelling response does not follow the left hull curve as shown in **Figure 3.10**.

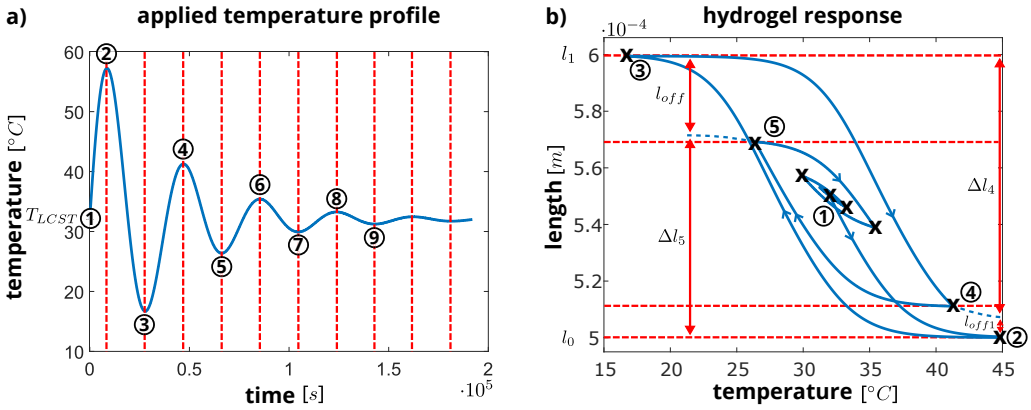

Figure 3.10: Internal hysteresis loops are highlighted for a depleting sinusoidal temperature profile.

The new swelling branch must start at point (4), which has a current length of $l(T,t)$ and should end at the saturation length l_1 for low stimulus temperatures. The new curve with brown color in **Figure 3.11** is utilized for inner loops. The brown curve has a shape and a mathematical description, which is similar to the left hull curve shown in blue, except that the lower bound l_0 is shifted by the offset length l_{off} upwards. The offset length l_{off} can be calculated from the following dimensional ratios:

$$\frac{l_1 - l(T,t)}{l_1 - l_{H_l}(T)} = \frac{l_1 - l_0 - l_{off}}{l_1 - l_0}, \tag{3.63}$$

which leads to:

$$l_{off} = l_{off1} = (l_1 - l_0) \cdot \left(1 - \frac{l_1 - l(T,t)}{l_1 - l_{H_l}(T)}\right), \tag{3.64}$$

where l_1 is the maximum potential phase-transition length, l_0 is the minimal potential phase change length, $l(T,t)$ is the current length at point (4) and $l_{H_l}(T)$ is the kinematic length of the left hull curve, which corresponds to the same stimulus temperature T.

In the next stage the ambient temperature is decreasing until point (5) is reached where another temperature direction change is detected. A new offset length is calculated, which is now defined by:

$$l_{off} = (l_1 - l_0) \cdot \left(1 - \frac{l(T,t) - l_0}{l_{H_r}(T,t) - l_0}\right). \tag{3.65}$$

The parameter l_{off1} is set to zero. Two offset parameters l_{off} and l_{off1} are necessary to control the lower bound and the gain of the sigmoidal function independently. The sigmoidal function is now described by seven parameters in system level simulation tools:

$$l(T) = \frac{l_1 - l_0 - l_{off}}{1 + \frac{1}{1+e^{k_u \cdot \left(T - T_{LCST} - T_{hyst}\right)}} + 0.5 \cdot e^{-k_l \cdot (T - T_{LCST} - T_{hyst})}} + l_0 + l_{off1}. \tag{3.66}$$

The same algorithm is applied for points (6) to (9). Asymmetric hysteresis loops that end outside the T_{LCST} value have also been verified in Matlab Simulink. A similar modeling approach is published in [120] and [121].

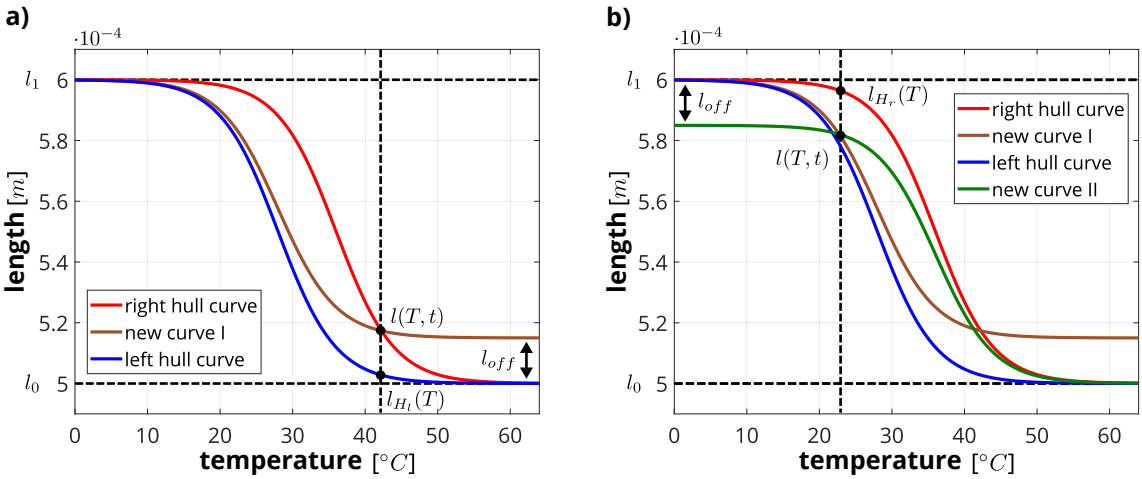

Figure 3.11: Calculation scheme for the offset length of inner hysteresis loops.

3.3.2 Transient Hysteresis

Transient hysteresis is caused by the damping parameter in the first-order differential equation, which is used to simulate the kinematic length. The damping coefficient represent the cooperative diffusion in hydrogels and leads to rate-dependent hysteresis cycles for sinusoidal stimulus signals.

Figure 3.12 shows a Matlab Simulink model, which is used to evaluate transient hysteresis effects. The left part of the model generates a depleting sinusoidal stimulus function with an initial amplitude of $25\,°\mathrm{C}$ and a static offset of $32\,°\mathrm{C}$, which has the same value as the lower critical solution temperature T_{LCST} of the hydrogel. The interpreted Matlab function in the center of the model calculates the quasi-static equilibrium length $l_{eq}(T)$ according to **Equation 3.26**. It follows a Simulink model of the first-order differential equation, which computes the kinematic length $l(T,t)$ with regard to the time t. No hysteresis offset parameters have been applied to the system model.

The left lower plot in **Figure 3.12** shows the stimulus dependent length change of the hydrogel. A depleting sine wave was simulated for ten cycles. Inner hysteresis loops end exactly at the T_{LCST} value. A second result plot is shown in the right lower part of the figure. Here, the static offset stimulus temperature was enlarged from $32\,°\mathrm{C}$ to $40\,°\mathrm{C}$. The inner hysteresis loops are asymmetric and end at $40\,°\mathrm{C}$ stimulus temperature.

The damping values in the presented example are highly enlarged. A transient hysteresis simulated with realistic values and frequencies shows almost identical swelling and shrinking curves. Transient hysteresis can usually be ignored. However, significant hysteresis effects have been observed in measurement. It leads to the assumption, that a quasi-static rate-independent hysteresis is existing in hydrogels. It requires reliable measurement data of hysteresis offset parameters for modeling and simulation in engineering applications. Hysteresis effects in hydrogels are published in [86], [87].

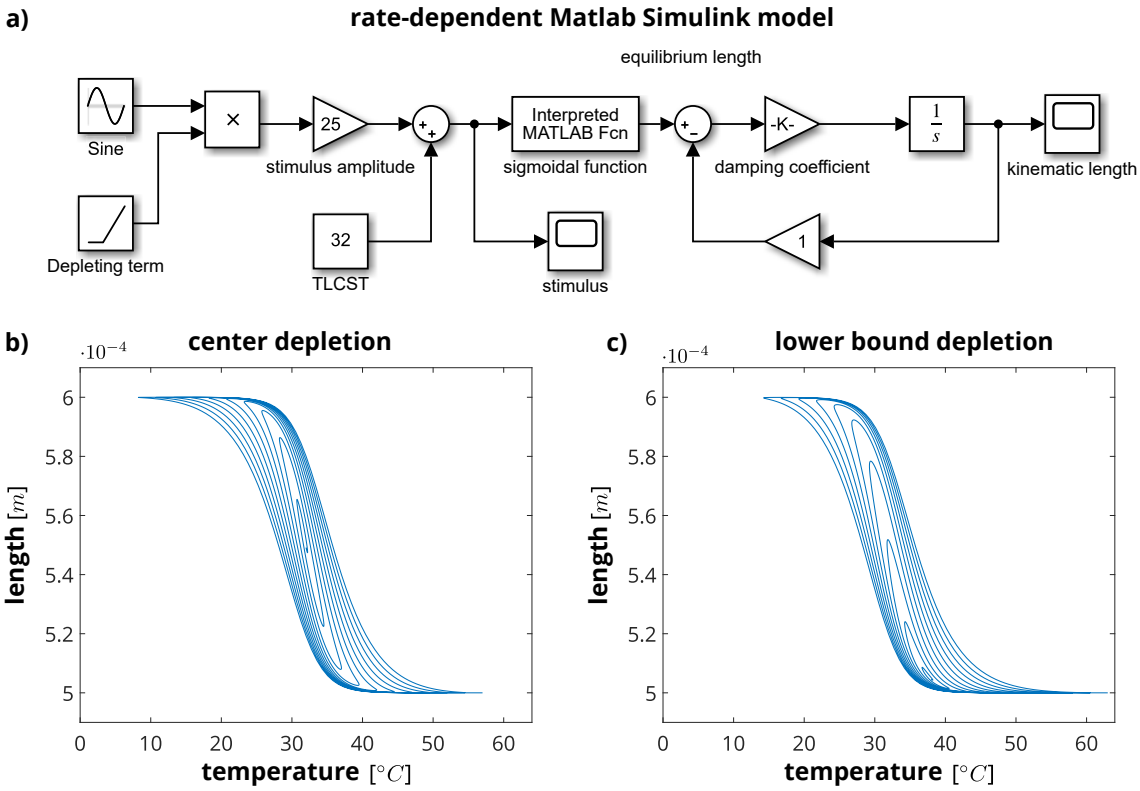

Figure 3.12: Rate-dependent hysteresis model and simulation results obtained in Matlab Simulink.

Chapter 4

Characterization of Hydrogel

content of chapter

Appropriate material properties are the key requirement for successfully modeling microfluidic components and hydrogel-based systems. In contrast to many well-known and well-defined materials in mechanical and electrical engineering, the properties of thin films in microelectronics or polymer materials in microfluidics are subject of large fluctuations. Those properties depend on structural dimensions, on the material composition and the manufacturing conditions. Properties published in the literature must be carefully evaluated for their validity, especially of prototypes or products, which are manufactured in facilities with new processes or process conditions.

For many design tasks it is necessary and sufficient to describe and optimize the functional behavior of devices using equations that quantify effects and interactions through phenomenological considerations. It is a typical engineering approach to measure macroscopic quantities for the elasticity, chemical diffusion and heat transfer or the swelling behavior in order to define the governing equations in component and system models. However, developing new designs needs also a deep understanding of microscopic effects and their impact on the performance. It has been shown that microscopic effects are important for assessing mechanical strength in overload situations, to quantify leakage rates, drift effects or the long-term reliability.

Chapter 4 focuses on methods, on the equipment and on analytical and on numerical approaches for the extraction of characteristic material properties through experimental evaluation of test structures and prototypes. Hydrogels are known to have fluctuating properties. A first reason is the statistical nature of the polymerization process where long-chain molecules are formed and interconnect to each other rather randomly. It affects the chain-lengths and distances, which finally influence the elastic and swelling properties of the hydrogel. A second and more important reason is the way of manufacturing in research laboratories where hydrogels are often synthesized manually. The lack of automation naturally causes variations in the processing time, composition of ingredients and the manufacturing conditions.

In the scope of this work, the statistical distribution of the gelation time is investigated for several PNIPAAm samples. There the transition from the liquid phase to the solid phase is of interest and can be measured by using rotating nanowires. For this experiment, the prepolymer solution is mixed evenly with these nanowires in a cuvette. These nanowires start to rotate through the magnetic field of the stirring plate and their angle of inclination is de-

tected optically by a reflecting laser beam. The light intensity is measured with a camera system where the optical signal modulates at twice the frequency of the rotating wires. The rotation stops and consequently the blinking when a solid phase is formed. The blinking motion of the laser beam is evaluated as an area change in a subsequent image processing routine. The normalized results of multiple experiments are shown in **Figure 4.1**. These experiments were repeated many times and the solutions where all applied by using precise pipettes under similar conditions. However, it can be seen in **Figure 4.1** that the gelation time varied significantly by almost 20 % despite of careful sample preparations. It indicates that the manual synthesis of reproducible hydrogels is not trivial. These experiments were carried out together with M.Sc. Katinka Kohl.

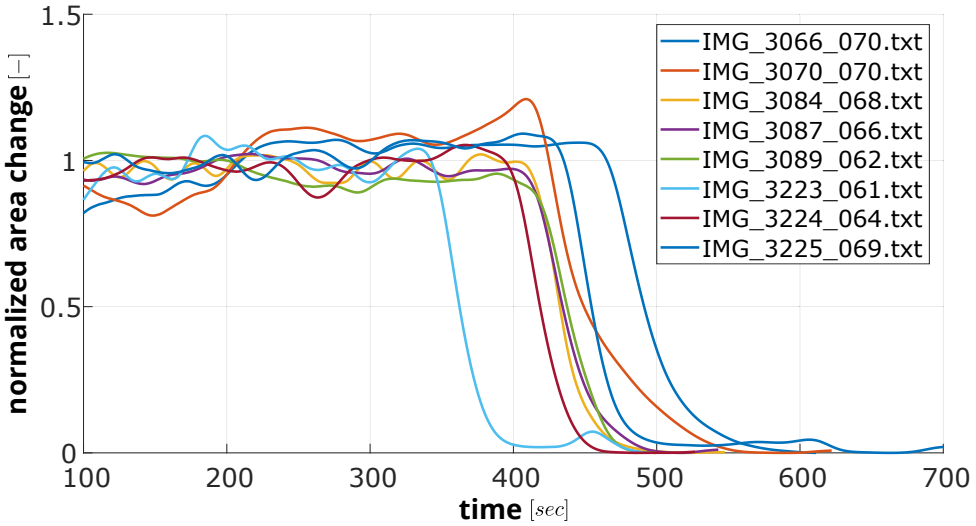

Figure 4.1: Exemplary measurements of the gelation of PNIPAAm samples. A high value corresponds to a rotating nanowire indicating a liquid phase. A close to zero value corresponds to fixed nanowires, indicating a solid phase.

Chapter 4 will demonstrate that computer-aided experimental characterization methods are vital to improve the accuracy and throughput compared to systems with manual inspections. In microsystems, a slight variation in quantities can affect the measured behavior significantly. It is known from sensitivity analyses, that the same absolute tolerances of input parameters cause stronger output deviations at lower nominal values. In the process of miniaturization, the dimensional tolerance of the hydrogel sizes do not shrink in the same way as the nominal dimensions.

All essential phenomenological hydrogel parameters must be characterized for a reliable microfluidic system design. Vital parameters are the static swelling behavior as a function of the stimulus, the rise time relationship for the transient response, the elasticity at different swelling states and hysteresis parameters. Complex microfluidic devices often undergo time and resource consuming manufacturing and assembling steps. Hence, comprehensive design and characterization technologies are essential for new components and systems with a high performance and yield.

In this chapter the measurement procedure is subdivided into three principle steps. The first step is the **data acquisition procedure**, where the equipment and the measurements

are automatically controlled by a computer program. Usually, a large amount of raw data must be stored on a disk, which can be challenging to conserve on a long-term perspective. The raw data may include images, videos and text files where the data samples have a very specific relationship to each other.

In a second step, the recorded data are processed and reduced in size as known from big data computer sciences. The ultimate goal of this **data evaluation procedure** is to find, compute and select core data, which are necessary for a clear input-output relationship of the phenomenological models.

In a third step, the processed data are transformed and adapted to specific mathematical equations in design systems. Targeted are simplified functions with one or multiple input parameters referenced as a response surface in computational engineering and measurement technologies. In this **data adaptation procedure**, the measured model parameters are represented by polynomial or other fit functions, which can be processed and evaluated efficiently during optimization or transient simulations.

4.1 Data Acquisition through Automated Measurements

The swelling kinetics are often measured manually where for example the weight of gel samples is detected at certain stimulus concentrations [69]. These tests are fast to establish and the mass change of hydrogel samples can be determined in a reasonable time.

However, the scope of this work is an automated computer-controlled measurement approach for the swelling kinetics. A camera-based system extracts a series of two-dimensional images of the swelling process and provides detailed information about the lateral swelling states. Average length and area changes can be calculated from image recognition procedures. Furthermore, the computer system can extract statistical data as mean values and standard deviations, which quantify the repeatability of the process. In contrast to weight measurement techniques, camera-based image recognition procedures provide also data about the local swelling behavior at outer edges and corners. Those measurement results describe the uniformity of the time and stimulus dependent swelling process and are important to assess the sealing behavior and potential leakage rates of the microvalve designs.

Another quantity is the initial stiffness and the stiffness change during the swelling process. However, accurate measurements are very difficult to carry out in practice. In **Section 4.1.2**, an experimental approach will be presented, which is similar to the detection of the gelation time as introduced in **Section 4.1.1**. In a liquid phase, the nanowires can rotate in the hydrogel solvent. In a solid phase, nanowires can only slightly oscillate at alternating magnetic stimulus signals. These oscillation amplitudes depend on the stiffness of the surrounding material and the applied driving forces. Then these experiments are recreated with parametric finite element models in order to extract the stiffness data by parameter adaptation methods. In particular, the stiffness of the hydrogel in the finite element model is increased or decreased until the numerical behavior corresponds to the measurement data.

An automated and user-friendly measurement set-up and data acquisition procedure is the goal in the following section.

4.1.1 Measuring the Swelling of Hydrogels

The measurement setup shown in **Figure 4.2** is developed to characterize the swelling behavior of the hydrogel. It can be separated in three main levels:

The **first layer** is the monitor and control level. It is a computer system with interface ports, which are controlled by a software program like LabVIEW. User routines with a GUI have been developed to connect controllers and devices, to define their target functionality and to organize the raw data storage. The downside is, that all devices must be programmable with open drivers and be supported by LabVIEW.

The **second layer** is the process level, at which all independent controllers operate. The outsourcing of certain functions from the computer level into a fieldbus system helps to maintain the performance of LabVIEW. For example, hardware based PID can often operate faster than software-controlled algorithms on the computer system of level one.

The **third layer** is the field layer in which various pumps, flow sensors, the microfluidic chip, heating systems and other laboratory devices are arranged and connected to each other. The data exchange procedure of the measurement system is very flexible. There is no need to connect all components to the next higher hierarchical level. For instance, the syringe pumps used in the setup can operate in a master-slave configuration, where one pump is controlled by the computer and then the signal is forwarded to one or more slave pumps by the master pump. To improve the accuracy, the volume flow rate in the system is permanently monitored by flow sensors. Deviations from the target behavior are recognized by a PID controller, which adjusts the pump output in a feedback loop.

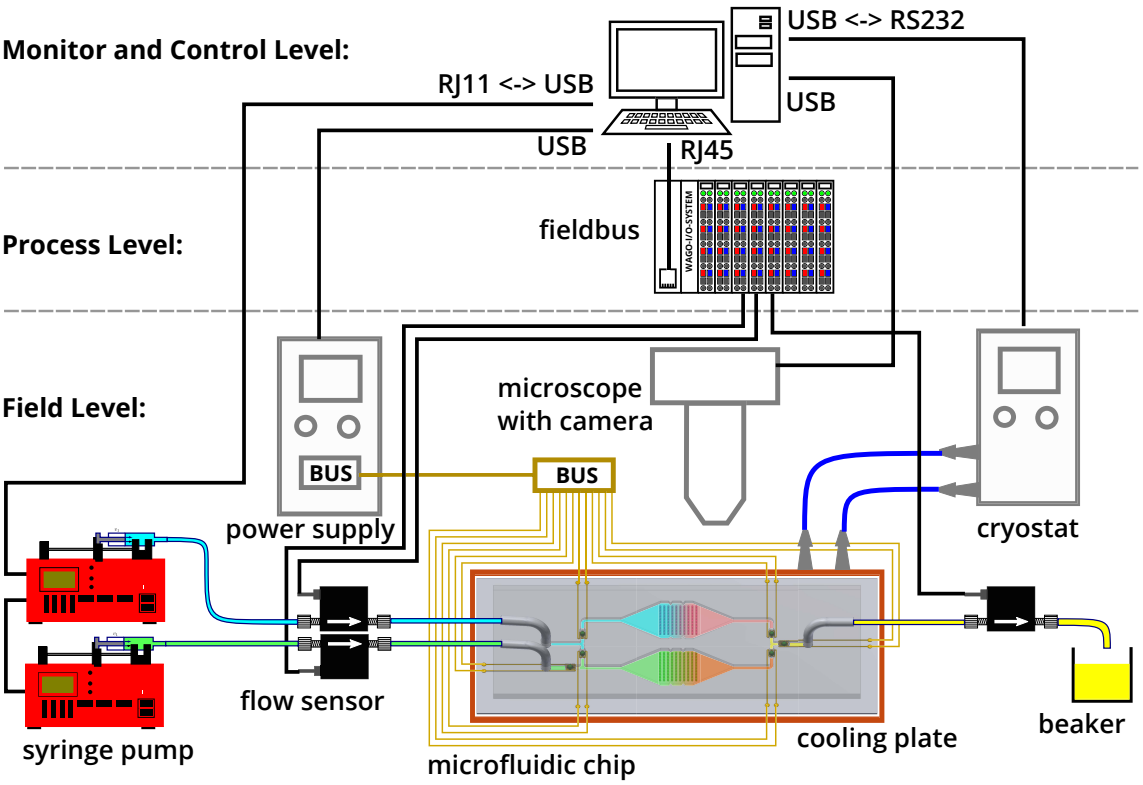

Figure 4.2: Exemplary measurement setup concept to characterize the hydrogel swelling.

The measurement setup allows to change independently the stimulus concentration, the volume flow rate and the temperature in the vicinity of the hydrogel. The stimulus concentration can be defined by two syringe pumps in the left lower part of **Figure 4.2**. The first reservoir contains the stimulus and the second one an aqueous solution. Depending on the applied pump rates, the stimulus concentration can vary from zero to the upper level defined by the concentration in the first reservoir.

The volume flow rate is primarily defined by the syringe pumps. However, it turned out that the true flow is slightly affected by the total fluidic resistance of the system. For this reason, the volume flow rate is measured and the pump outputs are controlled by two flow sensors. The temperature can be increased by an Indium-Titan-Oxid (ITO) heater and decreased by active cooling using a cryostat system. Measurements at the integrated temperature sensor have shown that the ITO heater can change the temperature almost instantaneously compared to the time constant of the hydrogel. The cryostat was necessary for two reasons, first to reduce the temperatures below ambient and second to increases the speed of cooling processes to reach time constants below one second.

A digital camera is mounted on a microscope to measure the lateral dimensions and the shape of the hydrogel. The camera resolution is usually set to 1600x1200 pixel and the frame rate to about $1\,\mathrm{Hz}$. With the magnification of the microscope it corresponds to a length resolution of about $1.25\,\mu\mathrm{m}$ per pixel. Higher resolutions are possible but will make the subsequent image handling, processing and storage more challenging. Furthermore, the resolution is clearly above the wavelength of visible light used for the inspection of a $500\,\mu\mathrm{m}$ object. It will encounter no challenge by the wavelength limitation of optical microscopes.

Three different stimulus signals are necessary to characterize the swelling behavior: A **slow ramp signal** is used to evaluate the quasi-static phase-transition behavior of the hydrogel. In practice, a triangular function is repeated several times with increasing and decreasing waveforms in order to average the measurement result over several cycles.

Then, a **pulse signal** is applied to measure the transient response. It provides information about the length dependent rise time of the hydrogel. The applied pulse function stimuli are not ideal especially for chemical concentrations. Here, the delay time starting from the mixing junctions at the inlet to the hydrogel specimen is velocity dependent. This time delay needs to be manually corrected in a separate data processing step. For this condition, a constant total volume flow rate is required. To change the ambient concentration level, the volume flow rate of two syringe pumps are increased and decreased by the same rate, which will apply an overall constant volume flow and still changes the resulting concentration level. For this behavior, **Equations 7.4** and **7.9** are used to calculate the time delay.

Finally, a **slowly depleting sinusoidal signal** around the lower critical solution temperature T_{LCST} has been utilized to measure quasi-static hysteresis parameters. The time duration to determine hysteresis effects is between several hours and a few days.

During each measuring step, an image with a corresponding text file entry is saved to the hard drive. The text file entry contains a time stamp, the applied volume flow rates, the temperature level of the cryostat and the applied voltage level of the ITO heater. Based on these values, the corresponding concentration and the applied temperature at the hydrogel can be readily determined in the post processing step.

Figure 4.3 shows the front-end for the swelling measurement station. On the left side is the current image of the camera, the frame rate and the resolution. A view panel allows to zoom and pan the image to the area of interest. The start-stop button activates the measurements for the specified time range. On the right side are settings for the equipment and the applied volume flow rates of both syringe pumps for the proposed measurement procedure.

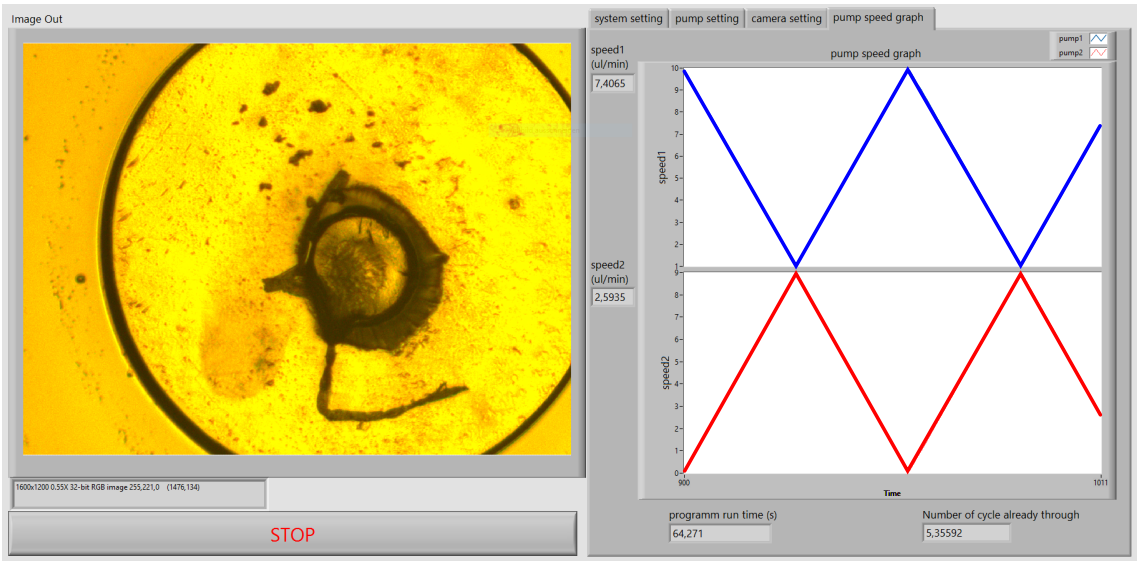

Figure 4.3: Examplary LabVIEW front panel for the hydrogel swelling experiment.

4.1.2 Contactless Measurement Concept to Determine the Core Stiffness of Hydrogels

Multiple methods exist to measure the stiffness of hydrogels. In macroscopic systems, the elastic properties are usually determined by tensile and shear testing experiments on larger specimens. In microscopic systems, not only the specimens but also the test equipment, in particular the probe tips, must be miniaturized. Clamping of samples to measure the force-displacement relationship is often difficult or even impossible, especially for small and highly flexible materials as hydrogels. Alternatively, the stiffness of miniaturized samples has been detected through micro-indentation testing [122], [123] or based on the atomic force microscopy [124], [125]. In [124], the AFM is utilized to detect the local surface stiffness of the material through colloidal probing of small gels with micrometer size.

Both, micro-indentation and atomic force-based testing methods utilize tiny tips or needles to measure the force-displacement relationship at the surface of the specimens. In the scope of this work, a collaborative research project was established between the University of Minnesota (Group of Professor Stadler) and the TU Dresden (Group of Professor Odenbach and Professor Richter). The aim of this project was the determination of stiffness parameters in the interior of the hydrogel using contactless measuring techniques. In previous work, stiffness measurements are carried out at the outer faces. The surface properties are expected to differ from the behavior within the volume. In addition, surface properties are not uniform since photolithographic technologies are used to structure the hydrogel. Light intensity fluctuations, like shadowing effects, occur at outer edges and therefore the light intensity does

not ideally jump from on to off in a photolithographic process. Instead there is a gradient, which depends on process conditions, the sample size and its location [126].

The new measurement setup, which is developed and tested during this project, is shown in **Figure 4.4**. It is similar to the gelation time experiments discussed earlier. Since full turns of magnetic nanowires in solid material are unreasonable for stiffness measurements, the nanowires of the hydrogel samples are just stimulated to small tilt angles or vibration amplitudes. The measurement approach can be outlines as follows:

In the initial state, all magnetic nanowires in the hydrogel have the same orientation. The alignment is achieved by a strong and homogeneous magnetic field impulse applied through a VSM. Perpendicular to the nanowires are two electro magnets, which create a torque, depending on the applied current signal. When the electromagnets are activated, the nanowires tilt slightly towards the poles. After switching off, the nanowires return nearly to the starting position. It indicates, that the material where the nanowires are embedded behaves almost elastic. The tilt angle depends on the applied torque, on the size of the nanowires and on the stiffness of the hydrogel. The angle of inclination is detected by the reflected laser light and was recorded with a digital camera. The light reflection in **Figure 4.4** is based on the magneto-optic Kerr-Effect [127], [128]. The stimulation process is repeated several times by a pulse function to observe results over many cycles.

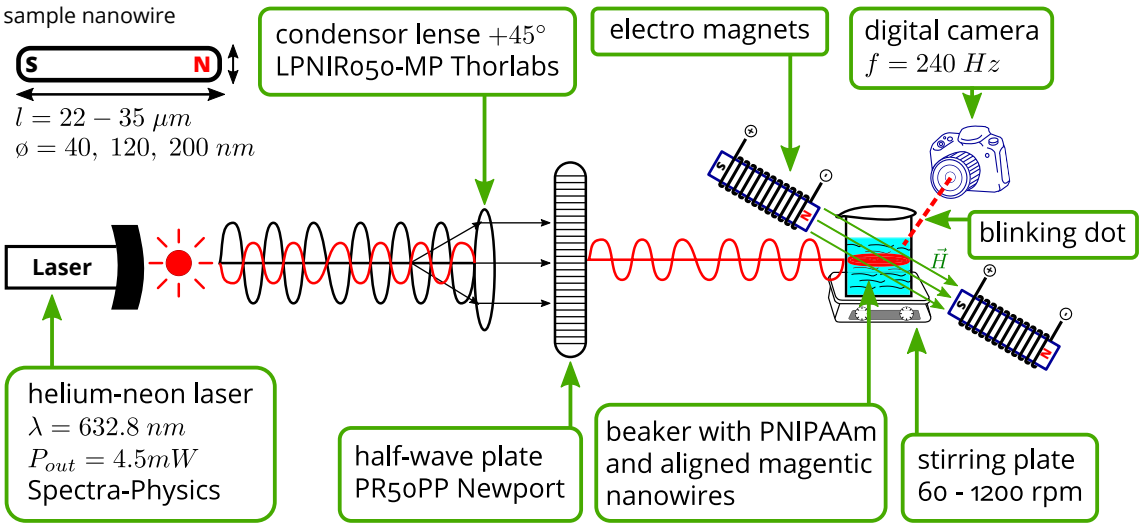

Figure 4.4: Schematic of the measurement setup consisting of a laser beam and 2 electromagnets creating the magnetic field $\vec{H}$. The field causes the aligned magnetic nanowires to deflect, which are used to determine the Young's modulus of the hydrogel material.

The light intensity measured by the digital camera is inverse proportional to the deflection amplitudes of the nanowires. **Figures 4.5** shows a typical transient response. The pulse frequency of the current applied to the electromagnets is about $1\,\mathrm{Hz}$ and the high value is about $10\,\%$ of the pulse duration. The light intensity gets smaller with increasing tilt angles, which depends on the optical setup. Finally, the signal difference between high and low value is proportional to the tilt amplitude.

In **Figure 4.5**, a little drift of the signal can be seen, which is superimposed to the pulse signal response. The light intensity decreases over time, which means that the angle of incli-

nation slowly increases during the measurements. The behavior reverses when the current at the electromagnets changes the direction. It indicates a viscoelastic behavior of the hydrogel, which should be further investigated in future experiments.

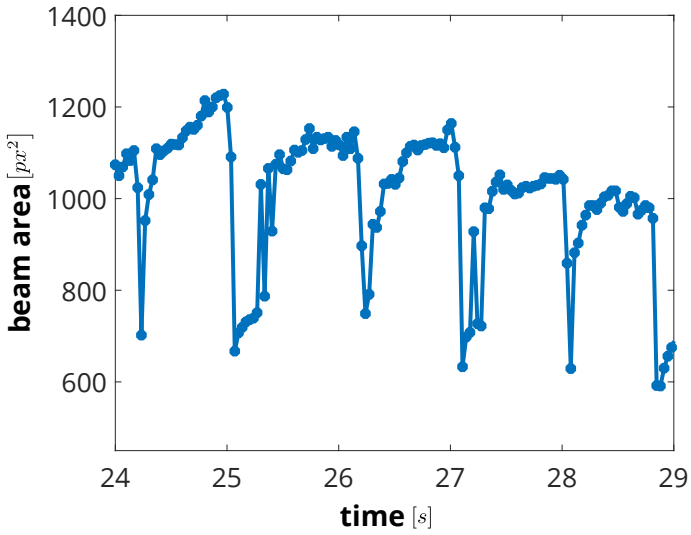

Figure 4.5: Image processing result, which is showing the illuminated area change of the laser beam over time when applying a pulse function at the electromagnets.

The measurement in **Figure 4.5** represent how far the nanowires can deflect within the gel. This rotation angle can be replicated in a finite element model where this angle of inclination to the applied magnetic force is adapted by changing the ambient material stiffness.

Contrary to the common rheology testing, the proposed method is a promising contactless measurement method. The nanowires with their rotation only apply a minimal force to the hydrogel to determine the core stiffness of the material. A classical rheology measurement setup consist of a cone-plate system and through the momentum needed to create an oscillating movement, the shear relaxation modulus G, the shear storage modulus G' and the shear loss modulus G'' of the material are determined. During the rheology experiment, the applied pressure to the material affects the characterization results [129].

4.2 Data Evaluation with Image Recognition

In the previous chapter, the data acquisition procedure to measure the hydrogel swelling and the stiffness change has been described in detail. Each image is linked with a text file, which contains the time stamp, the stimuli data and the volume flow rates. Several thousand images are usually taken to measure the swelling states and several hundred thousand images are necessary to measure an oscillating response of the nanowires. Each period of a pulse function needs to be resolved with 50 to 100 images to trace the rise and fall time in the transient response with acceptable accuracy and several hundred cycles have to be monitored to observe drift effects accurately.

The implemented data evaluation procedure is written in Matlab and uses several library functions of Matlab's image processing toolbox. All of the images obtained in the data acquisition procedure must be written into a video sequence since the storage and processing of

such a large number of images by individual graphic files is impractical. A GUI provides access to parameters that control the data evaluation procedure. A screenshot of the GUI for the swelling experiment is shown in **Figure 4.6**.

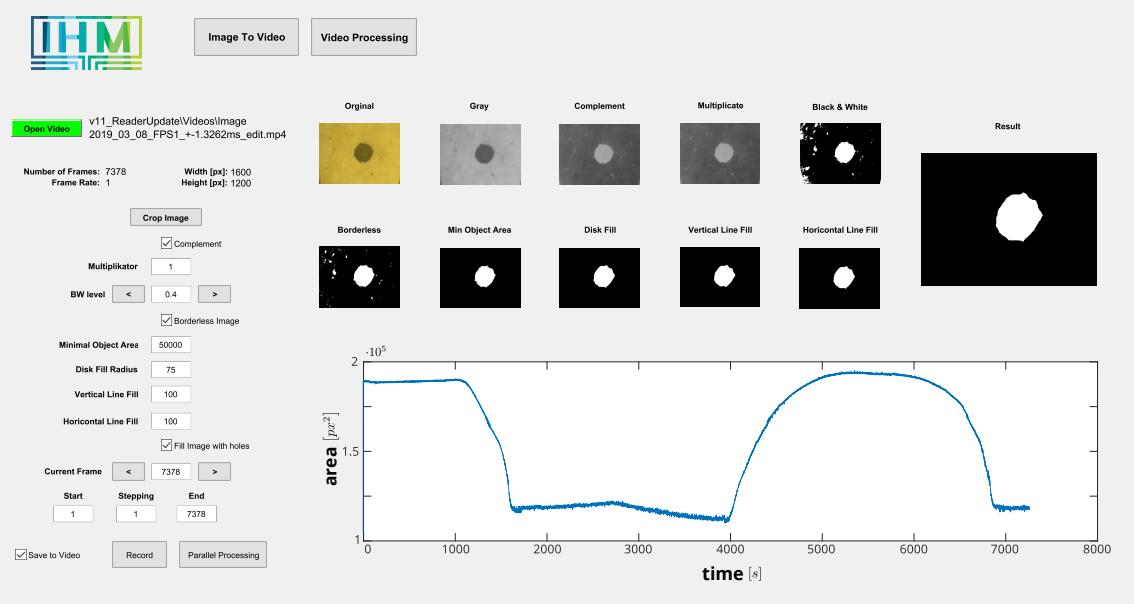

Figure 4.6: Graphical user interface to determine the size of the hydrogel for each image.

The data evaluation procedure will be explained for the hydrogel swelling results introduced in **Section 4.1.1**. As a first step, the selected video is loaded into the Matlab workspace and the first frame is processed by an image recognition routine based on predefined settings. The aim of the Matlab routine is to determine the surface area changes of the hydrogel during the swelling process. Often it is not easy to detect the area of the RGB images automatically because the hydrogel in the swollen state is transparent. At the beginning of the data evaluation process, the predefined settings must by modified and adapted to the current appearance of the images. Thereby it is recommended to start with an image of the swollen state, were the contours of the hydrogel are barely visible. After the image parameters have been adjusted, the collapsed state is verified whether a correct area is detected or not. The frame panels shown on the left lower part of **Figure 4.6** can be used to navigate through the images.

As a first step of the processing routine, the recorded RGB images are transferred to an 8-bit grayscale image with 256 shades of gray. The dark spot at the center is the hydrogel. The next step is to convert the grayscale image into a binary image with only black and white values. In practice, it is often difficult to find an appropriate threshold value, which distinguishes best between the hydrogel and the surrounding area. If the threshold would be set to 0.25, all pixels with gray levels between 0 and 64 become black, the other pixels become white. To adapt the threshold parameter by manual inspection, the users can “zoom” into the grayscale range. Zooming means that either the upper or the lower bound of the grayscale range can be modified by a scale factor defined in the graphical user interface (GUI). It changes the brightness of the images, as known for computer graphic tools. Thereby the edge between the hydrogel to the background is better visible. Finally, the user can adjust the threshold

value to define and distinguish black and white, which is shown in the right upper image in **Figure 4.6**. The checkmark in the GUI creates a complement of the images where the grayscale levels and the binary values can be reversed, because often a white area is better detectable than a black area.

In a next step, smaller artifacts with black or white scratches and dots are erased. In some cases, the outer contour is not recognized correctly, which means that the areas penetrate into each other. It happens especially in regions with low image contrast. Similar to algorithms known from computer graphics, the convex hull in the wrong area is approximated by line search algorithms to close the surface smoothly. Finally, the total area of the hydrogel is calculated from the number of white pixels in the images.

The result of the data evaluation is displayed in the right lower graph in **Figure 4.6** and shows the detected surface area in $\left[\mathrm{px}^2\right]$ with regard to the time. The automated image recognition process needs less than a second for each frame but the entire analyses of larger videos might take several hours. Therefore two regimes are implemented. One is the serial regime (started through the "Record" button), where each image is processed sequentially, the results are displayed in the GUI and the frame is saved to a file. At the end of the analysis, all the saved files are integrated to a video, for better inspection. If larger batches of the same video type (experiment) are evaluated, then the parallel toolbox feature can be used. For an "i7-4990 HQ" computer, four processes can be started at once, which cuts the processing time almost equally by a factor of four.

4.3 Data Fitting and Model Adaption

In the previous section, the measurement data captured in video sequences have been transformed to response curves, which describe the surface area in $\left[\mathrm{px}^2\right]$ during the swelling process depending on the applied stimulus. The response curves from slowly varying stimulus functions define the quasi-static behavior and the response curves at pulse functions provide additional information to define the damping term or the rise time in a transient simulation. After the data evaluation procedure discussed in **Section 4.2**, the response curves are represented by a series of datapoints mostly in pixel units. The goal of the following data adaptation procedure is to transform the results into useful characteristic dimensions, here from $\left[\mathrm{px}^2\right]$ to $[\mu\mathrm{m}]$, and to find parameters for simplified analytical functions that are used to model and simulate hydrogels in microfluidic systems. Thereby the results are recorded to a database, which will help to further predict the hydrogel behavior at sizes, that are not synthesized yet. These features support the parameter optimization routines of the microfluidic elements as presented in **Chapter 7**.

4.3.1 Quasi-static Response

As a first experiment the quasi-static response is evaluated for a PNIPAAm hydrogel with $2.5\,\%$ SA. Thereby the hydrogel is targeted to be a cube like element with a length and width of $500\,\mu\mathrm{m}$ and a height of $150\,\mu\mathrm{m}$. The synthesis and photo-structuring followed the standard lab procedure, which is described in [5], [70]. During the experiment, the concentration changes from pure water $C = 0\,\%$ to a $C = 23\,\%$ mixture of ethanol in water. In **Figure 4.7**, the blue

points represent the measurement results and the green line is the approximated analytical sigmoidal function that describes the swelling process for modeling and simulation.

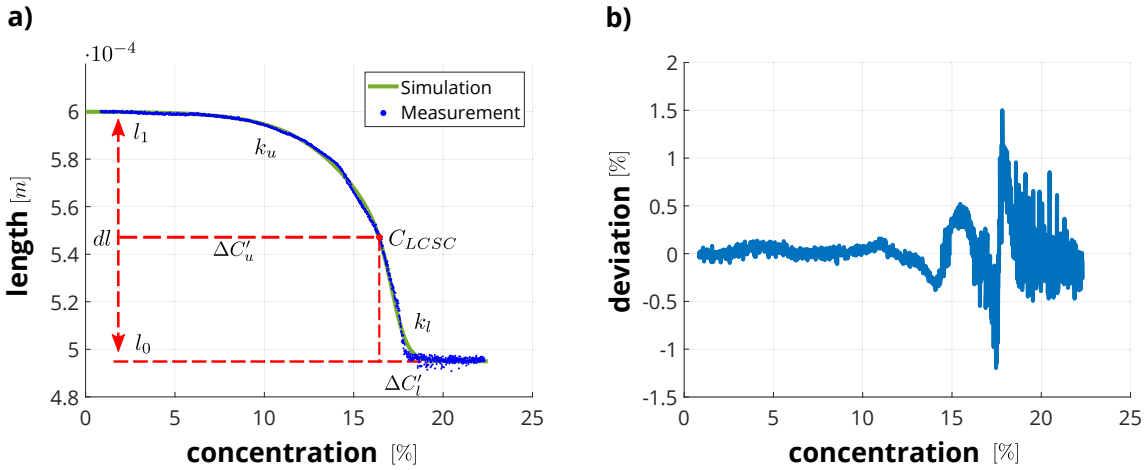

Figure 4.7: In a) the processed measurement data are shown in blue and the green line represents the sigmoidal function, which is adapted to the experimental results. In b) the deviation of the sigmoidal fit function to the measurement is plotted, which highlights a maximum of $1.5\,\%$ deviation.

The approximated analytical sigmoidal function according to **Equation 3.28** is defined by five parameters as shown in **Table 4.1**. All five parameters can either be determined manually by visual inspection or the values are extracted automatically by a function fit routine. The reference length l_0 and the length change Δl are obtained from the lower and upper bounds of the length parameter on the y-axis. The lower critical solution concentration C_{LCSC} corresponds to the x-axis value for a length, which is in the center between upper and lower bound. The last two parameters $\Delta C'_u$ and $\Delta C'_l$ describe the upper and lower curvature of the sigmoidal function and are defined by the distances on the x-axis to the C_{LCSC} value, at which the function values on the y-axis intersect the upper and lower bounds within a $5\,\%$ tolerance band.

The approximated analytical sigmoidal function is superimposed to the measurement data and the relative deviation is plotted for the given parameter set as shown in **Figure 4.7**. The parameters can easily be adapted to find optimal settings.

Table 4.1: List of parameters needed to describe the static behavior of the hydrogel.

parameter	Symbol	Value	Unit
length change	Δl	$105 \cdot 10^{-6}$	m
reference length	l_0	$495 \cdot 10^{-6}$	m
lower critical solution concentration	C_{LCSC}	17	%
concentration distance for upper curvature	$\Delta C'_u$	12	%
concentration distance for lower curvature	$\Delta C'_l$	2	%

In the experimental setup, the stimulus is gradually increased from $C \approx 0\,\%$ to $C \approx 23\,\%$ over the course of 90 minutes and the ramp signal was repeated four times to condition the hydrogel. About 8000 video frames from measurements have been processed of which 2000 datapoints are used to describe the response curve of the swelling behavior. The blue points

in **Figure 4.7** are approximated by an analytical function, which consists of five parameters. The maximum deviation is less than $1.5\,\%$ for this experiment.

4.3.2 Transient Response

The second measurement is a step response of the concentration change. The step function is used to define the damping parameter and the rise time for the transient swelling response. As discussed in **Section 3.2.3**, the dynamic behavior of the swelling process can be described by a first-order differential equation according to **Equation 3.55**. The step response of an ideal system would follow exactly an exponential function and the damping parameter describes how fast the swelling reaches the stationary state. For a linear system with a constant damping parameter, it corresponds to the rise time value, which defines the time span until $63\,\%$of the stationary state is reached.

In **Chapter 3**, it is demonstrated that the damping coefficient for the swelling and deswelling of hydrogels is different and depends on the current size. The damping coefficient $d(l)$ is a length-dependent function, which must be determined separately for the swelling and shrinking processes. Since $d(l)$ depends on the solution of the first-order differential equation, the system behaves nonlinear and must be analyzed numerically.

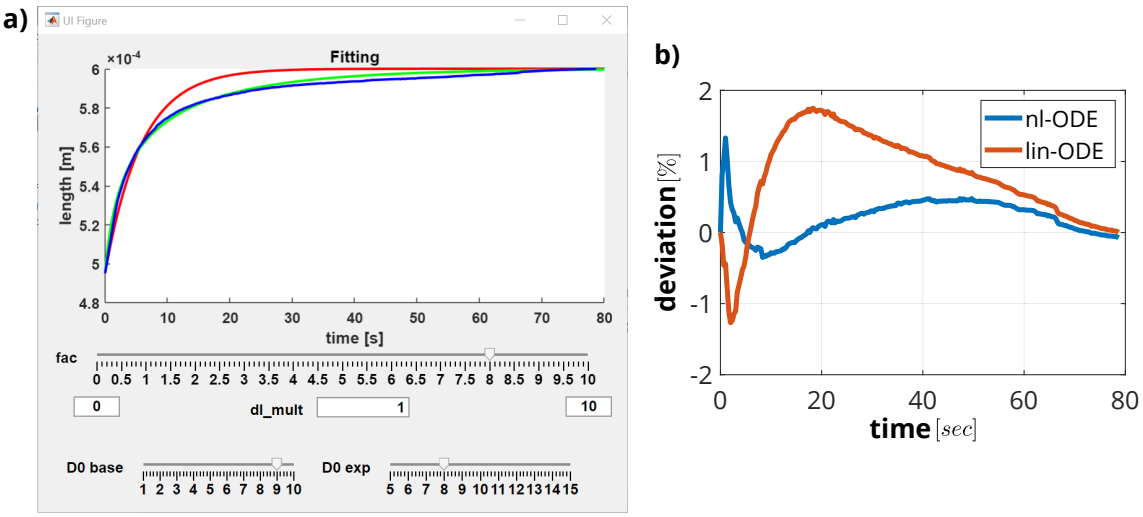

Figure 4.8: In a) the GUI is shown to adapt the transient model to the measurement result. In b) the deviation to the measurement data for both models are plotted.

In a hydrogel model, the damping parameter $d(l)$ is defined by:

$$d(l) = \frac{l(t)^2}{D_{coop} \cdot \left(\frac{l(t)}{l_0}\right)^{-3n}} \tag{4.1}$$

where $l(t)$ is the time response of the hydrogel's length, l_0 is the initial length, D_{coop} is the cooperative diffusion coefficient and n is a diffusion power factor.

The cooperative diffusion coefficient can span a wide range of several decades and it is often difficult to find suitable values by a function fit procedure. For this reason, the cooperative diffusion is separated into two parameters. m is used for a coarse adjustment as the expo-

nent and D_0 is for a fine tuning in the sliding scales of the GUI in **Figure 4.8**. The parameters are defined mathematically by:

$$D_{coop} = D_0 \cdot 10^{-m} \tag{4.2}$$

where D_0 is the base value of the cooperative diffusion coefficient D_{coop} and m is the exponent. The goal is now to adjust the parameters D_0, m and n so that the measured response $l(t)$ fits best to the numerical solution of the non-linear first-order differential **Equation 3.55**.

The parameter adaptation routine in **Figure 4.8** uses an embedded Simulink model to solve the differential equation in the background. Changes of the sliding scales are instantaneously plotted in the output window. The measurement results are shown in blue, curve fitting with a constant damping parameter is shown in red and the adapted curve according **Equation 4.1** is shown in green.

The red curve corresponds to models that use a linear ordinary differential equation and the green curve corresponds to models that use a nonlinear ordinary differential equation in subsequent system simulations. The right plot in **Figure 4.8** visualizes the relative deviation for both model types.

The parameters for the customized model are listed in **Table 4.2**. It is interesting that in particular the post-swelling effect can be adjusted with the diffusion power factor n. However, it differs between experiments and was often higher than specified in [114] (pp. 91 with $n = 0.75$).

Table 4.2: List of parameters needed to describe the dynamic behavior of the hydrogel.

parameter	Symbol	Value	Unit
base value of the cooperative diffusion coefficient	D_0	9	m^2/s
exponent value of the cooperative diffusion coefficient	m	8	-
diffusion power factor	n	2.6	-

With the proposed one camera setup, a three-dimensional displacement plot can not be efficiently determined especially for the transient motion. To scan a 3D object in real time, a stereo-microscopy setup could be implemented as a future project. Thereby at least a two-camera system with an angle to the targeted object are used, which continuously take pictures of the same hydrogel. Each pictures represents a two-dimensional view, from which in the post processing routine a three-dimensional motion of the swelling can be recreated through a pixel correlation method. This creates only additional processing efforts during the image recognition analysis and does not affect significantly the time critical measurement process. Inspiring work in this field is published in [130]–[132].

4.3.3 Hysteresis Response

The third measurement is focused on hysteresis. In order to trace static hysteresis parameters, the concentration level must be changed very slowly. The primary goal is to find the hysteresis offset concentrations that shift the swelling curve to the left and the shrinking curve to the right as shown in **Figure 4.9**. The hysteresis loop is mainly described by the offset value C_{hyst}.

The experimental characterization of hysteresis parameters is very time consuming and challenging. Measurements take several hours, syringe pumps must be refilled, the data management requires a large storage medium and bubble formations become more and more unavoidable.

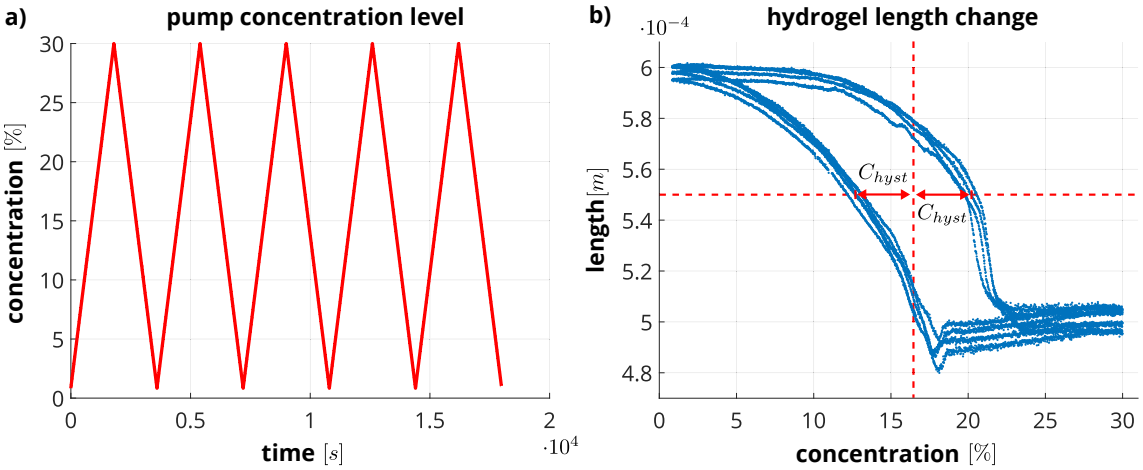

Figure 4.9: Measurement of hydrogel swelling hysteresis as a response to a ramped signal with a 60 min period shown in a). Here a constant hysteresis offset of $6\,\%$ between the swelling and shrinking is measured as shown in b).

In **Figure 4.9** the stimulus concentration is continuously ramped up and down at a period of 60 minutes. The hysteresis offset of about $6\,\%$ between swelling and shrinking is detected. To distinguish static and dynamic hysteresis effects, the stimulus frequency must be changed.

As hypothesized in **Section 3.3**, the dynamic hysteresis arises from the transient delay in the swelling response in relation to the stimulus. The hysteresis loop widens with higher frequency and with larger damping coefficients. At very low frequencies the dynamic hysteresis disappears and at very high stimulation frequencies the swelling process cannot follow the stimulus and the hydrogel remains in an intermediate state.

With the measurement setup shown in **Figure 4.2**, reproducible static hysteresis parameters were determined. The driving frequency has been increased by the factor of two and still the same hysteresis offset data could be observed. It clearly indicates the presence of a static hysteresis effect. In further experiments, internal hysteresis loops will be determined at depleting stimuli signals. However, it requires an automatic pump refill regime to avoid interrupts and contaminations during the measurement cycles.

Chapter 5

Modeling Swelling in Finite Elements

content of chapter

The finite element method (FEM) is a common engineering approach for modeling and simulation of field problems. The general idea is to subdivide the physical domain to be analyzed into a finite number of elements. The elements are connected to each other at interface nodes similar to circuit elements in network simulation tools. In contrast to discrete network elements in electronics, physical fields are continuous 2D or 3D domains where the elements represent a small local area or volume of the model. In 2D, elements have either a triangular or quadrilateral shape with three or four outer lines. In 3D, element shapes can be tetrahedral with four faces and hexahedral with six faces. Possible modifications are prism shaped and pyramid shaped elements with five outer faces. Quadrilateral and hexahedral elements have the best accuracy and efficiency but might be difficult to generated for complicated layouts with state-of-the-art meshing tools.

Finite elements can have either corner nodes (type 1) or corner and mid-side nodes (type 2). The first type is referred as linear elements. Linear means that the simulation results (displacements, temperatures, voltage potential) are approximated by linear interpolation functions on the outer lines or edges of 2D and 3D elements. The second type is referred as quadratic or high-order elements. Elements with mid-side nodes approximate the shape and result quantities of outer lines and edges through a quadratic relationship. It leads to a higher accuracy with the same number of elements but requires more computational resources. For several numerical reasons, elements with mid-side nodes are preferred in the following. It should be noted that "linear" in terms of linear elements is not correlated to the geometric linear simulation settings in FEM tools. It is only the method of interpolating the primary result quantities.

Finite element simulations can be used for different physical domains. The FEM tool ANSYS for instance, supports structural simulations in the mechanical domain, heat flow simulations in the thermal domain, simulations of electrical and magnetic fields and computational fluid dynamic (CFD) simulations based on the Navier-Stokes equation. As a matter of fact, finite element tools solve partial differential equations (PDE) by mathematical and numerical algorithms. In practice, several engineering problems are described by the same type of PDE. For instance, the Poisson's equation, which is implemented for heat flow elements, is utilized for diffusion problems and to calculate the Hagen-Poiseuille flow through arbitrary cross-sections in this work [133].

For many engineering applications, several physical fields act and interact in the same model domain. Examples are temperature fields, which introduce the thermal strain in the mechanical domain or the hydrogel swelling. There the concentration level of the stimulus is described by a diffusion process introducing a volume change in the mechanical domain. Both effects are mainly based on a one-way coupling between physical fields. Examples for bidirectional interactions are piezoelectric materials where electrical fields affect the mechanical behavior and vice versa. Another example are fluid-mechanical interactions where the mechanical swelling changes the fluidic resistance of a valve and, vice versa the applied fluid pressure deforms the hydrogel. Contrary to the piezoelectric effect where the physical fields interact in the same region, the described fluid-mechanical interactions appear at the interfaces between the domains. Combined simulations of different fields are referred as coupled-field analyses or multi-physics analyses in ANSYS [134].

Coupling effects can be directly implemented into the finite element formulation. ANSYS offers a series of multi-field elements where the governing equations and the related degrees of freedom are solved simultaneously. This approach is preferred for engineering applications where different fields interact in the same region. Examples are thermo-mechanical expansion, the piezoelectric effect or the diffusion-based swelling.

Alternatively, coupling effects can be considered indirectly by a load vector transfer method between two or more models, which simulate individual physical domains. The load vector transfer method is usually applied for coupled fields, which interact at interfaces but it is not restricted to it. Examples are fluid-mechanical interactions, which are discussed in **Section 5.4**.

Coupled field simulations are still very challenging research topics. Difficulties arise if the physical behavior and related interactions are not available in commercial finite element tools. An example is the thermodynamically correct implementation of the volume phase-transition of the hydrogel. In practice, the stimulus diffusion is not directly coupled to the swelling process. There is a time-delay between the stimulus and the solvent penetration into the polymeric network. The swelling process is affected by external surface loads on the hydrogel and by saturation or hysteresis effects. The research of Prof. Wallmersperger's group [100], [101] is very successful in developing finite element algorithms for modeling and simulation of physical effects in polymer materials.

5.1 Validity of the Model and Simulation Approach

The hydrogel-based microvalve for chemofluidic logic gates requires a description of the chemical, the mechanical and the fluidic domains and their interactions. The general idea is to control the fluid flow by the concentration level of the applied stimulus. The core element of the valve is a stimulus driven phase-transition hydrogel. The principle of operation will be shortly summarized.

The external stimulus reaches the surface of the hydrogel. A diffusion process begins, in which the stimulus level is dispersed into the material. This process is driven by the ion concentration gradient. Caused by a chemical process, the polymer network deforms and changes the volume where a solvent penetrates into the hydrogel or it is squeezed out of the

hydrogel. The expansion process is usually much slower as the diffusion process of the stimulus. The volume change seals or opens the fluid path in the valve. The swelling and shrinking process can likewise be controlled by a temperature change or other stimulus signals. There are three major physical effects, which are discussed in the following:

1. **Chemical domain:** The diffusion process of the stimulus into the hydrogel material.
2. **Mechanical domain:** The solvent penetration induces the swelling process of the hydrogel, which depends on the stimulus level.
3. **Fluidic domain:** The change of the fluidic resistance, which depends on the swelling or shrinking process. It finally affects the fluid flow through the valve.

The physical interactions are mainly unidirectional as described above. On the other hand, the fluid pressure affects also the shape of the hydrogel, which can cause a leakage flow. It will be discussed in **Chapter 6**.

Finite element simulations described in this chapter are utilized to extract characteristic properties of the microvalve for subsequent component and system simulations in Matlab Simulink. The final goal are efficient simulation models for larger microfluidic systems in Matlab Simulink, which capture the dynamic response with high accuracy. It will be shown that simple analytical terms are usually not precise enough and pure finite element simulation models are still subject of research. The data extraction procedure from FEM should be easy and straightforward in order to utilize the source code for other applications and design modifications.

The stimulus diffusion process from the surface into the chemical domain or backwards can be described by a heat flow analogous relationship in ANSYS:

$$\frac{\partial T(t,\vec{x})}{\partial t} = D_{th} \cdot \nabla^2 T(t,\vec{x}), \tag{5.1}$$

$$\frac{\partial C(t,\vec{x})}{\partial t} = D_C \cdot \nabla^2 C(t,\vec{x}), \tag{5.2}$$

where T is the temperature, which corresponds to the concentration level C in the hydrogel at the coordinate $\vec{x}$ and time t. Furthermore, D_{th} is the heat transfer coefficient, which corresponds to the concentration diffusivity D_C and ∇^2 is the Laplace operator.

The specified stimulus constrained at the surface of the hydrogel forms a Dirichlet boundary condition and the isolated bottom face with zero stimulus flow forms a Neumann boundary condition, which is automatically fulfilled without any specifications in finite element tools. Heat sources or related chemical substance generation sources inside of the hydrogel do not exist [135].

In a next step the chemical process, which causes the volume change is investigated. If the swelling response would follow instantaneous the stimulus propagation response $C(t,\vec{x})$ into the hydrogel, the thermal expansion effect could be used to describe the swelling or shrinking process accurately.

In practice, the hydrogel is triggered either by a temperature change or a concentration change. First the stimulus diffuses through the polymer material and then the hydrogel changes the volume through the diffusion of the ambient solvent. As discussed in

Section 3.2 the heat transfer coefficient and the concentration diffusion is much faster then the cooperative diffusion and therefore only the slowest process is considered. All other effects are considered as instantaneous.

If the thermal conductivity is adapted to the slowest process, the analogous heat flow relationship can be used to model the diffusion and the swelling processes. Both, the cooperative diffusion constant and the thermal expansion factors are usually extracted from experimental results as discussed in **Chapter 4**. The thermal expansion factor does not have to be a constant. An arbitrary mathematical function can be used to describe the resulting volume phase-transition behavior of a hydrogel. Details will be shown in **Section 5.2.3**.

In Doi *et al.* [81] and in Tanaka [111] the swelling behavior is directly related to a differential equation of the osmotic pressure, which leads to swelling displacements. Unfortunately, the proposed equations are difficult to solve for arbitrary geometries. However Doi states in [81] (equation 77), that the volume change ΔV must satisfy the following equation:

$$\frac{\partial V_{\Delta}(t,\vec{x})}{\partial t} = D_{coop} \cdot \nabla^2 V_{\Delta}(t,\vec{x}), \tag{5.3}$$

where D_{coop} depends on the osmotic modulus $\mathscr{K}$, the shear modulus $\mathscr{G}$ and the volume fraction of the solvent ϕ_0 as described in **Equation 3.49**. In Doi the osmotic pressure is used to describe the hydrogel swelling behavior but this is not a common boundary condition for a volume change in FEM.

Therefore the heat flow differential equation is used to describe the swelling kinetics in the following. Hydrogel swelling is not simply a thermal expansion problem but the parameters of the heat flow equations can be adapted in such a way that the true hydrogel behavior corresponds with numerical simulation results. Parameter adaptation of the measured behavior is widely used for modeling and simulation in engineering applications, especially when material properties are unknown or internal physical effects are too complicated or not fully understood.

It can be assumed that the thermal expansion coefficient describes the swelling behavior. The thermal strain is defined by:

$$\varepsilon_{th} = \int_{T_0}^{T} \alpha(T')\, dT' = \varepsilon_m, \tag{5.4}$$

where the temperature T corresponds to the stimulus concentration $C(t,\vec{x})$, $\alpha(T)$ is the stimulus dependent length expansion coefficient and ε_{th} is the thermal strain, which is equal to the mechanical strain ε_m if no external loads are applied at the system.

The thermal expansion coefficient will be adapted to measurements of the hydrogel swelling in **Section 5.2.3**. The adapted model allows for 3D simulations of the time and stimulus dependent volume phase-transition. Finite element simulations are necessary to determine the true surface profile during and after the swelling process. It has been demonstrated, that for a step response the hydrogel swells faster at outer edges and corners because the stimulus penetrates from different directions with short distances into the hydrogel. Furthermore, the hydrogel is clamped into a chamber or fixed at the bottom face, which leads to intricate deformation profiles caused by the mechanical suspension.

Despite of some model simplifications, the displacement states of the hydrogel can be simulated for arbitrary ranges of the stimulus level.

The stimulus dependent deformation profile is necessary to simulate the fluidic resistance of the valve in ANSYS CFX. The obtained fluidic resistances finally determine the fluid flow through the valve. It will be shown in **Chapter 6** that numerical simulations of the fluid flow are inevitable because the complex channel shape during the valve motion is too difficult to describe by analytical models, which are obtained by the Hagen-Poiseuille theory.

In summary, the primary goal is not to simulate the transient response of the entire valve with FEM. Rather, the following modeling steps provide essential and accurate finite element data for subsequent system simulations in Matlab Simulink:

1. Input data are various stimulus concentrations in the chemical domain.
2. Thermo-mechanical simulations determine the related swelling profiles for each stimulus level. The profile will be transferred to ANSYS CFX to define the true shape and size of the channel for the fluid flow simulations in the valve. Furthermore, the swelling at a characteristic point on the surface is monitored for subsequent function fit procedures.
3. Finally, the computational fluid dynamic tool ANSYS CFX simulates the fluidic resistances for all surface profiles of the hydrogel.

Both, the stimulus dependent shift of a characteristic point and the fluidic resistances are necessary for system models in **Chapter 6**. In the system models, the true dynamic behavior with a fast diffusion process of the stimulus and the slow swelling process will be modeled separately by different first-order differential equations. The rise time will be adapted to the length dependent swelling states what is complicated in finite element tools. In the system simulations, the fluidic resistance depends on the hydrogel displacements and not directly on the stimulus. Therefore, fit functions are necessary, which represent the fluidic resistance as a function of displacements at a characteristic point.

5.2 Thermo-Mechanical Model of the Hydrogel Expansion Behavior

In this section the theoretical background for modeling the thermal expansion of hydrogels is presented. The applied temperature at the surface represents the external stimulus of the system. The heat transfer is adapted to the cooperative diffusion constant, which describes the slowest process. Hence, the speed how the temperature change propagates into the hydrogel model corresponds to the speed of the solvent penetration. The solvent penetration is instantaneously coupled to the volume expansion, which is described by the thermal length expansion coefficient. After appropriate parameters and functions have been assigned to the heat transfer and to the expansion coefficients, the transient response describes the swelling kinetics of the hydrogel for subsequent data extraction procedures.

5.2.1 Change of the Length by Thermal Expansion

In order to determine the three-dimensional volume change of a hydrogel, the analytic equations are derived first for a one-dimensional length change caused by thermal expansion.

The coefficient of thermal expansion is based on the definitions in Callen [136] (pp. 84) and in [116] (pp. 30-32). The instantaneous thermal expansion coefficient α is defined as follows:

$$\alpha(T) = \frac{1}{l}\frac{dl}{dT}. \tag{5.5}$$

Thereby, **Equation 5.5** describes a temperature dependent thermal expansion coefficient $\alpha(T)$, the current length l and the differential length change dl based on a differential temperature change dT.

Equation 5.5 is now rearranged to define the differential thermal strain:

$$d\varepsilon_{th} = \frac{dl}{l} = \alpha(T)\, dT. \tag{5.6}$$

In structural mechanics, two different strain measures exist. The first one is the engineering strain ε_{eng} (also called Chauchy strain), which is the ratio of the total length change Δl to the initial length l_0 of the body. The second one is the logarithmic strain (also called Hencky strain) ε_{log}:

$$\varepsilon_{log} = \int_{l_0}^{l} \frac{1}{l'}\, dl' = \ln\left(\frac{l}{l_0}\right) = \ln\left(\frac{\Delta l}{l} + 1\right) = \ln\left(\varepsilon_{eng} + 1\right), \tag{5.7}$$

which is obtained by integrating the differential length change dl' with regard to the current length l. The logarithmic strain ε_{log} provides the correct measure of the final length l of systems, which undergo large deformations.

In a thermo-mechanical system, the differential mechanical strain is equal to the differential thermal strain if no external loads are applied at the system:

$$d\varepsilon_{log} = \frac{dl}{l} = d\varepsilon_{th} = \alpha(T)\, dT. \tag{5.8}$$

As a next step, the differential strain $d\varepsilon_{log}$ is integrated to obtain the final strain:

$$\int_{\varepsilon_{log0}}^{\varepsilon_{log}} d\varepsilon'_{log} = \varepsilon_{log} - \varepsilon_{log0} = \int_{T_0}^{T} \alpha(T')\, dT'. \tag{5.9}$$

With the assumptions that the strain is in equilibrium (static system) and the initial strain is zero ($\varepsilon_{log0} = 0$), the logarithmic strain is equal to:

$$\varepsilon_{log} = ln\left(\frac{l}{l_0}\right) = \varepsilon_{th} = \int_{T_0}^{T} \alpha(T')\, dT'. \tag{5.10}$$

The current length l according to thermal expansions can now be calculated by:

$$l = l_0 \cdot e^{\int_{T_0}^{T} \alpha(T')\, dT'}. \tag{5.11}$$

Assuming small deformations according to the linear theory, the new length would be:

$$l = l_0 \cdot \left(1 + \int_{T_0}^{T} \alpha(T')\, dT' \right). \tag{5.12}$$

ANSYS provides identical results for both strain measures, which can be activated or deactivated by the *"NLGEOM"* command.

5.2.2 Stress-Strain Relationship for Hydrogels

The response of the hydrogel to external mechanical and thermal loads is described by the stress-strain relationship of the material. The hydrogel will be considered elastic in the following section. Different elasticity models such as the linear elastic material described by Hook's law, the true stress-strain relationship at large deformations based on Hencky strain and an example of hyperelastic material properties, the Mooney Rivlin approach, will be discussed for the uniaxial extensions.

The linear stress-strain relationship according to Hook's law is described by:

$$P = \frac{F}{A_0} = \sigma = E \cdot \varepsilon_{eng} = E \cdot \frac{l - l_0}{l_0}. \tag{5.13}$$

Hook's law is based on initial settings for all geometrical dimensions. The mechanical normal stress σ is equal to the closing pressure P in the gap, which is calculated from the force F divided by the initial cross-sectional area A_0 of a body. Furthermore, the linear or engineering strain ε_{eng} is defined by the length change with $\Delta l = l - l_0$ divided by the initial length l_0 of the body. Linear elastic models are applicable for small deformations with a few percent strain. Linear models do not require an iterative solution procedure within finite element tools.

The true stress-strain relationship is applicable for small and large deformations. Large deformations occur in elastomers or especially in the hydrogels. If a body experiences large deformation, the true stress-strain relationship must be derived from the differential strain relationship. It is assumed that the deformations take place in a series of small increments where the strain and the stress is always related to the current length and the current cross-sectional area. It requires an iterative solution procedure within finite element tools. The true stress-strain relationship for uniaxial extensions is defined by:

$$P = \frac{F}{A} = \sigma = E \cdot \varepsilon_{log} = E \cdot \ln\left(\frac{l}{l_0}\right). \tag{5.14}$$

The current cross-sectional area A in the deformed state depends on the Poisson's ratio. Rubber like materials such as hydrogels are almost incompressible with a Poisson's ratio of about $\nu = 0.5$ Based on the volume conservation law, the current cross-sectional area A at large deformations can be calculated from the initial area A_0, the initial length l_0 and the current length l. Both length parameters can be replaced by the engineering strain:

$$A = A_0 \cdot \frac{l_0}{l} = \frac{A_0}{1 + \varepsilon_{eng}}. \tag{5.15}$$

The current area A is more difficult to calculate for models with compressible materials. For large deformations, the Poisson's ratio ν is defined by [137], [138]:

$$\nu = -\frac{\varepsilon_{log}^{T}}{\varepsilon_{log}^{A}} = -\frac{\ln\left(1+\varepsilon_{eng}^{T}\right)}{\ln\left(1+\varepsilon_{eng}^{A}\right)}. \tag{5.16}$$

where $\varepsilon_{log}^{A} = \ln\left(\frac{l}{l_0}\right)$ is the logarithmic strain in axial direction and ε_{log}^{T} the logarithmic strain in transverse directions of the body. Both values can likewise be expressed by the engineering strain parameters. **Equation 5.16** can be rearranged to:

$$\varepsilon_{log}^{T} = \ln\left(\frac{l^T}{l_0^T}\right) = \ln\left(\left(1+\varepsilon_{eng}^{A}\right)^{-\nu}\right) \tag{5.17}$$

and the current length l_T in transversal direction is defined by:

$$l^T = l_0^T \cdot \left(1+\varepsilon_{eng}^{A}\right)^{-\nu}. \tag{5.18}$$

It leads to the current cross-sectional area A for arbitrary Poisson's ratios at large deformations:

$$A = \frac{A_0}{\left(1+\varepsilon_{eng}^{A}\right)^{2\nu}}. \tag{5.19}$$

The true stress-strain relationship is activated by the *"NLGEOM"* command in ANSYS. Test cases with uniaxial displacement constraints give exactly the same results for strain, stress and reacting forces at arbitrary values for the Poisson's ratio.

The third elastic model, which has been investigated, is a two-parameter Mooney-Rivlin solid material behavior. Mooney-Rivlin solids are widely used in computational mechanics to model hyperelastic materials such as hydrogels. It is applicable for large deformations and allows for incompressible materials. The advantage of the Mooney-Rivlin model is that the material properties can be adjusted over a wide range by the C_{10} and C_{01} distortion parameters. The material model is available for several finite element types in ANSYS.

The true stress for uniaxial extensions of an incompressible Mooney-Rivlin material is defined by [139] (pp. 243):

$$\sigma_{MR_x} = 2 \cdot \left(C_{10}\left(\Lambda_x^2 - \frac{1}{\Lambda_x}\right) + C_{01}\left(\Lambda_x - \frac{1}{\Lambda_x^2}\right)\right), \tag{5.20}$$

where $\Lambda_x = \frac{l}{l_0}$ is the mechanical stretch in axial direction. The volume conservation law can be used to calculate the stretch $\Lambda_y = \Lambda_z = \frac{1}{\sqrt{\Lambda_x}}$ in transverse directions of the body. The current cross-sectional area depends on the transversal stretch and leads to the same results as demonstrated in **Equation 5.19**.

There are several ways published in literature to calculate or to adapt the Mooney-Rivlin parameters C10 and C01 to the desired material behavior [140] [141] (pp 95). Usually, the distortion parameters are adapted to the shear modulus G of the rubber like material. In case of uniaxial extensions, the distortion parameters can also be related to the Young's modulus. In order to compare all three elastic models in **Figure 5.1**, the assumption is made that for small displacements the slope of the stress-strain relationship should be equal to the Young's modulus E. This can be achieved by the following conditions:

$$C_{10/01} = \frac{E}{6} \cdot \left(\frac{1}{2} \pm \beta \right), \tag{5.21}$$

where β is a parameter to adapt the stiffness change of the compressed hydrogel. Tensile stress is not relevant for hydrogels in microfluidic applications. The left part of **Figure 5.1** shows the influence of the β parameter for compressive stress and the right plot compares the stress-strain relationship for all three elastic models.

For the following finite element simulations, the Young's modulus E is extracted from experimental results as discussed in **Chapter 4**. It has been shown that the elastic deformation (strain), which causes stress, is small but the thermal strain, which causes swelling, is between $10\,\%$ and $30\,\%$ for the chemical volume phase-transition of the hydrogel. Especially swelling requires an iterative solution procedure in ANSYS and both, the true stress-strain relationship and the Mooney-Rivlin approach provide satisfying results. The linear Hook's law is not applicable.

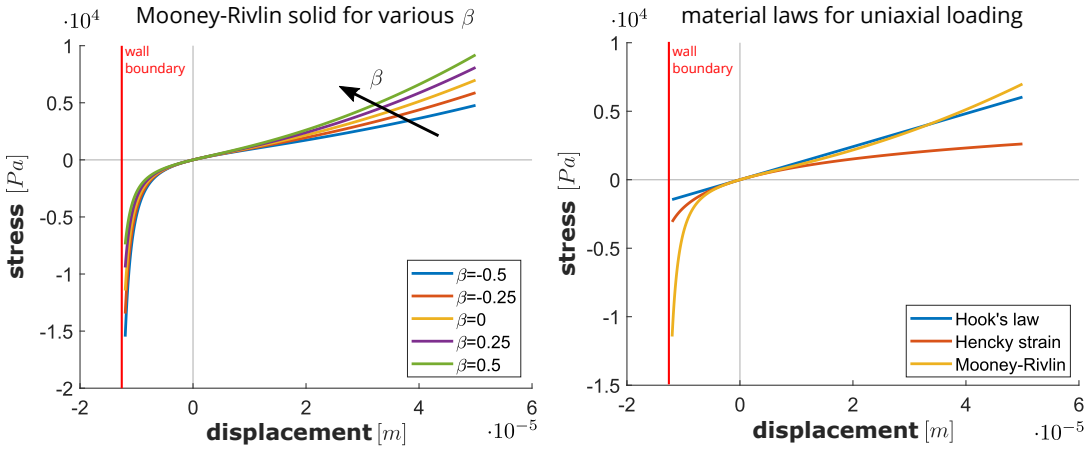

Figure 5.1: Pressure-strain response of material implemented with *"nlgeom,off"* in blue, *"nlgeom,on"* in red and with a Mooney-Rivlin approach in yellow for a material height of $h = 14.5\,\mu\text{m}$.

The relationship between total strain ε^t, elastic strain ε^{el}, thermal strain ε^{th} and resulting stress σ is defined by:

$$\sigma = E \cdot \varepsilon^{el} = E \cdot \left(\varepsilon^t - \varepsilon^{th} \right). \tag{5.22}$$

5.2.3 Thermal Volume Expansion and Parameter Adaptation

The correct implementation of the volume phase-transition behavior is an essential step to compute the fluidic resistance in **Section 5.4** accurately. Therefore, the thermal length expansion coefficient $\alpha(T)$ must be adapted to the volume swelling behavior of the hydrogel.

The thermal length change at the displaced position according to **Equation 5.11** is an exponential function and depends on the integral of the instantaneous thermal expansion function $\alpha^{in}(T)$ over the specified temperature range T. Hence, the function values $\alpha^{in}(T)$ in the whole range must be available for the numerical integration to calculate the thermal strain ε_{th}

and the resulting new length l. The $\alpha^{in}(T)$ values are assigned to the *"CTEX"* material property label in ANSYS.

It will be shown that $\alpha^{in}(T)$ can be an arbitrary function to adapt the thermal expansion results precisely to the measured or to the expected swelling behavior of the hydrogel. In literature [69], [98], [142]–[145], hydrogels are usually characterized by the volume swelling degree Q_V depending on the applied stimulus T. For a cubic solid element with length dimensions l_1, l_2 and l_3, the volume expansion Q_V is defined by:

$$Q_{V_{ANSYS}}(T) = \frac{V}{V_0} = \frac{l_1}{l_{01}} \cdot \frac{l_2}{l_{02}} \cdot \frac{l_3}{l_{03}} = e^{3 \cdot \int_{T_0}^{T} \alpha^{in}(T')dT'}. \tag{5.23}$$

Equation 5.23 describes the volume expansion process of solid models based on the true stress-strain relationship. An iterative solution procedure must by activated by the *"NLGEOM"* command in ANSYS to compute large deformation results correctly. The obtained exponential function in **Equation 5.23** must be adapted to true volume-phase change behavior of the hydrogel, which follows a sigmoidal function.

Several mathematical functions to describe the hydrogel swelling process have been discussed in **Section 3**. For demonstration, the simplified sigmoidal function in **Equation 5.24** will be used to explain the theoretical background for the following parameter adaptation process. A numerical algorithm is presented in **Appendix B**, **C** and **D**, which can be utilized to adapt an arbitrary volume-phase transition relationship to the volume expansion process in the finite element program ANSYS.

$$Q_{V_{HG}} = \frac{1}{1 + e^{-k \cdot (T - T_{LCST})}}. \tag{5.24}$$

Parameter adaptation means that material properties of the numerical models are mapped to the experimental behavior that the simulated swelling response in ANSYS corresponds to the measured volume swelling results for any stimulus range:

$$Q_{V_{ANSYS}} = e^{3 \cdot \int_{T_0}^{T} \alpha^{in}(T')dT'} = \frac{1}{1 + e^{-k \cdot (T - T_{LCST})}} = Q_{V_{HG}}. \tag{5.25}$$

The equilibrium **Equation 5.25** must be rearranged in such a way that the instantaneous thermal expansion function $\alpha^{in}(T)$ can be calculated for subsequent finite element simulations. In a first step, **Equation 5.25** is expressed by the natural logarithms $\ln(x)$ to eliminate the exponential function and then the integral is resolved by differentiating the equation according to T. It leads to the following equation:

$$\alpha^{in}_{nonlin}(T) = \frac{\partial}{\partial T}\left(\frac{1}{3} ln\left(Q_{HG}\right)\right) = \frac{k}{3} \cdot \frac{1}{1 + e^{k \cdot (T - T_{LCST})}}. \tag{5.26}$$

Sigmoidal functions are often used in simulation tools to model phase-transitioning effects. The parameters can easily be adapted to new designs and sigmoidal functions can be transformed or processed by many mathematical operations symbolically as show in **Equation 5.26**.

In linear finite element models, engineering strain $\varepsilon_{eng} = \frac{\Delta l}{l_0}$ is used to compute the deformation state. The displacements Δl are added to the reference length l_0 in order to formulate the new length with $l = l_0 + \Delta l$. Thermal strain $\varepsilon_{th} = \int_{T_0}^{T} \alpha^{in}(T')dT'$ is now equal to the engi-

neering strain ε_{eng} what leads to the following equation for the thermal length expansion:

$$\frac{l}{l_0} = 1 + \int_{T_0}^{T} \alpha^{in}(T')\, dT'. \tag{5.27}$$

For a cubic element, the linear volume swelling degree in ANSYS is described by:

$$Q_V = \frac{V}{V_0} = \left(1 + \int_{T_0}^{T} \alpha^{in}(T')\, dT'\right)^3. \tag{5.28}$$

The sigmoidal function of the hydrogel volume swelling and **Equation 5.28** can now be used to compute the instantaneous thermal expansion coefficient $\alpha^{in}_{lin}(T)$ for linear simulation options in finite element tools:

$$\alpha^{in}_{lin}(T) = \frac{\partial}{\partial T}\left(\sqrt[3]{Q_{HG}} - 1\right) = \frac{k}{3} \cdot \frac{e^{-k\cdot(T-T_{LCST})}}{\left(1 + e^{-k\cdot(T-T_{LCST})}\right)^{\frac{4}{3}}}. \tag{5.29}$$

In summary, a temperature dependent thermal expansion coefficient $\alpha^{in}(T)$ has been introduced to model a sigmoidal swelling behavior needed for the volume phase-transition of the hydrogel. The first model is applicable for non-linear simulation options in ANSYS where the true stress-strain relationship is activated by *"NLGEOM"*. The second model can be utilized for the linear case based on the engineering stress-strain relationship. Both models are summarized in **Figure 5.2**.

- **for large displacement** (Hencky strain) with $\varepsilon_{log} = \ln\left(\frac{l}{l_0}\right)$:

$$\alpha^{in}(T) = \frac{\partial}{\partial T}\left(\frac{1}{3} ln\left(Q_{HG}\right)\right). \tag{5.30}$$

- **for small displacements** (engineering strain) with $\varepsilon_{eng} = \frac{\Delta l}{l_0}$:

$$\alpha^{in}(T) = \frac{\partial}{\partial T}\left(\sqrt[3]{Q_{HG}} - 1\right). \tag{5.31}$$

Figure 5.2: Analytic overview to predict the thermal expansion coefficient for the geometric linear and nonlinear simulation run in ANSYS.

The instantaneous thermal expansion coefficient $\alpha^{in}(T)$ usually requires an iterative solution procedure in finite element tools where the temperature is continuously increased to integrate the thermal strain with varying $\alpha^{in}(T)$ values correctly. Equilibrium iterations are automatically activated for non-linear systems based in the true stress-strain relationship. Difficulties can occur for linear systems where the final state is calculated in a single solution step. Finite element tools simply evaluate the thermal expansion value for the target temperature T and do not account for varying values in the specified temperature range. In ANSYS, the instantaneous thermal expansion coefficient *"CTEX"* can be mapped to a secant coefficient of thermal expansion $\alpha^{se}(T)$ defined by the *"ALPX"* material parameter to avoid

numerical problems for linear systems. The approach is described in **Appendix C**.

In practice, more advanced sigmoidal or other functions can by utilized to map the swelling behavior of hydrogels. In ANSYS, temperature dependent material properties can either be defined by polynomial functions with a maximum order of four or by a lookup table with a maximum of 100 data points where the *"CTEX"* values are linearly interpolated between specified temperature samples. The approach is discussed in **Appendix D**.

5.2.4 Heat Transfer Coefficient

The heat flow equation of a homogeneous medium in a 3-dimensional space is defined by:

$$\frac{\partial T}{\partial t} = \frac{\lambda}{\varrho \cdot c_{th}} \cdot \left(\frac{\partial^2 T}{\partial x^2} + \frac{\partial^2 T}{\partial y^2} + \frac{\partial^2 T}{\partial z^2} \right) + \dot{Q}, \tag{5.32}$$

where $\dot{Q}$ is a heat generation rate per unit volume in the medium (heat source), $T\left(t, \vec{x}\right)$ is the temperature depending on the time t and the location $\vec{x}$, λ is the thermal conductivity, ϱ is the density and c_{th} is the specific heat capacity. For modeling and simulation of hydrogels, the head sources $\dot{Q}$ does not exist. The stimulus is applied by Dirichlet boundary conditions on the external surface of the hydrogel. Dirichlet boundary conditions are the specified temperature T at the outer face, which propagate in a transient process into the medium. The heat transfer coefficient is defined as follows:

$$D_{th} = \frac{\lambda}{\varrho \cdot c_{th}} = D_{coop}. \tag{5.33}$$

The unit of the thermal conductivity λ is $\left[\frac{W}{m \cdot K}\right]$. Together, the unit of the density $\left[\frac{kg}{m^3}\right]$ and the specific heat capacity $\left[\frac{J}{kg \cdot K}\right]$, the unit of the heat transfer coefficient D_{th} equation leads to the same units as expressed for the cooperative diffusion D_{coop} with $\left[\frac{m^2}{s}\right]$ [114] (pp.92 equation 50). Through adapting λ, ϱ and c_{th} the cooperative diffusivity can be directly implemented in FEM and the time constant, similar to **Section 3.2.2**, can be determined as follows:

$$\tau = \frac{l_c^2}{2 \cdot n \cdot D_{coop}}. \tag{5.34}$$

Thereby l_c represent the characteristic length and n is the the spatial dimension factor as introduced in **Figure 3.6**. The analytic equation of the cooperative diffusion D_{coop} is derived in **Section 3.2.1** leading to **Equation 3.37**. Theoretically the diffusion coefficient can be implemented directly by the material property diffusivity, which can be assigned in different directions by *"DXX"*, *"DYY"* and *"DZZ"* labels. However, ANSYS heat flow simulations are based on the material properties with labels *"KXX"* (thermal conductivity), *"DENS"* (density) and *"C"* (specific heat). The material parameters do not need to be constant during transient simulations. A stimulus dependent thermal conductivity $\lambda(T)$, for example, can be utilized to control a swelling dependent rise time τ or the slope in the transient response. Material properties may also depend on other model settings or even on simulation results in previous time steps. This feature can be utilized, if for example a post swelling hydrogel is described, where the hydrogel slowly swells at high temperatures with a high delay time what is not described by constant material parameters. A sample code for ANSYS APDL can be found in **Appendix E.4**.

5.3 Volume Phase-Transition of a Hydrogel implemented in ANSYS

The theoretical background for the diffusion and swelling process in a subsequent finite element simulation was explained for uniaxial loads and a simplified sigmoidal function in **Section 5.2**.

A routine in ANSYS APDL is developed and tested, which considers a multi-parameter sigmoidal function for the volume swelling process defined in **Equation 3.28** and visualized in **Figure 5.3**. It can be seen, that the curvature above and below of the critical solution temperature T_{LSCT} is strongly different. The upper and lower curvature parameters have been adapted to experimental results.

In a first step, the sigmoidal function of the volume swelling process in **Equation 3.28** is transformed to a function for the instantaneous thermal expansion coefficient $\alpha^{in}(T)$ based on the true stress-strain relationship (Hencky strain ε_{log}). The general approach corresponds to the algorithm in **Figure 5.2** and the results of the symbolic evaluation are defined in **Equation C.1** of **Appendix C**. The equation is visualized in the left part of **Figure 5.3**.

In a next step, the instantaneous thermal expansion coefficient $\alpha^{in}(T)$ must be mapped to the material parameter *"CTEX"* in ANSYS whereby 100 sample points can be defined for the linear material property interpolation routine in ANSYS. A numerical algorithm has been implemented in Matlab to find an optimized spacing between the sample points with the lowest deviation between the original $\alpha^{in}(T)$ function and the piecewise linear regression implemented by the ANSYS internal "CTEX" lookup table. The spacing between the sample points mainly depends on the curvature of the $\alpha^{in}(T)$ function as shown in **Figure C.2**.

The ANSYS APDL routine has been tested on a hexahedral solid model with the same dimensions as used for the hydrogel valve in **Chapter 6** and **7**. Static simulations of the thermo-mechanical swelling process in ANSYS take just a few seconds, the transient response can be analyzed in a few minutes.

Figure 5.3 shows the simulated swelling response of the hydrogel at different stimulus temperatures. It corresponds to the expected behavior. In static simulations, the shape of the hydrogel body does not change because the thermal expansion is the same in all spatial directions. The length change can directly by observed at characteristic points and the volume change is a post-processing feature in ANSYS.

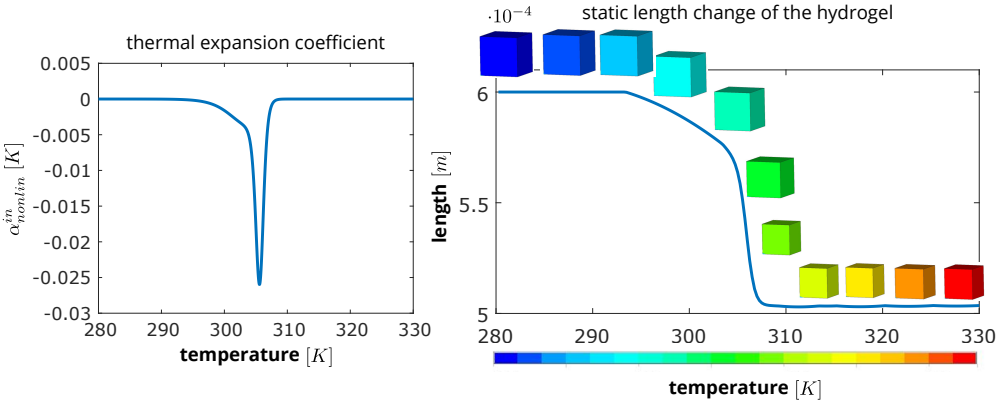

Figure 5.3: Hydrogel phase-transition behavior which is implemented through the *"CTEX"* command.

The transient response for fast varying stimulus changes leads to a non-uniform length expansion where the outer edges swell faster as the inner regions of the hydrogel. After the settling time is reached, the swelling profile is equal to the quasi-static state and forms a hexahedral shape.

5.4 Computational Fluid Dynamics

This chapter focuses on numerical simulations of the fluidic resistances in the computational fluid dynamic (CFD) program ANSYS CFX. CFX is a numerical solver for the Navier-Stokes equations in ANSYS. The fluidic resistance R_{Fl} is calculated from the applied pressure difference Δp between the inlet and outlet ports divided by the average volume flow rate $\dot{V}$ in the channel. The volume flow rate depends on the shape and dimension of the flow domain, which are affected by the hydrogel swelling process. Results are calculated from the stationary state in a transient simulation. Because of very low Reynolds numbers in microchannels, viscose friction is dominant and inertial effects can be ignored. Viscose friction depends on the dynamic viscosity of the media.

In the following, three different ways to calculate the fluidic resistances depending on the selling process of the hydrogel have been investigated.

The first approach is a single domain simulation in ANSYS CFX based on analytical moving wall boundary conditions. Moving wall boundary conditions are user defined displacements in x-, y- and z-directions at the interface of the hydrogel to the fluid channel. The given displacement constraints are linearly scaled in a transient simulation and the internal mesh follows smoothly the prescribed moving wall boundary conditions (mesh morphing).

The second approach is based on one-way FSI, which has been implemented and tested in ANSYS. During transient simulations, the interface displacements of the mechanical domain in ANSYS are continuously transferred to the fluid domain in CFX. In contrast to the first approach, the displacements are not simple scaled. The approach considers arbitrary time dependent deformation profiles at the interface. The internal mesh is either deformed by a mesh morphing procedure or, in case of difficulties, a new mesh is generated in the fluid domain. The second approach is more accurate, allows for complicated models and is numerically stable.

The third approach is based on a two-way fluid structure interaction (FSI) routine. Bidirectional interactions are necessary when the reaction of the fluid domain on the mechanical domain is important. It requires a bidirectional data exchange procedure between both solvers in each time step and a custom client-server communication based on internet sockets.

5.4.1 Analytic Mesh Morphing

The ANSYS CFX program offers moving wall boundary conditions for fluid flow simulations. The moving wall displacements are defined by analytical functions at the initial position. In terms of a hydrogel, the moving wall is mainly shifted in normal direction to the interface. The displacement increment is each time-step divided by the step size is equal to a wall velocity. It is automatically applied as a volume flow rate at the moving wall in CFX. In narrow gaps,

it creates a pressure change known from squeeze-film problems in lubrication theory [146], [147]. Tangential velocities cause shear forces in the fluid domain.

A second effect must be considered if the displacements are large compared to the element size. The moving wall shifts the interface nodes at the moving wall to a new position. A mesh morphing procedure must be activated to consider the changed geometry for the next time step. Mesh morphing is a numerical algorithm in ANSYS where the existing mesh is deformed or squeeze into the new geometry. The number of elements and their connections to nodes do not change.

There are several algorithms for mesh morphing published in literature [148] (pp. 5). The new position can be calculated in a separate static simulation where the fluid elements are considered as a soft mechanical material with given displacement constraints at moving and zero constraints at the fixed walls. The mesh deforms as known from mechanical simulations and the displacements are simply added to the original node location to get the morphed mesh. Another option is a Laplacian mesh update. The moving wall boundary conditions require three static simulations of the heat flow equation where the spatial displacements in x-, y- and z-directions are applied as temperature boundary conditions at the channel interface. The temperature at fixed walls is set to zero. The interior displacements correspond to the calculated temperature profile.

Mesh morphing works stable for moderate displacements and smooth surfaces of the moving wall. For larger displacements especially along sharp corners, the mesh becomes folded and tangled. A typical indicator is that the span angle of sidewalls exceeds a critical limit or the convex edges of the finite element mesh become concave. ANSYS detects those elements automatically and stops the solution routine with a negative volume element error message. Here, remeshing operations are not supported by the analytical moving wall boundary condition approach. Remeshing operations will be utilized for the one-way coupling based on the fluid structure interaction (FSI) in **Section 5.4.2**.

The performance and stability of the mesh morphing routine depends strongly on the model layout and on the initial finite element mesh quality. Several investigations have been performed in the scope this work on two-dimensional models of the hydrogel valve. **Figure 5.4 a)** shows the initial finite element mesh in the fluid channel. The white square with corner fillets at the center is the hydrogel, the blue area represents the fluid channel whereby the inlet is on the left and the outlet on the right.

The best performance could be achieved for quadrilateral elements where the outer edges are almost parallel and perpendicular to the motion direction. The elements have a trapezoidal shape where the radial edges point from the center of the hydrogel to the outer lines of the valve seat. Such a finite element mesh can be realized by an appropriate subdivision of the entire 2D-model into smaller quadrilateral areas, which support well defined structured (mapped) finite element meshes.

With above conditions, the mesh morphing procedure in CFX changes only the aspect ratio of the elements. The elements get thinner or wider but the sidewall angle is less affected. Such a deformation behavior is important because finite elements allow for large aspect ratios with high accuracy but sidewall angles are subject to a more restrictive error limitation.

With a trapezoidal initial mesh, the fluid channel between hydrogel and chamber wall could be compressed by about $99\,\%$ of the initial size as shown in **Figure 5.4 b)** and highly en-

larged in **c)**. The corner regions of the hydrogel need to be round and very densely meshed to accommodate the direction change of the outer element lines during the morphing process. **Figure 5.4 d)** shows the fluid flow velocity at the initial position. The numerical accuracy of the fluidic resistance at the morphed position has been verified with a CFX model where the same channel was directly implemented in CFX with fixed wall settings. The results of both models are almost identical.

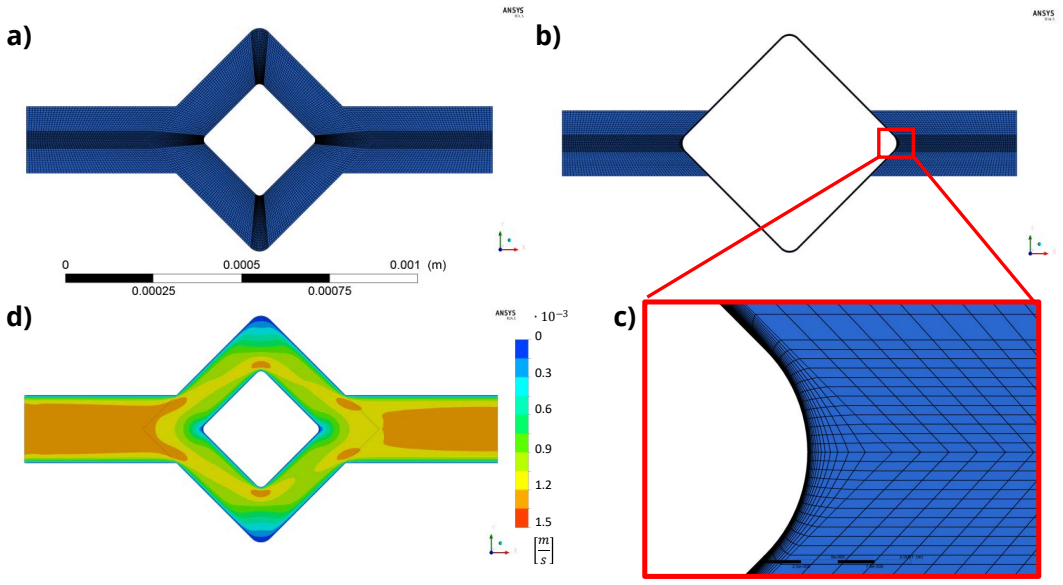

Figure 5.4: Analytical mesh morphing to determine the flow behavior for a swelling hydrogel. In a) the undeformed mesh and in b) the deformed mesh is shown. Thereby a compression of up to $99\,\%$ is achieved, which is magnified in c).

An interesting effect occurs in transient CFX simulations when the hydrogel swelling is simulated very quickly. At a gap of about $5\,\mu\mathrm{m}$, the pressure between the wall and the hydrogel suddenly increases to large values and CFX might fail to converge. The exponential pressure increase at closing gaps is known a squeeze-film effect in the literature. The physical reason for the squeeze-film effect is that the fluidic resistance in the gap between the hydrogel and the wall depends exponentially on the distance according to the Hagel-Poiseuille theory. The strong pressure increase is caused by the displaced volume of the incompressible liquid, which is squeezed from the narrow gap into the channels on the left and on the right. A slower swelling process reduces the pressure increase and leads to stable results. In real systems, however, the squeeze film pressure, would likewise hinder the hydrogel expansion and slows down the closing process of the microvalve.

The true geometry of the hydrogel in a microvalve is more complex and can only be represented in a 3D-model. Furthermore, the round corners and edges of the hydrogel do not fit exactly to the chamber walls. In practice, some parts of the gap close earlier and the remaining parts close later. There might be even a leakage flow because the hydrogel is commonly not able seal the entire cross-sectional area of the valve.

In the next section, a more complex geometry of a microvalve model with fluid structure interaction (FSI) is investigated, implemented and tested.

5.4.2 One-way Fluid Structure Interaction Modeling

In this chapter, a one-way fluid structure interaction (1-FSI) model is established and evaluated. One-way means, that all coupling effects go in one direction only, here, from the mechanical domain to the fluid domain. The mechanical domain simulation run is completely independent from the fluid domain results. On the other hand, the transient fluid domain simulations depend on mechanical results, which have to be updated in each time interval. The general approach is visualized in **Figure 5.5**.

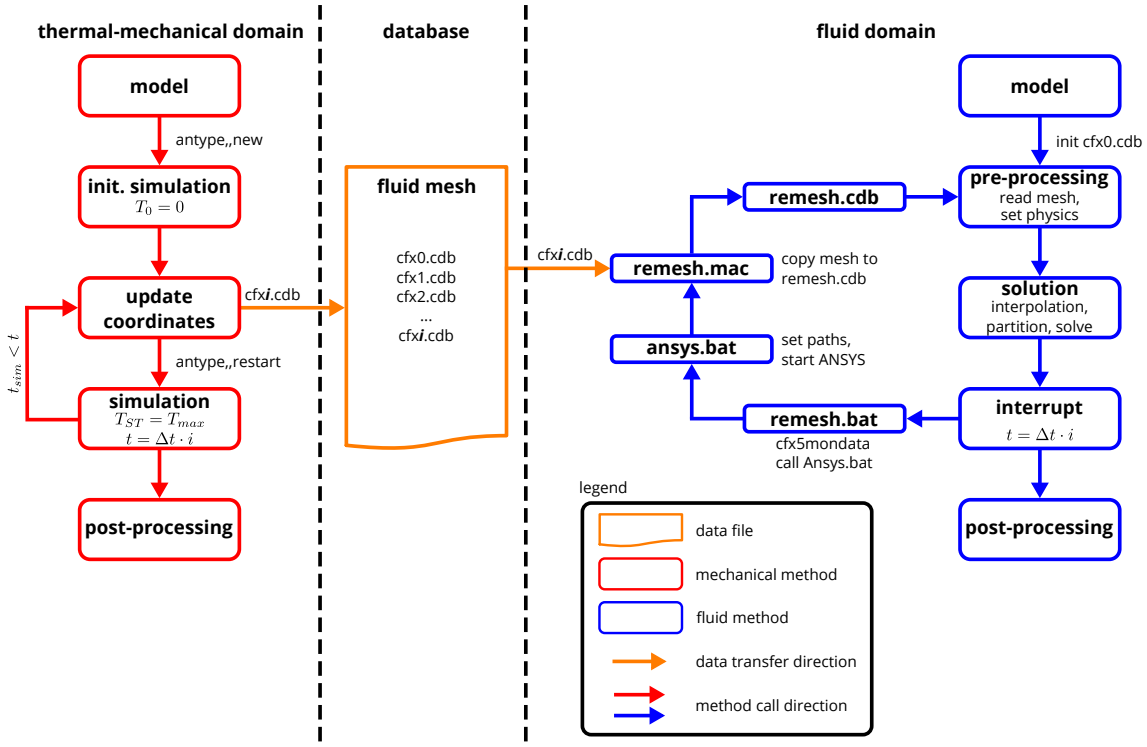

Figure 5.5: One-directional fluid structure interaction model routine implemented between ANSYS Mechanical and ANSYS CFX.

In the following, the mechanical domain model is executed first and then, as a second step, the fluid simulation is started. Hereby reactions of the fluid on the mechanical domain are ignored. The mechanical domain is actually a thermo-mechanical model where the temperature driven stimulus diffuses into the hydrogel and the swelling is calculated according to the adapted sigmoidal function. The displacements of the hydrogel surface change the fluid channel in CFX and the corresponding fluid resistance.

The stimulus temperature is applied at the outer face of the hydrogel. Both, a step function and a ramp function have been investigated. The thermo-mechanical finite element model does not only comprise the hydrogel region but also the fluid region of the valve as shown in **Figure 5.6**. The fluid region is modeled by dummy "MESH200" elements in ANSYS. The interface between both forms a moving wall and the other outer faces of the fluid elements are set to fixed wall boundary conditions.

The transient simulation of the thermo-mechanical domain is stopped at certain time intervals $t = \Delta t \cdot i$ where t is the current simulation time, Δt is the time-step size of the solver and i

defines the number of simulation-steps to the next stop. At each interrupt, the finite element dummy mesh in the fluid domain must be updated according to the deformed position of the hydrogel elements. It can be realized either by a mesh morphing or a remeshing procedure in ANSYS. Details can be found in the rezoning section of the ANSYS Advanced Analysis Guide in [148]. Compared to the mesh morphing algorithm, a remeshing routine is more stable and enables large deformations. Remeshing is not just a new mesh in the solid model volumes, rather remeshing has to consider local deformations at the interface to moving walls.

The updated fluid meshes at each interrupt (*.cdb files) are written to the database by the "CDWRITE" command in ANSYS. After the interrupt, the thermo-mechanical simulation continues with a restart routine. The "antype„restart" command loads to original mesh, the applied boundary conditions and applies the simulation results of the last time step. The transient simulation continues until the next interrupt is reached.

In the fluid domain, an initial model is necessary to define essential items such as boundary and load conditions as well as the fluid properties. In particular, the inlets and outlets, the fixed and moving walls must be labeled for computational fluid dynamic (CFD) simulations in ANSYS CFX.

Similar to the mechanical domain, the fluid solver must be stopped at the same time intervals. It is realized by an interrupt, which calls "remesh.bat". The routine saves the current simulation results for the next CFX restart and launches ANSYS Mechanical to load the current mesh from the thermo-mechanical domain results. The mesh is copied to "remesh.cdb", which is the default filename for the one-way FSI coupling in ANSYS CFX. The new deformed mesh is incorporated into the CFX database whereby all result data from the previous time-step must be mapped to the updated mesh. It is an internal interpolation procedure of the fluid solver. Then a new fluid simulation in the next time interval is carried out and the process repeats until the total simulation time is reached.

The routine in **Figure 5.5** has been utilized to simulated the fluidic resistance at different swelling states for system simulation in Matlab Simulink presented in **Section 6.1.5**. However, the routine is very powerful and accounts not only for the fluidic resistances but also for the transient response of the coupled fluid-mechanical system.

A stimulus step function has been applied in **Figure 5.6**. The left upper figure shows a quarter symmetric model in the initial state. The related flow velocities are visualized on the right. **Figure 5.6 b)** and **c)** illustrate the swelling process. It can be seen that the outer faces and the corner region swell first and then follows the inner part of the hydrogel. The left lower figure visualizes the shrinking process where the solvent diffusion likewise starts at the outer regions and the inner part follows delayed.

The one-way FSI coupling works accurate and stable for most engineering problems. However, difficulties arise for very narrow or even closing gaps in microvalve applications. With narrow gaps, the aspect ratio between the lateral dimension and the gap height becomes very large. Values of 100 and above are reasonable. A tetrahedral mesh leads to an excessive number of elements because the edge length of the finite elements should be in the same order of magnitude. Hexahedral elements perform much better and allow inherently for a large aspect ratio without loss of accuracy. However, the fluid velocity profile in a narrow gap is a parabolic function according to Hagen-Poiseuille. Convergence tests have shown that at least eight layers are necessary to simulate the fluidic resistance with acceptable accuracy in

narrow gaps. Automatic mesh generators have difficulties in properly remeshing the complex structure of the fluid domain.

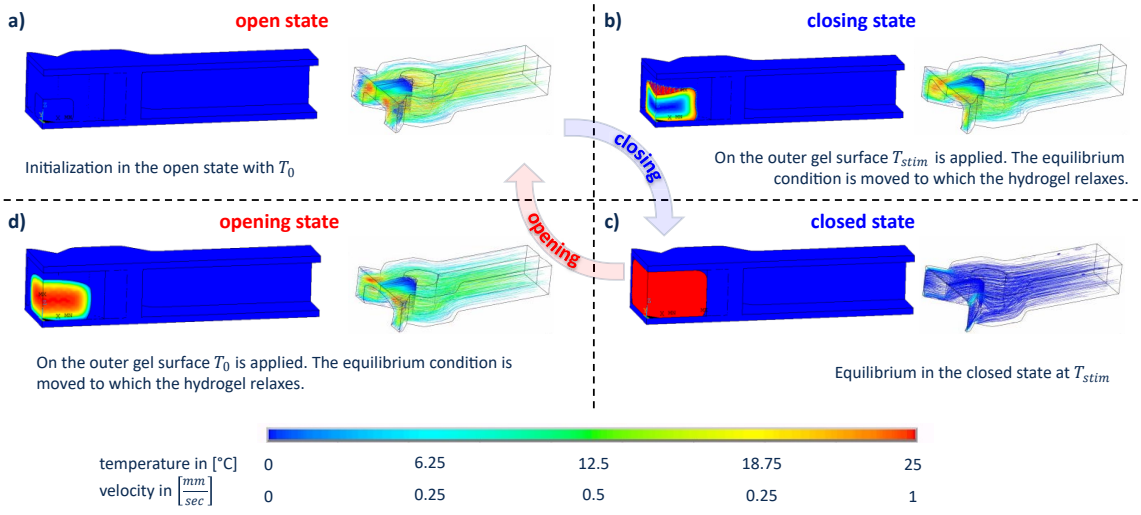

Figure 5.6: Based on the 1-FSI model, the deformation determined in the mechanical domain is translated into the fluid domain to predict the conductivity of the system for the closing and opening behavior.

ANSYS provides a powerful programming and design language referred APDL. APDL can not only be used to generate elements in the pre-process but also to control the solution routines for mesh morphing and remeshing procedures. **Figure 5.7** illustrates one example of modeling closing gaps for microvalve applications, which has been successfully implemented and tested.

The initial mesh is defined by hexahedral elements where the outer edges are parallel and perpendicular to the moving surface of the hydrogel. The swelling process squeezes the elements mainly in normal direction. In case of 3D-models, the default mesh morphing approach in ANSYS creates tangled elements where the element faces intersect each other at large deformations, which causes the negative volume element error. An example is marked by the red circle in **Figure 5.7 a)**.

For this particular case, the problem could be solved by implementing “guiding rails” for the inner finite element nodes. During mesh morphing, the inner element nodes can only slide along the colored bars shown in **Figure 5.7 c)**. It guarantees the hexahedral shape of finite elements during the deformation process even at very narrow gaps. Guiding rails can be modeled by beam elements with a very small tensile stiffness and a reasonable large bending stiffness. The beam elements form straight lines of variable length, on which the fluid elements can move and rotate easily. The distance between the layers is completely equal.

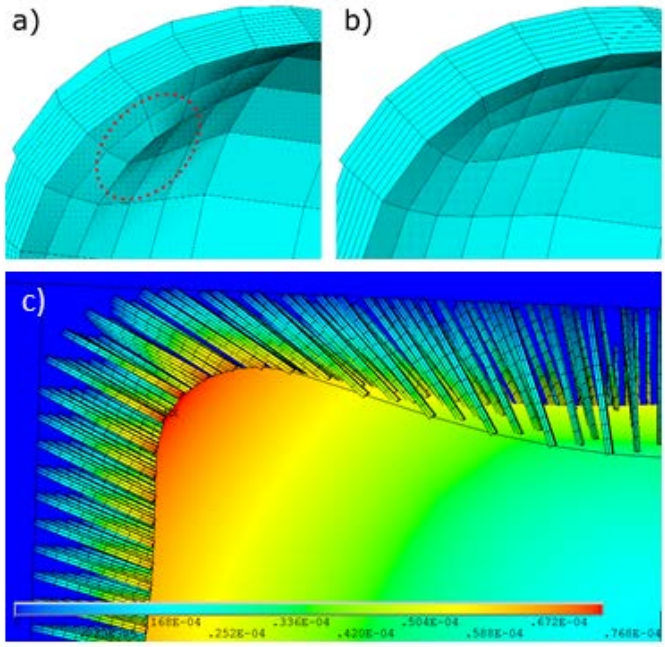

Figure 5.7: ANSYS: In a) a mesh break through is shown, which is stabilized by using mechanical beams in c) to create a more physical mesh morphing behavior as shown in b).

A totally closed gap is achieved by analytical terms. Element layers that are thinner than certain limits are deleted from the fluid mesh database. The approach shown in **Figure 5.7** works for a special class of applications but similar modeling techniques can be utilized for other examples too.

5.4.3 Towards a Two-way Fluid Structure Interaction Model in CFX

A two-way fluid structure interaction (2-FSI) modeling process has been studied and tested. In contrast to the previously discussed 1-FSI, the bidirectional interactions can also consider the influence of the fluid pressure on the mechanical domain and other interacting physical quantities.

The 2-FSI routing shown in **Figure 5.8** is based on the MFX in ANSYS, which is primarily intended for fluid structure interactions. The physical domain solvers are coupled by internal equilibrium iterations in each time step. The internal sub-loop is referred as stagger iterations in ANSYS.

The internal equilibrium iterations will be explained for the given example. In each time step, the mechanical displacements are transferred to the fluid domain and the temperature level of the surface boundary between the hydrogel and fluid wall is transferred to the mechanical domain. The result data are mapped onto the other mesh by interpolation procedures. Caused by the bidirectional interactions, the transferred data affect the transient response in the current time-step. For instance, the applied temperature profile of the fluid on the hydrogel surface is not ideal, causing a slightly different displacement shape in the mechanical domain. This mechanical motion affects the flow behavior of the microvalve.

Internal equilibrium iterations in the current time step must be repeated several times

until convergence is achieved. The implemented procedure is similar to the routine “restart”, in which the previous time step is simulated again with the new data from the internal stagger loops. In the case of convergence, the solvers begin with the next step in the outer loop, referred as time or main loop.

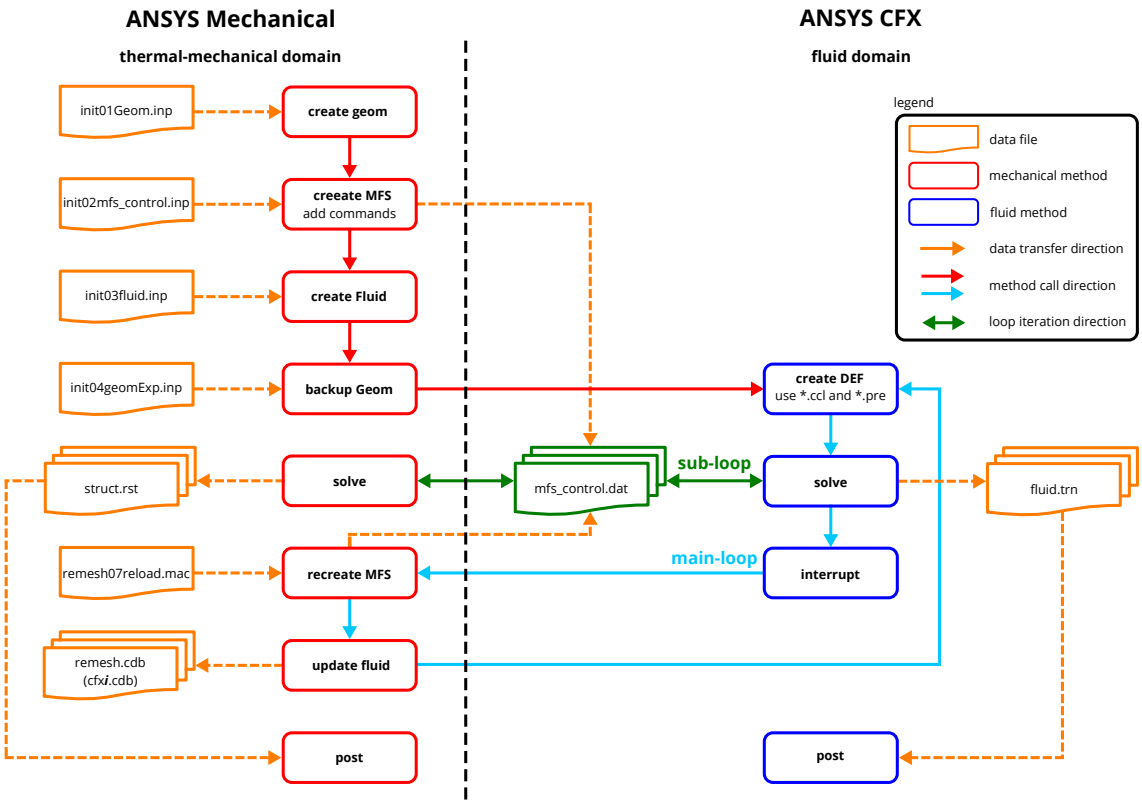

Figure 5.8: Two directional fluid structure interaction routine for ANSYS Mechanical and ANSYS CFX.

The 2-FSI data exchange process is controlled by instruction files and a communication protocol. The main file is “mfs_control.dat”, which specifies the data exchange procedure and the convergence behavior. It turned out that the bidirectional FSI coupling is very time consuming and the solvers often fail to converge. Even smaller loads and time steps did not produce better results. Bidirectional interactions in ANSYS CFX are rarely published. More promising approaches are recently reported in ANSYS Fluent, which is another CFD solver in ANSYS. Even with Fluent, bidirectional interactions are very challenging and this approach has not been pursued further.

The primary goal in **Chapter 5** is the extraction of precise fluidic resistance data of different swelling states for subsequent system simulations in Matlab Simulink. The one-way fluid structure interaction routine provides all data, which are necessary, for high accuracy and efficient system models. The system model generation is presented in the next chapter.

Chapter 6

Lumped Modeling

content of chapter

The previous chapter discusses finite element modeling technologies, where arbitrary and very complex geometries can be defined in a modeling process called Pre-Processing. In the next step, referred as Solution-Processing, different load and boundary conditions are applied on the models, which are solved either statically or in a time and frequency domain. In the final Post-Processing step, the model behavior is evaluated based on primary results data or based on user defined calculation routines. Characteristic properties such as the fluidic resistances, time constants of swelling processes or the volume change of hydrogels can be extracted with high accuracy.

The finite element results provide very important input information for lumped modeling technologies, which are widely utilized for the subsequent microfluidic component and system designs. Lumped modeling technologies create numerical models with a low number of governing equations, which are referred as ROM. If lumped parameter models are extracted from data obtained by field solvers based on FDM, finite element method (FEM), BEM or FVM, the reduction process is often referred as MOR in the literature [149]. Lumped models describe the internal behavior of components and systems by a small set of equations, which can be solved efficiently. A small set can include several hundred equations or parameters. However, finite element models have between several thousands and several millions degrees of freedom (DOF) and consequently equations. The huge number of DOF is the reason that larger technical systems and devices must be reduced in their complexity to perform optimization procedures and case studies in a reasonable time.

Lumped models can either be defined by analytical terms according to the theoretical background or by extracted result data from finite element simulations or measurements. Usually, design engineers utilized both concepts. Analytical based lumped parameter models are preferred during conceptual design. Finite element-based data extraction is utilized in the final stage of design where highly accurate models are created for the desired layout. Both approaches will be used in this chapter. For instance, the fluidic resistance of a microvalve can be estimated by Hagen-Poiseuille equations or extracted precisely from ANSYS CFX simulations whereby data are transferred to lookup tables or customized fit-function blocks in Matlab Simulink. The modeling approach where system models are iteratively improved at different levels of abstraction have been discussed in **Section 2** of this work.

Lumped models are created for different elements of the microfluidic toolbox. In this chapter, the general approach is discussed in detail for the CVPT model. This valve model is the core element in **Chapter 7** where multiple fluid components are assembled to larger fluidic logic circuits and analyzed in the time domain. It will be shown that highly efficient parameter studies can be performed for complex systems, which consist of multiple physical domains.

Essential features of lumped models can be changed by mask parameters or by modifying the implemented transfer-functions or lookup tables. The models can easily be adjusted to new designs and changed test conditions.

In general, three major lumped modeling approaches exist in computational engineering. The first one is a network description where the system elements are described by an across (potential) and a flow (current) quantity. This approach is widely used in electrical engineering but can be adapted to non-electrical systems by analogy relationships. The second approach is a signal flow description where physical quantities are routed from one element to the next one by directional connection lines. Signal flow models are widely used for controller and system design. The third approach allows a mixed signal description where an analogue signal model can be combined with digital model components. For now, only continuous models with either network descriptions or signal flow descriptions are of interest in this work.

There are many options regarding computer tools used for lumped modeling. The freeware tool LTspice is a widely used and well-known circuit simulator with no node or element limitations. The main focus of LTspice is on electrical network models, which can be extended to fluidic systems by analogy relationships. However, the software package Matlab has been chosen in the work because it supports both, network descriptions in Matlab Simscape and signal flow models in Matlab Simulink. Furthermore, the Matlab software suite offers a very versatile development platform ranging from numerical matrix operations, curve fitting procedures, image processing utilities, graphical user interface (GUI) programming libraries and toolboxes for measurement data extraction and evaluation. Matlab is not only interesting for academic research, it became also an industry standard in many engineering fields.

Advanced circuit simulators such as Cadence, Mentor Graphics or Synopsys could also be of interest for microfluidic system design. Those tools support several electronic design languages such as Verilog-A or VHDL-A and provide a large library of electronic circuit models. In industry, Cadence is a standard tool for electronic design automation of large-scale systems such as microprocessors or memory cells. However, Cadence is highly specialized and advanced but less used in academic class-room work and at small and medium enterprises.

6.1 The Chemical Volume Phase-transition Transistor Model

The chemical volume phase-transition transistor (CVPT) is the main element for logical chemofluidic circuits. A detailed description of the CVPT valve is important to accurately predict the behavior of the fluidic systems.

The model shown in **Figure 6.1**, is subdivided into five parts. The first part describes hysteresis parameters, based on the stimulus behavior at the hydrogel. The second part calculates the equilibrium length, based on the applied stimulus and the hysteresis values. Next,

the transient swelling behavior is calculated from the equilibrium length together with the rise time functions in part three. Part four calculates the swelling dependent stiffness change of the hydrogel, the elastic compression of the gel due to the fluid pressure and the sealing force, which is needed to predict the leakage rate.

Finally, the compressed length of the hydrogel is compared to the pre-calculated swelling states of the finite element model. A "FEM lookup" function interpolates the dimensional parameters of the gel and calculates the fluidic conductivity based on the results of the finite element model. In part five, the applied pressure difference across the valve is multiplied with the fluidic conductivity to calculate the volume flow rate of the medium, which propagates through the valve. The resulting flow rate is assigned by a controlled current source in the right part of **Figure 6.1**.

6.1.1 Static Hysteresis

The theoretical background for modeling the hysteresis effects in hydrogels has been explained in **Section 3.3**. In the following, the numerical implementation of the algorithms in Matlab Simulink and test cases to verify the approach on examples will be discussed in detail.

Several benchmark examples have shown that appropriate modeling techniques are vital to obtain a high performance during transient simulation runs. For instance, mathematical equations should not simply be copied into "Interpreted Matlab function blocks" because those blocks call the Matlab parser in each integration time-step, which takes time. Rather than, all equations and conditional code segments of the model should be assembled entirely from build-in blocks, which improves the performance by orders of magnitudes.

Hysteresis is the dependence of the state of a system on its history. Important are so-called turning points where the stimulus signals change from increasing to decreasing values and vice versa. Turing points do not depend on the direction of the stimulus or the flow transport in a channel, rather they depend on the moment where the stimulus-time function changes its direction. In the following, the direction is related to the signs of the time-derivatives (slope), which are positive for increasing and negative for decreasing stimulus functions. **Figure 3.9** shows an example case where the sigmoidal functions are shifted around the lower critical solution temperature T_{LCST} by an offset ΔT_{hyst} depending on the applied stimulus profile. A proper closing condition and its effects can now be fully analyzed.

A first step in the hysteresis part of the valve model will be the calculation of the time-derivatives of the stimulus as shown in **Figure 6.2**. The Boolean output 1 (called "if true") provides a true signal flag at the turning points, which triggers the calculation of new hysteresis parameters. Output 2 provides permanently the sign signal of the first derivative, which defines the direction of the stimulus change. The stimulus is applied at input 1 in **Figure 6.2**.

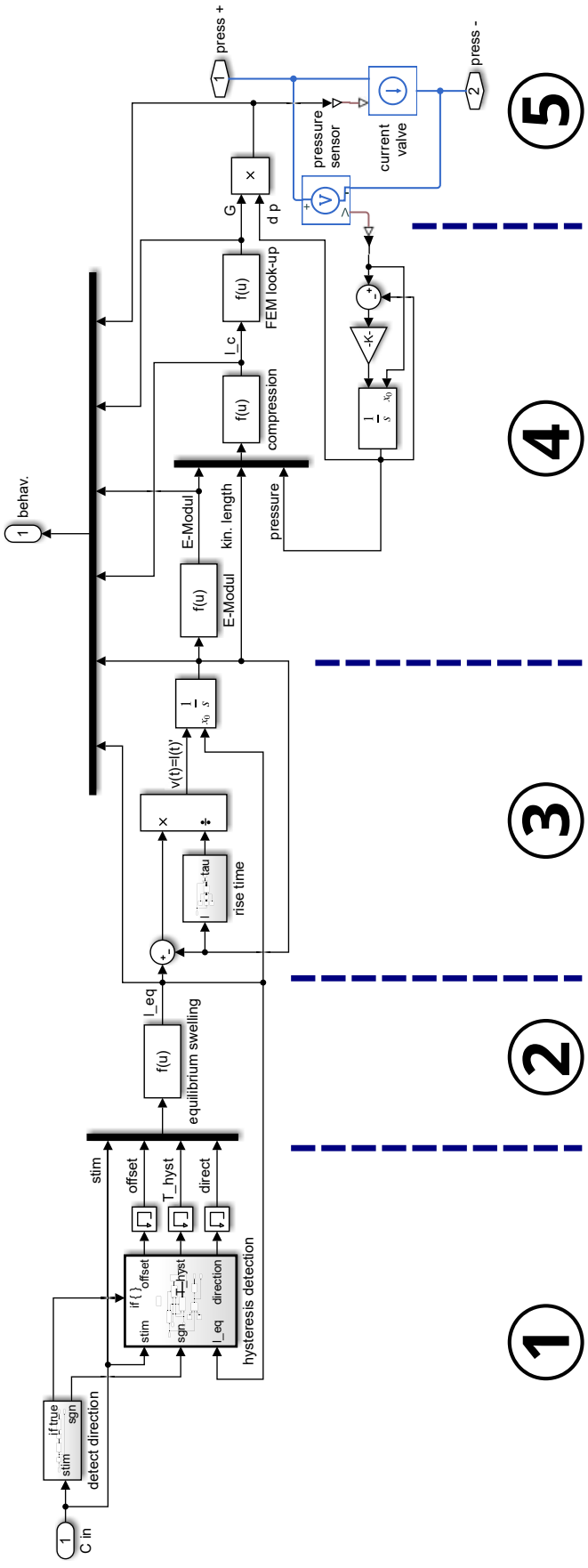

Figure 6.1: Signal flow model of a chemical volume-change phase-transition transistor, with hysteresis effect (1), sigmoidal phase-transition behavior (2), the transient response (3), the maximum sealing pressure (4) and the resulting flow model (5).

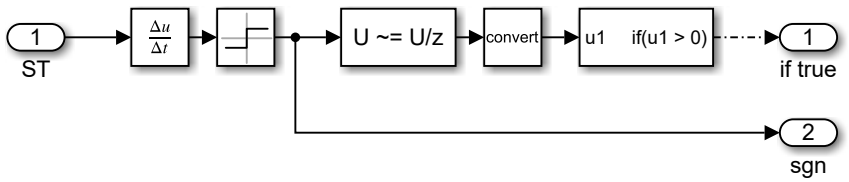

Figure 6.2: Subroutine to detect a direction change of the stimulus. Input is the stimulus signal ST, outputs are the Boolean flag indicating the turning point (output 1) and the sign value for the stimulus change (output 2).

The "detect direction" subsystem of **Figure 6.1** starts with a time derivative block and is followed by a sign block where the slope signal is transformed to a ± 1 value. Thereby, $+1$ represents an increase of the stimulus and -1 a decreasing stimulus. The next block determines whether the sign value has been changed or not. The trigger signal is set exactly one time-step after the slope change at the turning point. Hence, the "sgn" output port provides the direction of the stimulus after the turning point at the triggered event. For numerical reasons, the output signal must be converted into a double value and then into a Boolean value in order to get accepted by the if-conditions in the subsequent action blocks, which evaluate the trigger signal.

The following example uses the applied temperature profile as stimulus signal for the hysteresis effect. In the model parameter mask, a maximum hysteresis offset temperature ΔT_{hyst} must be defined, which describes the horizontal shift of the sigmoidal functions with regard to the lower critical solution temperature T_{LCST}. The implemented approach has been verified by a sinusoidal temperature profile, which covers the entire sensitivity range of the hydrogel from $T(t) = [0; 2 \cdot T_{LCST}]$. The outer hull curves of the equilibrium length can be observed in the hydrogel response plots in **Figure 3.8**. If the temperature is increasing, the right hull curve is set with $\Delta T_{hyst} = +4°C$ and, if the temperature is decreasing, the left hull curve is defined with $\Delta T_{hyst} = -4°C$.

The routine is initialized at the lower critical solution temperature T_{LCST}. In the first step (1), the temperature is increased and the hydrogel follows the second half of the sigmoidal function. Now the temperature is decreasing and a stimulus direction change is detected (2). The hysteresis temperature offset is set to $\Delta T_{hyst} = -4°C$ and shifts the sigmoidal function to the left. If the temperature is increasing in (3), the hysteresis offset is set to $\Delta T_{hyst} = +4°C$ what shifts sigmoidal function to the right.

As a next step, the internal loops are verified by a depleting sinusoidal temperature profile as shown in **Figure 3.10**. There, the hydrogel is initialized with $\Delta T_{hyst} = 0°C$ at the lower critical solution temperature T_{LCST}. By increasing the ambient temperature, the value of the equivalent length follows the unshifted sigmoidal function to the turning point, where a stimulus direction changes from increasing to decreasing values. Now it follows the left hull curve to the next turning point and then the right hull curve followed. From there, the functional behavior of the hysteresis models at internal loops can be observed and verified.

In **Figure 3.10**, the turning point (4) is out of the range of the upper and lower swelling length l_1 and l_0. It activates a routine to calculate the upper and lower offset length l_{off} and l_{off1}. The primary goal of the offset parameters is to shift the new left or right sigmoidal function into the turning point. The theoretical background has been explained in

Section 3.3. The offset length parameters are calculated from **Equation 3.64** and **Equation 3.65**. Both offset length parameters together with the hysteresis offset temperatures ΔT_{hyst} define the sigmoidal function needed for the equilibrium length l_{eq} according **Equations 3.66**.

In the next section, the implementation of the hysteresis effect in Simulink is discussed. The "hysteresis detection" subsystem calculates the offset length l_{off} parameters (output 1), the hysteresis offset temperature ΔT_{hyst} (output 2) and passes through the direction sign n_{sgn} signal from input 2 to output 3. The "hysteresis detection" block is only activated at the trigger event by the action port in **Figure 6.3**.

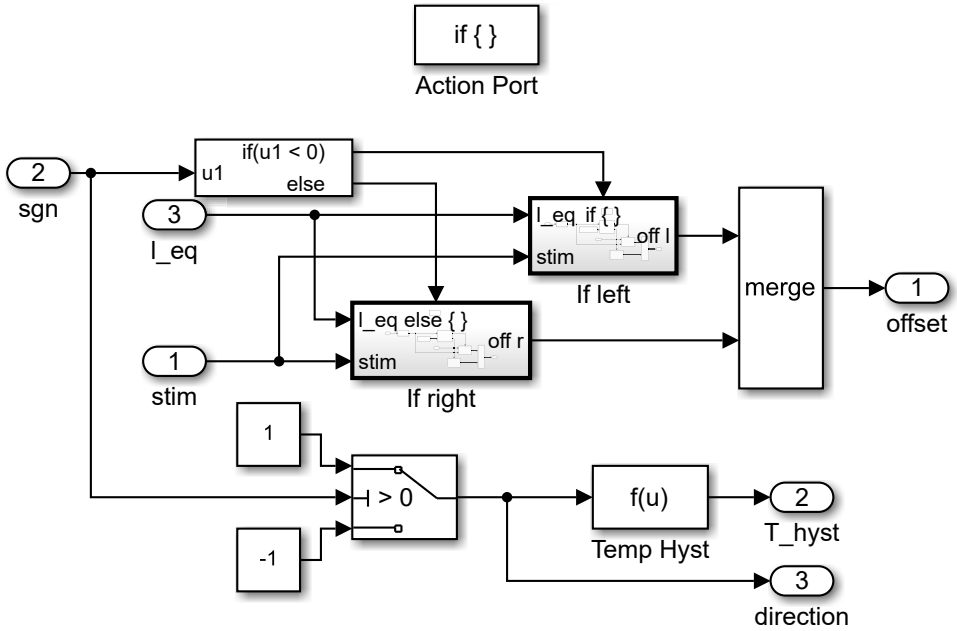

Figure 6.3: "Hysteresis detection" subsystem, which is used to determine the hysteresis parameters.

The direction sign n_{sgn} at input 2 is evaluated after the trigger event and takes the new slope after the turning point into account. The n_{sgn} values are positive after the turning points (3) and (5). It indicates an increasing stimulus value and activate the calculation of the right hull curve parameters in the "If right" subsystem. Negative n_{sgn} appear after the turning points (2) and (4) what activates the calculation of the left hull curve parameters.

Due to some performance issues, n_{sgn} is redefined at the switch to better hold the signal for the subsequent function block "Temp Hyst". In this function block, the hysteresis temperature ΔT_{hyst} is multiplied by the n_{sgn} signal to provide the desired offset temperatures. **Equation 3.64** and **3.65** are implemented in the "If right" and "If left" subsystems, which need the current equilibrium length $l_{eq}(T)$ and left or right hull curve $l_{H(r,l)}(T)$ values as input data. Both routines are shown in **Figure 6.4**.

In **Figure 6.4**, another if-condition is implemented. Only if the current length is within the hull curves ($l_{H_l}(T,t) < l(T,t) < l_{H_r}(T,t)$), then internal loop parameters are necessary and the offset length parameters l_{off} and l_{off1} are calculated. Otherwise, there are no internal hysteresis loops and the offset length parameters are set to zero.

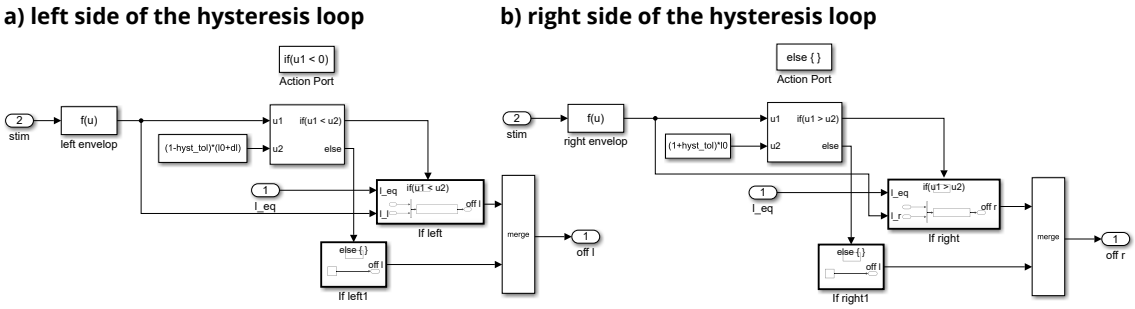

Figure 6.4: Sub-circuits to determine the offset parameters l_{off} and l_{off1} for the right and left hull curves.

For performance reasons, it is recommended to define another barrier, which is a little under the maximum or over the minimum swelling degree to avoid turning points in the saturation range. Numerical simulators are in general struggling with detecting close to zero values, for which a hysteresis tolerance hys_{tol} is introduced. The default value is set to $hys_{tol} = 1 \cdot 10^{-5}$ but can be changed in the model properties tab of the microvalve mask.

Both, the “detect direction” block of **Figure 6.2** and the “hysteresis detection” block of **Figure 6.3** are necessary to determine the hysteresis parameters, which are required to calculate the equilibrium length of the hydrogel. Thereby, the wiring of the signals is not trivial, because an algebraic loop appears due to the equilibrium length l_{eq} is coupled back from the “equilibrium swelling” to the “hysteresis detection” block. This algebraic loop is broken though the memory block as shown in **Figure 6.5**. Additionally, when the if-condition is not active, the parameters are still needed for subsequent calculations of the equilibrium length. For this reason, the memory blocks are also necessary to hold the outputs of the “hysteresis detection” subsystem until the next turning point is detected.

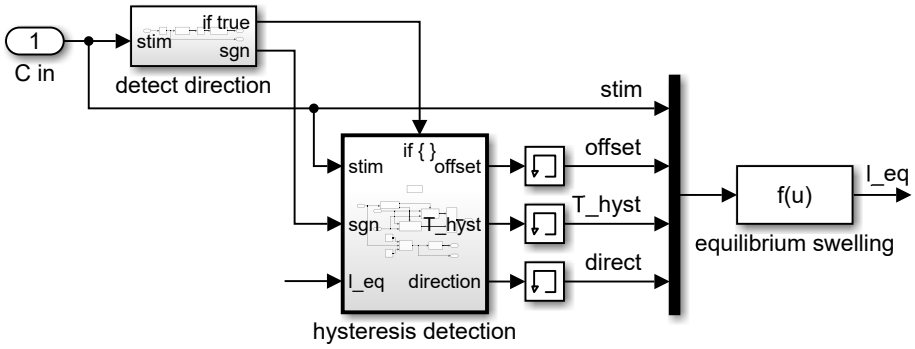

Figure 6.5: Simulink model to determine the hysteresis parameters for the CVPT model.

During experimental characterization of the static hysteresis behavior of hydrogels, the time range for tests should be set long enough to avoid interferences caused by the dynamic effects of swelling. It turned out that hydrogels swell and shrink very slowly and measurements take several days to predict internal hysteresis cycles with high accuracy. This long duration was the main motivation to develop fully automated and stable measurement routines to characterize the swelling behavior of hydrogels as discussed in **Section 4**.

6.1.2 Equilibrium Swelling Length – Quasi-static Behavior

The second part of the CVPT model shown in **Figure 6.1** is focused on calculating the equilibrium swelling length based on the sigmoidal function defined in **Equation 3.66**. The block "equilibrium swelling" calculates the quasi-static response of the hydrogel according to the stimulus signal, which is needed for the transient response analyzed in part three of the model.

The "equilibrium swelling" block requires the previously computed input parameters, which are the stimulus temperature "stim", the offset length "offset", the hysteresis temperature "ΔT_{hyst}" and the direction sign "direct" of the stimulus. All four parameters are bundled in the "Mux" block to a vector signal on a single wire, whereby the multiplexed data must be addressed by $u(1)$ for "stim", $u(2)$ for "offset" , $u(3)$ for "ΔT_{hyst}" and $u(4)$ for "direct" in the subsequent function block "equilibrium swelling". The multiplexing of signals not only serves to clarify the model layout. The main reason is that function blocks only allow one input and one output signal, as shown in **Figure 6.6**.

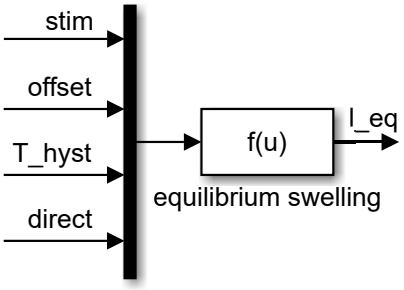

Figure 6.6: Standard function block to determine the equilibrium swelling length l_{eq} with a "Mux" block to bundle input signals.

Within the function block, the equilibrium length is calculated by the following multiparametric sigmoidal function, which has been introduced in **Section 3**:

$$l_{eq} = \frac{\Delta l - l_{off}}{1 + e^{-\frac{5}{\Delta T_u}\cdot(T(t)-T_{LSCT}-T_{hyst})} + 0.5 \cdot e^{-\frac{5}{\Delta T_l}\cdot(T(t)-T_{LSCT}-T_{hyst})}} + l_0 + l_{off} \cdot \frac{1-n_{sgn}}{2}. \quad (6.1)$$

In **Equation 6.1**, the four input parameters of the function block are the stimulus $T(t)$, the offset length l_{off}, the static hysteresis offset T_{hyst} and the temperature direction parameter n_{sgn}. The length change Δl, the reference length l_0, the upper and lower curvature width ΔT_u and ΔT_l, as well as the lower critical solution temperature T_{LCST} are defined in the CVPT mask and therefore exist as known parameters in the valve model.

6.1.3 Kinematic Swelling Length - Transient Behavior

Part three of the CVPT model shown in **Figure 6.1** is focused on calculating the kinematic length of the hydrogel based on the equilibrium swelling length computed in part two of the model. The kinematic swelling length describes the transient response of the swelling and shrinking processes after the stimulus signal changes.

The transient response is defined by a first-order differential equation as discussed in **Section 3.2**. The difference between quasi-static and the transient response is that the quasi-static equilibrium length follows instantaneous the stimulus signal changes. The measured transient response after a stimulus jump is an exponential function whereby the rise time depends on the direction of the length change (swelling or shrinking) and the current equilibrium length. Therefore, the following first-order differential equation can be used to describe the transient response of the hydrogel:

$$d(l) \cdot \dot{l}(t) + l(t) = l_{eq}(T), \tag{6.2}$$

whereby $l_{eq}(T)$ is the stimulus dependent equilibrium length, $l(t)$ the time response referred kinematic length and $d(l)$ the damping coefficient, which is here equal to the rise time $\tau(l)$ of the hydrogel.

Equation 6.2 is modeled by a control loop with an integrator block labeled as "$\frac{1}{s}$", a subsystem "rise time", which evaluates the rise time $\tau(l)$ of the differential equation and two routing blocks, which add and divide incoming signals as shown in **Figure 6.7**. From the numerical point of view, solving ordinary differential equations by integrators is more accurate and stable as using derivative blocks for the same task. The control loop with the integrator block actually solves **Equation 6.3**, which is identical to **Equation 6.2**. Additionally, the integrator block in **Figure 6.7** allows to define the initial conditions for the kinematic length at time $t = 0$:

$$\dot{l}(t) = \frac{l_{eq} - l(t)}{d(l)} = v(t). \tag{6.3}$$

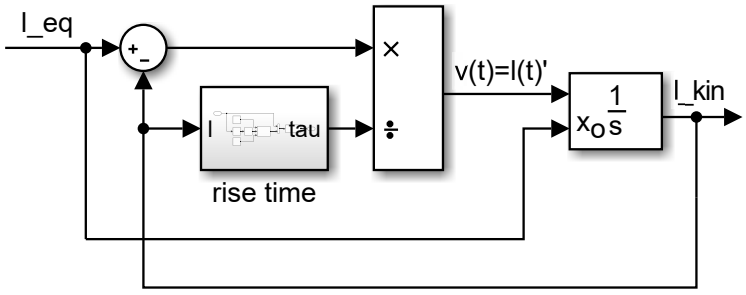

Figure 6.7: Control loop representing a first-order differential equation to determine the transient response of the swelling hydrogel.

The "rise time" block in **Figure 6.7** predicts the swelling time of the hydrogel. According to [114], the rise time depends on the current length $l(t)$ of the hydrogel and the cooperative diffusion coefficient D_{coop}, which is a function of the swelling degree Q. The swelling degree is approximate by a cubic function from the current kinematic length $l(t)$ and the initial (unswollen) length l_0 of the hydrogel according to **Equation 3.60** of **Section 3.2.3**.

However, experimental results have shown that the rise time of swelling hydrogels agree well with the theory but underestimates the shrinking behavior. Therefore, the first part of the "rise time" block in **Figure 6.8** is utilized to adjust the rise time function by scale factors. For swelling processes, the scale factor is set to 1 and for shrinking processes the scale factor is defined by D_{fac}, which can be modified in the mask parameter window of the valve model:

$$d = \begin{cases} 1 & \frac{dl}{dt} \geq 0 \\ D_{fac} & \frac{dl}{dt} < 0 \end{cases}. \tag{6.4}$$

Finally, the “rise time” function block is defined by:

$$\tau = d \cdot \frac{l(t)^{2-3n} \cdot {l_0}^{3n}}{D_0}, \tag{6.5}$$

whereby the first input signal is the current kinematic length $l(t)$, the second input parameters is the scale factor d with either 1 or D_{fac} for the rise time, D_0 is the base diffusion coefficient, l_0 the initial length in the unswollen state and n the power variable of the swelling process according to **Equation 3.50**.

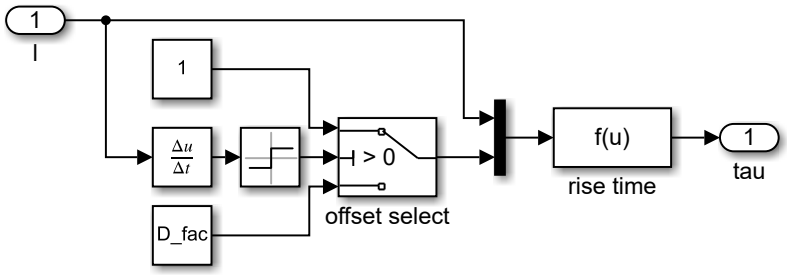

Figure 6.8: “Rise time” subsystem elements to predict the swelling time of the hydrogel.

6.1.4 Stiffness and Maximum Closing Pressure

Hydrogels undergo large dimensional changes whereby water or other solvent molecules penetrate into the polymeric network [150]. It results in a stiffness change, which can be described by a changing Young’s modulus during operation. In [125] the mechanical properties of hydrogels are measured and temperature depended functions of the Young’s modulus are shown on page 3239.

In the present work, it is hypothesized that the stiffness correlates more with the current length $l(t)$ than with the stimulus of the hydrogel. The swelling and consequently the length change of the hydrogel follows with a time delay to stimulus signals. Hence, the true physical behavior is better approximated if the stiffness, in particular the Young’s modulus, is described as a function of the kinematic length. Otherwise, a step signal of a temperature driven Young’s modulus would create a jump of the stiffness and a jump of the related displacement functions. These jumps are thermodynamically impossible from the physical point of view. Furthermore, the temperature driven approach would cause numerical problems due to algebraic loops.

The hydrogel network shows a maximum stiffness in the collapsed state. The solvent ,which penetrates during the swelling process into the hydrogel, softens the material. This requires a description where the stiffness is dependent on the size of the gel, which can be either the volume or the length change. This idea follows the multi-field theory in [151] where the hydrogel behavior is described in relationship between the solvent and the gel network.

According to **Chapter 3**, the Young's modulus is linearly interpolated between the swollen and the collapsed state. Therefore, the function block "E-Modul" in **Figure 6.9** is defined by:

$$E(l_{kin}) = E_1 - \frac{(E_1 - E_0) \cdot (l_{kin} - l_0)}{\Delta l}, \tag{6.6}$$

where the kinematic length l_{kin} is the input variable, E_1 is the Young's modulus in the collapsed state with a maximum value, E_0 is the Young's modulus in the swollen state with a minimal value, l_0 the initial length and Δl the total length change with $\Delta l = l_1 - l_0$. It should be noticed that a linear interpolation of the Young's modulus based on volumes changes could also be implemented. Different ways to transform length changes to volume changes for large deformations are discussed in **Appendix D**.

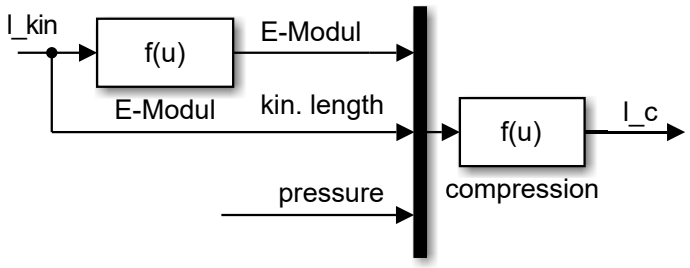

Figure 6.9: Simulink model elements to calculate the hydrogel compression at acting fluid pressure loads.

The hydrogel is a soft material, which deforms under pressure loads. However, hydrogels are almost incompressible because the Poisson's ratio is near to $\nu = 0.5$. A uniform pressure load around the hydrogel does not change the volume or leads to a deformation. For this reason, only local pressure differences are relevant for calculating elastic deformation states. In practice, the deformation is most important in the closed state where high pressure differences squeeze the solvent trough a small gap between the wall and the hydrogel surface. It creates a leakage flow, which can have a significant influence on the functional behavior of the valve.

The pressure difference Δp is directly available at the interface ports of the valve. In the closed state, the pressure difference at the ports is almost identical to the pressure difference at the hydrogel surfaces as shown in **Figure 6.10**. Measurements have shown that high pressure differences can squeeze the fluid through a closed valve. This physical behavior could only be partly reproduced by finite element simulations but the results illustrated the leakage problem.

The fluid pressure pushes a wedge-shaped gap at the interface between the wall and the hydrogel surface. At high pressure differences, the wedge-shaped gap moves from the high-pressure side to the low-pressure side, which finally leads to a leakage flow. During the opening process, the pressure in the wedge-shaped gap is almost constant. After the opening, there is a linear pressure drop in the gap. The displaced hydrogel from the top side is mainly pushed to the sidewalls at the low-pressure region. It is very difficult to describe the opening effect accurately but it can be estimated from the linear theory of an elastic continuum. The idea is that the gap opens if the fluid pressure difference is larger as the contact pressure of the hydrogel to the wall. The elastic deformation can be described by the following stress-

strain relationship:

$$\sigma = \Delta p = E\left(l_{kin}\right) \cdot \varepsilon. \tag{6.7}$$

In **Equation 6.7**, the mechanical stress σ is approximated by the applied pressure drop Δp over the valve, the engineering strain ε and the Young's modulus E, which are functions of the current kinematic length l_{kin}. The resulting compressed length l_c of the hydrogel becomes $l_c = l_{kin} - \Delta l$ leading to the following equation:

$$l_c = l_{kin} \cdot \left(1 - \frac{\Delta p}{E(l_{kin})}\right). \tag{6.8}$$

The Young's modulus E represents the stiffness per unit area for the compression effect of the hydrogel. The value can be adapted from measurement data or indirectly from the leakage flow rate at varying pressure loads Δp across the calve. The total stiffness depends not only on the hydrogel material property but also on the assembly, the chamber design and how the hydrogel is fixed in the chamber of the valve.

Figure 6.10 illustrates the pressure distribution in the fluid of a quarter symmetrical finite element model of the microvalve in the collapsed state **a)** and in the swollen state **b)**. In the collapsed state, there is a linear pressure drop in the valve caused by the fluidic resistance of the viscose solvent. In the swollen state is almost no fluid flow. The red colors indicate that the pressure is uniform from the inlet to the hydrogel surface. The same effect occurs at the outlet side with the low-pressure value.

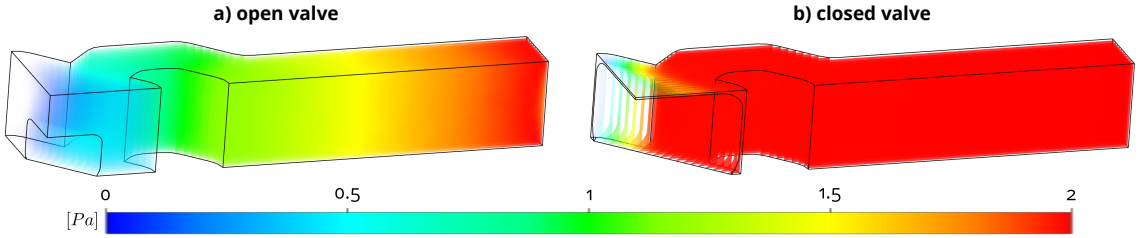

Figure 6.10: Opening and closing pressure distribution within the microvalve.

Due to in the Simulink model the compressed length is introduced, a significant compression occurs at high pressured values. In **Figure 6.11 b)**, a gap appears between the kinematic length and the compressed length, which does not appear in **a)** for the length plot at low pressure values. Respectively a sealing is achieved in case **a)** and a leakage is detected in case **b)**, because there the mechanical contact pressure of the hydrogel on the wall is smaller than the fluid pressure. The compressed length becomes visible and a small leakage flow rate can be observed.

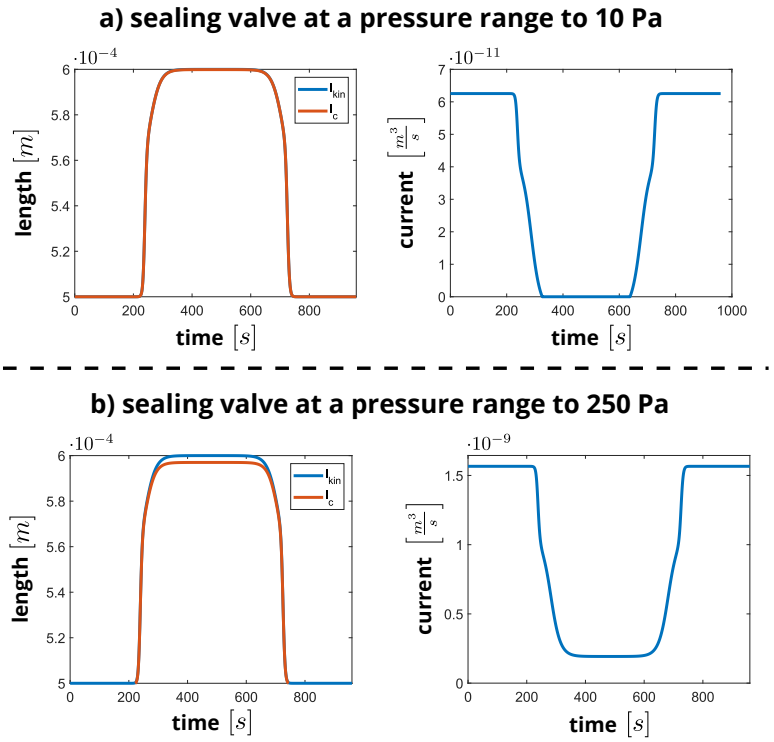

Figure 6.11: In a) a sealing at low pressures of up to $10\,\mathrm{Pa}$ is possible but around $250\,\mathrm{Pa}$ a leakage is detected.

The mechanical contact pressure of the hydrogel on the wall is a critical design parameter. The value should be estimated and compared to design rules of the microfluidic toolbox for manufacturing of prototypes. The highest possible contact pressure depends on the engineering strain and the Young's modulus in the swollen state. It can be approximated by:

$$p_{cl} = E_0 \cdot \left(\frac{l_1}{l_{gap} + l_0} - 1 \right), \tag{6.9}$$

whereby p_{cl} is the maximum closing contact pressure, E_0 the Young's modulus in the closed state, l_1 the maximum swelling length, l_0 the initial reference length and l_{gap} the gap between hydrogel and the fluidic wall.

In practice, a typical design task can be to define the required gap length l_{gap} of the microvalve, which can withstand a certain closing pressure. Then **Equation 6.9** can be transformed to the following form:

$$l_{gap} = \frac{l_1}{\frac{p_{cl}}{E_0} + 1} - l_0. \tag{6.10}$$

Another critical design parameter is the leakage flow. If the fluidic pressure difference is larger as the assumed closing pressure of the hydrogel, a leakage flow can appear, which affects the functional behavior. The largest fluidic pressure difference across the valve appears in the closed state.

Considering the worst case, the inlet pressure from external pumps acts entirely on the microvalve because it blocks the entire fluid flow. Consequently, the external pressure pumps

must be designed with lower values as the critical pressure level from **Equation 6.9**.

If the pressure drop on the closed microvalve condition is unsure, then a CFD simulation with an open circuit condition can be performed. Thereby the three dimensional chip layout is taken and the microvalve component is deactivated. Now two boundary walls are formed, one for the inlet and one for the outlet of the valve. The CFD model is analyzed and the critical pressure difference at the boundary walls can be determined.

6.1.5 Calculation of the Fluidic Conductance

The primary goal of the microvalve model is to control the volume flow rate at applied pressure and stimulus loads. The relationship between pressure and volume flow rate is defined either by the fluidic resistance or by the inverse, which is the fluidic conductance of the valve. Thereby the resistance is indirectly controlled by the applied stimulus. Based on previously defined steps, the stimulus is transformed into a length change of the hydrogel, which then affects the fluidic resistance and consequently the volume flow rate.

There are two ways to calculate the fluidic resistance in a Simulink model. The first approach is based on analytical equations and the second one is based on a numerical data extraction procedure where finite element simulation results are used to describe the fluidic resistance with a much higher accuracy. The analytical approach is discussed first.

The goal is to calculate the fluidic resistance analytically from the Hagen-Poiseuille equation for rectangular cross-sections. **Figure 6.12 a)** shows that the fluid domain around the hydrogel form an n-shaped channel. However, just adding the flow from each area creates large errors not only in the amplitude, but also during the closing motion. Therefore, in a second approach the entire area was approximated by a single area of the same length as shown in **Figure 6.12 b)**. During operation, the hydrogel at the center expands and changes the size of the fluid gap l_{gap} by the length change parameter $\Delta l'$.

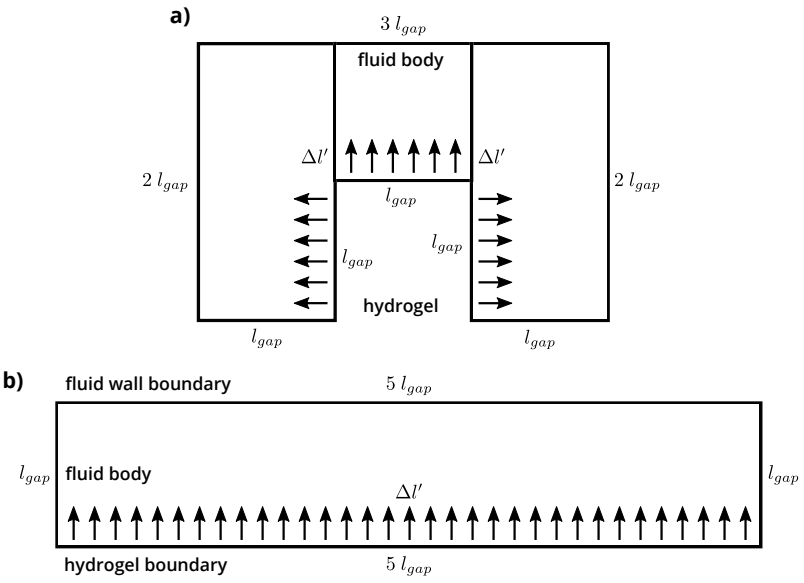

Figure 6.12: Schematic view of the true cross-section at the hydrogel chamber and the approximated rectangular area.

It will be shown that finite element simulations predict the fluidic resistances with a much better accuracy. However, analytical equations are simple to use and one can clearly see the influence of dimensional parameters and physical properties on the fluidic resistance. Analytical terms should be used for conceptual design and the finite element simulation is best used to improve accuracy. The pressure-flow relationship of rectangular channels according to the Hagen-Poiseuille equation is defined by [152]:

$$\dot{V}(\Delta l') = \frac{k(\Delta l') \cdot (l_{gap} - \Delta l')^3 \cdot 5 l_{gap}}{12 \cdot \eta \cdot l_{ch}} \cdot \Delta p, \tag{6.11}$$

whereby k is a geometry factor, l_{gap} represents the gap between the hydrogel and the fluidic wall, $\Delta l'$ is the hydrogels length change, which is determined with $\Delta l' = l_c - l_0$, η is the dynamic viscosity and l_{ch} is the mean channel length of the valve. The geometry factor k for rectangular cross-sections is given by [152]:

$$k(\Delta l') = 1 - \sum_{n=1}^{\infty} \frac{1}{(2n-5)^5} \cdot \frac{192}{\pi^5} \cdot \frac{l_{gap} - \Delta l'}{5 l_{gap}} \cdot \tanh\left((2n-1) \cdot \frac{\pi}{2} \cdot \frac{5 l_{gap}}{l_{gap} - \Delta l'}\right). \tag{6.12}$$

In the following model, the fluidic conductivity G is utilized instead of the fluidic resistance. The reason is that valves create infinite resistances in the closed state but never an infinite conductance in the open state. To avoid a singularity in transient simulations, the fluidic conductance has been implemented in the Simulink model elements. The aspect ratio of the rectangular cross-section (width to height) is 5 and increases during the swelling process. In that range, the geometry factor k changes only a few percent especially towards the closed state. It is not worth to evaluate **Equation 6.12** in each time-step, vrather the geometry factor has been set to a fixed value k_0, which is calculated in the open state. Additionally, **Equation 6.11** is redefined to a function of G_0 multiplied by the gap ratio, which goes with the power of three as shown in **Equation 6.14**. G_0 is the fluidic conductance in the open state:

$$G(l_0) = G_0 = \frac{5 \cdot {l_{gap}}^4 \cdot k_0}{12 \cdot \eta \cdot l_{ch}}. \tag{6.13}$$

Theoretically, the length change $\Delta l'$ can be larger as the fluid gap l_{gap} because no limiters or contact elements have been implemented in previously defined Simulink model elements for the hydrogel. Therefore, a case distinction through if-conditions is used in the following fluidic conductivity equation:

$$G(l_c) = \begin{cases} \left(\frac{l_{gap} - l_c + l_0}{l_{gap}}\right)^3 \cdot G_0 & \text{if } (l_c - l_0) < l_{gap} \\ 0 & \text{if } (l_c - l_0) \geq l_{gap}. \end{cases} \tag{6.14}$$

Equation 6.14 defines the fluidic conductance according to Hagen-Poiseuille as a function of the compressed length l_c of the hydrogel for the model shown in **Figure 6.12 b)**.

A second approach is to compute the fluidic conductance function of the valve based on the finite element results from **Chapter 5**. Contrary to analytic equations, in FEM arbitrary and very complex microvalve designs can be modeled, but an automatic extraction procedure for the conductivity behavior is needed. In order to later fit the results to a function, at first the

data points need to be extracted within ANSYS CFX. There, a two parameter vector is required and the first one contains the swelling displacements at a characteristic node on the top face of the hydrogel. This represents the hydrogels length change $\Delta l'$. The second parameters represents the conductivity and is calculated based on volume flow rate divided by the applied pressure drop at each displacement step. Based on these data points, an FEM-based conductivity function can be defined, which will include the fluid properties like dynamic viscosity and density, the geometric properties and energy losses, which normally is very challenging to determine for complex geometries. However, how these parameters affect the equation can not be easily determined and for the conceptual design phase, analytic equation are always recommended.

The extracted two parameter vector is now fitted with the curve fitting toolbox in Matlab and there the best agreement could only be achieved with an exponential functions as defined in **Equation 6.15**. Simpler polynomial fit functions based on the Vandermonde matrix approach [153] (pp. 36, 49) have been tested as well, but there especially along the displacement length, only insufficient accuracy could be achieved. Due to the curve fitting toolbox in Matlab is very efficient, actual geometric dependencies affecting the conductivity shape could be reasonably extracted allowing the FEM-fit also to be used for different length scales. For this design, if any parameter needs to be adjusted, no extra FEM model is needed and the behavior can be predicted accurately. The only parameters, which are not identified are labeled as a, b and c and most likely they are a function of the fluid properties and energy losses, which are still missing in the description. The amplitude of the conductivity is derived from the open state, which is here represented again by **Equation 6.13**. This method allows greater flexibility in adapting the conductivity shape, reduces modeling afford and measured inaccuracies can be compensated through the geometry factor. For the FEM fit function, the following equation is derived:

$$G(l_c) = \begin{cases} \left(a \cdot e^{b \cdot \frac{l_c - l_0}{l_{gap}}} + e^{c \cdot \frac{l_c - l_0}{l_{gap}}} \right) \cdot G_0 & \text{if } (l_c - l_0) < l_{gap} \\ 0 & \text{if } (l_c - l_0) \geq l_{gap}. \end{cases} \quad (6.15)$$

In **Figure 6.13 b)** it can be seen, that the exponential function of **Equation 6.15** (blue line) agrees well with the calculated finite element data points (red crosses). The fit parameters are $a = -1.6 \cdot 10^{-6}$, $b = 12.7$ and $c = -0.65$.

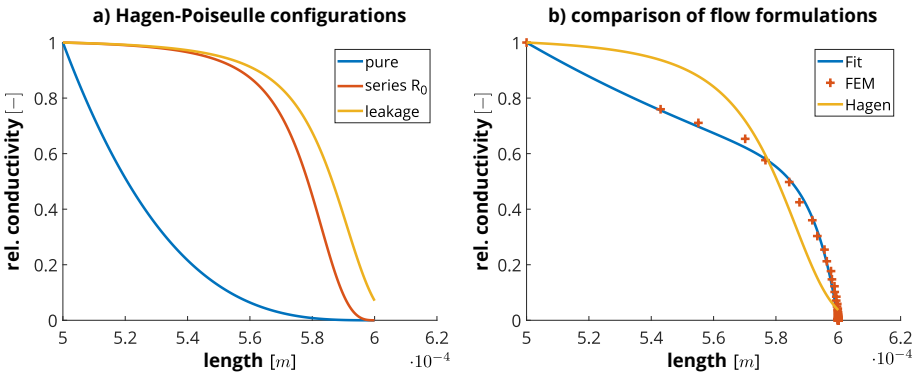

Figure 6.13: Normalized fluidic conductivity data based on Hagen-Poiseuille and FEM results.

However, if the analytic Hagen-Poiseuille plot in **Figure 6.13 a)** (blue line) is compared to the finite element fit in **Figure 6.13 b)** (blue line), it shows an obvious shape miss match. For a pure Hagen-Poiseuille function, close to the sealing stage at around $600\,\mu\mathrm{m}$, the gap distance is a close to zero number, which is then even more close zero due to the cubic power term of **Equation 6.14**. This makes conductivity changes in this area only very minimal, enhancing this flattening effect in the sealing region. If however, in the model a much higher series resistance is added, then the initial conductivity of the micro-valve is not dominate in the system. As it can be seen in the red line of **Figure 6.13 a)** the conductivity of the valve is only dominant during the almost sealed part, which significantly affects the overall conductivity and projects a path as predicted with FEM. However, still the final shape is not accurate and a closer approximation can only be achieved if a leakage is implemented (yellow line). In **Figure 6.13 b)** this yellow line is plotted, however accuracies are not satisfying.

In summary, it is demonstrated that pure analytical solutions can be adapted to the true physical behavior but it is very challenging and time consuming for complex systems. It is easier to extract characteristic parameters of complicated models from finite element simulations and transfer the results to network models or signal flow graphs for system design. The approach is referred as *combined simulations* in [133].

6.1.6 Modeling of the Fluid Flow through the Valve

In part five of **Figure 6.1**, the calculated conductivity is used to control the fluid flow of the valve. The fluid flow in channels or valves is described by the pressure-flow relationship whereby flow is the volume flow rate in this work (the mass flow rate is another option). The ratio between volume flow rate and applied pressure difference across the channel or valve is the fluidic conductance.

There are two ways to model the fluid flow in Matlab environment:

- **Simulink, using a signal flow graph:** A signal flow graph is a directional input-output relationship of physical signals. In fluidic systems, the applied pressure is usually the input and the resulting volume flow rate is the output signal. In case of the valve, the input pressure must be multiplied by the fluidic conductivity, which provides the output signal. As shown in **Section 6.2** and **6.3**, it will be difficult to model larger microfluidic systems and bidirectional interactions entirely in Simulink.
- **Simscape, using a network representation:** The pressure-flow relationship is modeled by a network representation as known from electrical engineering. Fluidic elements can directly be connected to other elements at interface ports. The fluid flow is bidirectional and both, across or flow signals can be applied at the interface ports. For instance, it is possible to connect either a pressure pump at the inlet or a syringe pump, which defines the volume flow rate. A Simscape network model for the fluid flow relationship with additional signal flow components in Simulink for the hydrogel swelling process depending on the applied stimulus has been shown in **Figure 6.1** and will be used in the following.

Figure 6.14 illustrates how to transfer Simulink model information to the network representation in Simscape. Till now, Simulink was utilized to calculate the stimulus dependent

fluidic conductivity of the valve. All Simulink model elements are shown in black, the Simscape model elements are shown in blue.

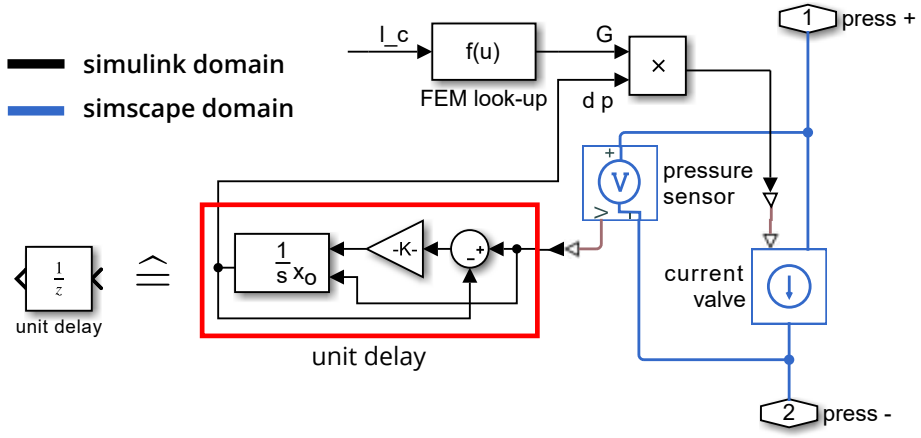

Figure 6.14: Flow model segment, which uses the Simulink domain (black lines) to implement the conductivity calculation and the Simscape domain (blue line) to implement the flow behavior of the micro-fluidic network.

The valve model in Simscape has two ports referred "press+" and "press-". The ports will be the interfaces to other microfluidic elements, such as channels, junctions, inlets (pressure or syringe pumps) or outlets, which drain the system. As known from Kirchhoff networks, each wire has an across quantity, which is pressure and a flow quantity, which is the volume flow rate.

A "pressure sensor" in **Figure 6.14** detects the pressure drop $\Delta p(t)$ across the valve and the "current valve" is a VCCS, which defines the volume flow rate for the fluidic network domain. The volume flow rate can be positive or negative, which switches the direction of the flow. The volume flow rate is the product of the fluidic conductivity calculated in Simulink and the measured pressure signal, which comes from Simscape. The volume flow rate $\dot{V}$ is defined by the following equation:

$$\dot{V}(l_c, t) = G(l_c, t) \cdot \Delta p(t). \tag{6.16}$$

Theoretically, the pressure signal obtained from Simscape must be multiplied by the fluidic conductivity calculated in Simulink and the result goes back to the voltage-controlled current source in Simscape. It forms an algebraic loop and leads to numerical issues as discussed in **Section 6.2**. It will be recommended in **Section 6.2.1**, that a unit delay model breaks the algebraic loop and leads to stable simulation conditions. A unit delay model holds and delays the input signal by one time-step. The implemented "unit delay" model shown in **Figure 6.14** consists of a sum block, a gain block, which specifies the delay time and an integrator.

The microvalve model is now ready to use in larger microfluidic systems, which will be the focus of **Chapter 7**. However, some details on system modeling are necessary to be presented in the following sections.

6.2 Circuit Descriptions Analogy for Microfluidic Applications

Modeling a hydrogel-based microvalve with signal blocks in the Matlab Simulink environment is extensively investigated in this work. The benefit hereby is the possibility to directly solve complex mathematical and differential equations within Simulink. A problem arises if different fluid elements described in Simulink will be linked together at the interface ports. In general, it is possible to model microfluidic systems or electronic networks entirely with signal flow graphs but it is difficult to realize and inconvenient. It requires a complex wiring with a lot of effort to fulfill Kirchhoff's flow conservation law at each interface node. The theoretical background and the implemented approach are shown in **Section 6.3.2**.

Alternatively, microfluidic systems can be entirely described in network simulators as LTspice. It is possible to implement the same model as a pure network description as demonstrated in [154] (pp. 402-406) [155]. The network models automatically consider Kirchhoff's flow conservation law at the interface nodes what is an essential benefit compared to signal flow graphs. However, a combination of network models with signal flow components appear most promising for modeling and simulation of microfluidic systems. The network model interface ports allow an easy and intuitive connection of library elements because now flow directions do not need to be considered. Additional, through the connected signal flow interface layer it enables an efficiently signal propagation based on advanced mathematical functions, which is necessary to model physical effects in hydrogels. Matlab offers a network description toolbox called Simscape, which has been shortly introduced in **Section 6.1.6**.

Simscape models can be combined with Simulink model components what will be investigated and discussed in the following sections.

6.2.1 Advantages and Limitations of Combined Simulink-Simscape Models

The microvalve model of **Figure 6.1** has been extended by a stimulus signal port as shown in the left of **Figure 6.15**. The stimulus port "ST" and the flow ports "press+" and "press-" are necessary to link the valve element to other components of a microfluidic system as discussed in **Chapter 7**. However, the microvalve model needs to be intensively tested regarding the accuracy and numerical stability before it can be used in larger system models.

It turned out that Simulink models and combined Simulink-Simscape models have some limitations, which are caused by the internal solver structure in Matlab. Simulink solvers are developed for transient simulations of ODE. Difficulties arise if ODEs are combined with AE in the same model. Algebraic equations describe constraints between physical signals, which are necessary to model static effects in the signal propagation chain. Static effects are defined by a gain block. The output signal follows the input signal simultaneously. There exist no time-derivatives in the differential equations and the response time and consequently the required time-step size of the solver tends to zero. Solving system models with DAE in Simulink is difficult in practice. Algebraic equations are referred "Algebraic loops" in the literature [156], [157].

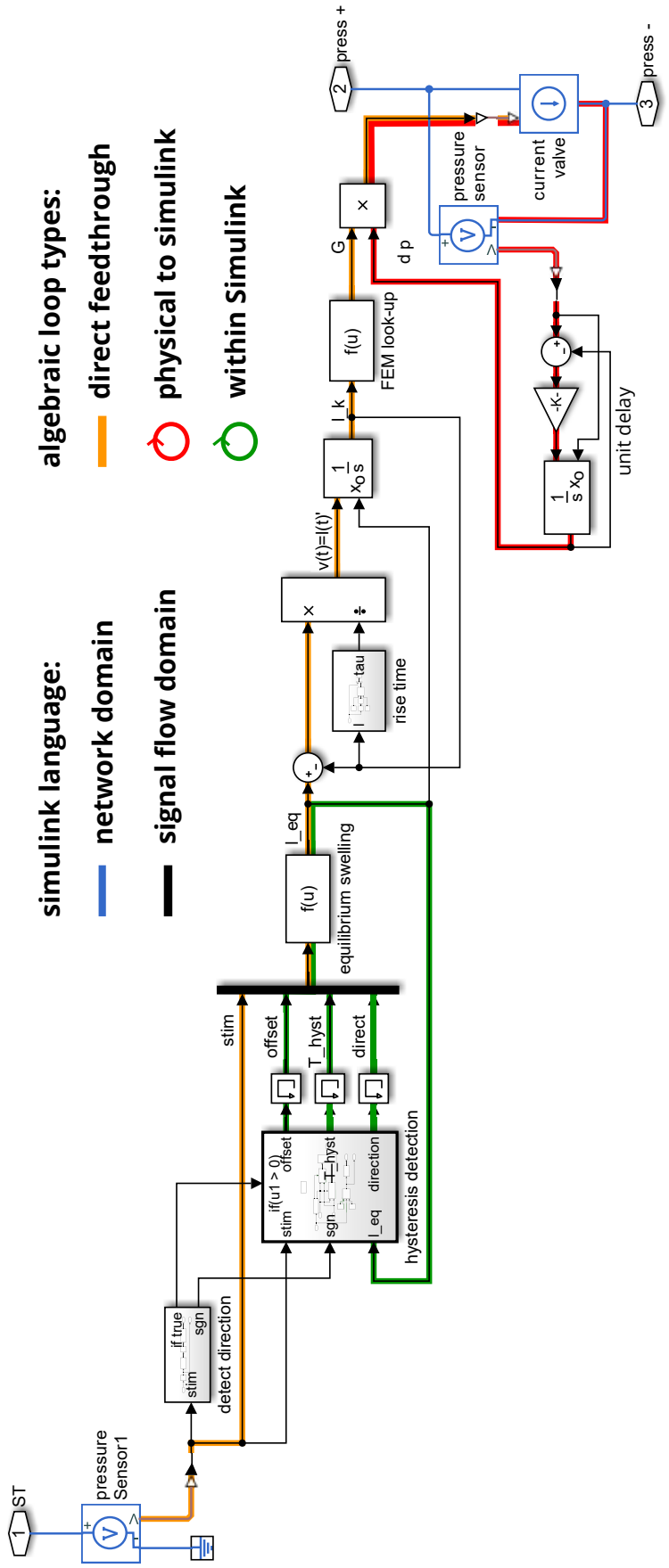

Figure 6.15: Mixed signal model combining the signal flow and network domain with highlighted algebraic loops.

In the valve model of **Figure 6.15**, two major algebraic loops occur:

- **A direct feed-through in Simulink**, which solves static equations. An example is the green loop in **Figure 6.15** where the equilibrium length of the hydrogel is calculated from an algebraic equation, which connects the output of the "equilibrium swelling" block directly with the input of the previously defined "hysteresis detection" block. The problem has been solved with the memory blocks, which create a non-direct feedthrough.
- **A direct feed-through in Simulink with Simscape library elements.** The red loop shows an example where the Simulink multiplier is connected at the output to a physical line in Simscape ("Simulink-PS Converter") and the input is taken from a "PS-Simulink Converter". The problem has been solved with the unit delay block, which creates a non-direct feed-through in Simulink.

All algebraic loops in the valve model have been eliminated by memory blocks or unit delay blocks to allow for stable simulation conditions. However, it turned out that combined Simulink-Simscape simulations have common problems if Simscape results are transferred to Simulink back and forth. The main reasons are different solver architectures and parameters such as implicit or explicit algorithms, the use of different multi-step methods for the time integration and the time-step size, which is adapted to the equations and the simulated response. The Matlab tool uses internal equilibrium iterations between solvers for the data exchange. In general, it works well if results go in one direction, either from Simulink to Simscape or vise versa.

Likewise, a bidirectional simulator coupling between Simulink and Simscape with intense data exchange works for most model settings in simulations with smooth waveforms. Numerical difficulties appeared at sudden signal changes of pulse functions or during changing model conditions, which require a very small time-step size.

To avoid numerical problems in future simulation runs, the signal flow graphs in Simulink have been entirely replaced by physical signal blocks in Simscape. Physical signal blocks are unidirectional library elements in Simscape, which work in the same way as Simulink library elements. Unfortunately, the Simscape model library is not as extensive and powerful as known from Simulink. However, all function blocks, which are necessary for microfluidic applications exist or have been adapted by user scripts in this work.

The microfluidic toolbox presented in **Chapter 7** uses only Simscape library elements for internal calculations. However, the powerful and highly advance Simulink features are still exploited for signal generation at the inputs and signal evaluation at the outputs because there is no bidirectional signal exchange between Simulink and Simscape.

In the network domain, several limitations exist as well. Here forbidden electrical circuits will cause convergence issues as well and lead to ill-defined circuits or system equations. In **Figure 6.16 a)** are two current sources in series, which will cause the weaker source to fail. In **b)** two voltage sources are in parallel with the assumption that $U_1 \neq U2$ will as well cause the weaker source to break. In **c)** a current source is placed in an open circuit condition, which causes run time errors. In terms of a microfluidic valve, the latter case happens if a syringe pump with a constant volume flow rate is connected to an ideal valve model in the swollen state. The pressure increases to infinity. The real valve creates a leakage flow due to the compressed length and leads to stable simulation results.

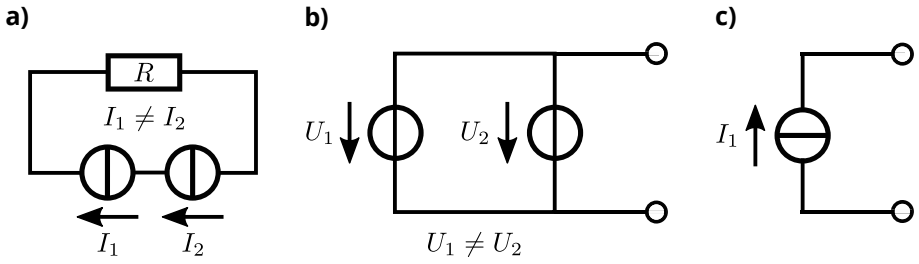

Figure 6.16: Forbidden network models for electronic circuits.

6.2.2 Requirements for Microfluidic Circuits

The main limitation of Matlab Simulink is that a bidirectional data exchange from and to Simscape library elements is numerically unstable.

Therefore, the Simulink model components of the CVPT microvalve need to be transferred entirely to the Simscape environment except model components, which are solely used for input signal settings or for signal evaluations at the output. Both, Simulink and Simscape support multi-domain simulations whereby the model components are differently color coded for better identification. In this work, the following domains are involved for modeling and simulations of microfluidic systems:

- **Signal flow domain**: The elements and connections are visualized in black and are unidirectional signals without any unit. Simulink model components are used for fluidic and stimulus source definitions. Furthermore, Simulink model components are implemented for results evaluation and visualization at the outputs.
- **Network domain** The network domain elements are visualized in blue, which is the default color for electrical networks with bidirectional signals. The fluid domain quantity pressure is mapped to the across quantity “voltage” and the volume flow rate to the quantity “current”.
- **Physical domain** The physical domain elements in Simscape are visualized in brown and are unidirectional physical signals with a specific unit. Signals can be extracted from the network domain by voltage and current sensors and can be applied to the network domain by controlled voltage and current sources.

Simscape library elements track physical domain signals based on their units. Converter blocks or other library elements only work properly if the units at the input, within the equations and at the output are consistent.

For chemofluidic logic circuits, the fluid domain is coupled to a transport domain of a stimulus. The fluid domain describes the pressure to volume-flow relationship of the solvent and the transport domain describes the concentration level and the concentration flow rate in the channel. Both domains are mapped to a voltage-current relationship in the network representation of Simscape.

Figure 6.17 shows a fluidic channel model with flow and transport domain features. The model will be discussed in **Section 7.1.2**. As known from network models, the channel element has interface ports at the left and at the right side. Since networks operate bidirectional, either one can be inlet or outlet. It depends on the applied pressure value. Furthermore, the

left and right ports are separated into the flow domain port “FL” and into the transport domain port “TR” for the stimulus signal.

It can be seen in **Figure 6.17** that the fluidic resistance of the channel element is controlled by a function block “C”, which depends on dimensional parameters of the channel and fluid properties of the solvent. The pressure drop across the channel is measured by a voltage sensor and transferred to the transport domain. Inside of the “two side delay” block are several subsystems, which describe the stimulus transport in the channel. The stimulus transport depends on the concentration levels at the interfaces and the pressure difference across the channel, which is transferred by the brown physical signal line from the flow domain to the transport domain.

Figure 6.17 illustrates that network elements and physical signal lines are necessary to describe elements of the micro-fluidic toolbox. Details are discussed in **Chapter 7**.

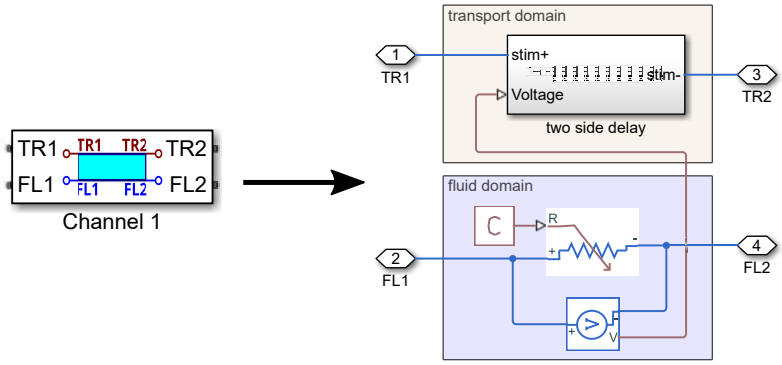

Figure 6.17: Microfluidic modeling scheme with a two-port element consisting of a fluid and transport domain layer.

Stimulus and flow sources as well as output features for signal evaluation or debugging purposes are modeled by Simulink library elements. Unidirectional coupling from Simulink to Simscape works stable. The use of Simulink allows for a large variety of stimulation settings and post-processing features at the output.

6.2.3 Graphical User Interfaces and Library Element Management

The library elements of the microfluidic toolbox must be user-friendly and accessibly by other users. In practice, characteristic parameters of channel elements or the microvalves must be adapted to new design layouts or to design modifications. For instance, the influence of dimensional tolerances, misalignments or changing solvent properties must be assigned prior transient simulation runs.

Simulink and Simscape support the programming of an interactive block mask window for user defined library elements. The mask window is mainly used to list all standard or existing design parameters of the library element, to display the associated units and to give a brief comment on the physical or technical context.

For design modifications, users can either change the mask parameter values manually or use Matlab commands in a batch mode to change parameters automatically. The batch mode is important for design optimization and case studies where a large number of layout

variants are analyzed and comparted with the target specification. Certain mask parameters can be linked to a Matlab-script, which evaluates larger functions or launches other software components to provide appropriate input data.

The source code and the underlying structure can be copied and executed on a new computer. In Matlab, a library browser is able to manage all existing Simulink and Simscape toolbox elements. The mask window includes also a help section, dependencies to other files and function blocks as well as a customized layout of each component.

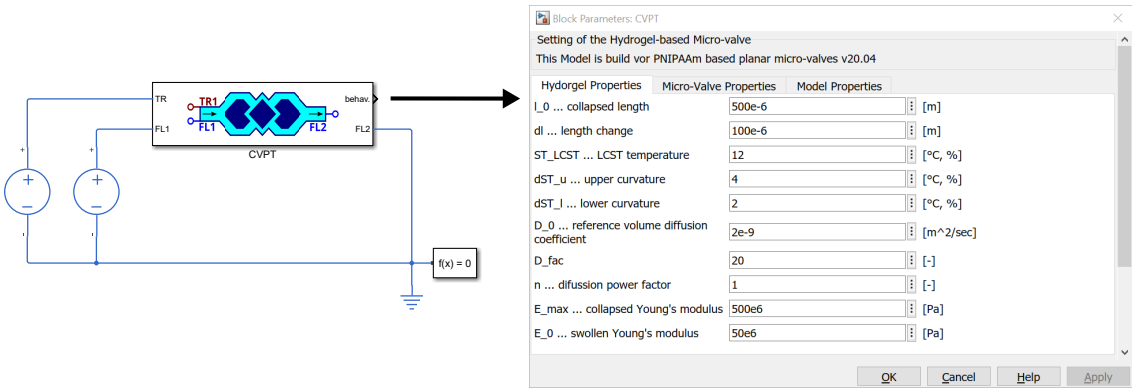

Figure 6.18: Layout concept for the microfluidic toolbox. Each custom element has a mask, where the parameters are entered in SI units.

For larger systems, Matlab supports several strategies to reuse library elements of several modifications in the same model. Multiple blocks (instances) can be referenced to the same library element with different parameter settings. It reduces the time for code generation and accelerates the simulation runs. Another important feature is a “Variant System” whereby different model configurations of the same library element can be activated prior transient simulations. Customized model configurations can be, for example, the analytical or the numerical description of the fluidic conductance of the valve.

6.3 Modeling Techniques for the Chemical Volume Phase-transition Transistor (CVPT)

In this chapter, different simulation methods are highlighted to model the chemical volume phase-transition transistor. The first model in **Section 6.3.1** is entirely based on electronic components and is implemented in the network simulator LTspice. It is highly abstracted and describes only the most important features of the valve. The second model in **Section 6.3.2** is entirely implemented in Matlab Simulink. It will be shown that micro-fluidic model elements based on signal flow graphs can be connected at the interface ports as known from electronic circuits. However, it requires a lot of modeling effort for the wiring and needs an “algebraic constraint” block for each interface node. The third model introduced in **Section 6.3.3** is entirely implemented in Matlab Simscape based on a mixed physical-network model description, which combines physical signal lines for the unidirectional data transfer and network elements with bidirectional data transfer. The last model is most promising and will be used in **Chapter 7**.

6.3.1 Network Description of CVPT

The first hydrogel-based model is implemented in the electronic network simulator LTspice. The model is published in [154] (pp. 402) and contains most essential components of the valve. It is a very good example to illustrate modeling of multiple physical domains with basic electronic network elements. It is fast and captures the general behavior of the valve. In [158] the microvalve example was extended by sigmoidal functions to describe the volume phase transition effect with a higher accuracy. The model is shown in **Figure 6.19**.

It consists of three physical domains, the thermal domain, which calculates the temperature change in the device, the polymer domain, which determines the length change of the hydrogel and a fluidic domain, which computes the flow behavior through the microvalve. The stimulus signal in the given example is the applied external temperature of the valve.

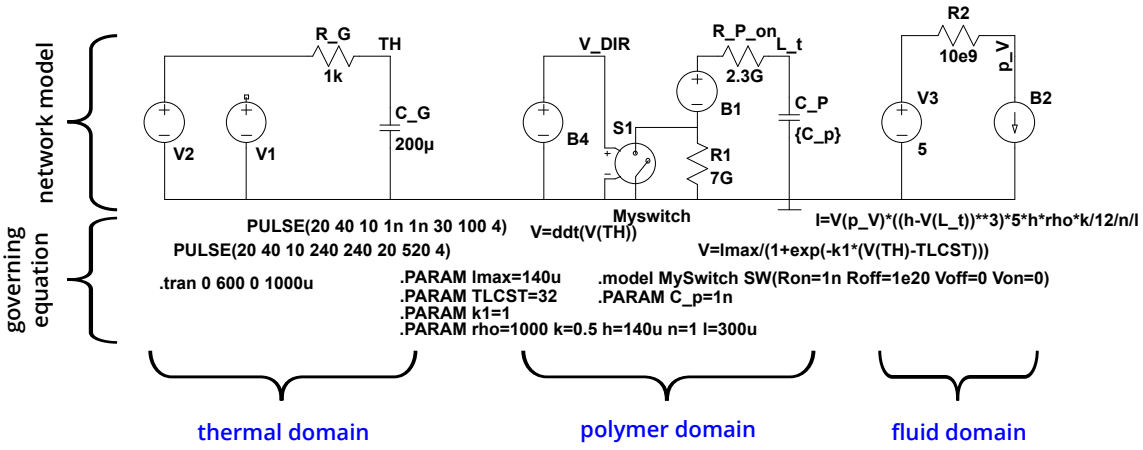

Figure 6.19: LTspice network model of the hydrogel-based microvalve.

The left segment in **Figure 6.19** describes the thermal domain, where the external temperature change (for example of a heater) propagates into the device and in particular into the hydrogel. The temperature change in the hydrogel provides the input signal for the next part of the model where the swelling behavior of the polymer is analyzed. The thermal domain is described by a first-order differential equation, which can be mapped to an RC-circuit in the electrical domain. The external temperature defines the stimulus value U_{V2} in **Equation 6.17** and corresponds to the voltage signals of source V1 or V2. The temperature change of the hydrogel U_{TH} is computed by the RC-circuit elements R_G and C_G. The temperature change U_{TH} is equal to the voltage signal across the capacitor and can be called from the LTspice database by the $V(TH)$ command whereby TH is a user defined label for the wire between R_G and C_G:

$$R_G C_G \cdot \dot{U}_{TH} + U_{TH} = U_{V2}. \tag{6.17}$$

The transient response is determined by the rise time $\tau = R_G \cdot C_G$ and forms an exponential function after a step signal as shown in **Equation 6.18**. The rise time τ defines the time duration until the average temperature change in the valve chamber reaches $63\,\%$ of the applied stimulus:

$$U_{TH}(t=\tau) = U_{V2} \cdot \left(1 - e^{-\frac{t}{\tau}}\right) = 0.6321 \cdot U_{V2}. \tag{6.18}$$

The next segment in **Figure 6.19** describes the polymer domain, where the equilibrium length change of the hydrogel $V(L_t)$ is computed from the average stimulus concentration $V(TH)$. The VCVS B1 is utilized to defined the sigmoidal function in **Equation 6.19**. The output voltage of B1 corresponds to the functions value U_{HG} in **Equation 6.19** and the control voltage is U_{TH} or $V(TH)$ in LTspice notation:

$$U_{HG} = \frac{U_{max} - U_0}{1 + e^{-k \cdot (U_{TH} - U_{LCST})}} + U_0. \tag{6.19}$$

The transient swelling behavior of the hydrogel is represented by the kinematic length change. The swelling response is likewise described by a first-order differential equation and analyzed by an RC-circuit. As discussed earlier, the rise time is different for the swelling and the shrinking process. The voltage-controlled voltage source B4 is driven by the first time derivative of the stimulus (command: $ddt(V(TH))$), which is the slope of the temperature-time function. If the slope is positive for increasing temperatures, the voltage source B4 opens the switch S1. Both resistors are in a series connection and must be added together according to **Equation 6.20**. Increasing temperatures are related to a shrinking process with a larger rise time. For decreasing temperatures, the switch is closed and creates a short circuit across the resistor R1 whereby R1 is deactivated:

$$\tau = \begin{cases} (R_P + R_1) \cdot C_P & \frac{dT}{dt} \geq 0 \\ R_P \cdot C_P & \frac{dT}{dt} < 0 \end{cases}. \tag{6.20}$$

The kinematic length l_{kin} corresponds to the voltage signal U_L at the wire marked with "L_t". The right part of **Figure 6.19** describes the flow domain of the microvalve. In this model, the Hagen-Poiseuille equation of rectangular cross-sections is used to define the fluidic conductance. In **Equation 6.21**, the conductance is multiplied by the pressure difference Δp across the microvalve, which defines the volume flow rate $\dot{V}$ as a current i:

$$i = \frac{k_0 \cdot (h - U_L)^3 \cdot 5w}{12 \cdot \eta \cdot l_{ch}} \cdot \Delta p. \tag{6.21}$$

The pressure difference across the valve is defined by the voltage source V3 and the volume flow rate is assigned by the voltage-controlled current source B2 according to integrators. It can be seen in **Figure 6.19** that a series resistor B2 has been added to the flow domain. Resistor B2 represents the remaining fluidic resistances from the inlet to the outlet of the valve model. Likewise, a series resistor has been assigned in **Section 6.1** as shown in **Figure 6.13** to improve the accuracy.

In LTspice, the microvalve behavior has been replicated and it is shown that the tool is suitable to describe microfluidic components and systems. However, it is possible but it can be difficult to model complicated effects with electrical network elements. Physical interactions are implemented by controlled voltage and current sources, which measure physical quantities in the network and calculate the output signal by mathematical equations.

From the numerical point of view, the controlled voltage and current sources act similar to

signal flow graphs or physical signals lines in Simulink or Simscape. In LTspice, the interactions are assigned by equations to the network elements, Simulink and Simscape use a graphical representation to model interactions and physical effects.

After the simulation, the data needs to be transferred to another program for plotting and data fitting. If additional simulation features such as graphical user interfaces (see **Figure 4.8**) or layout synthesis (see **Section 7.4**) are required, a flexible simulator environment is necessary. Here Matlab can fulfill all these tasks and therefore it is also recommended to directly build and develop the models within Matlab. Nevertheless, it could be demonstrated in this chapter, that the development of microfluidic circuit models is possible in LTspice.

6.3.2 Signal Flow Description of CVPT

In this chapter, the previously discussed LTspice model, is transferred to a signal flow description in Matlab Simulink with the goal to investigate the performance, advantages and limitations.

There will be two major differences between both models. First, the signal flow graph is unidirectional and second, the pressure-flow relationship of the network must be divided into separated pressure and volume flow signal lines. If network models are transferred to a signal flow graph, one must decide whether pressure or the volume flow rate will be the input. If pressure is selected as input, volume flow sources (syringe pumps) can only be defined by a controlled feedback loop. The controlled loop requires an “add” block and an “algebraic constrained” as shown in **Figure 6.21**.

The Simulink model in **Figure 6.20** visualizes all essential components of the microvalve. Similar to electronic library elements, the first port of the valve becomes the index “i” and the second port the index j. The pressure difference across the valve is assigned at the voltage ports “pressure i” and “pressure j” and the volume flow rate is calculated at the current ports “flow i” and “flow j”. Depending on the applied pressure signals, the flow response can go in both directions. Positive signs indicate a flow into the fluidic element and a negative sign that the flow comes out of the channel.

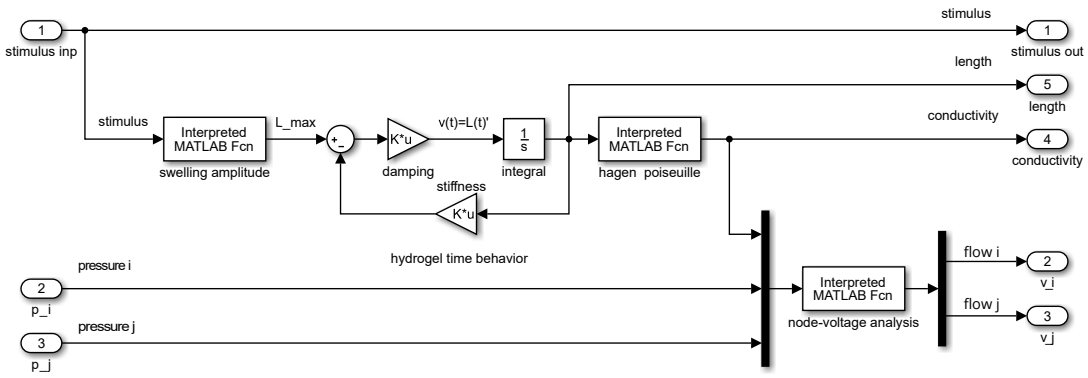

Figure 6.20: In Matlab Simulink, the microvalve behavior is now transformed to a block signal model, where the transient behavior is simulated though the integrator block and the fluid behavior is implemented though a node-voltage analysis.

The RC-circuit element, which calculates the kinematic swelling length l_{kin} in the LTspice model is replaced by a control loop as shown in the center of **Figure 6.20**. The theoretical background was introduced in **Section 6.1.3** and operates here in the same way. The hydrogel swelling with the related sigmoidal function is implemented in the "swelling amplitude" block and the fluidic conductivity is defined in the "hagen poiseuille" block.

The biggest challenge in the Simulink model is to find a proper description for the flow conservation rule at interface ports, which link several interface nodes together. In the network representation the pressure-flow relationship is defined by:

$$\begin{pmatrix} G & -G \\ -G & G \end{pmatrix} \begin{pmatrix} p_i \\ p_j \end{pmatrix} = \begin{pmatrix} \dot{V}_i \\ \dot{V}_j \end{pmatrix}, \tag{6.22}$$

where p_i and p_j are the pressure values and $\dot{V}_i$ and $\dot{V}_j$ are the volume flow rates at the interface. The coefficient G in the conductance matrix is the fluidic conductivity according to Hagen-Poiseuille. The matrix equation can be easily solved in the "node-voltage analysis" block without having to form the inverse.

The problem appears if multiple fluid elements are connected to the same node. Kirchhoff's law states that the sum of all flow components at a node must be equal to zero. This is implemented through an "algebraic constraint" block, which increases or decreased its output value until the sum of the inputs are zero. From the numerical point of view, the "algebraic constraint" forms an algebraic equation, which is solved in each time step. The calculated output value is the across quantity at the node, which fulfills Kirchhoff's law. For electrical systems, it would be the voltage at the node, in fluidic systems it is the pressure at the interface node. The computed pressure value has to be applied at all pressure ports of the fluid elements, which are attached to the node.

Kirchhoff's law and especially the sign rule shall be explained on a simple example shown in **Figure 6.21**. A volume flow rate of $10\,\mu\mathrm{l/min}$ is applied at the inlet of a junction which connects to a valve on the left and on the right. Port "j" of the left valve is referred "CVTP1_j" and the port "i" of the right valve is referred "CVTP2_i". Both ports are connected to the current source at the same node "i". The volume flow into both valves becomes $5\,\mu\mathrm{l/min}$.

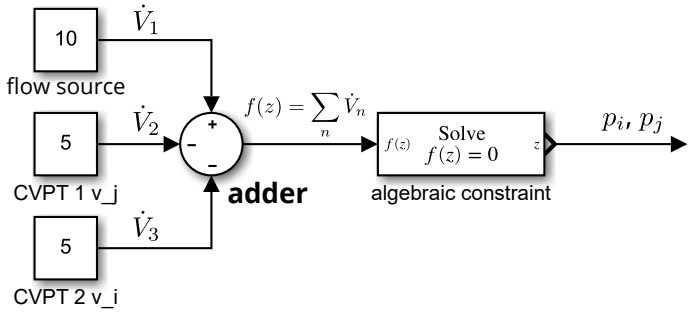

Figure 6.21: Simulink concept implementing a fluidic node by a sum-function block, which is then solved through an algebraic constraint to equate to zero by increasing the pressure of the adjacent system.

As known from electrical circuits, the volume flow is defined "positive" at the following conditions:

- **External flow:** The volume flow at inlet sources $\dot{V}_{source}$ goes into a system.
- **Internal flow:** The volume flow from a node $\dot{V}_{elem}$ goes into a library element.

Kirchhoff's law states that the flow from all external sources minus the flow to library elements must be zero:

$$\sum \dot{V}_{source} - \sum \dot{V}_{elem} = 0. \tag{6.23}$$

Kirchhoff's law can be implemented for interface nodes with the help of an "add" block, which calculates the total flow according **Equation 6.23**. All connections from external volume flow sources are added and all connections from internal library elements are subtracted at the summation point. The subsequent "algebraic constraint" calculates the pressure signal, for which **Equation 6.23** is in equilibrium. The pressure signal must be connected to all pressure input ports, which are attached to the node.

The general approach of connecting multiple fluidic library elements has been tested. **Figure 6.22** shows a series connection of two microvalves. The inlet pressure is $5\,\mathrm{Pa}$ and the outlet pressure is set to zero. The fluidic conductivity depends on the applied stimulus. The calculated volume flow rate becomes $3.89\,\mathrm{\mu l/min}$. The left ports with the index "i" provide a positive flow result and the right ports with index "j" a negative flow result. On the left, the flow goes into the valve elements and on the right, the flow comes out of the valve elements. Even larger systems can be modeled with the presented approach [47].

In summary, fluidic library elements can be modeled by pure signal flow graphs. However, the connection of interface ports is not intuitive. It requires numerous connecting wires and Simulink library elements to satisfy Kirchhoff's law. The biggest problem is that each interface node creates an algebraic loop, which has to be solved by delay blocks to guarantee stable numerical results. The implementation and investigation of a pure Simulink model is not pursued further in the work.

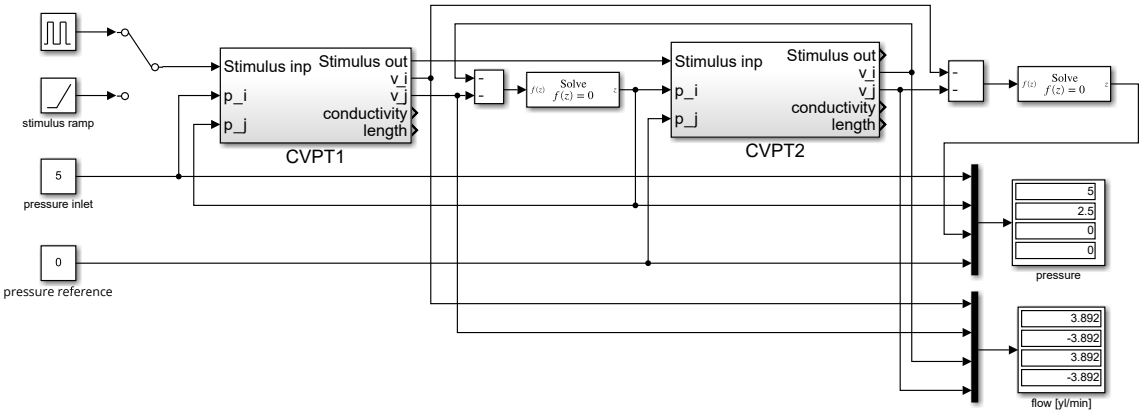

Figure 6.22: Pure signal flow model, which simulate the behavior of two microvalves in series. Thereby the pressure and flow variable are determined through a algebraic constrained function block.

6.3.3 Mixed Signal Flow and Network Model for CVPT

A third model of the microvalve has been implemented and tested with Simscape library elements. It consists of a network representation for the fluid flow and physical signal components for multi-physical effects, such as the hydrogel swelling. The modeling process is straightforward and the layout is easy to implement and understand. The model works numerically stable and can be simulated in the transient domain with high efficiency. All library elements, which are necessary for the micro-fluidic toolbox are adapted to the **mixed signal flow and network model** approach. The micro-fluidic toolbox elements are tested in several examples. It will be the focus of **Chapter 7**.

One reason for switching to Simscape are the algebraic loops in Simulink. There are several workarounds, which have been published in literature and have been investigated in the work. However, it works stable for a special class of examples but leads to problems at sudden signal changes of pulse and step functions. Another reason is that the signal routing at the interface ports is cumbersome and slows down the simulation performance.

The **mixed signal flow and network model** in Simscape uses electronic library components to model the fluid flow. This method is very powerful because the fluidic elements can intuitively be connected at the interface ports to represent a larger fluidic system. Simscape provides a large variety of library elements to model fluidic networks. The system model can either be assembled from library elements manually, by copy and paste, or in a batch mode, by Matlab commands. The later one is like writing a netlist of the model as known in electronic design automation.

For the physical signal domain exist several library elements but it is not sufficient to represent all features, which are necessary for multi-physical interactions in complex systems. However, custom equations or functions of a block can be implemented by ssc-script files. It is a special Simscape language, which allows do define physical effects, to assign and modify parameters and to create physical connections between elements. The implemented features are processed by the compiler and create implicit differential algebraic equation (DAEs). The ssc-script design language is similar to Verilog-A or VHDL-A code.

Contrary to the signal flow description within Matlab Simulink, creating multiple instances of the same custom component does not require multiple instances of the ssc-description file. Therefore, the transition of the implemented micro-fluidic toolbox to a new computer system is done by simply coping a library folder along with all the examples. It works automatically on different systems, which is important for the reuse and distribution of the developed code.

Chapter 7

Micro-Fluidic Toolbox

content of chapter

In this chapter, the modeling and simulation of chemofluidic logic circuits will be presented. The ultimate goal is a microfluidic toolbox which can be used to assemble larger chemo- and microfluidic systems from basic library elements. Similar approaches are widely used in electronic design automation where circuits are represented by parametric electronic components, which are described by physical quantities at the interface ports. Each interface port is defined by an across quantity, which is a voltage and a flow quantity, which is a current.

In the following, a similar approach will be utilized for micro-fluidic networks. Essential elements like sources, channels, junctions and valves are needed to predict the functional behavior of complex fluidic logic circuits. Microfluidic components comprise multiple physical domains what makes modeling and simulation complicated. It will be shown that the microfluidic toolbox is vital for the rapid prototyping process. Advanced models can be created in shortest time even by less trained users. The accuracy and efficiency can be adapted to special needs by using analytical terms for the conceptual design, by adapting parameters from finite element simulations for more detailed investigations or by replacing design parameters from experimental results after manufacturing of real-world prototypes.

7.1 Microfluidic Components

In this section, essential microfluidic components which are used to simulate logical chemofluidic circuits are introduced. Challenging in the simulation of logical chemofluidic circuits is that all elements consist of a fluid domain with a pressure-flow relationship and a transport domain where a stimulus quantity with a certain concentration level propagates through the system. Both physical domains are unidirectionally or bidirectionally coupled. In most cases, the volume flow of the fluid domain affects solely the propagation of the stimulus concentration referred unidirectional coupling. This is common for channels and junctions. More complicated are bidirectional interactions where the concentration level acts backwards onto the fluid flow through a concentration triggered change of the fluidic resistance. This happens for hydrogel-based microvalves, which are discussed in **Section 7.1.4**.

Microfluidic elements have not only fluid domain input and output quantities, such a pressure and volume flow, but additionally transport domain properties. The fluid domain proper-

ties are modeled by generalized Kirchhoff networks using analogy considerations. The problem arises from modeling the transport domain, which requires additional stimulus quantities that can be the concentration level of ions, the concentration of chemical substances or simply the temperature of the fluid at the inputs or within the system. A general view on both models is shown in **Figure 7.1**.

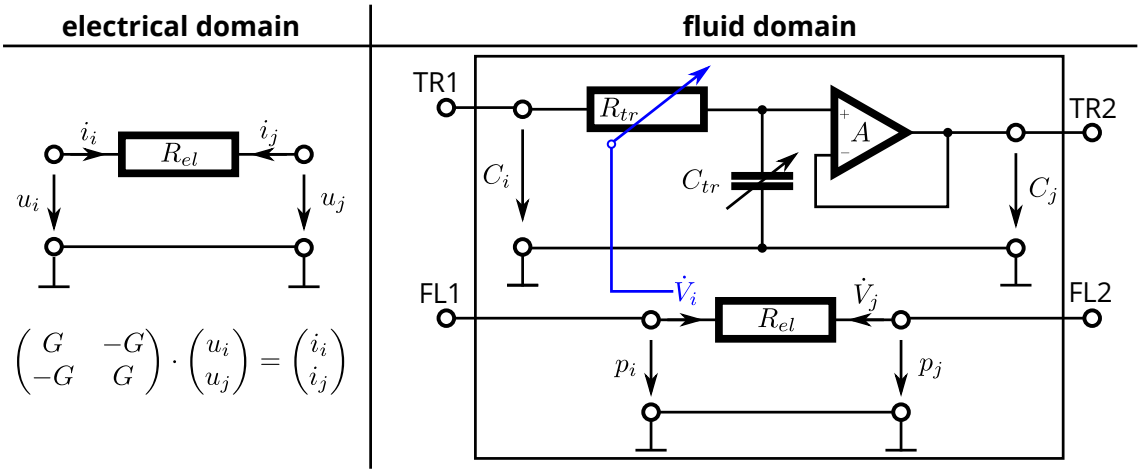

Figure 7.1: A basic electronic domain element compared to a microfluidic channel with fluid (FL) and transport (TR) domain quantities. The fluid and transport domains are here unidirectionally coupled.

Microfluidic circuits can be efficiently modeled in Matlab Simulink and in Matlab Simscape. Simulink provides features for a signal-flow representation and Simscape for a generalized Kirchhoff network with across (voltage) and flow quantities (current). Both types of model representations can be combined in order to take advantage from both fundamental simulation methods.

The fluid domain is efficiently modeled by Kirchhoff networks in Matlab Simscape because the pressure-flow relationship can directly be mapped to a voltage-current relationship. The fluidic resistance of micro-channels corresponds to the electrical resistance of a wire or a resistor. Junctions of channels or resistor networks appear automatically by linking interface nodes of channels together as known from electronic circuit design. Active components like valves are similar to transistors and can be represented by controlled voltage or current sources such as, voltage-controlled voltage sources (VCVS), voltage-controlled current sources (VCCS), CCVS or CCCS. Appropriate data for the controlled source can be defined by fit functions (curve fitting) or lookup tables. Beside to Matlab Simscape, further commercial simulation tools are LTspice, Cadence or Mentor Graphics.

However, several model features are easier accessible by signal-flow graphs in Simulink. Signals can be processed by a large variety of mathematical operations such as multiplication, summation, integration, differentiation or using arbitrary user defined functions with single or multiple inputs. Of course, electronic design languages as Verilog-A or VHDL-A provide likewise mathematical functions for signal evaluation and processing. The main advantage of Matlab Simulink is the huge variety of toolboxes and library elements for customized models and their solver efficiencies.

The fluidic toolbox is based on the following declarations:

- **Fluid domain:** The across quantity is a pressure level and flow quantity is a volume flow rate.
- **Transport domain:** The across quantity defines the concentration level implemented as a voltage signal and the flow quantity defines the ion-flow rate implemented as a current signal. The concentration level can alternatively be implemented by a directional signal flow using Simulink blocks or by directional physical signal lines in Simscape.

In practice, the stimulus transport can go in forward and backward directions, which is difficult to realize in simulation tools. The problem is obvious for models with directional signal lines in Simulink and Simscape, which must be switched to a second path to model the backward flow. The same difficulties can also appear in generalized Kirchhoff networks, which are inherently bidirectional. For instance, delay lines shown in **Section 7.1.2** are typically modeled by active low-pass filters. This type of electronic circuit works only in one direction, not just in the computer model but also in practice. Engineering applications have a fixed input-output relationship. In microfluidic applications, delay lines and other components must work in both directions, which will be shown in the next chapters. In contrast to the fluid domain, the transport domain requires switches to capture the true physical behavior in forward and backward directions of the stimulus.

7.1.1 Fluid Sources and Stimuli Sources

For each microfluidic network, sources need to be defined for flow and stimulus functions in order to evaluate the functional behavior of fluidic components and their interactions in the global device or system environment. Sources represent signals of different physical domains but are mapped by analogy relationships to voltage and current sources in Simscape. For the **fluid domain**, voltage sources (across quantity) are pressure pumps, and current sources (flow quantity) are fluidic syringe pumps, which deliver a user defined volume flow rate. For the **transport domain**, voltage sources are utilized to apply the stimulus signal for the concentration level at the inlet as a boundary condition. Current sources for ion-concentrations are seldom used in practice.

It should be noticed that all across quantities are related to a ground potential. At least one ground potential must be defined for the fluid domain to avoid numerical issues. For instance, if a fluidic system is driven by syringe pumps at all inlets, at least one node must be set to ground. It is usually the output of the experimental test bench, which is set to ambient pressure and represents the drain outlet.

Typical sources for engineering applications are DC-sources for time independent values, AC-sources for sinusoidal quantities and transient sources such as step, pulse and ramp signals. Arbitrary other user defined functions are possible. Signals can be superimposed for simulation runs.

In **Figure 7.2**, three typical signal types for characterizing a fluidic component are shown on the left. The first function is a sinusoidal function, which depletes with an exponential function around the LCST. The next source is a pulse signal block, which also can be utilized to generate a step function or to approximate a Dirac delta function. The last signal type is the ramp signal, which is used to mimic a constant decrease and increase of a signal (triangle

wave). In the last case, a negative slope is defined to decreasing a stimulus for the first half of the simulation time and then, through the zero crossing and the absolute block, to increase the signal for the second part of the simulation period.

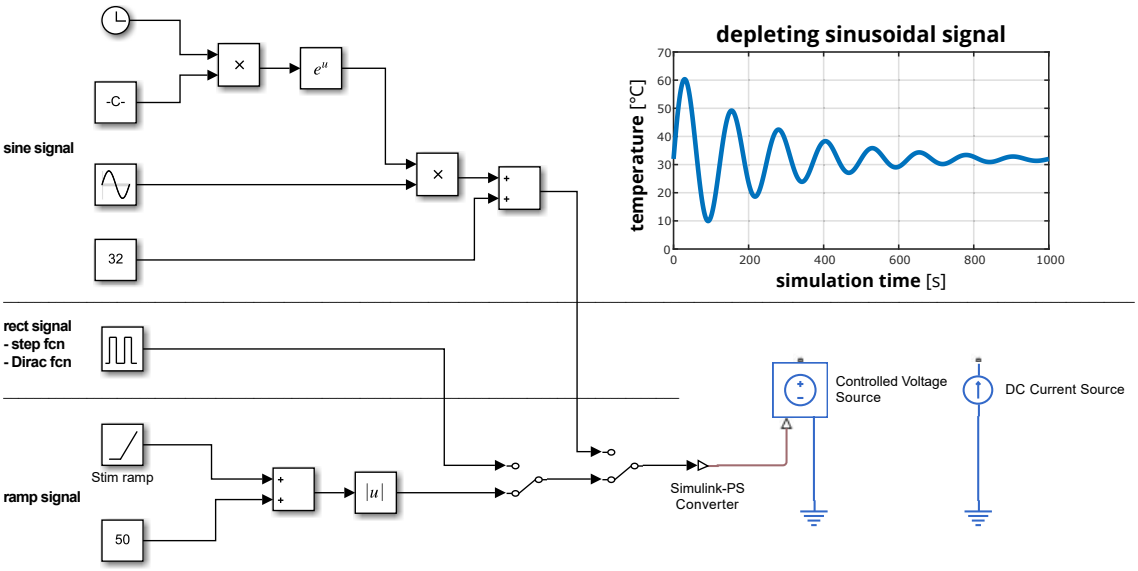

Figure 7.2: The applied source functions are described in the Simulink domain and the results are transferred to Simscape as input for the controlled sources. The syringe pump is modeled as a current source and the pressure pump is modeled as a voltage source.

7.1.2 Fluidic Resistor with Bidirectional Stimulus Transport

The first element of the microfluidic toolbox is a **Channel** element. It replicates the fluid flow and the stimulus transport in a micro-channel. The channel element has bidirectional interfaces on each side, which are either input or output depending on the direction of the fluid flow. The flow domain is defined by the interface ports FL1 and FL2 whereby their across and flow quantities provide access to the pressure-flow relationship. The flow domain is entirely described by the fluidic resistance. In microfluidics with liquid media, the inertial and compressive properties of the fluid can be ignored, which means, that the flow follows instantaneous the pressure changes and behaves like a static system.

The transport domain is defined by the interface ports TR1 and TR2, which are likewise bidirectional. Thereby the direction of the port is determined by the sign of the fluidic volume flow. This direction change is automatically recognized and adapts the internal configuration by switches, which can occur multiple times during transient simulations. The system inlets and outlets of the user model must be treated differently. All system inlets must be linked to a stimulus source of the type voltage to provide a user defined concentration level for the ingoing flow. The system outlets must be set to ground to drain the system.

A vital feature of the transport domain is to account for the delay time of the concentration flow. The average delay time depends on the average volume flow velocity, the diffusion coefficient and the channel volume. In the model, the average volume flow velocity is calculated from the fluidic resistance and the pressure difference. Caused by the viscosity of the

medium and adhesion effects at walls, the fluid velocity within channels is not uniform. For channels with circular cross-sections, the maximum velocity at the center is twice as large as the average velocity. Similar values can be found in literature for rectangular cross-sections [159] (pp. 359). On the other hand, the fluid velocity of layers, which are close to the channel walls tends to zero. Consequently, the stimulus does not simply propagate through the channel with the average speed of the fluid flow. In practice, first changes of the concentration can be observed earlier at the outlet, theoretically at about $50\,\%$ of the expected delay time, as calculated from the average flow velocities. Short pulse or half sinusoidal stimulus functions flatten out as they propagate through the channel what leads to mixing effects. Even with finite element tools, it has been shown that it is still very difficult to accurately predict the microfluidic flow and the true mixing behavior [6].

The implemented approach to model the transport behavior takes the above considerations into account. First, the transport delay based on the average propagation speed approximates the stimulus motion through the channel and second, short pulses flatten out over time but guarantee the conservation of the total stimulus concentration level. The implemented model is based on a series of active low-pass filters as proposed in [160]. Furthermore, the model is extended by signal line switches to account for different flow directions.

Conservation of the total stimulus concentration level means that the integral of the stimulus calculated over time must be identical at the inlet and at the outlet if media propagate through the channel. Consequently, the area below of the concentration over time functions must be identical even for curves, which flatten out. The library element of the channel and input parameters of the mask are shown in **Figure 7.3**.

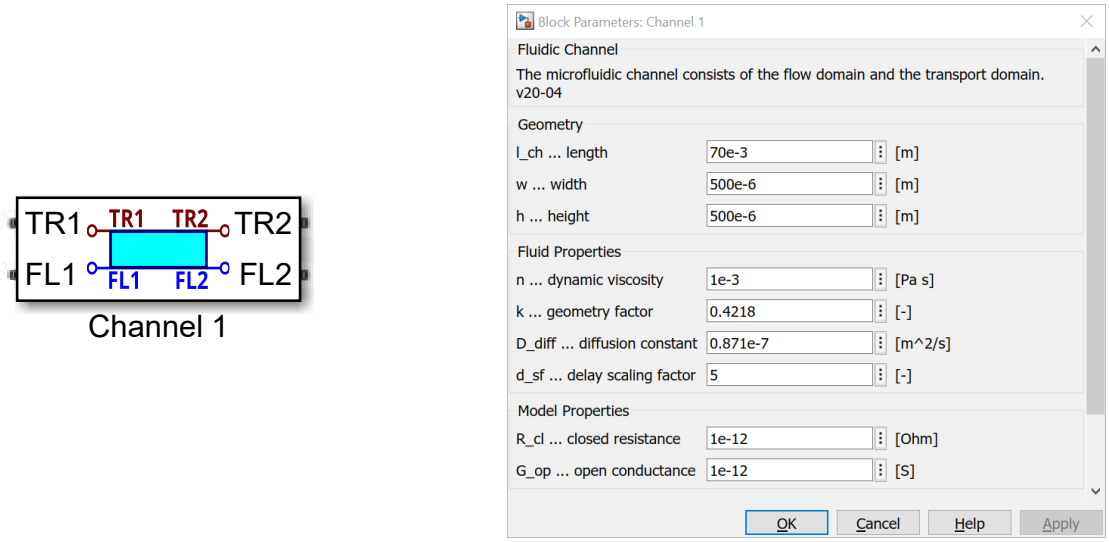

Figure 7.3: The layout of the library element channel and related model input parameters.

In **Table 7.1** the design parameters of the channel element are listed exemplarily. It starts with dimensional parameters, which are the channel length l_{ch}, the width w and the height h of the channel. It is followed by fluid properties such as the dynamic viscosity η and the diffusion coefficient D_{diff}. At the end of the mask are parameters to adapt model specific properties. It is the geometry factor k, the delay scaling factor d_{sf}, the closed resistance R_{cl} and open

conductance G_{op} of the switches used in Simscape. The default value of the geometry factor k is defined through **Equation 6.12** but can be modified to user defined numbers. The default delay scaling factor d_{sf} is set to 5, which is often measured for ethanol triggered PNIPAAm. Changing the closed resistance R_{cl} and open conductance G_{op} values might be necessary to improve the solver performance.

Table 7.1: List of parameters used to determine the fluidic resistance and stimulus delay.

parameter	Symbol	Value	Unit
geometry parameters			
mean channel length	l_{ch}	$1 \cdot 10^{-3}$	m
channel width	w	$500 \cdot 10^{-6}$	m
channel height	h	$500 \cdot 10^{-6}$	m
fluid properties			
dynamic viscosity	η	$1 \cdot 10^{-3}$	$\mathrm{Pa\,s}$
geometry factor	k	0.4218	-
ethanol-water diffusion coefficient	D_0	$0.871 \cdot 10^{-9}$	$\mathrm{m^2/s}$
time delay scaling factor	d_{sf}	5	-
model properties			
closed resistance	R_{cl}	$1 \cdot 10^{-12}$	Ω
open conductance	G_{op}	$1 \cdot 10^{-12}$	S

In general, the microfluidic resistance of channels can only be described exactly by analytical terms for circular and elliptical cross-sections. Any other shape, such as rectangular cross-sections, which are considered in the following, is approximated from the Hagen-Poiseuille equation. Thereby the Hagen-Poiseuille equation requires a numerical solution of the Poisson's equation to calculate the local fluid velocity within the channel and those results have to be integrated across the rectangular channel to calculate the average flow velocity needed for the fluidic resistance [161]. Poisson's equation can be solved for arbitrary cross-sections by a 2D heat flow analogy with FEM-tools and integrating results is supported by FEM post-processing commands. The numerical approximation leads to a geometry factor k, which depends on the ratio of channel width to height. For rectangular channels, results correspond exactly to **Equation 6.12**. Consequently, the fluidic resistance is defined by:

$$R = \frac{\Delta p}{\dot{V}} = \frac{12 \cdot \eta \cdot l_{ch}}{k \cdot h^3 \cdot w}. \tag{7.1}$$

Equation 7.1 is implemented in the constant source block "C" shown in **Figure 7.4**. The output of the source block is connected to the variable resistance element and transfers the user defined fluidic resistance to the channel representation. The pressure drop across the resistance is routed to the transport domain and provides information about the flow direction and the average volume flow rate. For channel elements, it is a unidirectional domain coupling of the information between the flow and the transport domain but the flow and transport between ports are bidirectional.

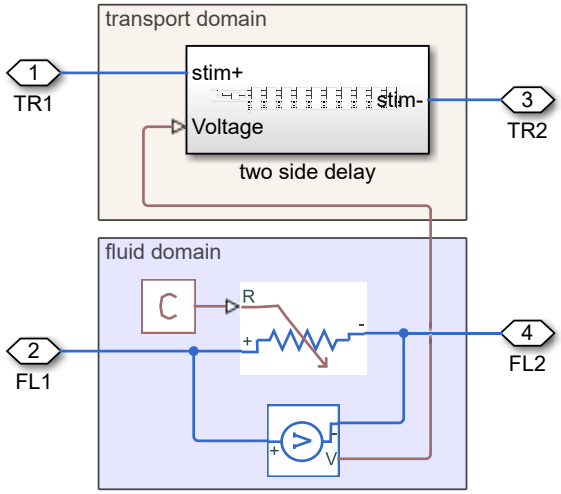

Figure 7.4: Model of the flow domain, which is unidirectionally coupled with the transport domain.

As a next step, the transport behavior is introduced. The transport delay is based on a series of active low-pass filters as shown in **Figure 7.1**. Each low-pass filter element consist of an RC-circuit and a voltage buffer realized by an operational amplifier. In total, ten chain elements are implemented in each channel whereby multiple channels can be linked together to mimic different cross-sections or larger delay lines. Each low-pass filter element is described by a first-order partial differential equation:

$$\tau \cdot \dot{C}(t) + C(t) = C_0(t), \tag{7.2}$$

where $C_0(t)$ is the concentration level at the input, $C(t)$ the calculated concentration at the output and τ the delay time between each element. τ is the product of the resistance and the capacitance.

Using a series of active low-pass filters for the transport equation to resolve the spatial distribution of the stimulus was introduced in [160]. Hereby, the fluid channel is discretized in a finite number of volumes and each volume is represented by an RC-circuit. As indicated in **Figure 7.1** the RC-circuit of subsequent chain elements are charged by voltage-controlled voltage sources (VCVS). It takes the current voltage potential from the previous capacitor and applies it to the next RC-circuit whereby each chain element is galvanically isolated. It is very important that no current flow goes to the next chain element as shown in **Figures 7.8**.

In contrast to previous work, the implemented channel element allows for a bidirectional stimulus transport. Furthermore, the model parameters are calculated automatically and the channel element can be taken from a library and transferred to user models by copy and paste.

Bidirectional fluid flow is realized by voltage-controlled switches, which change the signal path in forward and backward directions. In the Simscape model, the switches are driven by voltage signals what is the reason that the pressure drop across the element is evaluated to determine the flow direction and not the volume flow. If the voltage drop across the resistance is positive, then the fluid and the stimulus travel from left to right. The switches

recognize a true state and move to the upper position. If false, the switches are down and the stimulus transport goes from right to left during transient simulation runs. It is very important that the forward and backward paths take the same capacitances to pick up the voltage level. Separated capacitances would create jumps in the voltage signal after the chain switches the direction.

In **Figure 7.5**, a model with two chain elements is presented exemplarily. Switches are normally OFF (false) as shown in the figure. A positive pressure drop across the channel activates all switches to the ON position (flip upwards) and the stimulus transport is routed from left to right. All voltage-controlled voltage sources have a gain factor of $A_V = 1$ and the delay time is specified by the parameter τ, which is assigned to the RC-circuit elements. The very first capacitor of each direction path does not contribute to the delay line. It acts as a decoupling element as known from electronic circuits and stores the input voltages, which are needed after the chain switches directions.

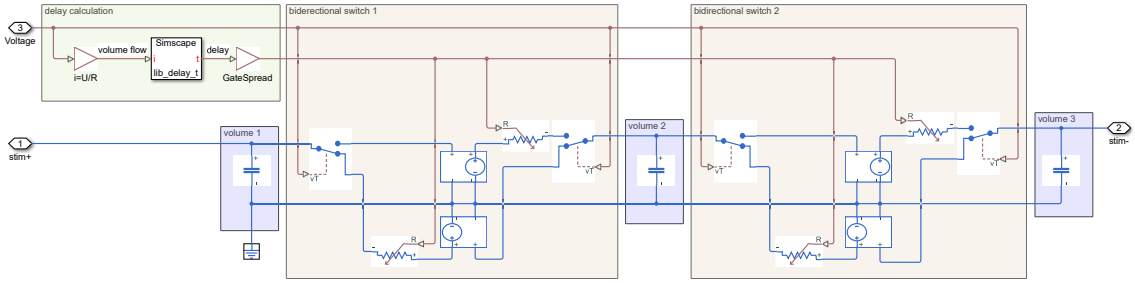

Figure 7.5: Reduced model of the transport domain with two active low-pass filter elements.

The delay time of active low-pass filters is primarily related to the rise time τ of the RC-circuits. The parameter τ represents the time needed to charge a capacitor to about $63\,\%$. Depending on the expected accuracy, the settling time can be defined 3τ where $95\,\%$ charging is reached or 5τ with $99.3\,\%$. Charging is always related to an ideal voltage jump at the input. In the following, the delay scale factor d_{sf} will be set to 5 and n_c is the number of elements in the chain. The delay scale factor can be changed in the model mask as shown in **Figure 7.3**:

$$\tau_e = \frac{t_D}{d_{sf} \cdot n_C}. \tag{7.3}$$

As a next step, the time delay t_D needs to be determined for two different scenarios. In a first case, the transport delay t_{trans} is based on the average volume flow velocity. This case happens if the average flow velocity is larger as the diffusion velocity. Here the transport delay is calculated from the total volume of the channel V divided by the current average volume flow rate $\dot{V}$ as shown in the following equation:

$$t_{trans} = \frac{V}{\dot{V}} = \frac{l_{ch} \cdot h \cdot w}{\dot{V}}. \tag{7.4}$$

In a second case, the transport delay t_{diff} is based on the diffusive behavior, where the diffusion coefficient D_{diff} (unit $\left[\frac{m^2}{s}\right]$) describes the concentration flow within the volume at applied stimulus gradients. The transport delay depends quadratic from the channel length l_{ch} [152] (pp. 92):

$$t_{Diff} = \frac{{l_{ch}}^2}{D_{diff}}. \tag{7.5}$$

In the Simscape model, a custom library block is used to calculate the time delay. An if-condition switches between flow-based and diffusion-based stimulus transport. The transport delay of **Equation 7.4** is set true if $t_{trans} < t_{diff}$, which happens for the following condition:

$$\dot{V} > \frac{w \cdot h \cdot D_{diff}}{l_{ch}}. \tag{7.6}$$

Equations 7.4 to **7.6** are implemented in the Matlab-script and can be summarized as:

$$t_D = \begin{cases} \frac{l_{ch} \cdot h \cdot w}{abs(\dot{V}) + n_0} & \text{abs}\left(\dot{V}\right) > \frac{w \cdot h \cdot D_{diff}}{l_{ch}} \\ \frac{{l_{ch}}^2}{D_{diff}} & \text{else} \end{cases}. \tag{7.7}$$

It should be noticed that a small zero threshold tolerance n_0 is added in the first part of **Equation 7.7**. It is necessary because Simscape solves all system model equations in each time step independent whether they are used or not. If-conditions are evaluated after calculating the block data, which leads to singularities for zero volume flows during transient simulation runs. **Figure 7.6** shows schematically how a concentration profile within the channel shifts to the right.

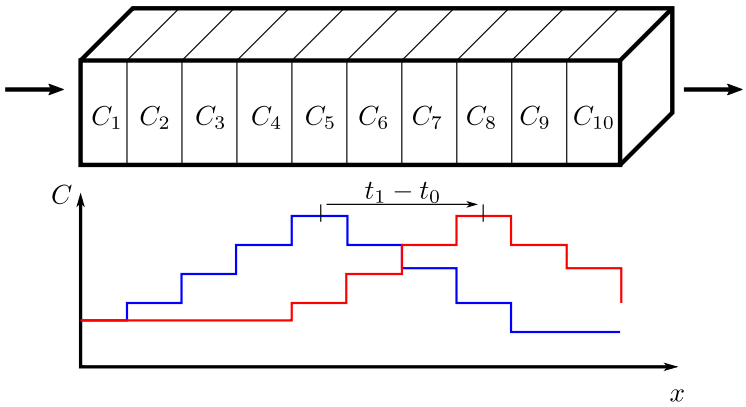

Figure 7.6: Scheme of a rectangular microfluidic channel, which is discretized into 10 volume elements. Each volume element holds a certain concentration value, which is passed to the neighboring volume element. The diagram shows an idealized shift of the concentration distribution along the channel at time t_0 (blue) and at time t_1 (red).

The previous example illustrates an idealized delay line. In **Figure 7.7** the active low-pass filter is modeled with ten volume elements and a total delay of 300 seconds. The left blue curve shows the stimulus function at the inlet and the right orange curve shows the stimulus response at the outlet. Additional curves in between visualize the stimulus functions at internal nodes. It can be seen how the stimulus wave propagates through the channel and that the spacing between curves is equidistant. Sharp slope changes at pulse functions get smooth as expected. The half sine wave on the right illustrates that short stimulus functions decrease their peak amplitudes. Concentration changes at the outlet can be observer earlier

as specified by the delay time. Furthermore, the overall concentration stimulus widens along each volume element. The time integral of each stimulus function is identical and validates the conservation of the ion-concentrations in the model.

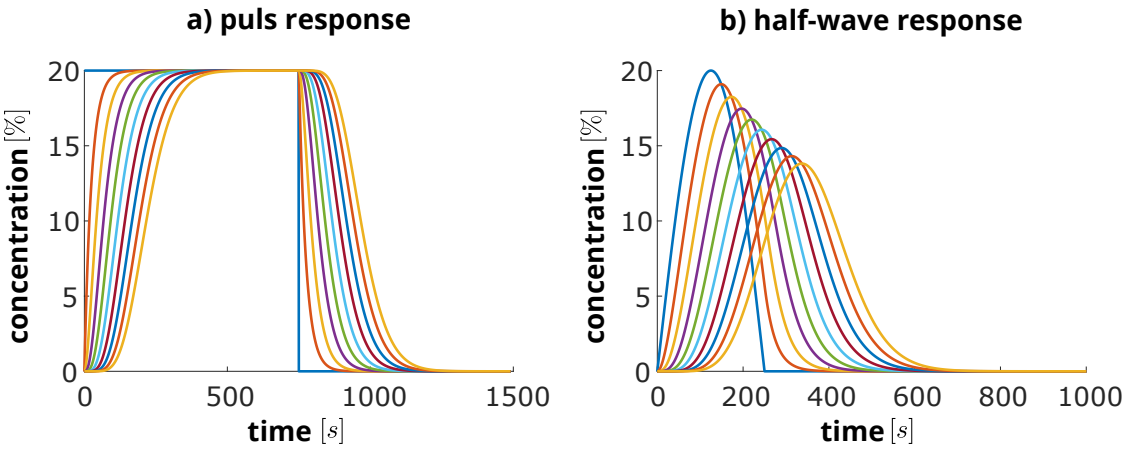

Figure 7.7: Stimulus response of the transport model for a constant time delay of 300 seconds. a) shows the stimulus response curves for a pulse function and b) for a half sine wave.

In the previous example, each volume element is galvanically isolated through a voltage-controlled voltage source. For comparison, the model is analyzed with the same parameters but the RC-circuit elements are directly connected to the next one. The RC-based transmission line is also called n-th order passive low-pass filter and is extensively described in [162] (pp. 30-39). However, the model does not provide the targeted shift of stimulus curves as shown in **Figure 7.8**.

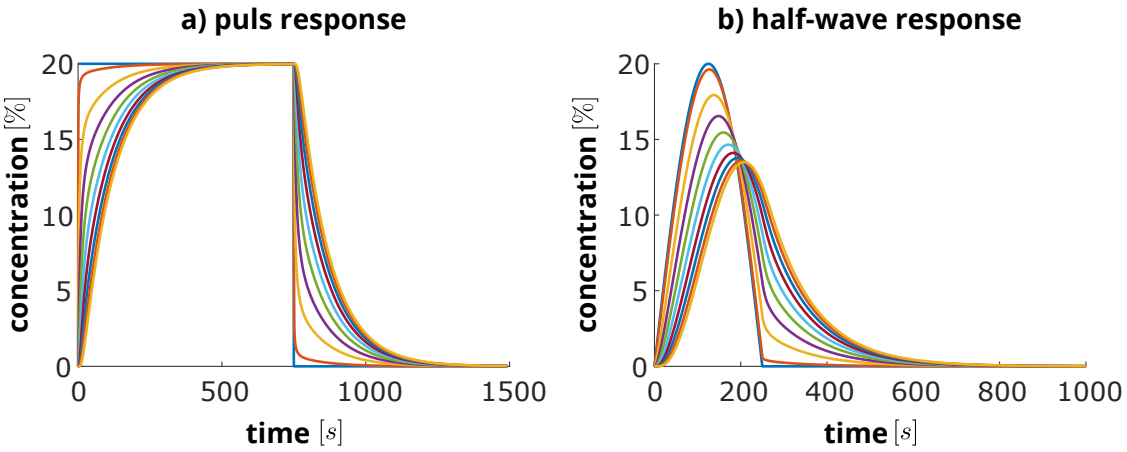

Figure 7.8: Stimulus response of the RC-based transmission line without galvanic isolation for a) a pulse response and b) a half-wave response.

In a third example, a standard library element of Simulink and Simscape, the transport delay block, is implemented in the channel element of the micro-fluidic toolbox. A series of transport delay blocks move the stimulus function defined at the inlet with a perfectly identical delay from one volume element to the next one. Results are shown in **Figure 7.9**.

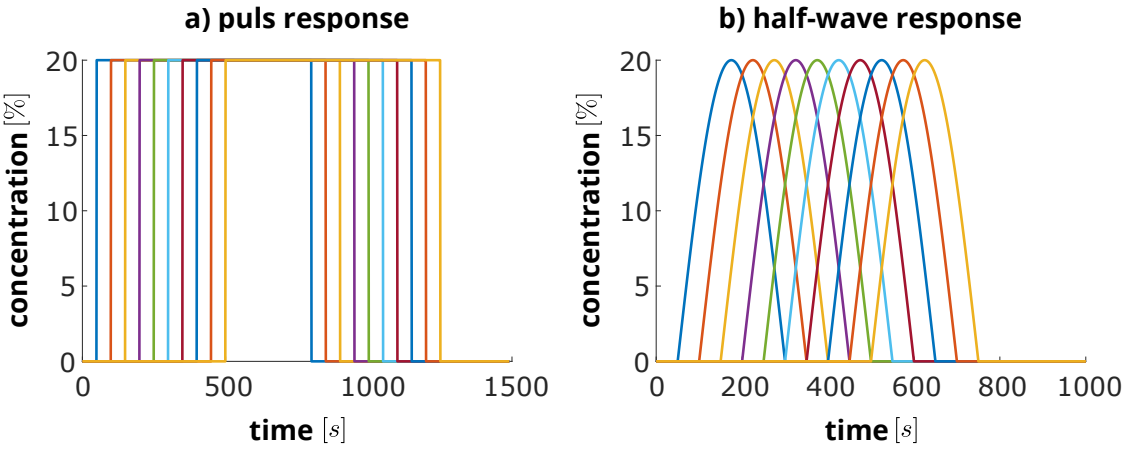

Figure 7.9: Stimulus response of the channel element based on the transport delay library element of Matlab for a) a pulse response and b) a half-wave response.

Both, Simulink and Simscape provide only unidirectional signal-block elements to model the transport delay. If the direction of a signal changes, there is no access to the internally saved data. Even with two signal lines, each facing in opposite directions, jumps in the resulting signal occur since internal signal values are not accessible by users. Another disadvantage is that the mixing behavior of the previously discussed examples can hardly be implemented. The build-in library element is interesting for a special class of micro-fluidic applications but restricts a lot of interesting features, which are possible with active low-pass filters used in the following applications.

7.1.3 Junctions

The next element of the microfluidic toolbox is a **Junction** element. In microfluidics, junctions are used to merge or to distribute the fluid flow and the stimulus signal from or to different channel elements. A junction with three ports is implemented in the toolbox and if more are needed, then the junction can be cascaded. The primary goal of the junction is to determine the fluid flow and stimulus level, which is transferred to the outlet port(s). In the following example, a T-junction is considered where two inlets with $\dot{V}_1$ and $\dot{V}_2$, and one outlet $\dot{V}_3$ exist. The flow rate $\dot{V}_3$ of the outlet is determined by Kirchhoff's law with:

$$\dot{V}_3 = \dot{V}_1 + \dot{V}_2. \tag{7.8}$$

Kirchhoff's law is automatically implemented for the fluid domain by using the classical network theory. No custom elements are required. In contrast, the resulting stimulus at the outlet C_3 is not only depending on the applied stimuli C_1 and C_2, but also on the corresponding volume flow velocities $\dot{V}_1$ and $\dot{V}_2$ with:

$$C_3 = \frac{C_1 \cdot \dot{V}_1 + C_2 \cdot \dot{V}_2}{\dot{V}_1 + \dot{V}_2}. \tag{7.9}$$

Equation 7.8 and **7.9** describe only one special case. For the transport domain of T-junctions, there are six different configurations possible, which have to be implemented

and configured separately. These are logical combinations of one input and two outputs and vice versa, two inputs and one output. Additionally, zero value input flows on all ports need to be considered to avoid numerical singularities. In contrast to the fluid domain, the transport domain needs a special treatment of all cases since only input flows contribute to the stimulus transport at the outlet(s). All these configurations require an algebraic equation with if-conditions to calculate the stimulus for the output port(s). These if-conditions distinguishes if a port is an inlet or an outlet port. Consequently, junctions which allow a changing input-output functionality during operation require conditional equations and voltage-controlled switches in the Simscape model representation.

An example model for a typical junction is shown in **Figure 7.10**. Here, each port is accompanied with a channel element and an applied pressure source. The fluidic resistance of all channels is $R_{fl} = 3.2 \cdot 10^{10}\,\mathrm{Pa\,s/m^3}$. Port 1 forms the outlet. The ground is connected to port 1 to drain the microfluidic system. Port 2 is an inlet with a pressure level of $7.5\,\mathrm{Pa}$ and a concentration level of $20\,\%$. Port 3 is also an inlet with a pressure level of $10\,\mathrm{Pa}$ and a concentration level of $10\,\%$. From the electrical point of view, the T-junction forms a star connection of resistors with a pressure value at the center of $5.8\,\mathrm{Pa}$. **Figure 7.10** shows the model layout as well as the result data such as volume flow rates (in $[\mathrm{m^3/s}]$) and the stimulus levels (in $[\%]$) at all ports.

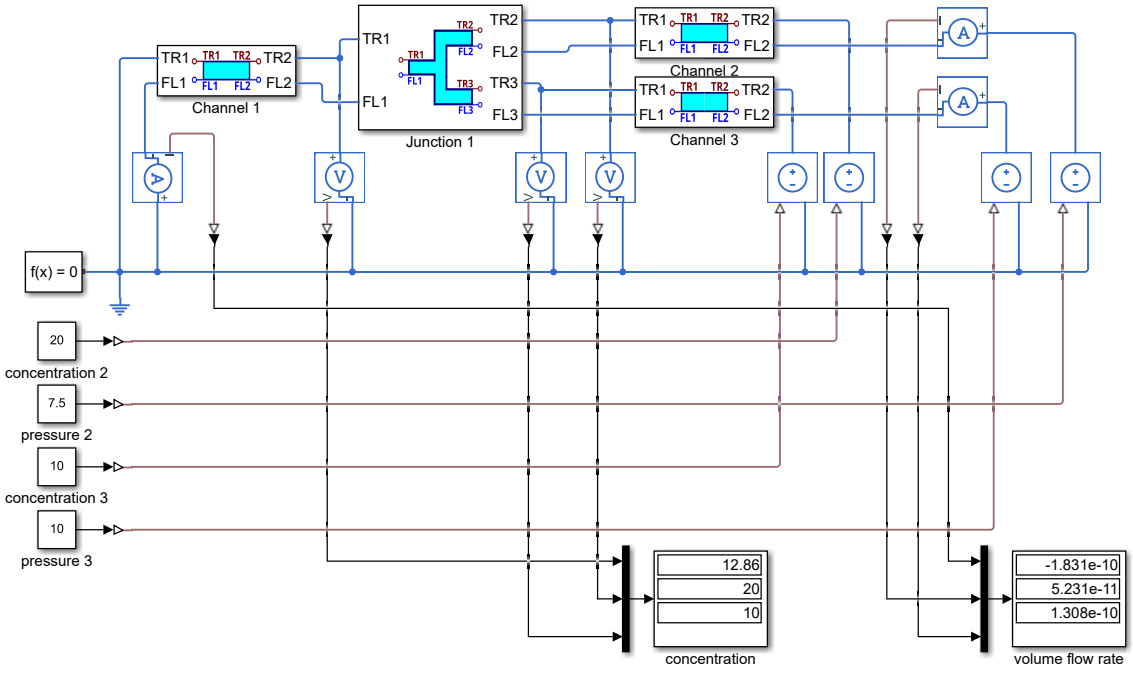

Figure 7.10: Example model of a junction element with two input and one output port. Pressure loads and stimulus sources are applied at the inputs and the concentration and volume flow rate is observed at the output.

In the following, Kirchhoff's law will be applied to model the transport domain. Three controlled current sources are utilized to calculate the concentration level, which contributes from each port. The currents are non-zero for input ports with positive volume flow rates. Currents of output ports are set to zero by if-conditions realized by switches in the Simscape model. All currents are superimposed at a reference node in the network representation.

The total current is identical to the concentration level at the outlet(s). In order to provide a voltage signal at the outlets, the total current goes through a unit resistor in **Figure 7.11**. The voltage drop across the unit resistor is finally transferred to all output ports by voltage-controlled voltage sources. The following equations show the mathematical terms used for the voltage-controlled current sources:

$$i_1 = \frac{C_1 \cdot \dot{V}_1 \cdot (\dot{V}_1 \geq 0) \cdot (C_1 \geq 0)}{\dot{V}_1 \cdot (\dot{V}_1 \geq 0) + \dot{V}_2 \cdot (\dot{V}_2 \geq 0) + \dot{V}_3 \cdot (\dot{V}_3 \geq 0) + (\dot{V}_1 \leq 0)(\dot{V}_2 \leq 0)(\dot{V}_3 \leq 0)}, \tag{7.10}$$

$$i_2 = \frac{C_2 \cdot \dot{V}_2 \cdot (\dot{V}_2 \geq 0) \cdot (C_2 \geq 0)}{\dot{V}_1 \cdot (\dot{V}_1 \geq 0) + \dot{V}_2 \cdot (\dot{V}_2 \geq 0) + \dot{V}_3 \cdot (\dot{V}_3 \geq 0) + (\dot{V}_1 \leq 0)(\dot{V}_2 \leq 0)(\dot{V}_3 \leq 0)}, \tag{7.11}$$

$$i_3 = \frac{C_3 \cdot \dot{V}_3 \cdot (\dot{V}_3 \geq 0) \cdot (C3 \geq 0)}{\dot{V}_1 \cdot (\dot{V}_1 \geq 0) + \dot{V}_2 \cdot (\dot{V}_2 \geq 0) + \dot{V}_3 \cdot (\dot{V}_3 \geq 0) + (\dot{V}_1 \leq 0)(\dot{V}_2 \leq 0)(\dot{V}_3 \leq 0)}, \tag{7.12}$$

$$i_c = i_1 + i_2 + i_3. \tag{7.13}$$

Equation 7.10 to **7.13** are implemented in a custom function block shown in the center of **Figure 7.12**. To variable operate each input, additional if conditions are needed to disable or enable a ports influence based on the volume flow, e.g. $\dot{V}_1 \geq 0$ and the concentration level $C_1 \geq 0$. For example, if *true* then a 1 value is created and if false then a 0 value is created, essentially disabling the term.

The current outputs of that function block provide the stimulus signal for all three ports. Exemplarily, the signal routing is shown for port 1 in **Figure 7.11**. If the volume flow rate at port 1 is positive the switch is activated and flips down. Port 1 transfers the volume flow rate and the stimulus signal at the brown wires to the custom function block. The output of the custom function block (signal i_1) is routed at the right brown wire to the controlled current source and contributes to the total stimulus of all outlets. If port 1 becomes the outlet, the volume flow rate is negative and the switch stays in the OFF position as shown in **Figure 7.11**. The voltage-controlled voltage source transfers the total concentration level, which is measured at the reference node to the across quantity of the port 1.

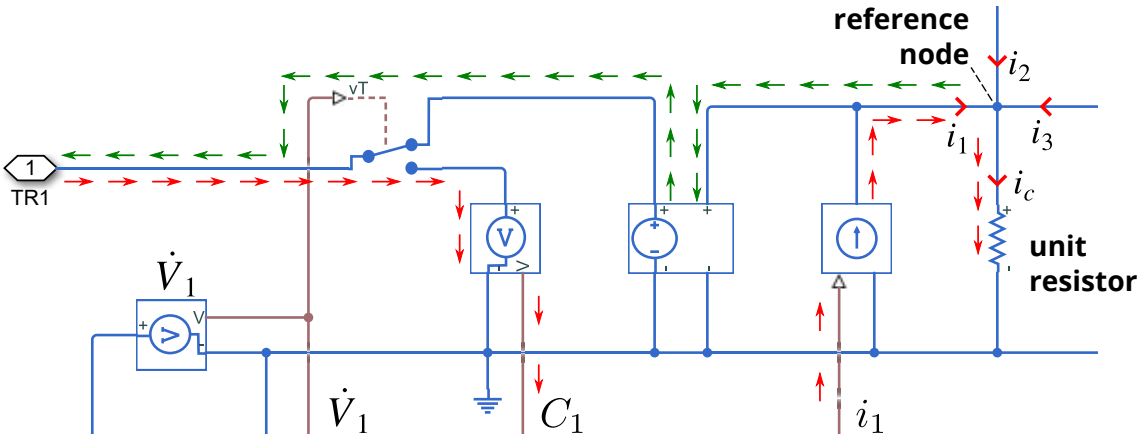

Figure 7.11: The figure shows the switching functionality of the transport domain model at port 1. The switch flips down (true position) if the port forms an inlet. Otherwise it stays in the upper position and forms an outlet port.

The model of **Figure 7.11** is expanded for all three ports as shown in **Figure 7.12**.

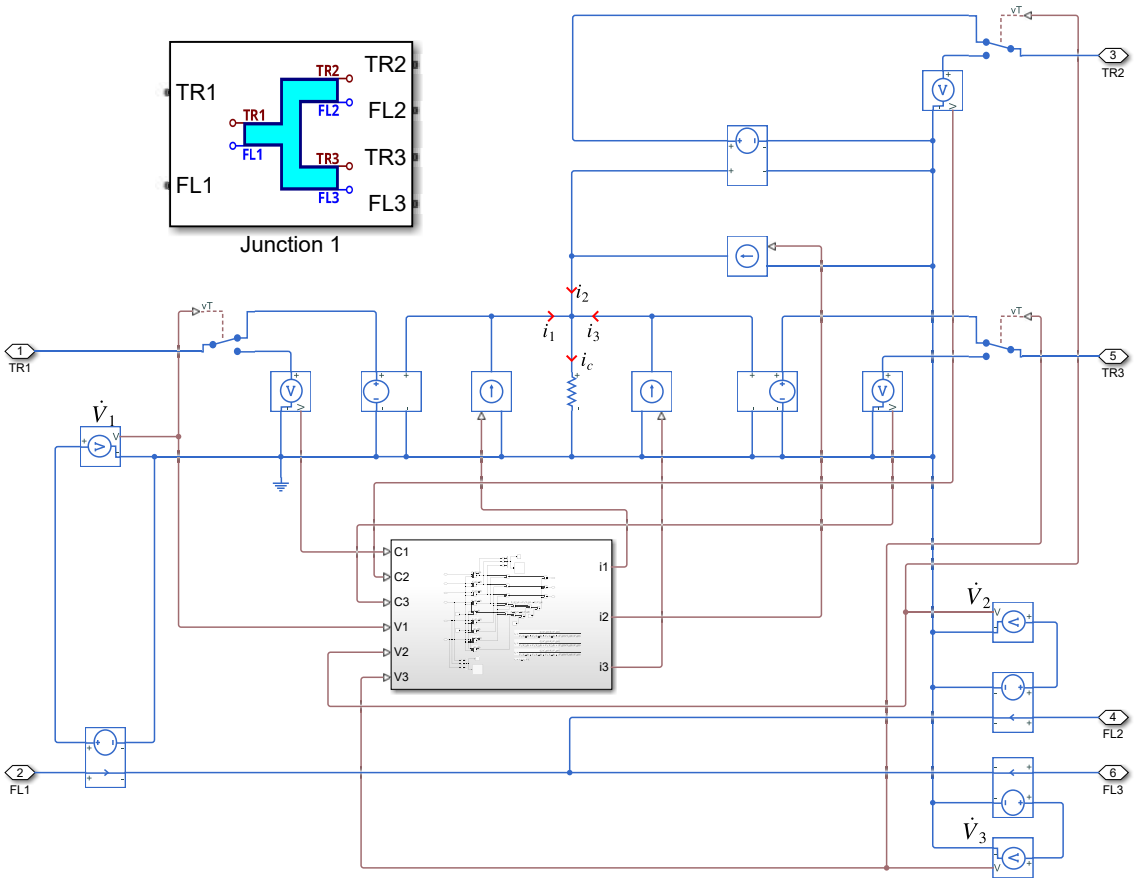

Figure 7.12: Model of a junction element with three ports. Each port provides flow and transport domain interfaces.

The junction element can directly be connected to stimulus sources, to channel elements or to chemical transistors, which are discussed in the next chapter. Junction elements have no fluidic resistance. Hence, a pressure load at junctions without channel elements creates infinite volume flow rates. Furthermore, the junction element assumes ideal mixing. For microfluidic applications, channel elements should always be attached to the ports of junction elements to provide smoother stimulus response functions at the outlets and to account for realistic mixing effects [6]. Junction elements do not require any user defined parameters.

7.1.4 Chemical Volume Phase-transition Transistor

The last element of the micro-fluidic toolbox, which is the most essential component in chemofluidics is the hydrogel-based microvalve. The valve element behaves like a transistor in electrical engineering and can be used to control the current flow between two ports (source and drain) depending on a signal at a third port (gate). For chemofluidic applications, the stimulus signal of the transport domain controls the fluidic resistance of the valve and consequently the volume flow rate in the fluid domain. One can see a clear similarity to transistors. If the fluid flow is reduced or even blocked, the stimulus transport is also affected

what leads to bidirectional domain coupling in the library element. From the physical point of view, the valve is a chemical volume phase-transition transistor (CVPT). The general behavior has been explained earlier and essential model components were introduced in **Chapter 6**.

The valve element is shown in **Figure 7.13**. On the left is the custom library element and on the right are user parameters to adapt model features. The ports "*TR*", "*FL1*" and "*FL2*" describe the transport and flow domain. In contrast to the proposed layout in **Section 6.2.2**, several internal parameters of the valve are passed to a block-signal description with the output "*behav.*" for results evaluation and debugging purposes.

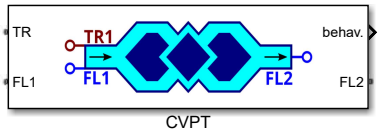

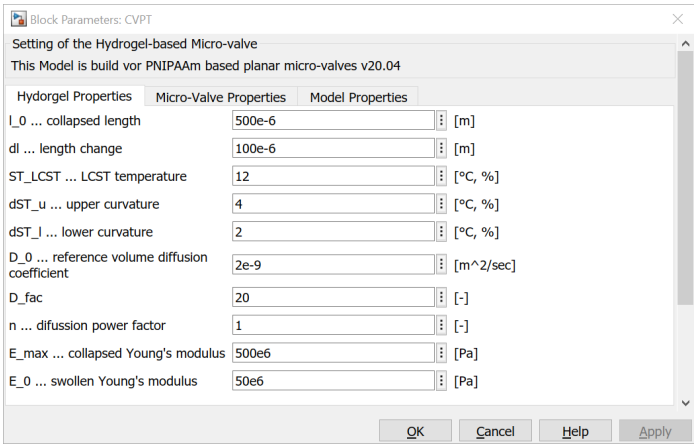

Figure 7.13: The layout of the library element valve and related model input parameters.

Table 7.2 lists user defined parameters, which are necessary to modify the behavior of the microvalve. The parameters comprise properties of the hydrogel, the valve dimensions, fluid properties and model settings.

Table 7.2: List of parameters used to determine the microvalve behavior.

parameter	Symbol	Value	Unit
Hydrogel properties			
collapsed state	l_0	$500 \cdot 10^{-6}$	m
length change	dl	$100 \cdot 10^{-6}$	m
lower critical solution temperature	ST_{LCST}	12	°C, %
upper curvature distance	dST_u	4	°C, %
lower curvature distance	dST_l	2	°C, %
reference volume diffusion coefficient	D_0	$2 \cdot 10^{-9}$	m^2/s
diffusion factor	D_{fac}	20	-
collapsed Young's modulus	E_{max}	$500 \cdot 10^6$	Pa
swollen Young's modulus	E_0	$50 \cdot 10^6$	Pa
microvalve properties			
mean flow length	l_{ch}	$4.8 \cdot 10^{-3}$	m
gap between hydrogel and wall	l_{gap}	$80 \cdot 10^{-6}$	m
fluid properties			
dynamic viscosity	η	$1 \cdot 10^{-3}$	Pa s
model properties			
geometry factor	k	0.75	-

The valve model corresponds to the model presented in **Section 6.1**, which has been intensively discussed and investigated. However, it turned out that a signal transfer between Simulink and Simscape should not go back and forth. In general, it works but slows down the simulation runs and can cause convergence problems caused by algebraic loops. The valve model of **Chapter 6** has been reworked and signal-flow lines in Simulink are replaced by physical signal lines in Simscape. The physical behavior of both modeling features can be described in the same way but models and the syntax of equations are different.

The modified valve library element is shown in **Figure 7.14**. It will be used to demonstrate the transistor like behavior in three examples, which follow in **Section 7.3**. Hysteresis effects are neglectable for these applications and related model components are removed to improve the performance in further simulation runs.

The Simscape model of the valve consists of four sections:

- **Part 1** calculates the equilibrium length of the hydrogel depending on the stimulus concentration according to **Equation 7.14** (block “lib_valve_static”). Furthermore, the block “diff” calculates the slope of the stimulus signal, which is necessary to calculate the time constant for the volume change of the hydrogel. The time constant is different for swelling and shrinking as shown in **Equation 7.16**.
- **Part 2** calculates the transient change of the hydrogel length. The kinematic length is calculated from a first-order differential equation and is modeled by a low-pass filter.
- **Part 3** calculates the stiffness change of the hydrogel depending on the kinematic length (block“lib_valve_Emod”). Furthermore, the block “lib_valve_comp” calculates the elastic compression and contact pressure of the hydrogel based on the pressure signal and the calculated stiffness value.
- **Part 4** calculates the fluidic resistance based on the hydrogel expansion (block “lib_valve_resist”). The fluidic resistance at different swelling states is extracted from FE-data, which are represented by a fit-function as shown in **Section 6.1.5**. The block “lib_valve_gr” limits the travel range at closing gaps.

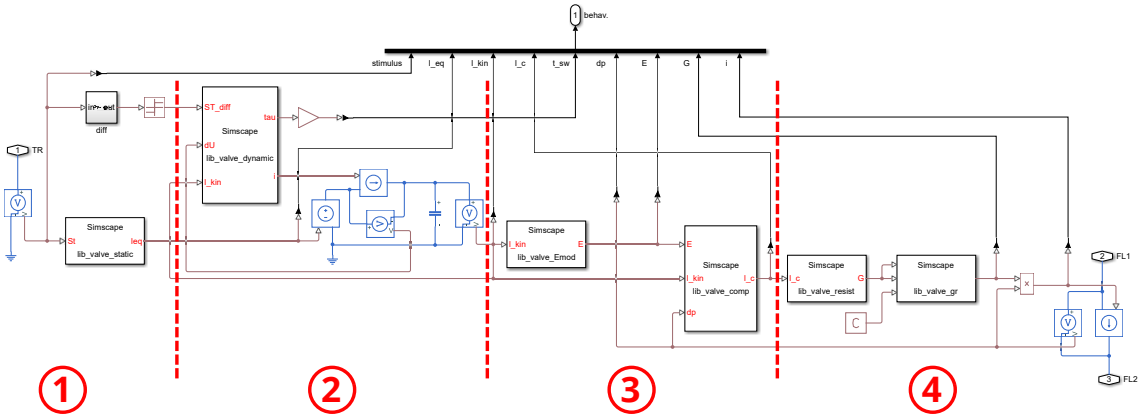

Figure 7.14: The network based chemical volume phase-transition valve library element.

Some necessary changes of the valve model will now be explained on a few examples. Simulink uses signal flow lines and user defined function blocks. In contrast, Simscape uses physical signal lines for unidirectional signal transfer. The following example shows how to

calculate the equilibrium length and the kinematic length of the hydrogel depending on the stimulus concentration. In a first step, the stimulus value is detected by a voltage sensor, which takes the across quantity from the network model and copies the information to the physical signal line. The stimulus value provides the input signal for the following volume-phase change equation defined in a custom function block:

$$l_{eq}(C) == \left(\frac{dl}{1 + \frac{1}{1+e^{-\frac{5}{dC_u}\cdot\left(\frac{C}{\{1,'V'\}}-C_{LCST}\right)}} + 0.5 \cdot e^{\frac{5}{dC_l}\cdot\left(\frac{C}{\{1,'V'\}}-C_{LCST}\right)}} + l_0 \right) \cdot \{1,'V'\}\,. \tag{7.14}$$

There are two differences in Simscape compared to Simulink functions. First, equations are defined by two equal signs in a row ("==") and second, units of all terms in the equations must be consistent. In **Equation 7.14**, the stimulus parameter is provided with a voltage unit, which needs to be canceled out since all other parameters of the equation are unitless. The result must be a voltage again whereby the unit is added at the end of the above term.

Another example where the source code must be changed are parts with time derivatives. Simulink has a library element for derivatives, which does not exist in Simscape. Derivatives in Kirchhoff networks can be calculated with a unit capacitor and controlled voltage and current sources. The unit capacitor calculates the time derivative of a voltage signal and the current through the capacitor is transferred to the output by a current-controlled voltage source. Derivatives are more difficult to realize in a physical signal line model. **Figure 7.15** illustrates the concept, which is implemented in the "diff" block for the valve in this work. It requires an "add" block, a "gain" block and an "integrator" block. It solves a first-order differential equation with a time constant, which is equal to the time-step size t_{step}. The output signal for the derivative is taken directly between the gain block and the multiplier block.

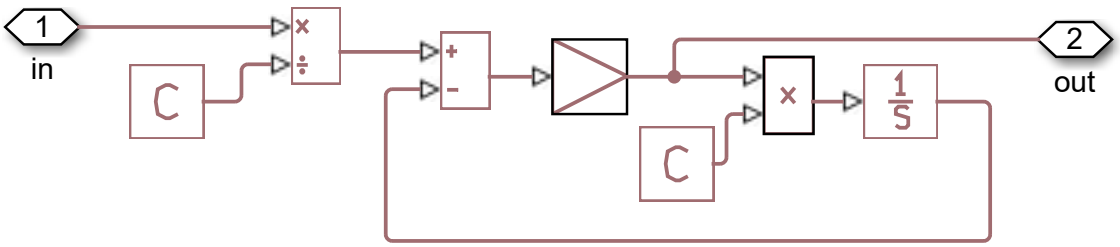

Figure 7.15: Physical block-signal model, which is used to calculate time derivatives in Simscape.

Figure 7.15 solves the following first-order differential equation:

$$\frac{\partial C}{\partial t} = \frac{C_n - C_{n-1}}{t_{step}}, \tag{7.15}$$

whereby τ is equal to the time step size t_{step}, C_n is the input signal and C_{n-1} the signal value of the previous time step. The "C-blocks" are necessary for unit conversions. Derivatives are approximated from the signal change during the last time step. Smaller deviations of the

result are not critical because the element is only used for detecting the forward and backward directions in the custom element "lib_valve_dynamic.ssc". The custom element finally calculates the time constant τ of the system based on the following if-condition:

$$\tau = \frac{\left(\frac{l_{kin}}{\{1,'V'\}}\right)^{(2-3n)} \cdot l_0^{3n}}{D_0} \cdot \begin{cases} b & \frac{dST}{dt} > 0 \\ 1 & \frac{dST}{dt} \leq 0 \end{cases}. \tag{7.16}$$

The time constant it transferred to the RC-circuit, which calculates the transient response of the hydrogel swelling process. The equilibrium length is the input voltage of the RC-circuit and the kinematic length is the voltage across the capacitor at the output. The capacitance is set to one (unit capacitance) and the time constant τ is assigned to the resistor. In part two of the model, the resistor is replaced by a controlled current source, which leads to the same physical behavior but allows infinite resistance values. Part two shows how information of physical signal lines can be transformed back to quantities of the network representation using controlled current sources. The controlled current source is implemented by:

$$i = \frac{U}{R} = \frac{\Delta U_i}{\tau}. \tag{7.17}$$

In summary, due to the implementation of the new valve model in the network domain, the algebraic loop issues do not exist, which improves significantly the performance of the model. All four sections are redesigned from the numerical point of view. Simulink based signal flow lines are replaced by physical signal lines, which are recommended for implicit solvers used in Simscape. On the other hand, the theoretical background and the implemented physical equations are identical to **Section 6.1**.

7.2 Microfluidic Matlab Toolbox

The examples in this chapter illustrate that the new micro-fluidic toolbox strongly shortens the development cycle of microfluidic systems. It is a very important step towards computer-aided design automation for a new class of systems where microfluidic components are coupled with a stimulus transport. The library elements presented in **Section 7.1** allow for modeling and simulation of a large variety of logic fluidic systems. The first example in the following will be a chemofluidic NAND gate, which demonstrates that the toolbox is able to investigate model components for digital microfluidic systems. The next example is a chemofluidic decoder, which translates the concentration level of a stimulus signal into a series of discrete output values. It is similar to an analog to digital converter in microelectronics and can be used to give notice at critical concentration levels of chemical substances. Typical applications could be safety related systems, process control in micro analytics or health monitoring systems based on a lab-on-a-chip. The third example is a chemo-fluidic oscillator. In contrast to widely known oscillators for mechanical or electronic systems, it creates a periodic change of a stimulus signal and the related flow rate. The oscillator parameters can be controlled in a wide range by the dimensional design of the microfluidic components. Chemo-fluidic oscillators can be used for various devices in chemical, biological or medical applications [163]–[165].

Modeling and simulation for design and optimization of microfluidic components is complicated and needs a lot of experience. The design is strongly related to the manufacturing process and the cleanroom capabilities. Furthermore, designed products must be characterized and unknown model parameters are determined on test structures. Results provide valuable input data for the model parameter and the implemented algorithms of the toolbox elements. Design automation is challenging but inevitable for several reasons:

- Library elements comprise a lot of knowledge about the physical background and the implemented numerical algorithms. They can be continuously improved by several users especially in case of open source software. It would be a waste of labor to implement everything several times.
- The progress in microfluidics leads definitely to a standardization of basic components, from which new systems are assembled. It is proven in microelectronics and came true recently in the field of MEMS that parametric library elements are widely used in application specific software tools.
- Microfluidic design is an iterative process and requires a large number of model variants, which have to be analyzed, optimized and compared to each other. The model generation must be automated in order to save time and to avoid mistakes. In future, design rules should be implemented to account for special needs of local cleanroom processes and specific foundry services.
- The platform for design automation should support a wide variety of applications and customers. The micro-fluid toolbox is written in Matlab. Matlab software products are affordable and commonly used for engineering applications in academia and industry. The number of toolboxes is continuously growing and Matlab offers interfaces to electronic design languages as Verilog and VHDL.
- The microfluidic toolbox is excellent for academic education to explain the theoretical background on examples and to visualize results data. It can be used in academic research and class room teaching to make examples come alive.

The models of the microfluidic toolbox can be adapted to new layouts by design parameters and script files. Matlab scripts support data extraction from experimental results and adapt parameters by curve fitting technologies. Similar routines are available to extract finite-element-data for the fluidic resistance. A graphical user interface visualizes obtained results and supports curve fitting by interactive parameter input windows and sliders to sweep characteristic model data. An example is shown in **Figure 4.8.**

7.3 Modeling Chemofluidic Logic Circuits

This section discusses three examples of microfluidic logic circuits. The first one is a chemofluidic NAND, the second one a microfluid decoder and the third one a chemo-fluidic oscillator. The first two examples were developed by M.Sc. Anthony Beck from the TU Dresden and the model of the chemo-fluidic oscillator is introduced in [37].

7.3.1 Chemofluidic NAND Gate

The following example is a NAND gate, which can be utilized in microfluidic logic circuits to perform digital operations based on a stimulus concentration. A NAND gate produces an output, which is false if all its inputs are true as shown in **Figure 7.16**.

The chemofluidic NAND operates with two pressure pumps, which deliver either a high or a low concentration value at the logic ports A and B. If both signals are high, for example $C_H = 15\,\%$ ethanol in water, then the hydrogel in the microvalve unswells and opens the valve. If both concentrations are low, the hydrogel swells and blocks the valve. Interesting is the behavior in between, where one pump provides a high and one a low concentration level. After junction 2, the mixed concentration becomes about $C_H = 7.5\,\%$ ethanol in water. This value is designed to be below of the swelling threshold (LCST) and the hydrogel keeps the valve closed. Hence, the valve is only open if both inputs provide a high stimulus signal.

It should be noticed that the valve blocks only the fluid flow coming from the syringe pumps, which are discussed next. The fluid flow from the logical ports A and B is always open. The fluid with the stimulus flows around the hydrogel in a region called “bypass”. For that reason, the FL2 port of channel 6 is connected to the ground to drain the flow coming from inputs A and B.

Further microfluidic components are necessary to transfer the swollen and unswollen state of the valve to the NAND output. Two syringe pumps provide a constant volume flow rate whereby syringe pump 1 is designed to deliver a much larger volume flow rate as syringe pump 2. If syringe pump 1 dispenses a high concentration level and syringe pump 2 a low concentration level, the fluidic logic circuit operates as a NAND gate, otherwise it would be an AND gate.

The stimulus transfer from the syringe pumps to the output depends mainly on the fluidic resistance R_1 of channel 1, which is the connection between the syringe pumps. The fluidic resistance of channel 1 must be much larger as all other fluidic resistances, including the valve in the open state. On the other hand, it must be lower as the resistance of the valve in the closed state.

Now, two different scenarios are possible:

- The valve is closed $R_{CVPT} = \infty$, which happens only if A & B are true. The volume flow from both syringe pumps goes to the output because the valve is blocked. The high concentration provided by syringe pump 1 is dominant at the output because their volume flow rate is much larger as those from syringe pump 2.
- The valve is open, which happens only if A or B is false. The volume flow from syringe pumps 1 goes almost entirely thru the valve caused by the high resistance of channel 1 ($R_{CVPT} \ll R_1$). Syringe pump 2 becomes dominant and provides a low concentration level at the output.

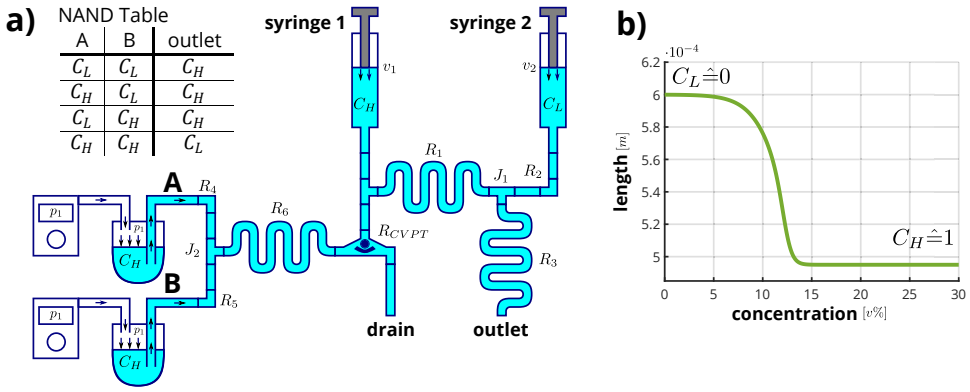

Figure 7.16: a) Schematic representation of the chemofluidic NAND circuit with inputs A and B. b) Swelling curve of the hydrogel depending on the stimulus level.

The Matlab Simscape model of the chemofluidic NAND circuit is shown in exemplarily. It can be seen, that the numerical representation of the fluidic logic circuit by library elements of the toolbox is very intuitive. Pressure pumps and inlet concentration levels are defined by voltage sources. The drain is set to ground. The library elements must be connected correctly as known from electronic network models.

In a second step, appropriate parameters are assigned to the channel and valve elements. It will be part of the optimization procedure to find proper dimensions and physical parameters. However, the new model configuration is automatically generated in Simscape after changing input parameters of the library elements. The compilation takes about a minute, which must be done just once. Transient simulations are very fast, several thousand steps take only seconds.

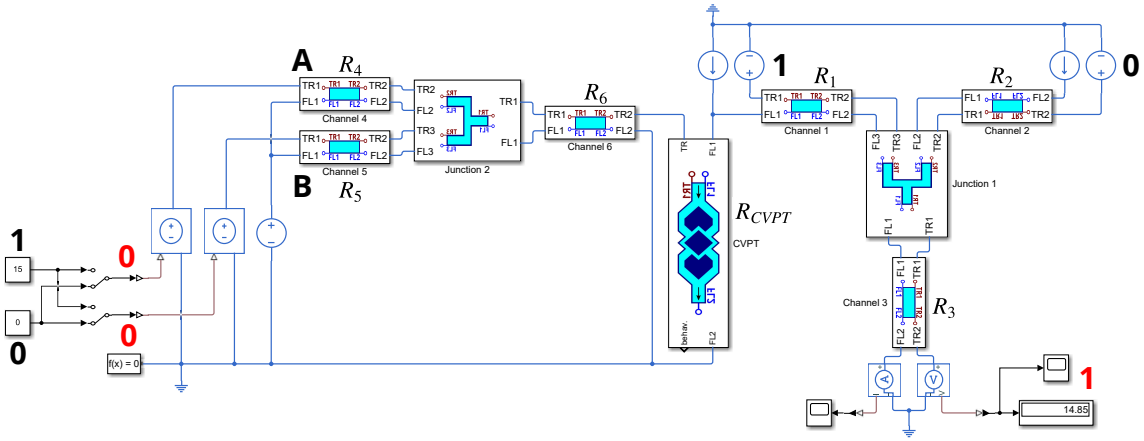

Figure 7.17: Microfluidic model of the NAND logic circuits implemented in Matlab Simscape.

The chemofluidic NAND model representation is not just a digital system with four output states. The Simscape model analyses the transient response and provides valuable system information for engineers. Result data are the response time after switching input states and critical input values (concentration levels, the pressure at pumps, flow rates at syringe pumps) where the system might fail. It supports users to find proper layout data, which are the geometrical dimensions of the system.

7.3.2 Chemofluidic Decoder Application

In electronics, analog-to-digital decoders are used to translate an analog signal into a digital signal with a specified resolution. The following example shows, how the previously discussed NAND structures can be used for a chemofluidic decoder. The idea and the following layout were proposed by M.Sc. Anthony Beck from the TU Dresden.

A series of fluidic NAND gates are utilized to determine an unknown concentration level $C_?$ of a liquid. The concentration level shall not directly be determined by analog sensing, rather the concentration level should be classified into a set of discrete ranges with upper and lower bounds. For several applications it is not necessary to know the exact value of a stimulus in a liquid. Often, unknown substances have to be classified in, for example “below average”, “normal range”, “above average”, “critical” and “dangerous”. It is a typical approach in biomedical engineering, especially for the quality assurance for organs, tissues and cells.

Theoretically one needs $(n-1)$-NAND gates to classify substances into n-categories. The threshold value of each NAND gate is adjusted to the lower bound of each category. Assuming a successive order of NANDs, the first one recognizes all solvents, which belong to the first category and so on. The last NAND finds liquids of the last category and the remaining liquids, which are above. It is an idealized view on the application. Extraction of measurement data by comparisons of bounds is a widely used approach in sensor technologies and can minimize costs.

The flowing example is based on a decoder with three NAND gates. The liquid with the unknown concentration is routed to the first input port of each NAND. The other input port of each gate is attached to a reference concentration, which have $5\,\%$, $10\,\%$ and $15\,\%$ concentration level. The threshold concentration (LCST) of all NAND gates is $12\,\%$. Consequently, the first NAND recognizes solvents with a concentration below $19\,\%$, the second one below $14\,\%$ and the last on, which are below and above $9\,\%$. There might be some overlap between ranges but is works well. **Figure 7.18** shows the general layout of the chemofluidic decoder.

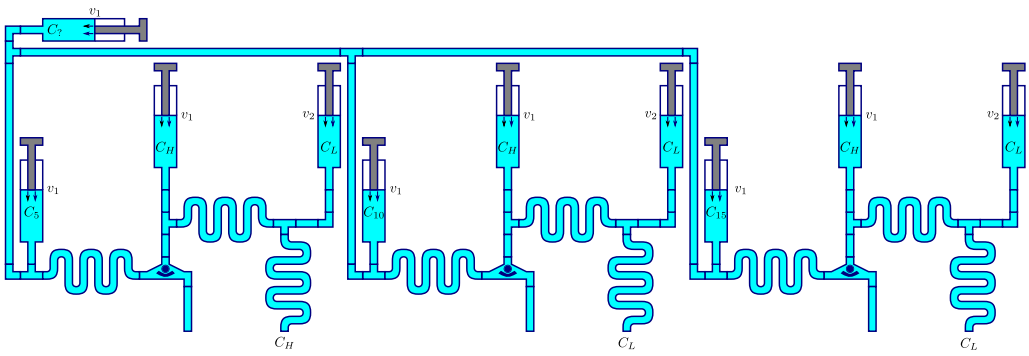

Figure 7.18: Conceptual layout of a chemofluidic decoder consisting of three NAND gates. It allows to classify liquids into four categories.

Figure 7.19 visualizes the decoder model in Simscape. The model generation is very simple. Subsequent NAND gates can be generated by copy and paste. Just the reference concentrations must by adjusted manually. The decoder demonstrates that larger arrays of microfluidic circuits for highly integrated microfluidic applications such as referred in [166] can be handled with ease.

Modeling of microfluidic arrays is important to investigate the interactions of NAND gates, which share the same channels for the fluid flow. Similar to electrical circuits, there is a flow dependent pressure drop if one NAND opens the valve, which can affect the behavior of adjacent elements. The cross-talk among array elements can often being minimized by assigning appropriate channel dimensions but will not entirely disappear.

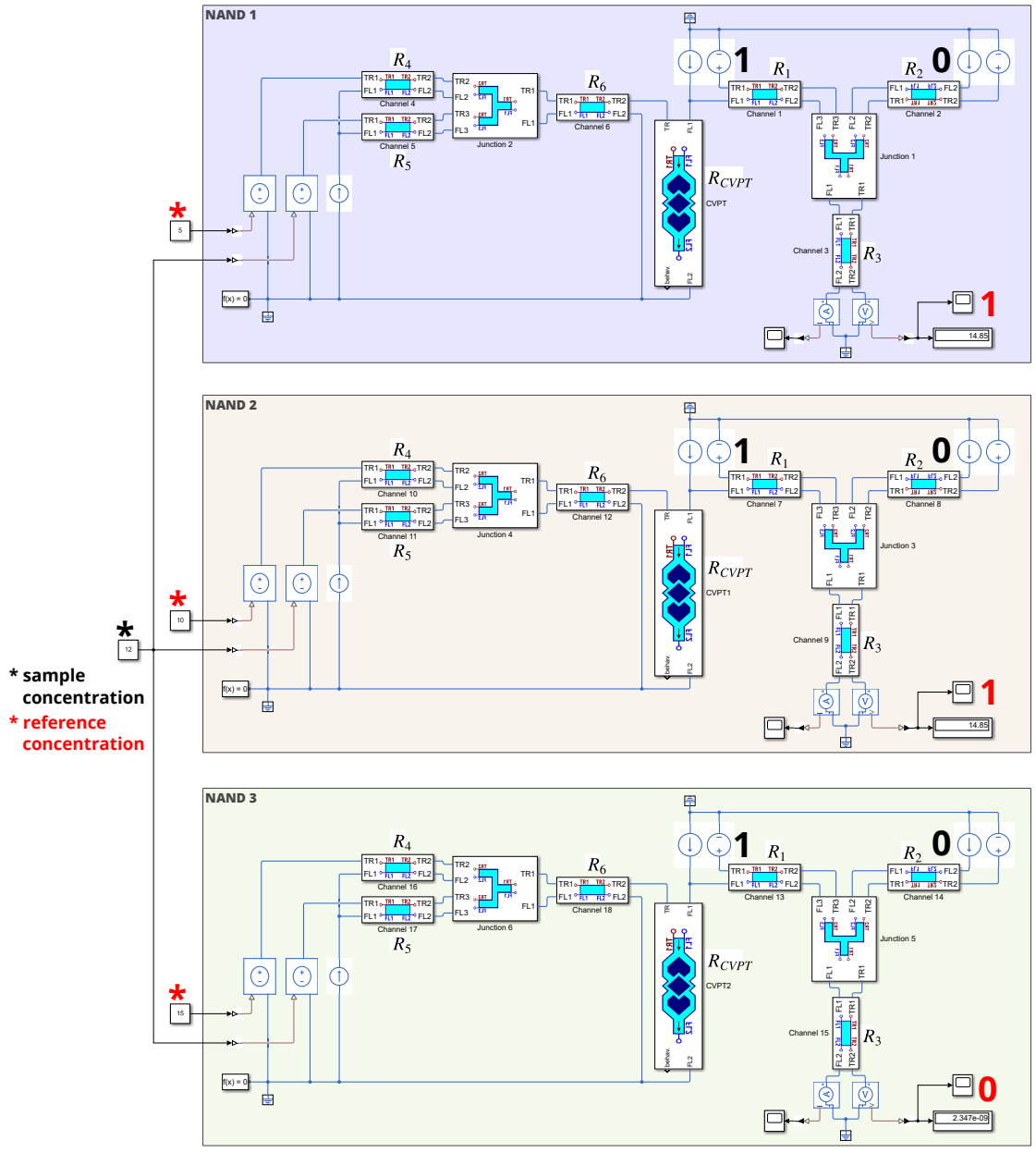

Figure 7.19: Microfluidic circuit model of the decoder based on three NAND gates. Each gate is attached to a different reference solution with values of $5\,\%$, $10\,\%$ and $15\,\%$ concentration level.

In **Figure 7.20** a triangle wave signal is applied at the stimulus input of the decoder. The first NAND switches from low to high at about $18\,\%$ concentration level, the second one at about $13\,\%$ and the third one at about $8\,\%$. The values are a little lower than expected what

means that the valves open at a slightly lower concentration level as specified by the threshold concentration (LCST). The dashed lines in **Figure 7.20** show the switching states of the NANDs.

The LCST value is the point of inflection of the sigmoidal function, which describes the swelling behavior of the hydrogel. At the point of inflection, the equivalent length is approximately in the middle between the swollen and the unswollen state. In practice, the valve opens earlier, right after the hydrogel starts to shrink what happens at a slightly lower concentration rate. It can be recognized by the internal signals of the decoder elements.

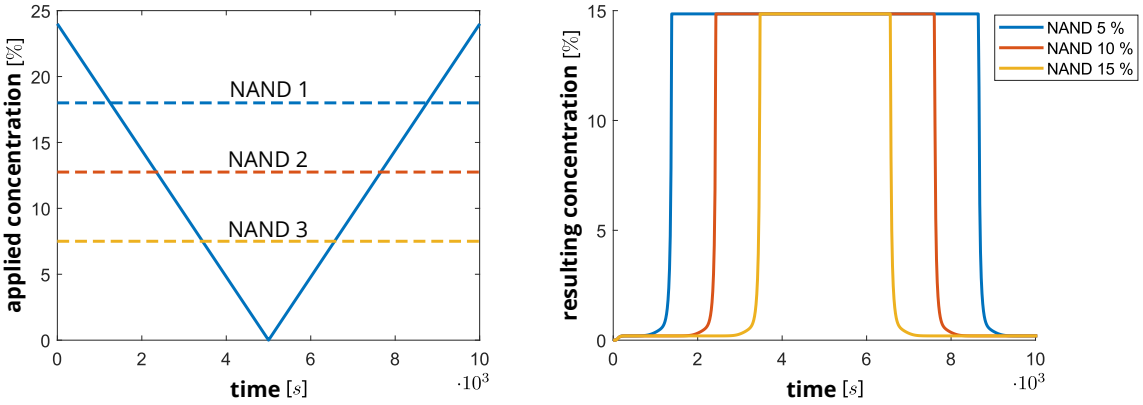

Figure 7.20: Quasi-static response of each NAND gate. The applied concentration level is a ramped signal and the resulting concentration level of all three NANDs is shown on the right.

7.3.3 Chemo-Fluidic Oscillator

An oscillator is a device, which produces an oscillating (periodic) output signal at time-constant input signals with a fixed clock frequency. In the present case, the oscillator consists of chemo-fluidic components, which create a periodic stimulus and fluid-flow response. It should be noticed, that periodic does not mean sinusoidal, rather the stimulus output is triggered with a specific period duration.

The design shown in **Figure 7.21** consists of two inlets and two outlets. The first inlet is connected to a pressure pump with two voltage sources. The first one represents a pressure pump with a constant pressure level of 8000 Pa. The second voltage source defines the stimulus level, which is set to zero (pure water, $C_{H_2O} = 0\,\%$). Inlet 1 drives an aqueous solution through the system.

The second inlet is connected to a syringe pump. The current source defines a constant volume flow rate of $1\,\mu\mathrm{l/min}$ and the adjacent voltage source defines a concentration level of $40\,\%$ ethanol in water solution. Both signals are mixed at the junction after the buffer line. Then, the solvents are driven through a delay line and finally reach the hydrogel-based microvalve. If the valve is closed at low concentration levels, the solvents flows through a bypass into a syringe pump, otherwise the solvent flows through the valve. The syringe pump at the bypass is used to control the circle time of the oscillator and the output signal is monitored at the valve. **Figure 7.21** shows the conceptual circuit, which has been published in [37].

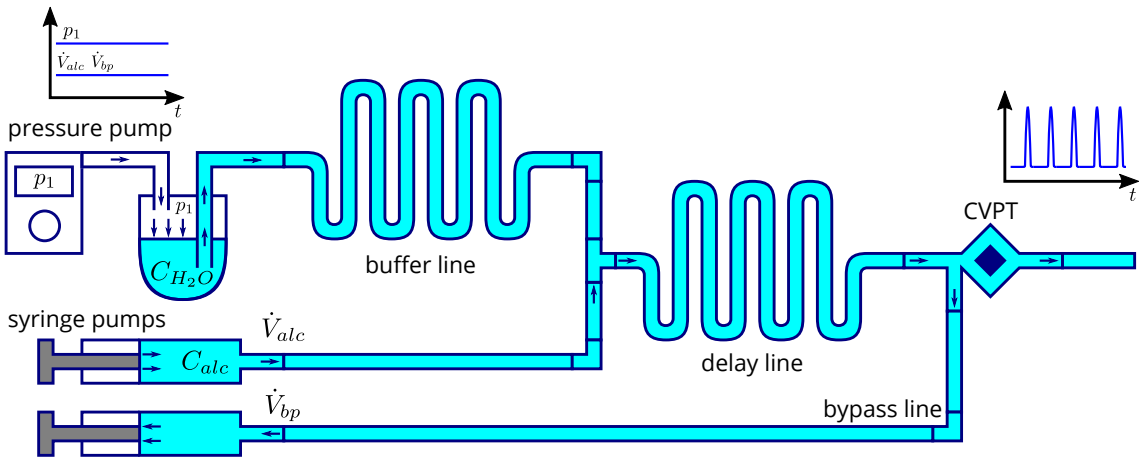

Figure 7.21: Conceptual circuit design of the chemo-fluidic oscillator.

Self-oscillating systems are based on a negative feedback loop. The clock frequency is essentially determined by the parameters of the syringe pump and the parameters of the delay line. To calculate the clock frequency, it is essential to understand the operating principle of the system.

The oscillation sequence is initialized at a zero stimulus value. In the initial state ($t = 0$), the hydrogel is unswollen and the valve is open. Consequently, the fluidic resistance in the system is comparably low and the pressure pump at inlet 1 is dominant in the system. In the aqueous solution, the hydrogel starts to swell and the fluidic resistance of the system is increasing. When the microvalve closes, the syringe pump of inlet 2 is dominant because the flow of a current source is independent of the attached fluidic resistance. This syringe pump provides a fluid with a high concentration level, which will reach the microvalve dependent on the applied flow rate of the bypass at a certain time delay t_{delay}. Now the hydrogel unswells, the fluidic resistance decreases and the pressure source is dominant again. This behavior is repeated continuously whereby the oscillating stimulus and fluid flow signal can be observed at the outlet of the valve.

Based on the concept shown in **Figure 7.21**, a Simscape model has been implemented, which contains library elements of the fluidic toolbox. Stimulus, pressure and flow sources are attached at the inlets as described above. The syringe pump at the outlet of the bypass has been set to a flow rate of $0.7\,\mu\mathrm{l/min}$.

According to [37], the flow rate of the bypass is designed to be lower as the flow rate of the syringe pump at the inlet. Thereby an interesting effect occurs, which can be quantified with simulation results of the model. If the valve is closed, the syringe pump at inlet 2 drives $70\,\%$ of the fluid through the delay line and $30\,\%$ of the fluid into the buffer line. Hence, the buffer line needs to be long enough that the stimulus does to reach the pressure pump at inlet 1 and contaminates the reservoir. Additionally, it can be seen in the simulation results that the concentration history in the buffer line affects the clock frequency of the oscillator. The Simscape model of the chemofluidic oscillator is shown in **Figure 7.22**.

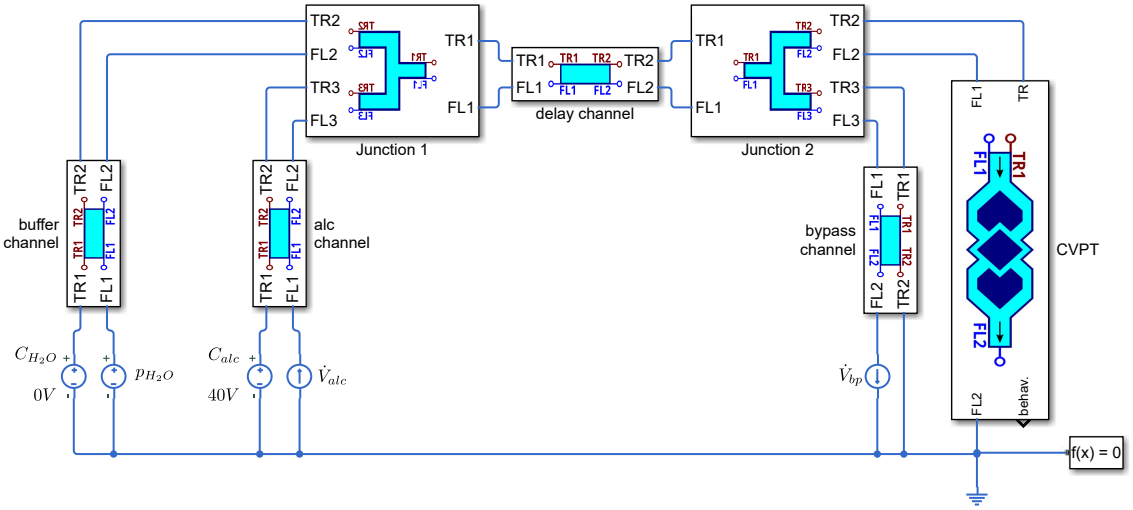

Figure 7.22: Microfluidic circuit model of the chemo-fluidic oscillator.

Transient simulations provide valuable information about the system response and the influence of input and model parameters on the performance, especially at the output but also at internal signal lines. Furthermore, simulation results are very important to fully understand the operating principle, to optimizes parameters in order to get the desired clock frequency and to assess the influence of tolerances and parameter variations on the behavior. It takes about 100.000 times steps to analyze the functional behavior whereby the simulations take about 20 seconds on the computer. The graphs in **Figure 7.23** show the following simulation results at the microvalve:

- Stimulus concentration level C at the hydrogel valve: Results can be between $0\,\%$ and $40\,\%$ according to stimulus sources at the inlet.
- Pressure drop Δp across the hydrogel valve: Peak values are in the order of the pressure value, which is assigned to the pump at inlet 1.
- Equilibrium length l_{eq} (blue) and kinematic length l_{kin} (red) of the hydrogel: The range is defined by the valve parameters, which are the collapsed length and the length change. The current values depend on the stimulus concentration.
- Young's modulus E of the hydrogel: The range is defined by the valve parameters, which are the collapsed and the swollen Young's modulus. The values depend on the kinematic length.
- Swelling time t_{sw} of the hydrogel: The value is defined by **Equation 7.16**. Several model parameters affect the value.
- Volume flow rate through the valve: The resulting volume flow rate depends on the fluidic resistances, the pressure and the flow sources of all model elements.

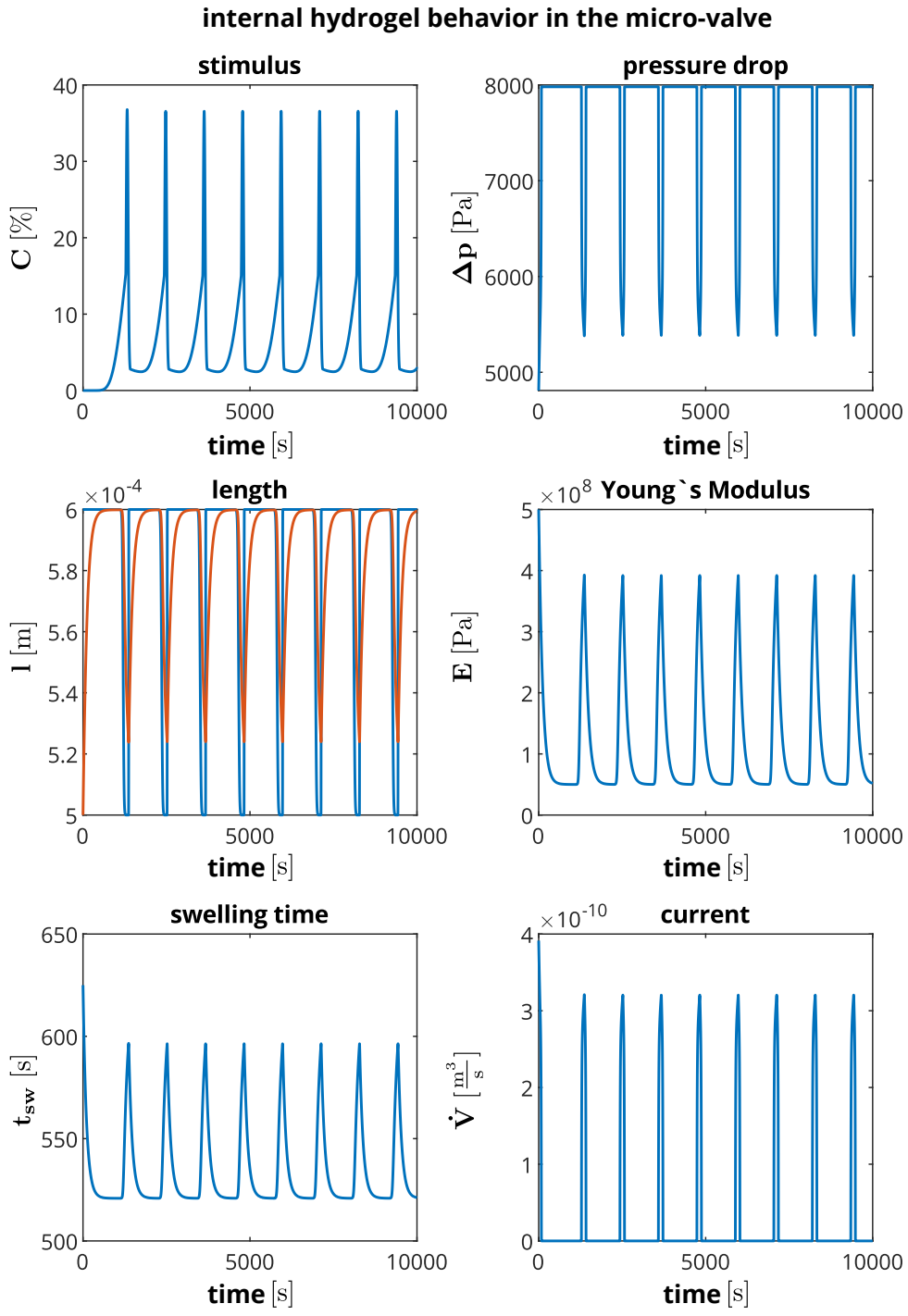

Figure 7.23: Transient simulation results of the chemo-fluidic oscillator shown in **Figure 7.22**.

In practice, the obtained clock frequency or period duration depends on many parameters of the microfluidic system. It is only possible to calculate correct values by transient simulations, which take most important effects into account.

Theoretically, the period duration is mainly defined by the transport delay of the stimulus in the delay channel. According to **Equation 7.4**, the transport delay is the ratio of the volume to the average volume flow rate of the fluid in the channel. The volume V_{delay} is defined by the channel dimensions, which are $150\,\mu m$ depth, $50\,\mu m$ channel width and $400\,mm$ channel length. The volume flow rate is defined by the bypass syringe pump, which is $\dot{V}_{bp} = 0.7\,\mu l/min$. Consequently, the transport delay is about 2600 seconds. It should be equal to the period duration of the oscillator.

The values obtained in **Figure 7.23** are much lower. The reason for the discrepancy can be traced in the simulation results of the above model. The swelling threshold of the given hydrogel (C_{LCST}) is at a concentration level of about $12\,\%$. However, the applied stimulus concentration C_{alc} is set to $40\,\%$. In this case, the delay line increases the applied concentration level towards the swelling threshold in a much shorter time. Therefore the oscillator period can be predicted by using the following approximation:

$$t_{oszi} \approx \frac{V_{delay}}{\dot{V}_{bp}} \cdot \frac{C_{LCST}}{C_{alc}} \tag{7.18}$$

To verify this hypothesis, the stimulus concentration at the inlet is reduced from $40\,\%$ to $20\,\%$. The period duration increases from about 1000 seconds to 1400 seconds. A concentration level of $15\,\%$ leads to a period direction of about 2000 seconds, which is in the order of the expected value. The true period duration does not only depend on the delay line. The swelling time of the hydrogel affects the transient response too.

The effect of shortening the response time by higher stimulus or drive signals is widely used in electrical engineering. It is called over-excitation and is applied for switches and other actuators.

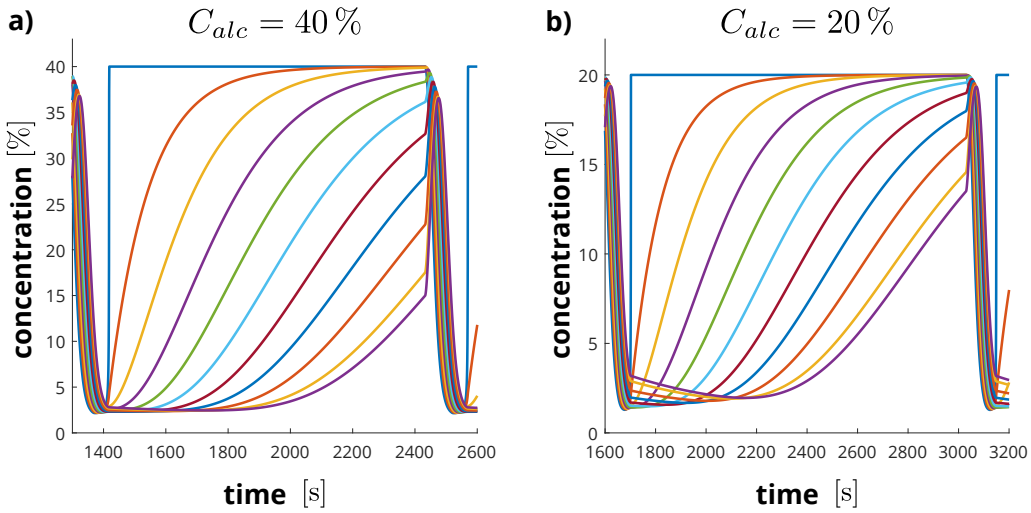

Figure 7.24: Stimulus concentration levels at the internal volume elements of the channel with $40\,\%$ and $20\,\%$ inlet stimulus.

Figure 7.24 shows the stimulus concentrations at internal volume elements of the delay channel at $40\,\%$ and $20\,\%$ stimulus concentration at the inlet of the syringe pump. The lower purple line marks the output of the channel element. It can be seen, that the concentration levels suddenly jump at about $12\,\%$ stimulus signal. The sharp increase is due to the switching behavior of the valve, which strongly decreases the fluidic resistance to the valve outlet.

7.4 Layout Synthesis

The previous examples have shown that the library elements of the microfluidic toolbox support modeling and simulation essentially. Designers can assemble larger microfluidic systems on the computer and analyze their behavior. During conceptual design, they must modify the layout, change the component and input parameters, evaluate the simulation results and compare the behavior with the product requirements. It is a long-term design cycle with many iterations. After the design matches the target specifications, designers have to run a large number of statistical simulations (e.g. Monte-Carlo-Simulations) to assess the influence of manufacturing tolerances, material property deviations and changes of environmental conditions (temperature, pressure, humidity) on the system performance. The results allow to estimate the yield during production and the accuracy of the devices.

Design automation requires a framework, which generates the model, modifies the parameters, starts the simulations and evaluates data automatically according to a special schema. Hence, modeling and simulation must be processed in a batch mode. It means that models can be generated, simulated and evaluated by script files to synthesize new designs at a high level of automation.

State-of-the-art simulation tools as the finite element program ANSYS, Matlab Simulink and Simscape as well as electronic design tools like Cadence support designers to run models in batch mode. A first concept for automatic generation of fluid models based on this toolbox is developed during the course of this work. The concept uses an approach where the arrangement and connection of microfluidic library elements in the system are defined by identification numbers of adjacent elements. They define the interconnection of sources, channels, junctions, corner elements and valves in a system. The placement and routing were supported by user defined port orientation settings for each element. The components are placed in a fixed grid.

Figure 7.25 a) shows the model input file and **b)** the obtained arrangement of components in grid cells. It was just a first case study on automated model and layout generation in Matlab.

a)

	1	2	3	4	5	6
1	'Modul ID'	'Modul na...	'Modul type'	'Connected...	'Orientatio...	'Staus flag'
2	1	'Modul1'	'Valve'	[2,9,32,33,...	[3,2,2,1,4,4]	1
3	2	'Modul2'	'Channel'	[1,3]	[1,3]	1
4	3	'Modul3'	'Junction'	[4,2,5]	[4,1,2]	1
5	4	'Modul4'	'Corner'	[3,6]	[2,3]	1
6	5	'Modul5'	'Corner'	[3,7]	[4,3]	1
7	6	'Modul6'	'Connector'	4	1	1
8	7	'Modul7'	'Channel'	[5,8]	[1,3]	1
9	8	'Modul8'	'Connector'	7	1	1
10	9	'Modul9'	'Connector'	1	3	1
11	10	'Modul10'	'Corner'	[1,11]	[2,3]	1
12	11	'Modul11'	'Connector'	10	1	1

b)

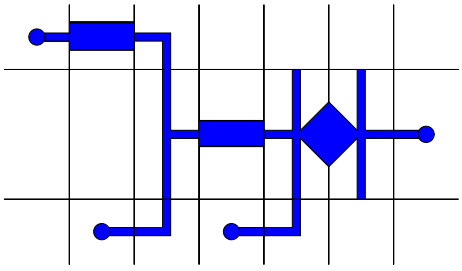

Figure 7.25: Model input file and the obtained simplified layout of a chemofluidic oscillator.

The implementation of an automated model generator with simulation and evaluation capabilities including a graphical user interface takes a lot of effort and has not been done yet, but a promising concept shall be shown as final part of this work. It addresses interesting research topics for future work.

The concept is based on the presented library elements and will be explained on the example model of the chemo-fluidic oscillator. The library elements in **Figure 7.26** can be addressed by a reference name and placed into the model file with the help of connecting points (nodes) shown in orange. Model sources and sinks have one connecting point, channel elements have two and junction elements and valves have three connecting points. Channel elements are subdivided into:

- **Mixing channels:** Mixing channels have a meandering shape and consider the fluidic resistance, the transport delay and a mixing model. This channel allows two phase separated fluids to enter at the inlet, enforce a mixing though the windings and flow out as an ideal mixed fluid.
- **Flow channel:** Flow channel elements model the fluidic resistance and a transport delay in a microchannel. Mixing effects are ignored.
- **Fluid link elements:** Fluid link elements are utilized for microchannels with a comparably low resistance. Link elements connect flow ports and/or stimulus ports by idealized lines, which have neither a fluidic resistance nor a transport delay. The elements are similar to interconnecting wires in electrical engineering.

The microvalves may be designed in many different variants. So far, two types of valves have been designed for the planar fluidic logic circuits. The first one is the chemical volume phase-transition transistor (CVPT), which has the bypass at the inlet (type 1) and the other one is a valve model, where the hydrogel blocks the collector at the outlet (type 2). Another element type could be a membrane isolated CVPT (MIS-CVPT) valve, where two flow channels are isolated through a membrane. In this case, the hydrogel actuates the membrane from one side and seals the flow channel on the other side. Details can be found in [167].

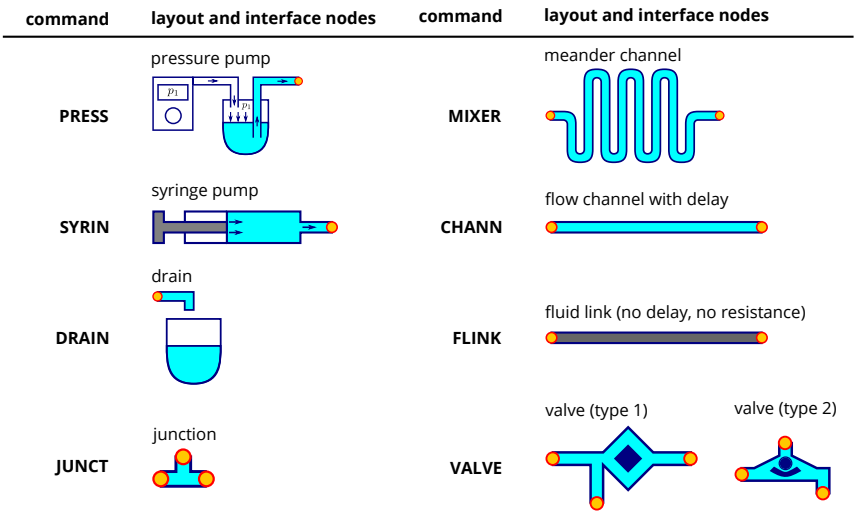

Figure 7.26: Library elements of the fluid toolbox with reference name and connecting points.

In **Figure 7.27**, the model of the chemo-fluidic oscillator is subdivided into 13 connecting points (nodes) and 14 elements. Nodes can be placed by commands (in batch mode) or graphically by pointing devices on the computer screen. In batch mode, connecting points can be defined by a command name (NLOC) followed by the reference number and the x- and y-coordinates. For instance, "NLOC, 1, 0, 40;" defines connecting point number 1 at the x-y-coordinates 0 and 40 mm in a Cartesian coordinate system.

Elements are placed between connecting points. Likewise, this can be done graphically or by commands such as "VALVE, 1, 9, 10, 12;" for instance. It means that a valve element with reference number 1 is attached to the connecting points 9 (inlet), 10 (bypass) and 12, which is the outlet of the flow, which passes through the valve. Fluid link elements are set between connecting point 6 and 7 for example. The tool should automatically create a connecting element, which consists of a horizontal and a vertical channel with a corner element in between, which can have either round or straight edges.

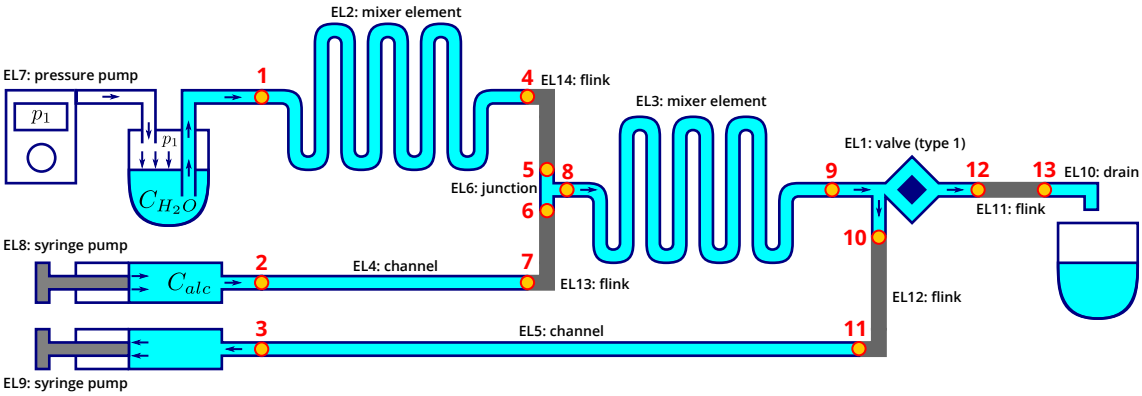

Figure 7.27: Automatically generated model of the chemo-fluidic oscillator with sources and sinks.

Parameters of library elements are assigned by a left mouse click on the element, which has to be modified. Such a feature is already implemented in the microfluidic toolbox. Alternatively, parameters can be assigned by commands to individual library elements such as the "PROP" commands shown in **Table 7.3**.

Further data to be assigned are loads and constraints such as "VSCR, 7, 8000" to define a DC-pressure load of 80 mbar to the pressure pump of element 7 or "ISCR, 8, 1.67e-11", which assigns $1\,\mu\mathrm{l/min}$ to the upper syringe pump.

It is followed by simulation settings for the total simulation time and time-step size. After starting the simulation runs, one can evaluate characteristic data and calculate post-processing results by further commands. The commands "GETP, p_valve, press, 9;" and "GETP, v_flow, flow, 9;" copy the pressure value and the volume flow rate at connecting point 9 to the user parameters "p_valve" and "v_flow", which are stored to the workspace. An example for post-processing is the "INTG, c_output, stim, 8" command sequence, which integrates the stimulus response at the end of the delay line. The input batch file could contain commands, which are shown in **Table 7.3**.

Table 7.3: Typical commands to generate, solve and evaluate models in a batch-mode.

```
% Connecting point location
NLOC, 1, 0, 40;
NLOC, 2, 0, 10;
NLOC, 3, 0, 0;
NLOC, 4, 50, 40;
NLOC, 5, 50, 35;
NLOC, 6, 50, 25;
NLOC, 7, 50, 10;
NLOC, 8, 55, 30;
NLOC, 9, 105, 30;
NLOC, 10, 110, 25;
NLOC, 12, 125, 30;
NLOC, 13, 140, 30;
% Element assignment
VALVE, 1, 9, 10, 12;
Mixer, 2, 1, 4;
Mixer, 3, 8, 9;
CHANN, 4, 2, 7;
CHANN, 5, 3, 11;
JUNCT, 6, 5, 6, 8;
PRESS, 7, 1;
SYRIN, 8, 2;
SYRIN, 9, 3;
DRAIN, 10, 13;
FLINK, 11, 6, 7;
FLINK, 12, 4, 5;
FLINK, 13, 10, 11;
FLINK, 14, 12, 13;
```

```
% Property assignment
% Correspond to mask data of Fig. 7.13 & 7.3
PROP, 1, 1, 500e-6, 100e-6, 12, 6, ...;
PROP, 2, 150e-6, 500e-6, 0.4, ...;
...
% Element loads and constrains
% Similar to SPICE with DC-, AC- and transient
% time functions of voltage and current sources
VSCR, 7, 8000;
ISCR, 8, +1.67e-11;
ISCR, 9, -1.17e-11;
...
% Simulation settings
% Total simulation time, time-step size
% Further solver settings, start simulation
TIME, 10000, 0.03;
SOLV, trans;
...
% Post-processing commands
% Assign results to user defined parameters
GETP, p_valve, press, 9;
GETP, v_flow, flow, 9;
...
% Integrates the stimulus over time
% Evaluates the stimulus conservation law
INTG, c_input, stim, 8;
INTG, c_output, stim, 9;
```

Another important step would be the automatic generation and evaluation of finite element models to extract characteristic properties of toolbox elements. Finite element models have already been extensively used in this work to extract properties for the fluidic resistance, to analyze the swelling behavior and to extract stiffness changes of the hydrogel. Likewise, routines exist and have been utilized for curve fitting procedures to transfer finite element results back to the Matlab Simulink and Simscape models. The theoretical background has been investigated but needs to be implement into user-friendly procedures, which can be processed automatically.

Finally, the mask layout must be generated for manufacturing of prototypes and later products. The mask layout depends on the shape and lateral dimensions of all model components. In some cases, the mask layout differs strongly from the Simscape schematics. For example, pressure pumps and syringe pumps are usually external devices, which are connected by a tube to the inlets. The mask layout needs additional information about the adaptor, which transfers the fluid from the macrosystem into the microsystem. Mask layout data have to be translated into a specific mask data format such as GDSII, GERBER, CIF, DXF or DWG.

Chapter 8

Summary and Outlook

The goal of this thesis was to develop an automated modeling and simulation approach for microfluidic and chemofluidic systems with a special focus on hydrogel-based microvalves. The models should capture essential features and most important interactions of fluidic components in larger microfluidic systems. The behavioral models are primarily intended for system simulations where a large number of different configurations and design modifications must be analyzed and optimized in a reasonable time. The models predict the system response on the computer for different load and operating conditions before starting a time consuming and costly manufacturing process of prototypes.

The core element of the presented models is a hydrogel-based microvalve. It is an autonomous microfluidic component, which controls the fluid flow depending on the volume swelling rate of a stimulus sensitive hydrogel and operates as a *chemofluidic transistor*. The volume change influences the cross-sectional area of a fluid channel in a valve chamber and consequently the fluidic resistance. Typical stimuli are the temperature, chemical substances or the ion concentration, which offers a wide variety of applications such as chemical sensing, lab-on-chip systems for medical applications or chemofluidic logic circuits, which have been presented in **Chapter 7**.

The operating principle is primarily related to the swelling response of a hydrogel. In physics, the theory of quasi-static swelling and the swelling kinetics are derived from thermodynamic energy formulations in combination with the fundamentals of elasticity in continuum mechanics. It has been shown in **Chapter 3** that the governing equations depend on empiric terms, which strongly affect the obtained results. Furthermore, the swelling functions on the physical level of abstraction depend on parameters (for example the interaction enthalpy and entropy or the polymer permeability), which are difficult to measure for varying hydrogel compositions and alternative stimuli sources.

An important goal of this thesis is the quantification of the material properties of hydrogels based on phenomenological parameters that can be measured and extracted with standard laboratory equipment. Computer-controlled swelling experiments have been developed and tested, which detect the surface area of hydrogels through optical inspections as shown in **Chapter 4**. A following image recognition routine provides swelling data for different stimuli-time functions. Slowly varying stimulus ramps are used to measure the quasi-static swelling response and stimulus step functions are applied to calculate the time constant of the volume change for transient simulations. The time constant together with dimensional parameters of the hydrogel enable the calculation of the cooperative diffusion coefficient for modeling of the swelling kinetics. Characteristic parameters of the swelling response such as the minimum and maximum volume or length, the lower critical solution temperature or the upper and lower curvature range have been adapted to sigmoidal fit functions for subsequent component and system models.

Chapter 5 uses the measured material properties to analyze the three-dimensional displacement response of the hydrogel by finite element simulations in ANSYS. The FE-models are based on a thermo-mechanical analogy relationship where the swelling-stimuli function is represented by the instantaneous thermal expansion coefficient implemented by a set of sample points. The cooperative diffusion of the solvent is mapped to the heat transfer coefficient and the elasticity can be either implemented by the Youngs's modulus and the Poisson's ratio or the Mooney-Rivlin material law for incompressible solids. The swelling states at different stimuli levels are transferred to the fluid domain in the valve by moving wall boundary constraints. The preferred coupling approach is based on a one-way fluid structure interaction model. Interactions in both directions are not necessary for the target application and have shown numerical instabilities. Finally, transient computational fluid dynamic simulations, in ANSYS-CFX provide accurate data for the fluidic resistances of the microvalve at different swelling states. The result data are represented by a mathematical response function which is implemented in a Matlab library element for subsequent system simulations.

Modeling and simulation of a hydrogel-based microvalve has been investigated in **Chapter 6**. Essential modeling features are the static and transient hysteresis, the quasi-static equilibrium length of a characteristic dimensional parameter, the transient swelling response, the influence of elastic deformations on the swelling state, the contact pressure and the related leakage rates as well as the fluidic resistance and the associated volume flow rate at applied pressure sources at the interface ports. The microvalve model was gradually developed, implemented and tested in Matlab Simulink using signal flow graphs. It could be demonstrated that the simulation of microvalve component is numerically stable and physically accurate.

The interactions with other microfluidic components require generalized Kirchhoffian network elements to represent the bi-directional flow-pressure relationship at the interface ports. It was planned to combine the Simulink-Simscape interface of the Matlab tool to couple the signals flow graphs to network representations. However, numerical instabilities appeared in multi-component simulations, which are caused for example by unavoidable algebraic loops.

Stable and accurate solutions could only be obtained after all model components had been transferred to Simscape. The problem was not caused by the combination of signal flow graphs and network models, it is rather related to the data exchange from Simscape over Simulink back to Simscape, which is reasoned with the different internal solver architecture and the equilibrium iterations. The modified Simscape models still utilizes signal flow graphs from a different domain space in combination with network representations to efficiently describe fluidic components and their interactions to adjacent elements. It is a certain indicator that in future releases of Matlab this issue can be fixed.

In **Chapter 7**, the final implementation of all library elements of the microfluidic toolbox is discussed in detail. It starts with a brief introduction to fluid and transport domain quantities and modeling approaches for pressure sources, volume flow sources (syringe pumps) and stimuli sources. If follows a model for channel elements, which describes the fluidic resistance and the transport delay for bi-directional flow conditions. The next library component is a junction element, at which three other fluidic elements can be connected to separate or merge the fluid and stimulus flow. The junction represents a true bi-directional fluid flow and

stimulus transport what means that the inlet or outlet ports can change directions during operations. The last element is the hydrogel-based microvalve, which allows for modeling of arbitrary stimulus-based volume phase-transition curves to control the fluid flow in microfluidic networks.

The library elements of the microfluidic toolbox have been intensively tested on three examples. The first test case is a chemofluidic NAND-gate, which illustrates the transistor-like behavior of the hydrogel-based microvalve in a chemofluidic logic circuit. The next example is a chemofluidic decoder that can be used to classify continuous stimuli levels into specific categories. It behaves like an analog-to-digital converted in electronics and demonstrate that the toolbox can handle large amount of microfluidic components. The last test case is a chemofluidic oscillator, which creates a periodic flow signal with a fixed clock frequency. Here the challenge is, that the solver needs to handle constant inputs and compute a varying output through an unstable hydrogel state definition, which seems counter-intuitive for solver designs.

All three examples demonstrate that larger chemofluidic logic circuits are possible and can be efficiently designed with the help of the microfluidic toolbox and its simulation framework. The simulation framework includes the computer-controlled measurement setup for hydrogel material properties, the finite element interfaces to extract characteristic component models for the swelling states or the resulting fluidic resistances, and last but not least the Matlab capabilities for data evaluation or results visualization.

Future work could be focused on new library elements for the microfluidic toolbox, an improved graphical support for the model generation process and the layout synthesis concept for design optimization and mask layout generation.

The microfluidic toolbox currently contains most important functional element for chemofluidic logic circuit. New elements would be necessary for other applications such as chemical sensing devices or lab-on-chip systems for diagnostics and drug development. Examples are mixers, nozzles, heaters, filters, droplet generators, reaction chambers, reservoirs for reagents and sections for CE [168], HPLC [169] and PCR [170].

Models of microfluidic devices and systems can be generated by pick and place from library elements and essential parameters can be set or modified by a graphical user interface (GUI). The generation and simulation process are highly automated. On the other hand, new models with modified material compositions, new designs of the hydrogel-based microvalve and additional library elements need to be implemented manually. The ultimate goal is to support a consistent and automated design flow starting from the material property extraction, the solid and finite element method (FEM) generation process to the data transfer from FEM to the microfluidic library elements. The entire design process should be accompanied by a design rule check and a graphical visualization of the next steps.

A fully automated layout synthesis exceeds the current possibilities in microfluidic design. Envisioned is a computer-supported layout optimization in an highly interactive and automated design flow. Essential library elements and their interconnections should be defined manually. The library elements are placed at the initial position and can be moved with pointing devices (for example the computer mouse) in the designated area. Routing of the fluid channels and interconnects follows automatically as known from printed circuit board design. The schematic layout of the library elements and their physical behavior should be bidi-

rectional associative. It means that changes in the layout modify physical parameters and changed physical parameters provide a new layout proposal. The seconds case is more complicated but feasible since microfluidic components are two dimensional structures with a well-defined thickness. Lateral dimensions are modified within the design range and in the designated area. The entire system will be analyzed and compared with the target specifications. Optimization algorithms provide design suggestions and the mask layout can be generated automatically.

Appendix

content of chapter

A 2D Thermo-Mechanical Solid Element for the Finite Element Method

In this chapter, a 2D thermo-mechanical solid element for finite element simulations will be introduced. The finite element routine has been implemented in Matlab to get a deeper understanding of numerical methods with the goal to enhance the data extraction procedures of the microfluidic toolbox in future. The Matlab source code is developed for an 8-node thermo-mechanical coupled field element and allows for linear static simulations. The theoretical background is based on [171] (pp. 162-211). The 2D-solid element is an extension of the 1D-truss element described in **Section 3.1.2**.

The starting point of the following description is the **elastic stiffness matrix** of the mechanical domain, which is referred $[K_{uu}]_e$ in **Equation 3.23**. Each finite element node of the 2D-solid element has two mechanical motion degree of freedom (DOF) referred u and v, which describe the mechanical displacements in x- and y-direction and one thermal degree of freedom, which is the nodal temperature T. The mechanical element stiffness matrix $[K_{uu}]_e$ is defined by:

$$[K_{uu}]_e = \int_V [B_M]^T [D_M][B_M]\, dV = \int_{A(x,y)} h[B_M]^T [D_M][B_M]\, dx\, dy = \int_{A(x,y)} f(x,y)\, dx\, dy \qquad \text{(A.1)}$$

where $[B_M]$ is the element strain matrix, $[D_M]$ is the elasticity matrix of the material and $f(x,y)$ is an arbitrary function to demonstrate the approach. For 2D-solid models, the element volume V can be expressed by the element area A and its thickness h. The stiffness matrix is the result of a 2D-integral on the element area, which is defined by the corner and mid-side nodes of the finite elements as shown in the left of **Figure A.1**. The numerical integration can be simplified if the global node coordinates (represented by x-y-values) are mapped to a unit element (represented by ξ-η-values) in a natural coordinate system.

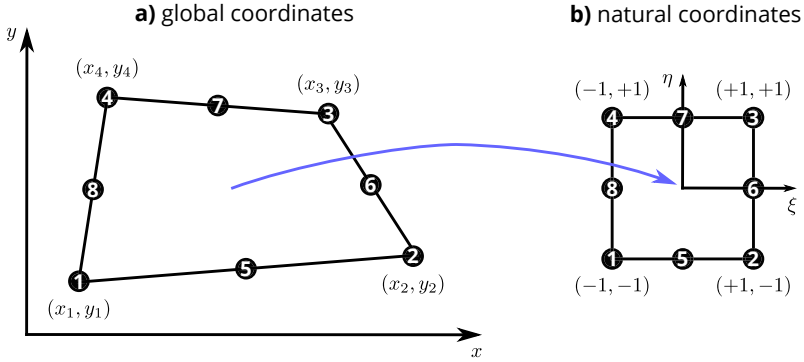

Figure A.1: Coordinate mapping from an arbitrary element with x-y-coordinates to a unit cell element with ξ-η-coordinates in the range of $[-1,+1]$.

The transformation from the x-y-coordinate system into the ξ-η-coordinate system is considered by the Jacobian determinant $\det|J|$ in functional analysis. The calculation of the Jacobian matrix J is defined in **Equation A.13**. In finite element tools, the integration in natural ξ-η-coordinates is implemented by a Gaussian quadrature, which approximates the result from a weighted sum of function values of $f(\xi,\eta)\det|J|$ at specified points within the domain

of integration.

$$\int\limits_{A(x,y)} f(x,y)\,dx\,dy = \int\limits_{-1}^{+1}\int\limits_{-1}^{+1} f(\xi,\eta)\det|J|\,d\xi\,d\eta = \sum_{j=1}^{m_j}\sum_{i=1}^{m_i} w_i w_j f(\xi_i,\eta_j)\det|J| \tag{A.2}$$

The locations ξ_i and η_i and the weights w_i and w_j of Gaussian points are defined in **Table A.1**. Two integration points in both directions are recommended for two-dimensional 8-node solid elements in finite element tools. The sum of all weights must be two and the accuracy n defines the polynomial order of shape functions, which can be approximated exactly [171] (pp. 180).

Table A.1: Lookup table for Gauss points [171] (pp. 180).

Point Number m_i**,** m_j	**Location** ξ_i**,** η_j	**weights** w_i**,** w_j	**Accuracy** n
1	0	2	1
2	$\pm\frac{1}{\sqrt{3}}$	1	3
3	$\pm\sqrt{0.6}$, 0	$\frac{5}{9}$, $\frac{8}{9}$	5

The location of Gaussian points for all three levels is shown in **Figure A.2**.

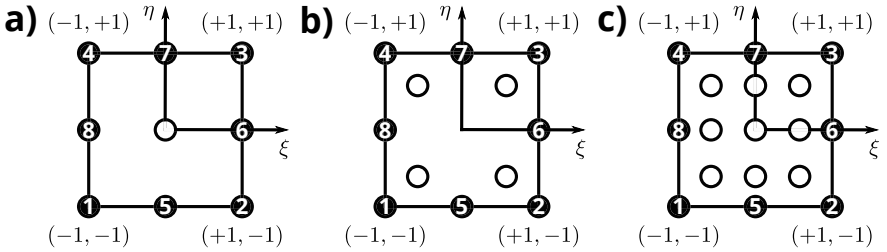

Figure A.2: Gaussian integration points for a two-dimensional solid element with a) $m = 1$, b) $m = 2$ and c) $m = 3$.

The general idea of finite element technologies in the mechanical domain is the extraction of the system behavior from the force-displacement relationship at interface nodes. Displacements at internal points are interpolated by shape functions from the results at finite element nodes and mechanical strain or stress is calculated from local derivatives of the shape functions. Finally, it allows to calculate the strain matrix $[B_M]$ of **Equation A.1** exclusively from the coordinates of the finite element nodes.

Each finite element node i is related to a polynomial shape function $N_i(\xi,\eta)$ whereby the function value at the node i must be one and the function values at all other node positions must be zero. The shape functions for the finite element corner nodes are defined by:

$$\begin{aligned} N_1 &= -\frac{1}{4}(1-\xi)(1-\eta)(1+\xi+\eta) \\ N_2 &= -\frac{1}{4}(1+\xi)(1-\eta)(1-\xi+\eta) \qquad -1 \le \xi \le 1 \\ N_3 &= -\frac{1}{4}(1+\xi)(1+\eta)(1-\xi-\eta) \qquad -1 \le \eta \le 1 \\ N_4 &= -\frac{1}{4}(1-\xi)(1+\eta)(1+\xi-\eta) \end{aligned} \tag{A.3}$$

and the mid-side nodes are described by:

$$\begin{aligned} N_5 &= \frac{1}{2}(1-\xi^2)(1-\eta) \\ N_6 &= \frac{1}{2}(1+\xi)(1-\eta^2) \qquad -1 \leq \xi \leq 1 \\ N_7 &= \frac{1}{2}(1-\xi^2)(1+\eta) \qquad -1 \leq \eta \leq 1 \\ N_8 &= \frac{1}{2}(1-\xi)(1-\eta^2) \end{aligned} \tag{A.4}$$

The displacements of all eight finite element nodes in x- and y-directions are arranged in a nodal displacement vector $(q)_e$ with the following order:

$$(q)_e = \begin{pmatrix} u_1 & v_1 & u_2 & v_2 & u_3 & v_3 & \cdots & u_8 & v_8 \end{pmatrix}^\intercal \tag{A.5}$$

where u are displacements in x-direction and v are the displacements in y-direction. Likewise, all eight nodal shape functions $N_i(\xi, \eta)$ are arranged in a matrix notation:

$$[N(\xi,\eta)] = \begin{pmatrix} N_1 & 0 & N_2 & 0 & N_3 & 0 & \cdots & N_8 & 0 \\ 0 & \underbrace{N_1}_{\text{node 1}} & 0 & \underbrace{N_2}_{\text{node 2}} & 0 & \underbrace{N_3}_{\text{node 3}} & \cdots & 0 & \underbrace{N_8}_{\text{node 8}} \end{pmatrix} \tag{A.6}$$

where $[N(\xi, \eta)]$ is referred matrix of shape functions and N_1 - N_8 are the corresponding shape functions of the involved finite element nodes. The displacements at internal points with local coordinates ξ and η can now by interpolated by:

$$\begin{pmatrix} u(\xi,\eta) \\ v(\xi,\eta) \end{pmatrix} = [N(\xi,\eta)] \cdot (q)_e \tag{A.7}$$

The next step will be the computation of mechanical strain ε at internal points of the finite element. The mechanical strain components ε_{xx}, ε_{yy} and γ_{xy} are calculated from the displacement derivatives with regard to the global x- and y-coordinates. Since the nodal displacement vector components are constant numbers, the derivatives are solely calculated from the nodal shape functions.

$$(\varepsilon) = \begin{pmatrix} \varepsilon_{xx} \\ \varepsilon_{yy} \\ \gamma_{xy} \end{pmatrix} = \begin{pmatrix} \frac{\partial u(\xi,\eta)}{\partial x} \\ \frac{\partial v(\xi,\eta)}{\partial y} \\ \frac{\partial u(\xi,\eta)}{\partial y} + \frac{\partial v(\xi,\eta)}{\partial x} \end{pmatrix} = \begin{pmatrix} \frac{\partial}{\partial x} & 0 \\ 0 & \frac{\partial}{\partial y} \\ \frac{\partial}{\partial y} & \frac{\partial}{\partial x} \end{pmatrix} \cdot [N] \cdot (q)_e = [B_M] \cdot (q)_e \tag{A.8}$$

Equation A.8 implies that mechanical strain can be expressed by the nodal displacement vector $(q)_e$ and the strain matrix $[B_M]$. The strain matrix consists of the following coefficients:

$$[B_M] = \begin{pmatrix} \frac{\partial N_1}{\partial x} & 0 & \frac{\partial N_2}{\partial x} & 0 & \frac{\partial N_3}{\partial x} & 0 & \cdots & \frac{\partial N_8}{\partial x} & 0 \\ 0 & \frac{\partial N_1}{\partial y} & 0 & \frac{\partial N_2}{\partial y} & 0 & \frac{\partial N_3}{\partial y} & \cdots & 0 & \frac{\partial N_8}{\partial y} \\ \frac{\partial N_1}{\partial y} & \frac{\partial N_1}{\partial x} & \frac{\partial N_2}{\partial y} & \frac{\partial N_2}{\partial x} & \frac{\partial N_3}{\partial y} & \frac{\partial N_3}{\partial x} & \cdots & \frac{\partial N_8}{\partial y} & \frac{\partial N_8}{\partial x} \end{pmatrix} \tag{A.9}$$

According to **Equations A.1** and **A.2**, the strain matrix must be evaluated at the Gaussian points to calculate the element stiffness matrix $[K_{uu}]_e$. The evaluation of **Equation A.9** is not

straightforward since the coefficients of the strain matrix are functions of natural coordinates and the derivatives have to be evaluated with regard to global coordinates. The dependency can be resolved by the chain rule of partial differentiation:

$$\frac{\partial N_i}{\partial \xi} = \frac{\partial N_i}{\partial x}\frac{\partial x}{\partial \xi} + \frac{\partial N_i}{\partial y}\frac{\partial y}{\partial \xi} \tag{A.10}$$

$$\frac{\partial N_i}{\partial \eta} = \frac{\partial N_i}{\partial x}\frac{\partial x}{\partial \eta} + \frac{\partial N_i}{\partial y}\frac{\partial y}{\partial \eta} \tag{A.11}$$

which can be expressed in matrix notation by:

$$\begin{pmatrix} \frac{\partial N_i}{\partial \xi} \\ \frac{\partial N_i}{\partial \eta} \end{pmatrix} = \begin{pmatrix} \frac{\partial x}{\partial \xi} & \frac{\partial y}{\partial \xi} \\ \frac{\partial x}{\partial \eta} & \frac{\partial y}{\partial \eta} \end{pmatrix} \cdot \begin{pmatrix} \frac{\partial N_i}{\partial x} \\ \frac{\partial N_i}{\partial y} \end{pmatrix} = [J(\xi,\eta)] \cdot \begin{pmatrix} \frac{\partial N_i}{\partial x} \\ \frac{\partial N_i}{\partial y} \end{pmatrix} \tag{A.12}$$

The term $[J(\xi,\eta)]$ is referred as Jacobian matrix, which is calculated from the differentials of shape functions in natural coordinates multiplied by the matrix of nodal coordinates at the Gaussian points:

$$[J(\xi,\eta)] = \begin{pmatrix} \frac{\partial N_1}{\partial \xi} & \frac{\partial N_2}{\partial \xi} & \cdots & \frac{\partial N_8}{\partial \xi} \\ \frac{\partial N_1}{\partial \eta} & \frac{\partial N_2}{\partial \eta} & \cdots & \frac{\partial N_8}{\partial \eta} \end{pmatrix} \cdot \begin{pmatrix} x_1 & y_1 \\ x_2 & y_2 \\ \vdots & \vdots \\ x_8 & y_8 \end{pmatrix} \tag{A.13}$$

The inverse of the Jacobian matrix can then be used to transform the derivatives of shape functions from natural to global coordinates as necessary for the terms in **Equation A.9**.

$$\begin{pmatrix} \frac{\partial N_i}{\partial x} \\ \frac{\partial N_i}{\partial y} \end{pmatrix} = [J(\xi,\eta)]^{-1} \begin{pmatrix} \frac{\partial N_i}{\partial \xi} \\ \frac{\partial N_i}{\partial \eta} \end{pmatrix} \tag{A.14}$$

Finally, the matrix of elastic constants for 2D-plane stress applications is defined by:

$$[D_M] = \frac{E}{1-\nu^2} \begin{pmatrix} 1 & \nu & 0 \\ \nu & 1 & 0 \\ 0 & 0 & \frac{1-\nu}{2} \end{pmatrix} \tag{A.15}$$

where E is the Young's modulus and ν is the Poisson's ratio. The mechanical element stiffness matrix $[K_{uu}]_e$ of **Equation A.1** can now be calculated from the strain matrix $[B_M]$, the Jacobian matrix $[J]$, the matrix of elastic constants $[D_M]$, the thickness h of the element and the Gaussian weights w_i and w_j. The matrix operations lead to a 16x16 matrix, which corresponds to the number of element nodes multiplied by the number of the respective degrees of freedom.

The **thermal conductivity matrix** $[K_{TT}]_e$ of **Equation 3.23** can be calculated in a similar manner:

$$[K_{TT}]_e = \sum_{i=1}^{m_i}\sum_{j=1}^{m_j} w_i w_j \left(h[B_T]^T[D_T][B_T]\det|J|\right) \tag{A.16}$$

where $[B_T]$ is the matrix of the thermal gradients and $[D_T]$ is the conductivity matrix of

the material. The thermal gradients are defined by:

$$[B_T] = \begin{pmatrix} \frac{\partial N_1}{\partial x} & \frac{\partial N_2}{\partial x} & \frac{\partial N_3}{\partial x} & \dots & \frac{\partial N_8}{\partial x} \\ \frac{\partial N_1}{\partial y} & \frac{\partial N_2}{\partial y} & \frac{\partial N_3}{\partial y} & \dots & \frac{\partial N_8}{\partial y} \end{pmatrix} \tag{A.17}$$

and the conductivity matrix of the material $[D_T]$ is given by:

$$[D_T] = \begin{pmatrix} k_{xx} & 0 \\ 0 & k_{xx} \end{pmatrix} \tag{A.18}$$

where k_{xx} and k_{yy} are the thermal conductivity coefficients in x- and y-directions, which are often labeled as λ. The thermal conductivity matrix $[K_{TT}]_e$ is an 8x8 matrix.

Finally, the **thermoelastic stiffness matrix** $[K_{uT}]_e$ of **Equation 3.23** is defined by:

$$[K_{uT}]_e = \sum_{i=1}^{m_i} \sum_{j=1}^{m_j} -w_i w_j \left(h[B_K]^T [D_K][N] \det|J| \right) \tag{A.19}$$

where $[B_K]$ is the strain-displacement matrix, (D_K) is the vector of thermoelastic coefficients and (N) is the vector of shape functions. The strain-displacement matrix $[B_K]$ contains the first two lines of the mechanical strain matrix $[B_M]$, since thermal expansion does not create shear strain. The vector of thermoelastic coefficients (D_K) is defined by:

$$[D_K] = \frac{E}{1-\nu^2} \begin{pmatrix} 1 & \nu \\ \nu & 1 \end{pmatrix} \cdot \begin{pmatrix} \alpha \\ \alpha \end{pmatrix} \tag{A.20}$$

where E is the Young's modulus, ν is the Poisson's ratio and α is the thermal expansion coefficient. The vector of shape functions (N) is:

$$(N(\xi,\eta)) = \begin{pmatrix} N_1 & N_2 & N_3 & N_4 & N_5 & N_6 & N_7 & N_8 \end{pmatrix} \tag{A.21}$$

The thermoelastic stiffness matrix $[K_{uT}]_e$ is a 16x8 matrix and describes the unidirectional coupling between the thermal and the mechanical domain caused by thermal expansion. The elastic stiffness matrix $[K_{uu}]_e$, the thermal conductivity matrix $[K_{TT}]_e$ and the thermoelastic stiffness matrix $[K_{uT}]_e$ are finally combined to a 24x24 element stiffness matrix as shown in **Equation 3.23**.

The assembly process of all finite element matrices into a global system matrix is illustrated in **Figure A.3**. The element matrix consists of eight nodes, which are labeled with *i, j, k, ... , p* and each node has three degrees of freedom, which are labeled u, v and T. An element table defines the relationship between element node numbers and the system node numbers, which are integers in a successive order defined by the mesh generator. In the given case, the first element is linked to the global system nodes 1, 3, 125, 123, 2, 83, 124, 82. **Figure A.3** shows exemplarily, how the first 18 coefficients of the element stiffness matrix are transferred to the global system matrix. The assembly process is implemented by nested *FOR*-loops, which process all elements, followed by the nodes and finally all internal degrees of freedom. Displacement and temperature boundary constraints are modeled by Lagrangian multipliers according to **Equation 3.21**. Details can be found in the source code provided in **Appendix E.3**.

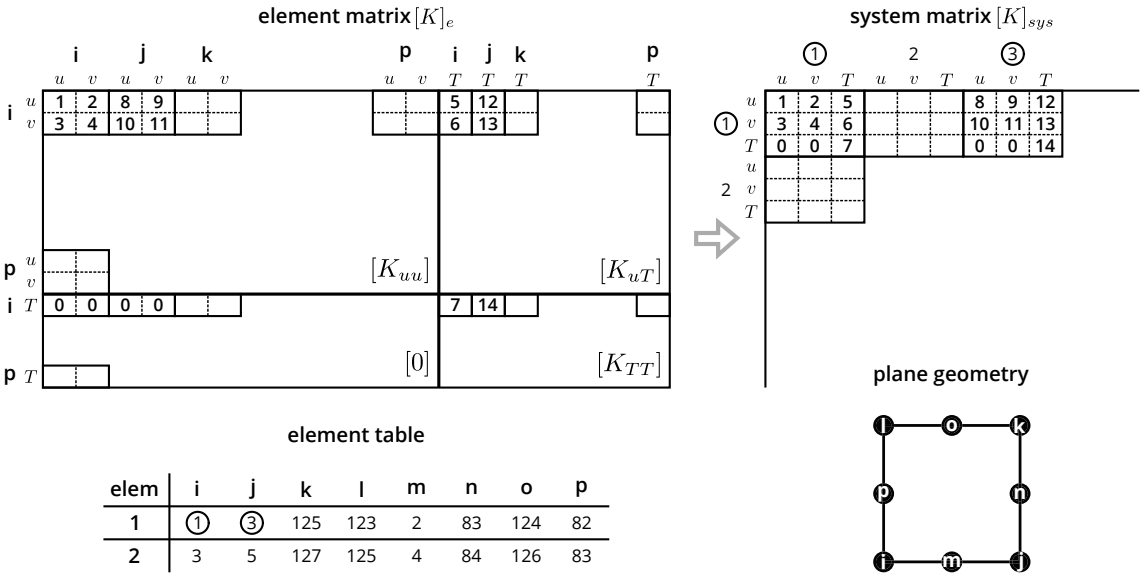

Figure A.3: Schematic view on the system matrix assembly procedure.

Figure A.4 illustrates two simulation results of the expansion process. The left part visualizes the temperature profile and the swelling state at the beginning of the solvent diffusion process (referred as intermediate state) and the right part the final equilibrium state. It is a rough approximation based on a linear theory for the two-dimensional case. The finite element tool ANSYS provides identical results as shown in the lower part of **Figure A.4**.

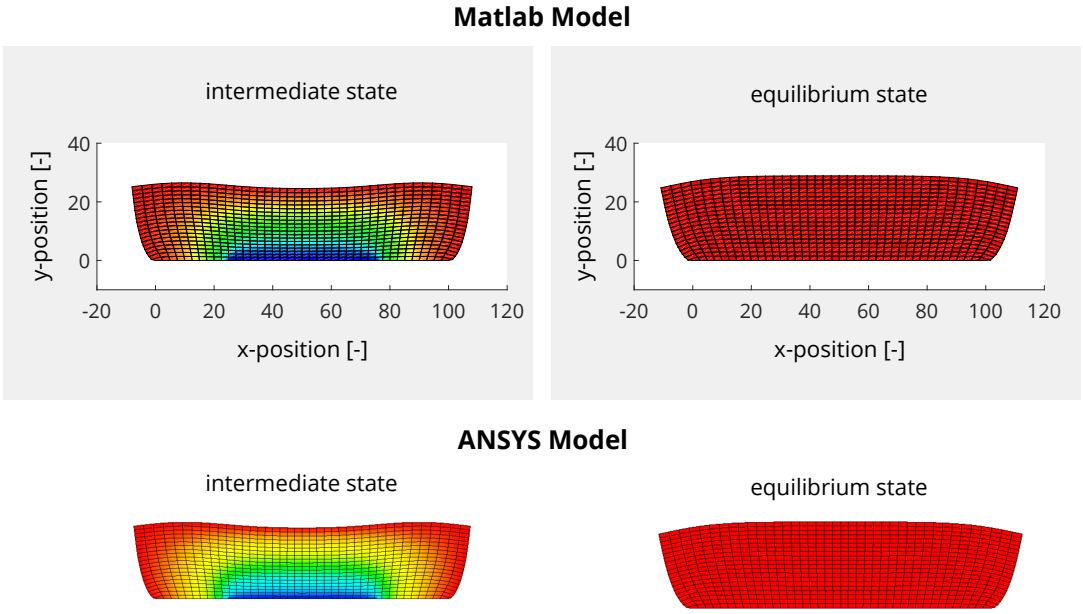

Figure A.4: Comparison of Matlab and ANSYS results of thermal expansion process.

B Thermal Expansion Equation for ANSYS

In the finite element tool ANSYS, the thermal expansion can be modeled with two different methods [116] (pp. 9-10). The first approach is based on a SCTE, which is referred as $\alpha^{se}(T)$. The SCTE values can be defined by the material properties command *"MP"* of ANSYS. The command supports anisotropic expansion settings, in which the values in spatial directions are assigned by the labels *"ALPX"*, *"ALPY"* and *"ALPZ"*. The thermal strain ε_{th} is calculated by:

$$\varepsilon_{th} = \alpha^{se}(T)\,(T - T_{ref}) \tag{B.1}$$

where T_{ref} is the reference temperature and T is the temperature assigned to the finite elements. The second approach is based on the ICTE, which is referred as $\alpha^{in}(T)$. The ICTE values can be assigned by the labels *"CTEX"*, *"CTEY"* and *"CTEZ"* in different spatial directions. Here, the thermal strain ε_{th} is calculated by:

$$\varepsilon_{th} = \int_{T_{ref}}^{T} \alpha^{in}(T')\,dT' \tag{B.2}$$

The main difference is that $\alpha^{se}(T)$ is interpreted as a mean value for thermal expansion between a reference temperature T_{ref} and the current element temperature T in finite element simulations. The SCTE approach extracts the $\alpha^{se}(T)$ value for given temperatures and calculates the thermal strain ε_{th}. Iterative solution procedures to trace thermal expansion values in the temperature range are not necessary. In contrast, $\alpha^{in}(T)$ is interpreted as an instantaneous thermal expansion and represents the slope of the strain-temperature relationship. An iterative solution procedure is necessary to trace thermal expansion in the operating range. **Figure B.1** illustrates the physical background of both expansion factors.

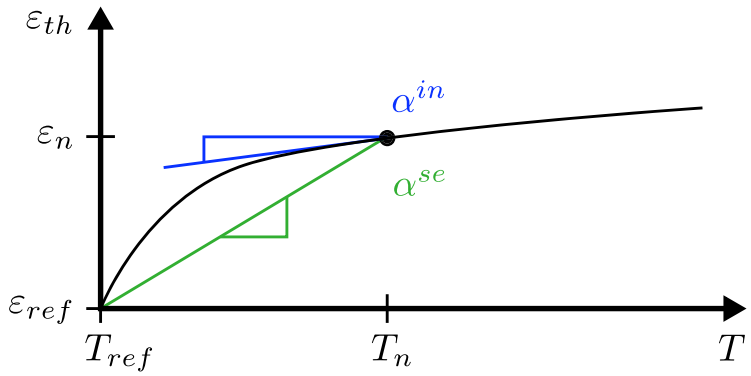

Figure B.1: Implementation of $\alpha^{se}(T)$ and $\alpha^{in}(T)$ for the thermal strain ε_{th} at different temperatures T [172] (pp. 18).

The relationship between both coefficients of thermal expansion is shown in **Equation B.3**. It is possible to convert SCTE values in ICTE values and vice versa. The volume phase-transition of hydrogels is strongly nonlinear and follows a sigmoidal function in the finite element models. Both, SCTE and ICTE values can either be assigned by a polynomial function of the 4^{th} order or by a look-up table with up to one hundred data points whereby the values in between are linearly interpolated. The SCTE approach must be

applied for linear static simulations since equilibrium iterations are not necessary.

$$\alpha^{se}(T) = \frac{\int_{T_{ref}}^{T} \alpha^{in}(T')\, dT'}{T - T_{ref}} \tag{B.3}$$

C Linear Regression of the Thermal Expansion Equation for ANSYS

The secant or instantaneous thermal expansion coefficients can either by implemented by a 4^{th} order polynomial function or by a look-up table with up to one hundred sample points. The thermal expansion coefficient for the volume phase-transition of hydrogels is usually described by sigmoidal functions, which can hardly be approximated by low order polynomials. On the other hand, look-up tables should be generated automatically and transferred to the ANSYS commands *"mptemp"* and *"mpdata,ctex"* to quantify thermal expansion effects in finite element simulations.

Look-up tables should not simply contain data points with equidistant spacing in the operating range. Sigmoidal functions strongly change their slope close to the lower critical solution temperature (LCST) and flatten at high and low stimulus temperatures. The density of sample points is directly related to the curvature of the thermal expansion relationship. Linear sections allow for large spacings and the sections with large second derivatives need narrow sample points.

The transfer of sigmoidal functions to an appropriate instantaneous thermal expansion coefficient is introduced in **Section 5.2.3**. However, **Equation 5.26** is simplified for a two-parameter sigmoidal function. Real thermal expansion coefficient with different curvatures for the upper and lower range of the volume phase-transition are discussed in **Section 3.1.3**. The sigmoidal functions are evaluated in MathCAD based on the source code provided in **Appendix E.4**. The analytical relationship is defined by:

$$\alpha^{in}\left(T(i)\right) = \frac{1}{3} \cdot \frac{(Q_1 - Q_0) \cdot \left(\frac{k_u \cdot e^{k_u (T - T_{LCST})}}{\left(1 + e^{k_u (T - T_{LCST})}\right)^2} + 0.5 k_l \cdot e^{-k_l (T - T_{LCST})} \right)}{\left(\frac{Q_1 - Q_0}{1 + \frac{1}{1 + e^{k_u (T - T_{LCST})}} + 0.5 \cdot e^{-k_l (T - T_{LCST})}} + Q_0 \right)} \cdots$$
$$\cdots \cdot \frac{1}{\left(1 + \frac{1}{1 + e^{k_u (T - T_{LCST})}} + 0.5 \cdot e^{-k_l (T - T_{LCST})}\right)^2} \tag{C.1}$$

Equation C.1 can be adapted by five parameters to represent a wide range of swelling functions. User defined parameters are the minimum swelling degree Q_0, the maximum swelling degree Q_1, the lower critical solution temperature T_{LCST}, the lower curvature distance k_l and the upper curvature distance k_u as listed in **Table 3.2**. The obtained curve is visualized in **Figure 3.5**. The next step is the calculation of sample points for the look-up table, which fit best to the curve defined in **Equation C.1**.

The regression algorithm starts with the slope at the first sample point, which is located at the left side of the curve. It creates a straight line and the deviation between the curve and

the line is calculated at equidistant steps. Two cases are evaluated next:

- The deviation between the curve and the straight line is smaller than a specified tolerance. A new control point is set in order to mark the last position where the straight line fulfills the specified tolerance range to the curve.
- The deviation is larger as the specified tolerance range. The last control point becomes a new sample point for the look-up table. A new slope is calculated and the algorithms starts from the last marked position.

The number of samples points is evaluated at the end of the curve. If the number of samples exceeds the upper limit of 100 points, the tolerance range is enlarged, otherwise the tolerance range is reduced. The tool starts a new line search algorithm until the number of samples is exactly one hundred. The search algorithm takes just a few seconds.

The algorithm is visualized in **Figure C.1** for the current stimulus temperature $T(i-1)$. The existing slope m_{old} is defined by:

$$m_{old} = \frac{\alpha(i-1) - \alpha(i-2)}{T(i-1) - T(i-2)} \tag{C.2}$$

The mathematical equation of the straight line is based on a linear function, which is defined by $y = m \cdot x + n$. The parameter n becomes:

$$n = \alpha(i-1) - m_{old} \cdot T(i-1) \tag{C.3}$$

A new data point α_{pred} at the stimulus temperature $T(i)$ on the straight line can be predicted by:

$$\alpha_{pred}(i) = m_{old} \cdot T(i) + n \tag{C.4}$$

Based on the analytic $\alpha^{in}(i)$ and the predicted $\alpha_{pred}(i)$ values, an absolute deviation $\Delta\alpha$ is calculated from:

$$\Delta\alpha = abs\left(\alpha^{in}(i) - \alpha_{pred}(i)\right) \tag{C.5}$$

A new slope m_{new} must be assigned if the deviation $\Delta\alpha$ is larger as the specified tolerance:

$$m_{new} = \frac{\alpha(i) - \alpha(i-1)}{T(i) - T(i-1)} \tag{C.6}$$

In this case, $T(i-1)$ becomes a new sample point for the ANSYS loop-up table and the old slope m_{old} will be replaced by the new slope m_{new}. The routine goes to the next sample $T(i+1)$ and continues with **Equation C.2**.

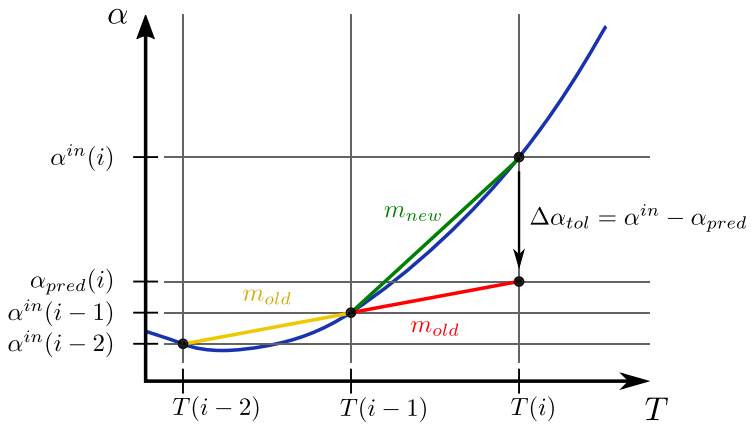

Figure C.1: Linear regression algorithm to predict 100 sample points along the specified curve.

The results of the regression analysis are shown in **Figure C.2**. The blue curve in plot a) visualizes the function values of the instantaneous thermal expansion coefficient $\alpha^{in}(T)$ with regard to the stimulus temperature T. The curve is defined by **Equation C.1**. The red dots are the data points for the look-up table, which are transferred to ANSYS. It can be seen that sample points have a high density at regions with large slope changes. The curves in plot b) illustrate the first, second and third derivatives for data evaluation purposes. Plot c) shows the deviation between the specified curve and the sample points for the data export to ANSYS. The utilized Matlab routine "hydexp_nonlinfit.m" is provided in **Appendix E.4**. The output data are automatically transferred to APDL for subsequent finite element simulations. Similar fit functions to represent hydrogel swelling are introduced in [173], [174].

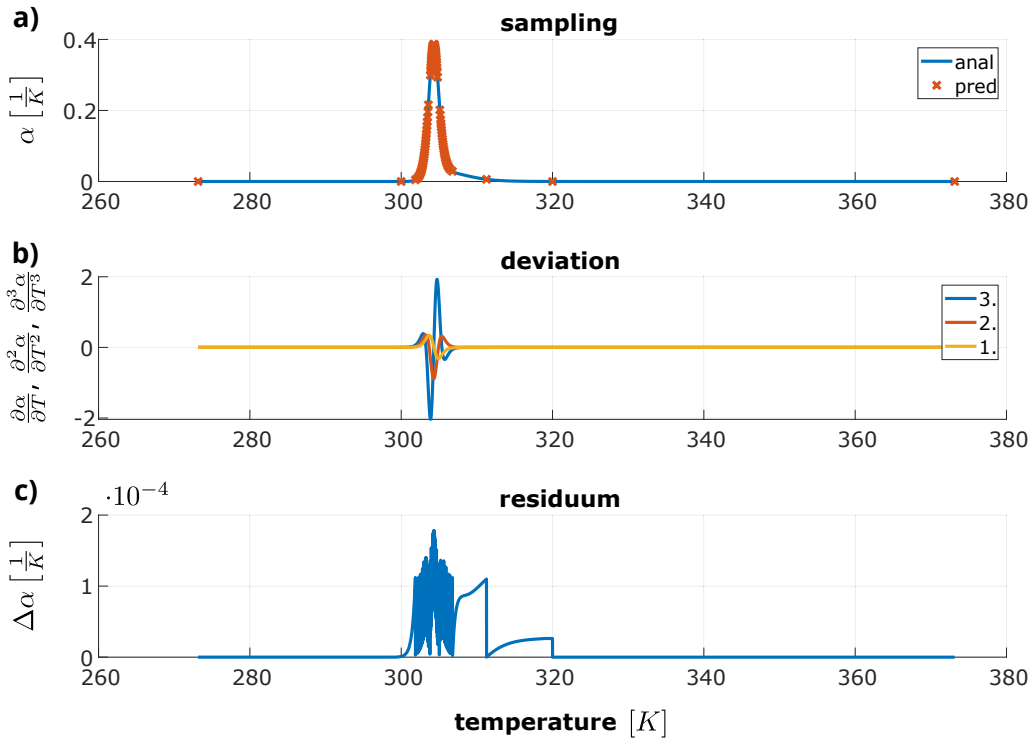

Figure C.2: Instantaneous thermal expansion curve and results of the regression analysis.

D Comparing different Mechanical Strain Definitions

In **Section 5.2**, different strain measures have been introduced. The logarithmic strain ε_{log} (also known as Hencky strain) is widely used for large deformations, and the engineering strain ε_{eng} refers to small deformations. It is often difficult to decide whether large or small deformations exist in practical applications. The mechanical strain is also used to describe the volumetric strain, which is the change in volume ΔV divided by the initial volume V_0 or the volume swelling degree Q. Both volume measures are very important to characterize hydrogels for different applications. Likewise, linearized or non-linear models can be applied to describe the mathematical background.

Table D.1 illustrates examples where the new length and the volume change (volumetric strain) are calculated for small, moderate and large thermal expansion values. The thermal expansion is defined by the thermal strain ε_{th}, which is the product of the thermal expansion coefficient α and the temperature change ΔT. Exemplarily, thermal strain will be set to $\varepsilon_{th} = 0.01$ to model small deformations, to $\varepsilon_{th} = 0.1$ to model moderate deformations and to $\varepsilon_{th} = 1.0$ to model large deformations. It should be noticed that the swelling rates of hydrogels can be even larger than one. The initial length l_0 has been set to 10 units.

The logarithmic strain is also referred as true strain in mechanical engineering and describes both, large and small deformations correctly. In the second column of **Table D.1**, the new length and the volume change has been analyzed for all three strain ranges. One can clearly observe a non-linear relationship between these steps. The thermal strain was enlarged by the factor of ten between all three case. The length and volume change between small and moderate strain scales linear but the change between moderate and large deformations is much higher as expected by the linear theory.

The logarithmic strain can by understood as a series of tiny linear strain changes, which are applied during the thermal swelling process. It is approximated by a slow increase of the stimulus temperature change in, for example 100.000 sub-steps. The volume change is calculated exactly for a cubic volume of the hydrogel. Results are in the third column, which is referred incremental change in **Table D.1**. The results are identical to the logarithmic case.

Column number four is related to the engineering strain theory. Results are identical to the logarithmic strain theory for small deformations, results are acceptable for moderate deformations but results differ strongly for large deformations. As a design rule, logarithmic strain measures must be applied for deformations, which are in the order of $\varepsilon = 0.1$ or larger. If the number of steps for the incremental change in column three is reduced to 1, it gives identical results to the engineering strain approach. Such a one-step change is listed in column number five of **Table D.1**.

Finally, the volume change is linearized in column number six. Both, the new length and the volumetric strain vary linearly with the thermal strain. A linearization of the volume change is acceptable for small and moderate deformations but shows wrong results for a large thermal strain. The theoretical background of the volumetric strain is shown in **Equation D.1**:

$$\frac{\Delta V}{V_0} = \frac{l^3 - l_0^3}{l_0^3} = (1+\varepsilon)^3 - 1 = \varepsilon^3 + 3\varepsilon^2 + 3\varepsilon \tag{D.1}$$

For very small strains like $\varepsilon \leq 0.01$, the higher order terms of **Equation D.1** can be neglected leading to the assumption, which is used in column number six:

$$\frac{\Delta V}{V_0} = \varepsilon^3 + 3\varepsilon^2 + 3\varepsilon \overset{\varepsilon \ll 1}{\approx} 3\varepsilon = \varepsilon_x + \varepsilon_y + \varepsilon_z \tag{D.2}$$

Supporting **Table D.1**, a MathCAD script of the examples is provided in **Appendix E.5**. The theory of logarithmic strain is activated by the command *"nlgeom,on"* in the finite element program ANSYS. It requires an iterative solution procedure in order to calculate the true strain and the true stress result data.

For modeling and simulation of hydrogels, the measured volume swelling degree Q is mapped to the instantaneous coefficient of thermal expansion (ICTE). If the approach is implemented correctly, the measured length or volume changes are identical to the simulated values. As shown in **Figure 5.2** and discussed in **Section 5.2.3**, the ICTE functions can either be adapted to the logarithmic strain theory (case 1) or to the engineering strain theory (case 2). The ICTE functions are different for both cases. On the other hand, if case 1 is simulated with *"nlgeom,on"* in ANSYS and the case 2 is simulated with *"nlgeom,off"*, the swelling results are identical because the same theory was applied for both cases. However, logarithmic strain should always be activated for large deformations in real applications.

Table D.1: Numerical example of different length and volumetric strains.

	$l_0 = 10$, $\varepsilon_{th} = \alpha\Delta T$				
	logarithmic	**incremental change**	**engineering**	**one-step change**	**linearized**
strain	$\varepsilon_{log} = \ln\left(\frac{l}{l_0}\right) = \varepsilon_{th}$		$\varepsilon_{eng} = \frac{dl}{l_0} = \varepsilon_{th}$		$\varepsilon_{eng} = \frac{dl}{l_0} = \varepsilon_{th}$
new length	$l_{log} = l_0 \cdot e^{\varepsilon_{th}}$	`l=lo; anz=100000; for i=1:anz l=l*(1+e_th/anz); end`	$l_{eng} = l_0 \cdot (1 + \varepsilon_{th})$	`l=lo; anz=1; for i=1:anz l=l*(1+e_th/anz); end`	$l_{lin} = l_0 \cdot (1 + \varepsilon_{th})$
volumetric strain	$\frac{\Delta V}{V_0} = e^{3\cdot\varepsilon_{th}} - 1$	$\frac{\Delta V}{V_0} = \frac{l^3 - l_0^3}{l_0^3}$	$\frac{\Delta V}{V_0} = (1 + \varepsilon_{th})^3 - 1$	$\frac{\Delta V}{V_0} = \frac{l^3 - l_0^3}{l_0^3}$	$\frac{\Delta V}{V_0} = 3 \cdot \varepsilon_{th}$
$\varepsilon = 0.01$	$l = 10.101$	$l = 10.101$	$l = 10.1$	$l = 10.1$	$l = 10.1$
	$\frac{\Delta V}{V_0} = 0.03$	$\frac{\Delta V}{V_0} = 0.03$	$\frac{\Delta V}{V_0} = 0.03$	$\frac{\Delta V}{V_0} = 0.03$	$\frac{\Delta V}{V_0} = 0.03$
$\varepsilon = 0.1$	$l = 11.052$	$l = 11.052$	$l = 11$	$l = 11$	$l = 11$
	$\frac{\Delta V}{V_0} = 0.35$	$\frac{\Delta V}{V_0} = 0.35$	$\frac{\Delta V}{V_0} = 0.331$	$\frac{\Delta V}{V_0} = 0.331$	$\frac{\Delta V}{V_0} = 0.3$
$\varepsilon = 1$	$l = 27.183$	$l = 27.183$	$l = 20$	$l = 20$	$l = 20$
	$\frac{\Delta V}{V_0} = 19.085$	$\frac{\Delta V}{V_0} = 19.085$	$\frac{\Delta V}{V_0} = 7$	$\frac{\Delta V}{V_0} = 7$	$\frac{\Delta V}{V_0} = 3$

E Supporting Documents

In this chapter, an overview of the supporting documents is provided, which help to better trace assumptions. The provided scripts require the following programs:

xmcd-files:	Mathcad 15.0
m-files:	Matlab 2015a
MF toolbox:	Matlab 2020a

E.1 Analytic Static Swelling

PhysicoStaticF.m	Matlab source code: Analytic static swelling behavior used to plot **Figure 3.1**
PhysicoStaticD.xmcd	Mathcad File: Analytic static swelling behavior derived from the Helmholtz free energy equation

E.2 FEM - Matrix Method

ThermalBeam.xmcd	Mathcad File: Analytical example file to calculate the deflection of the FEM Matrix Method described in **Section 3.1.2**

E.3 8 Node Finite Element Routine

8NodeFEM.m	Matlab source code: Routine to implement an 8 node plane element for **Section 3.1.2** 8 node plane element with plane stress
8NodeFEM.inp	Ansys source code: Ansys Routine to verify the Matlab routine

E.4 FEM - Script to create the CTEX table data

hydexp_nonlinfit.m	Matlab source code: Script to automatically create the CTEX table data for ANSYS APDL as described in **Appendix C**
v2_AdvA.xmcd	Mathcad File: Analytical example of the implementation of the thermal expansion coefficient in ANSYS to implement the volume phase-transition
ANSYSrun.inp	Ansys APDL: Source Code of the swelling hydrogel Actuator implementing the volume phase-transition behavior.

E.5 Comparison of Solid Mechanics

SolidMech.xmcd	Mathcad File: Comparison of Hook's law with engineering and Hencky strain and the Mooney Rivlin solid.
voluchange.xmcd	Mathcad File: Numerical example of the different lengths and volumetric strains

List of Figures

List of Tables

Bibliography

[1] A. Folch, *Introduction to BioMEMS*, 1st ed. CRC Press, 2013, p. 528, ISBN: 9781466509382.

[2] D. Podbiel, L. Boecking, H. Bott, J. Kassel, D. Czurratis, F. Laermer, R. Zengerle, and J. Hoffmann, „From CAD to microfluidic chip within one day: rapid prototyping of lab-on-chip cartridges using generic polymer parts“, *Journal of Micromechanics and Microengineering*, vol. 30, no. 11, p. 115 012, Nov. 2020. DOI: 10.1088/1361-6439/aba5dd.

[3] B. He, B. J. Burke, X. Zhang, R. Zhang, and F. E. Regnier, „A picoliter-volume mixer for microfluidic analytical systems“, *Analytical Chemistry*, vol. 73, no. 9, pp. 1942–1947, May 2001. DOI: 10.1021/ac000850x.

[4] D. Simon, F. Obst, S. Haefner, T. Heroldt, M. Peiter, F. Simon, A. Richter, B. Voit, and D. Appelhans, „Hydrogel/enzyme dots as adaptable tool for non-compartmentalized multi-enzymatic reactions in microfluidic devices“, *Reaction Chemistry and Engineering*, vol. 4, no. 1, pp. 67–77, 2019. DOI: 10.1039/c8re00180d.

[5] F. Obst, D. Simon, P. J. Mehner, J. W. Neubauer, A. Beck, O. Stroyuk, A. Richter, B. Voit, and D. Appelhans, „One-step photostructuring of multiple hydrogel arrays for compartmentalized enzyme reactions in microfluidic devices“, *Reaction Chemistry and Engineering*, vol. 4, no. 12, pp. 2141–2155, 2019. DOI: 10.1039/c9re00349e.

[6] P. J. Mehner, F. Obst, D. Simon, J. Tang, A. Beck, D. Gruner, M. Busek, D. Appelhans, U. Marschner, B. Voit, and A. Richter, „Modeling Hydrogel-Controlled Micro-Reactors for Enzyme Assays With Finite Elements for Improved Flow and Filling Distribution“, in *Volume 1: Development and Characterization of Multifunctional Materials; Modeling, Simulation, and Control of Adaptive Systems; Integrated System Design and Implementation*, American Society of Mechanical Engineers, Sep. 2018, ISBN: 978-0-7918-5194-4. DOI: 10.1115/SMASIS2018-8027.

[7] S. Y. Teh, R. Lin, L. H. Hung, and A. P. Lee, „Droplet microfluidics“, *Lab on a Chip*, vol. 8, no. 2, pp. 198–220, 2008. DOI: 10.1039/b715524g.

[8] S. N. Bhatia and D. E. Ingber, „Microfluidic organs-on-chips“, *Nature Biotechnology*, vol. 32, no. 8, pp. 760–772, Aug. 2014. DOI: 10.1038/nbt.2989.

[9] H. Kimura, Y. Sakai, and T. Fujii, „Organ/body-on-a-chip based on microfluidic technology for drug discovery“, *Drug Metabolism and Pharmacokinetics*, vol. 33, no. 1, pp. 43–48, Feb. 2018. DOI: 10.1016/j.dmpk.2017.11.003.

[10] S. B. Lim, W. Di Lee, J. Vasudevan, W.-T. Lim, and C. T. Lim, „Liquid biopsy: one cell at a time“, *npj Precision Oncology*, vol. 3, no. 1, p. 23, Dec. 2019. DOI: 10.1038/s41698-019-0095-0.

[11] H. Yin and D. Marshall, „Microfluidics for single cell analysis“, *Current Opinion in Biotechnology*, vol. 23, no. 1, pp. 110–119, Feb. 2012. DOI: 10.1016/j.copbio.2011.11.002.

[12] J. El-Ali, P. K. Sorger, and K. F. Jensen, „Cells on chips“, *Nature*, vol. 442, no. 7101, pp. 403–411, Jul. 2006. DOI: 10.1038/nature05063.

[13] S. K. Sia and L. J. Kricka, „Microfluidics and point-of-care testing“, *Lab on a Chip*, vol. 8, no. 12, p. 1982, 2008. DOI: 10.1039/b817915h.

[14] L. R. Volpatti and A. K. Yetisen, „Commercialization of microfluidic devices“, *Trends in Biotechnology*, vol. 32, no. 7, pp. 347–350, Jul. 2014. DOI: 10.1016/j.tibtech.2014.04.010.

[15] B. M. Maoz, A. Herland, E. A. Fitzgerald, T. Grevesse, C. Vidoudez, A. R. Pacheco, S. P. Sheehy, T. E. Park, S. Dauth, R. Mannix, N. Budnik, K. Shores, A. Cho, J. C. Nawroth, D. Segrè, B. Budnik, D. E. Ingber, and K. K. Parker, „A linked organ-on-chip model of the human neurovascular unit reveals the metabolic coupling of endothelial and neuronal cells“, *Nature Biotechnology*, vol. 36, no. 9, pp. 865–877, Oct. 2018. DOI: 10.1038/nbt.4226.

[16] D. Nesic, R. Whiteside, M. Brittberg, D. Wendt, I. Martin, and P. Mainil-Varlet, „Cartilage tissue engineering for degenerative joint disease“, *Advanced Drug Delivery Reviews*, vol. 58, no. 2, pp. 300–322, May 2006. DOI: 10.1016/j.addr.2006.01.012.

[17] S. V. Murphy and A. Atala, „3D bioprinting of tissues and organs“, *Nature Biotechnology*, vol. 32, no. 8, pp. 773–785, Aug. 2014. DOI: 10.1038/nbt.2958.

[18] P. J. Mehner, T. Liu, M. B. Karimi, A. Brodeur, J. Paniagua, S. Giles, P. Richard, A. Nemtserova, S. Liu, R. Alperin, S. Bhatia, M. Culpepper, R. J. Lang, and C. Livermore, „Toward engineering biological tissues by directed assembly and origami folding“, in *Origami6*, Providence, Rhode Island: American Mathematical Society, 2015, pp. 545–555, ISBN: 978-1-4704-1876-2. DOI: 10.1090/mbk/095.2/17.

[19] C. Livermore, L. Tian, R. Lang, X. Xie, and R. Alperin, *Folded multi-material microfluidic devices for tissue engineering*, US20180264474A1, 2018.

[20] A. J. DeMello, „Control and detection of chemical reactions in microfluidic systems“, *Nature*, vol. 442, no. 7101, pp. 394–402, Jul. 2006. DOI: 10.1038/nature05062.

[21] P. Yager, T. Edwards, E. Fu, K. Helton, K. Nelson, M. R. Tam, and B. H. Weigl, „Microfluidic diagnostic technologies for global public health“, *Nature*, vol. 442, no. 7101, pp. 412–418, Jul. 2006. DOI: 10.1038/nature05064.

[22] G. Whitesides, L. Woodford, and A. A. Flowers, „Solving problems“, *Lab on a Chip*, vol. 10, no. 18, p. 2317, 2010. DOI: 10.1039/c0lc90036b.

[23] M. N. Esbin, O. N. Whitney, S. Chong, A. Maurer, X. Darzacq, and R. Tjian, „Overcoming the bottleneck to widespread testing: a rapid review of nucleic acid testing approaches for COVID-19 detection“, *RNA*, vol. 26, no. 7, pp. 771–783, Jul. 2020. DOI: 10.1261/rna.076232.120.

[24] S. Böhm, G. J. Burger, M. T. Korthorst, and F. Roseboom, „Micromachined silicon valve driven by a miniature bi-stable electro-magnetic actuator“, *Sensors and Actuators, A: Physical*, vol. 80, no. 1, pp. 77–83, Mar. 2000. DOI: 10.1016/S0924-4247(99)00298-8.

[25] O. Français and I. Dufour, „Enhancement of elementary displaced volume with electrostatically actuated diaphragms: application to electrostatic micropumps“, *Journal of Micromechanics and Microengineering*, vol. 10, no. 2, pp. 282–286, Jun. 2000. DOI: 10.1088/0960-1317/10/2/330.

[26] S. Shoji, B. Van der Schoot, N. de Rooij, and M. Esashi, „Smallest dead volume microvalves for integrated chemical analyzing systems“, in *TRANSDUCERS '91: 1991 International Conference on Solid-State Sensors and Actuators. Digest of Technical Papers*, IEEE, IEEE, 1991, pp. 1052–1055, ISBN: 0-87942-585-7. DOI: 10.1109/SENSOR.1991.149077.

[27] P. L. Bergstrom, J. Ji, Y. N. Liu, and K. D. Wise, „Thermally Driven Phase-Change Microactuation“, *Journal of Microelectromechanical Systems*, vol. 4, no. 1, pp. 10–17, Mar. 1995. DOI: 10.1109/84.365365.

[28] Q. Zhang, M. Zhang, L. Djeghlaf, J. Bataille, J. Gamby, A.-M. Haghiri-Gosnet, and A. Pallandre, „Logic digital fluidic in miniaturized functional devices: Perspective to the next generation of microfluidic lab-on-chips“, *ELECTROPHORESIS*, vol. 38, no. 7, pp. 953–976, Apr. 2017. DOI: 10.1002/elps.201600429.

[29] N. S. G. K. Devaraju and M. A. Unger, „Pressure driven digital logic in PDMS based microfluidic devices fabricated by multilayer soft lithography“, *Lab on a Chip*, vol. 12, no. 22, p. 4809, 2012. DOI: 10.1039/c2lc21155f.

[30] J. A. Weaver, J. Melin, D. Stark, S. R. Quake, and M. A. Horowitz, „Static control logic for microfluidic devices using pressure-gain valves“, *Nature Physics*, vol. 6, no. 3, pp. 218–223, Mar. 2010. DOI: 10.1038/nphys1513.

[31] M. Rhee and M. A. Burns, „Microfluidic pneumatic logic circuits and digital pneumatic microprocessors for integrated microfluidic systems“, *Lab on a Chip*, vol. 9, no. 21, pp. 3131–3143, 2009. DOI: 10.1039/b904354c.

[32] P. N. Duncan, S. Ahrar, and E. E. Hui, „Scaling of pneumatic digital logic circuits“, *Lab on a Chip*, vol. 15, no. 5, pp. 1360–1365, 2015. DOI: 10.1039/C4LC01048E.

[33] A. Richter, D. Kuckling, S. Howitz, T. Gehring, and K. F. Arndt, „Electronically controllable microvalves based on smart hydrogels: Magnitudes and potential applications“, *Journal of Microelectromechanical Systems*, vol. 12, no. 5, pp. 748–753, 2003. DOI: 10.1109/JMEMS.2003.817898.

[34] K.-F. Arndt, D. Kuckling, and A. Richter, „Application of sensitive hydrogels in flow control“, *Polymers for Advanced Technologies*, vol. 11, no. 8-12, pp. 496–505, Aug. 2000. DOI: 10.1002/1099-1581(200008/12)11:8/12<496::AID-PAT996>3.0.CO;2-7.

[35] R. H. Liu, Q. Yu, and D. J. Beebe, „Fabrication and characterization of hydrogel-based microvalves“, *Journal of Microelectromechanical Systems*, vol. 11, no. 1, pp. 45–53, 2002. DOI: 10.1109/84.982862.

[36] P. Frank, D. Gräfe, C. Probst, S. Haefner, M. Elstner, D. Appelhans, D. Kohlheyer, B. Voit, and A. Richter, „Autonomous Integrated Microfluidic Circuits for Chip-Level Flow Control Utilizing Chemofluidic Transistors“, *Advanced Functional Materials*, vol. 27, no. 30, p. 1700430, Aug. 2017. DOI: 10.1002/adfm.201700430.

[37] G. Paschew, J. Schreiter, A. Voigt, C. Pini, J. P. Chávez, M. Allerdißen, U. Marschner, S. Siegmund, R. Schüffny, F. Jülicher, and A. Richter, „Autonomous Chemical Oscillator Circuit Based on Bidirectional Chemical-Microfluidic Coupling“, *Advanced Materials Technologies*, vol. 1, no. 1, p. 1600005, Apr. 2016. DOI: 10.1002/admt.201600005.

[38] R. Greiner, M. Allerdissen, A. Voigt, and A. Richter, „Fluidic microchemomechanical integrated circuits processing chemical information“, *Lab on a Chip*, vol. 12, no. 23, pp. 5034–5044, 2012. DOI: 10.1039/c2lc40617a.

[39] C. Rivet, H. Lee, A. Hirsch, S. Hamilton, and H. Lu, „Microfluidics for medical diagnostics and biosensors“, *Chemical Engineering Science*, vol. 66, no. 7, pp. 1490–1507, Apr. 2011. DOI: 10.1016/j.ces.2010.08.015.

[40] S. Yadavali, H. H. Jeong, D. Lee, and D. Issadore, „Silicon and glass very large scale microfluidic droplet integration for terascale generation of polymer microparticles“, *Nature Communications*, vol. 9, no. 1, p. 1222, Dec. 2018. DOI: 10.1038/s41467-018-03515-2.

[41] J. Hoffmann, M. Plötner, D. Kuckling, and W.-J. Fischer, „Photopatterning of thermally sensitive hydrogels useful for microactuators“, *Sensors and Actuators A: Physical*, vol. 77, no. 2, pp. 139–144, Oct. 1999. DOI: 10.1016/S0924-4247(99)00080-1.

[42] D. Kuckling, J. Hoffmann, M. Plötner, D. Ferse, K. Kretschmer, H.-J. P. Adler, K.-F. Arndt, and R. Reichelt, „Photo cross-linkable poly(N-isopropylacrylamide) copolymers III: micro-fabricated temperature responsive hydrogels“, *Polymer*, vol. 44, no. 16, pp. 4455–4462, Jul. 2003. DOI: 10.1016/S0032-3861(03)00413-0.

[43] Y. Xia and G. M. Whitesides, „Soft Lithography“, *Angewandte Chemie International Edition*, vol. 37, no. 5, pp. 550–575, Mar. 1998. DOI: 10.1002/(SICI)1521-3773(19980316)37:5<550::AID-ANIE550>3.3.CO;2-7.

[44] H. Lorenz, M. Despont, P. Vettiger, and P. Renaud, „Fabrication of photoplastic high-aspect ratio microparts and micromolds using SU-8 UV resist“, *Microsystem Technologies*, vol. 4, no. 3, pp. 143–146, May 1998. DOI: 10.1007/s005420050118.

[45] J. McDaniel, W. H. Grover, and P. Brisk, „The case for semi-automated design of microfluidic very large scale integration (mVLSI) chips“, in *Design, Automation & Test in Europe Conference & Exhibition (DATE), 2017*, IEEE, Mar. 2017, pp. 1793–1798, ISBN: 978-3-9815370-8-6. DOI: 10.23919/DATE.2017.7927283.

[46] A. Voigt, J. Schreiter, P. Frank, C. Pini, C. Mayr, and A. Richter, „Method for the Computer-aided Schematic Design and Simulation of Hydrogel-based Microfluidic Systems“, *IEEE Transactions on Computer-Aided Design of Integrated Circuits and Systems*, vol. 0070, no. c, pp. 1–1, 2019. DOI: 10.1109/TCAD.2019.2925354.

[47] P. J. Mehner, A. Beck, A. Voigt, U. Marschner, and A. Richter, „Reduced order model of a hydrogel-based microvalve with pressure, flow and concentration correlations“, in *2018 Symposium on Design, Test, Integration & Packaging of MEMS and MOEMS (DTIP)*, IEEE, May 2018, pp. 1–5, ISBN: 978-1-5386-6199-4. DOI: 10.1109/DTIP.2018.8394195.

[48] W. Kuhn, O. Kunzle, and A. Katchalsky, „Dénouement de molécules en chaînes polyvalentes par des charges électriques en solution“, *Bulletin des Sociétés Chimiques Belges*, vol. 57, no. 10-12, pp. 421–431, Sep. 1948. DOI: 10.1002/bscb.19480571002.

[49] H. Huang, Z. P. Mao, and W. D. Yu, „Swelling Behavior of Stimuli-Sensitive Hydrogels Based on N-Isopropylacrylamide and Sodium Acrylate Copolymer“, *Research Journal of Textile and Apparel*, vol. 13, no. 2, pp. 1–8, May 2009. DOI: 10.1108/RJTA-13-02-2009-B001.

[50] E. Karadağ and D. Saraydin, „Swelling of superabsorbent acrylamide/sodium acrylate hydrogels prepared using multifunctional crosslinkers“, *Turkish Journal of Chemistry*, vol. 26, no. 6, pp. 863–875, 2002.

[51] H. Huang, D. Zhang, Z. Mao, W. Yu, and H. Yan, „Fast responsive and strong swelling hydrogels based on N- isopropylacrylamide with sodium acrylate“, *Journal of Applied Polymer Science*, vol. 112, no. 1, pp. 123–128, Apr. 2009. DOI: 10.1002/app.28457.

[52] T. Tanaka, „Collapse of gels and the critical endpoint“, *Physical Review Letters*, vol. 40, no. 12, pp. 820–823, Mar. 1978. DOI: 10.1103/PhysRevLett.40.820.

[53] W. Li, H. Zhao, P. R. Teasdale, R. John, and S. Zhang, „Synthesis and characterisation of a polyacrylamide-polyacrylic acid copolymer hydrogel for environmental analysis of Cu and Cd“, *Reactive and Functional Polymers*, vol. 52, no. 1, pp. 31–41, Jul. 2002. DOI: 10.1016/S1381-5148(02)00055-X.

[54] R. A. Siegel and B. A. Firestone, „pH-Dependent Equilibrium Swelling Properties of Hydrophobic Polyelectrolyte Copolymer Gels“, *Macromolecules*, vol. 21, no. 11, pp. 3254–3259, Nov. 1988. DOI: 10.1021/ma00189a021.

[55] T. Tanaka, C. Wang, V. Pande, A. Y. Grosberg, A. English, S. Masamune, H. Gold, R. Levy, and K. King, „Polymer gels that can recognize and recover molecules“, *Faraday Discussions*, vol. 101, pp. 201–206, 1995. DOI: 10.1039/FD9950100201.

[56] A. Suzuki and T. Tanaka, „Phase transition in polymer gels induced by visible light“, *Nature*, vol. 346, no. 6282, pp. 345–347, Jul. 1990. DOI: 10.1038/346345a0.

[57] T. Tanaka, I. Nishio, S. T. Sun, and S. Ueno-Nishio, „Collapse of gels in an electric field“, *Science*, vol. 218, no. 4571, pp. 467–469, Oct. 1982. DOI: 10.1126/science.218.4571.467.

[58] M. Irie, Y. Misumi, and T. Tanaka, „Stimuli-responsive polymers: chemical induced reversible phase separation of an aqueous solution of poly(N-isopropylacrylamide) with pendent crown ether groups“, *Polymer*, vol. 34, no. 21, pp. 4531–4535, Nov. 1993. DOI: 10.1016/0032-3861(93)90160-C.

[59] A. Richter, G. Paschew, S. Klatt, J. Lienig, K. F. Arndt, and H. J. P. Adler, „Review on hydrogel-based pH sensors and microsensors“, *Sensors*, vol. 8, no. 1, pp. 561–581, Jan. 2008. DOI: 10.3390/s8010561.

[60] A. Richter, S. Howitz, D. Kuckling, K. Kretschmer, and K. F. Arndt, „Automatically and electronically controllable hydrogel based valves and microvalves - Design and operating performance“, *Macromolecular Symposia*, vol. 210, no. 1, pp. 447–456, 2004. DOI: 10.1002/masy.200450650.

[61] F. Obst, A. Beck, C. Bishayee, P. J. Mehner, A. Richter, B. Voit, and D. Appelhans, „Hydrogel microvalves as control elements for parallelized enzymatic cascade reactions in microfluidics“, *Micromachines*, vol. 11, no. 2, p. 167, Feb. 2020. DOI: 10.3390/mi11020167.

[62] S. Binder and G. Gerlach, „Intramolecular force-compensated hydrogel-based sensors with reduced response times“, *tm - Technisches Messen*, vol. 86, no. 4, pp. 227–236, Apr. 2019. DOI: 10.1515/teme-2019-0004.

[63] J. Erfkamp, M. Guenther, and G. Gerlach, „Enzyme-Functionalized Piezoresistive Hydrogel Biosensors for the Detection of Urea“, *Sensors*, vol. 19, no. 13, p. 2858, Jun. 2019. DOI: 10.3390/s19132858.

[64] N. Gulnizkij and G. Gerlach, „Modelling and model verification of an autonomous threshold sensor for humidity measurements“, *Journal of Sensors and Sensor Systems*, vol. 9, no. 1, pp. 1–6, Jan. 2020. DOI: 10.5194/jsss-9-1-2020.

[65] J. Niskanen and H. Tenhu, „How to manipulate the upper critical solution temperature (UCST)?“, *Polymer Chemistry*, vol. 8, no. 1, pp. 220–232, 2017. DOI: 10.1039/C6PY01612J.

[66] K. K. Bansal, P. K. Upadhyay, G. K. Saraogi, A. Rosling, and J. M. Rosenholm, „Advances in thermo-responsive polymers exhibiting upper critical solution temperature (UCST)“, *Express Polymer Letters*, vol. 13, no. 11, pp. 974–992, 2019. DOI: 10.3144/expresspolymlett.2019.85.

[67] K. K. Bansal, P. K. Upadhyay, G. K. Saraogi, A. Rosling, and J. M. Rosenholm, „Advances in thermo-responsive polymers exhibiting upper critical solution temperature (UCST)“, *Express Polymer Letters*, vol. 13, no. 11, pp. 974–992, 2019. DOI: 10.3144/expresspolymlett.2019.85.

[68] J. Niskanen and H. Tenhu, „How to manipulate the upper critical solution temperature (UCST)?“, *Polymer Chemistry*, vol. 8, no. 1, pp. 220–232, 2017. DOI: 10.1039/C6PY01612J.

[69] S. Haefner, M. Rohn, P. Frank, G. Paschew, M. Elstner, and A. Richter, „Improved PNIPAAm-Hydrogel Photopatterning by Process Optimisation with Respect to UV Light Sources and Oxygen Content“, *Gels*, vol. 2, no. 1, p. 10, Mar. 2016. DOI: 10.3390/gels2010010.

[70] A. Beck, F. Obst, M. Busek, S. Grünzner, P. J. Mehner, G. Paschew, D. Appelhans, B. Voit, and A. Richter, „Hydrogel Patterns in Microfluidic Devices by Do-It-Yourself UV-Photolithography Suitable for Very Large-Scale Integration“, *Micromachines*, vol. 11, no. 5, p. 479, May 2020. DOI: 10.3390/mi11050479.

[71] D. Biswal and J. Z. Hilt, „Analysis of oxygen inhibition in photopolymerizations of hydrogel micropatterns using FTIR imaging“, *Macromolecules*, vol. 42, no. 4, pp. 973–979, Feb. 2009. DOI: 10.1021/ma801600c.

[72] M. S. S. Häfner, „Komponenten- und Technologieentwicklung zur mikrofluidischen Abbildung einer biotechnologischen Prozesskette“, Ph.D. dissertation, Technische Universität Dresden, 2018, p. 194.

[73] P. Frank, S. Haefner, G. Paschew, and A. Richter, „Rounding of negative dry film resist by diffusive backside exposure creating rounded channels for pneumatic membrane valves“, *Micromachines*, vol. 6, no. 11, pp. 1588–1596, 2015. DOI: 10.3390/mi6111442.

[74] P. Frank, „Microfluidic Chemical Integrated Circuits Based on Stimuli-Responsive Hydrogels for On-Chip Flow Control“, Ph.D. dissertation, Technische Universität Dresden, 2017, p. 190, ISBN: 9783959470223.

[75] M. Busek, S. Gruenzner, T. Steege, F. Schmieder, U. Klotzbach, and F. Sonntag, „Design, characterization, and modeling of microcirculation systems with integrated oxygenators“, *Journal of Sensors and Sensor Systems*, vol. 5, no. 1, pp. 221–228, 2016. DOI: 10.5194/jsss-5-221-2016.

[76] E. Starke, „Kombinierte Simulation - eine weitere Methode zur Optimierung elektromechanischer Systeme“, Ph.D. dissertation, Technische Universität Dresden, 2010.

[77] G. Gerlach and W. Dötzel, *Introduction to Microsystem Technology*, R. Pething, Ed. Wiley, 2008, p. 376, ISBN: 9780470058619.

[78] VDI-2206, „Entwicklungsmethodik für mechatronische Systeme – Design methodology for mechatronic systems“, Tech. Rep. June, 2004, pp. 1–118.

[79] Landau, *THEORY OF ELASTICITY*, 7. Jul. 1960, vol. 13, pp. 44–46, ISBN: 9780750626330.

[80] A. Voigt and A. Richter, „Polymer Gels as EAPs: Fundamentals“, in *Electromechanically Active Polymers*, Cham: Springer International Publishing, 2016, pp. 3–26. DOI: 10.1007/978-3-319-31530-0_1.

[81] M. Doi, „Gel dynamics“, *Journal of the Physical Society of Japan*, vol. 78, no. 5, p. 052 001, May 2009. DOI: 10.1143/JPSJ.78.052001.

[82] J. Yoon, S. Cai, Z. Suo, and R. C. Hayward, „Poroelastic swelling kinetics of thin hydrogel layers: Comparison of theory and experiment“, *Soft Matter*, vol. 6, no. 23, pp. 6004–6012, 2010. DOI: 10.1039/c0sm00434k.

[83] Y. Li and T. Tanaka, „Kinetics of swelling and shrinking of gels“, *The Journal of Chemical Physics*, vol. 92, no. 2, pp. 1365–1371, 1990. DOI: 10.1063/1.458148.

[84] A. Peters and S. J. Candau, „Kinetics of Swelling of Spherical and Cylindrical Gels“, *Macromolecules*, vol. 21, no. 7, pp. 2278–2282, Jul. 1988. DOI: 10.1021/ma00185a068.

[85] A. Richter, S. Howitz, D. Kuckling, and K. F. Arndt, „Influence of volume phase transition phenomena on the behavior of hydrogel-based valves“, *Sensors and Actuators, B: Chemical*, vol. 99, no. 2-3, pp. 451–458, May 2004. DOI: 10.1016/j.snb.2003.12.014.

[86] K. Kamemaru, S. Usui, Y. Hirashima, and A. Suzuki, „Irreversible Swelling Behavior and Reversible Hysteresis in Chemically Crosslinked Poly(vinyl alcohol) Gels“, *Gels*, vol. 4, no. 2, p. 45, May 2018. DOI: 10.3390/gels4020045.

[87] W. Toh, T. Y. Ng, J. Hu, and Z. Liu, „Mechanics of inhomogeneous large deformation of photo-thermal sensitive hydrogels“, *International Journal of Solids and Structures*, vol. 51, no. 25-26, pp. 4440–4451, Dec. 2014. DOI: 10.1016/j.ijsolstr.2014.09.014.

[88] R. Pelton, „Poly(N-isopropylacrylamide) (PNIPAM) is never hydrophobic“, *Journal of Colloid and Interface Science*, vol. 348, no. 2, pp. 673–674, Aug. 2010. DOI: 10.1016/j.jcis.2010.05.034.

[89] M. L. Huggins, „Solutions of long chain compounds“, *The Journal of Chemical Physics*, vol. 9, no. 5, p. 440, May 1941. DOI: 10.1063/1.1750930.

[90] M. L. Huggins, „Thermodynamic Properties of Solutions of High Polymers: the Empirical Constant in the Activity Equation“, *Annals of the New York Academy of Sciences*, vol. 44, no. 4, pp. 431–443, Nov. 1943. DOI: 10.1111/j.1749-6632.1943.tb52763.x.

[91] P. J. Flory, „Themodynamics of high polymer solutions“, *The Journal of Chemical Physics*, vol. 10, no. 1, pp. 51–61, Jan. 1942. DOI: 10.1063/1.1723621. arXiv: 9809069v1 [arXiv:gr-qc].

[92] P. J. Flory, „Network structure and the elastic properties of vulcanized rubber“, *Chemical Reviews*, vol. 35, no. 1, pp. 51–75, Aug. 1944. DOI: 10.1021/cr60110a002.

[93] C. L. Ogg, *Determination of Molecular Weight*, 4. Cornell University Press, 1966, vol. 49, pp. 744–749, ISBN: 0801401348. DOI: 10.1093/jaoac/49.4.744.

[94] P. J. Flory and J. Rehner, „Statistical Theory of Chain Configuration and Physical Properties of High Polymers“, *Annals of the New York Academy of Sciences*, vol. 44, no. 4, pp. 419–429, Nov. 1943. DOI: 10.1111/j.1749-6632.1943.tb52762.x.

[95] P. J. Flory and J. Rehner, „Statistical mechanics of cross-linked polymer networks I. Rubberlike elasticity“, *The Journal of Chemical Physics*, vol. 11, no. 11, pp. 512–520, Nov. 1943. DOI: 10.1063/1.1723791. arXiv: 9809069v1 [arXiv:gr-qc].

[96] S. Hirotsu, „Softening of bulk modulus and negative Poisson's ratio near the volume phase transition of polymer gels“, *The Journal of Chemical Physics*, vol. 94, no. 5, pp. 3949–3957, Mar. 1991. DOI: 10.1063/1.460672.

[97] N. Hamzavi, A. D. Drozdov, Y. Gu, and E. Birgersson, „Modeling Equilibrium Swelling of a Dual pH- and Temperature-Responsive Core/Shell Hydrogel“, *International Journal of Applied Mechanics*, vol. 8, no. 3, p. 1650039, Apr. 2016. DOI: 10.1142/S1758825116500393.

[98] S. Binder, A. T. Krause, B. Voit, and G. Gerlach, „Bisensitive Hydrogel With Volume Compensation Properties for Force Compensation Sensors“, *IEEE Sensors Letters*, vol. 1, no. 6, pp. 1–4, Dec. 2017. DOI: 10.1109/lsens.2017.2774922.

[99] K.-J. Bathe, *Finite Element Procedures*, 2nd ed. Watertown, MA, 2014, p. 1043, ISBN: 978-0979004957.

[100] T. Wallmersperger and D. Ballhause, „Coupled chemo-electro-mechanical finite element simulation of hydrogels: II. Electrical stimulation“, *Smart Materials and Structures*, vol. 17, no. 4, p. 045012, Aug. 2008. DOI: 10.1088/0964-1726/17/4/045012.

[101] D. Ballhause and T. Wallmersperger, „Coupled chemo-electro-mechanical finite element simulation of hydrogels: I. Chemical stimulation“, *Smart Materials and Structures*, vol. 17, no. 4, p. 045011, Aug. 2008. DOI: 10.1088/0964-1726/17/4/045011.

[102] P. Leichsenring and T. Wallmersperger, „Modeling and simulation of the chemically induced swelling behavior of anionic polyelectrolyte gels by applying the theory of porous media“, *Smart Materials and Structures*, vol. 26, no. 3, p. 035007, Mar. 2017. DOI: 10.1088/1361-665X/26/3/035007.

[103] P. Leichsenring, „Modellierung und Simulation elektroaktiver Polymergele mittels der Theorie Poröser Medien“, Ph.D. dissertation, Technische Universität Dresden, 2018.

[104] M. Sobczyk, „Modellierung und Simulation von Hydrogelen und hydrogelbasierten Schichtsystemen“, Ph.D. dissertation, Technische Universität Dresden, 2018.

[105] T. Wallmersperger, K. Keller, B. Kröplin, M. Günther, and G. Gerlach, „Modeling and simulation of pH-sensitive hydrogels“, *Colloid and Polymer Science*, vol. 289, no. 5-6, pp. 535–544, Apr. 2011. DOI: 10.1007/s00396-011-2404-1.

[106] B. Kalman and S. Kwasny, „Why tanh: choosing a sigmoidal function“, in *IJCNN International Joint Conference on Neural Networks*, vol. 4, IEEE, 1992, pp. 578–581, ISBN: 0-7803-0559-0. DOI: 10.1109/IJCNN.1992.227257.

[107] A. N. Spiess, C. Feig, and C. Ritz, „Highly accurate sigmoidal fitting of real-time PCR data by introducing a parameter for asymmetry“, *BMC Bioinformatics*, vol. 9, no. 1, p. 221, Dec. 2008. DOI: 10.1186/1471-2105-9-221.

[108] G. Strang, *Differential Equations and Linear Algebra*, 5th ed. Wellesley-Cambridge Press Wellesley, 2014, ISBN: 978-0-9802327-9-0.

[109] M. E. Harmon, D. Kuckling, P. Pareek, and C. W. Frank, „Photo-Cross-Linkable PNIPAAm Copolymers. 4. Effects of Copolymerization and Cross-Linking on the Volume-Phase Transition in Constrained Hydrogel Layers“, *Langmuir*, vol. 19, no. 26, pp. 10 947–10 956, Dec. 2003. DOI: 10.1021/la030217h.

[110] T. Tanaka, L. O. Hocker, and G. B. Benedek, „Spectrum of light scattered from a viscoelastic gel“, *The Journal of Chemical Physics*, vol. 59, no. 9, pp. 5151–5159, 1973. DOI: 10.1063/1.1680734.

[111] T. Tanaka and D. J. Fillmore, „Kinetics of swelling of gels“, *The Journal of Chemical Physics*, vol. 70, no. 3, pp. 1214–1218, 1979. DOI: 10.1063/1.437602.

[112] L. D. Landau, E. M. Lifshitz, A. M. Kosevich, J. B. Sykes, L. P. Pitaevskii, and W. H. Reid, *Theory of Elasticity*, ser. Course of theoretical physics. Elsevier Science, 1986, ISBN: 9780750626330.

[113] S. Whitaker, „Flow in porous media I: A theoretical derivation of Darcy's law“, *Transport in Porous Media*, vol. 1, no. 1, pp. 3–25, 1986. DOI: 10.1007/BF01036523.

[114] K.-F. Arndt, F. Krahl, S. Richter, and G. Steiner, „Swelling-Related Processes in Hydrogels“, in 2009, pp. 69–136. DOI: 10.1007/978-3-540-75645-3_3.

[115] F. Leroy, *Molecular Driving Forces. Statistical Thermodynamics in Biology, Chemistry, Physics, and Nanoscience*, 2. Apr. 2013, vol. 11, pp. 231–231, ISBN: 9780815344308. DOI: 10.1080/1539445x.2011.619612.

[116] P. Kohnke, *10.2. Thermoelasticity*, 19.0. Canonsburg, 2018, pp. 297–299. DOI: www.ansys.com.

[117] H. D. Baehr and K. Stephan, „Wärmeleitung und Diffusion“, in *Wärme- und Stoffübertragung*, Berlin, Heidelberg: Springer Berlin Heidelberg, 2019, pp. 121–311. DOI: 10.1007/978-3-662-58441-5_2.

[118] A. Kloczkowski and A. Kolinski, „Theoretical Models and Simulations of Polymer Chains“, in *Physical Properties of Polymers Handbook*, New York, NY: Springer New York, 2007, pp. 67–81. DOI: 10.1007/978-0-387-69002-5_5.

[119] A. Richter, „Quellfähige Polymernetzwerke als Aktor-Sensor-Systeme für die Fluidtechnik“, Ph.D. dissertation, Technische Universität Dresden, 2002, ISBN: 9783183944088.

[120] S. Casoria, G. Sybille, and P. Brunelle, „Hysteresis modeling in the MATLAB/Power System Blockset“, *Mathematics and Computers in Simulation*, vol. 63, no. 3-5, pp. 237–248, Nov. 2003. DOI: 10.1016/S0378-4754(03)00070-3.

[121] M. T. Engelhardt, *Asymmetric minor hysteresis loop model and circuit simulator including the same*, 2009.

[122] E. Breel and V. U. Amsterdam, „Characterizing the micro-mechanical properties of PNIPAAm hydrogel microstructures“, *Optics11*, no. March, 2016. DOI: 10.13140/RG.2.1.2509.4809.

[123] B. Mau, J. Erfkamp, M. Günther, and T. Wallmersperger, „Experimental determination of material parameters for an enhanced modeling of polyelectrolyte gels“, in *Electroactive Polymer Actuators and Devices (EAPAD) XXI*, Y. Bar-Cohen and I. A. Anderson, Eds., SPIE, Mar. 2019, p. 81, ISBN: 9781510625877. DOI: 10.1117/12.2513180.

[124] M. Seuss, W. Schmolke, A. Drechsler, A. Fery, and S. Seiffert, „Core-Shell Microgels with Switchable Elasticity at Constant Interfacial Interaction“, *ACS Applied Materials and Interfaces*, vol. 8, no. 25, pp. 16 317–16 327, Jun. 2016. DOI: 10.1021/acsami.6b04339.

[125] S. Schmidt, M. Zeiser, T. Hellweg, C. Duschl, A. Fery, and H. Möhwald, „Adhesion and mechanical properties of PNIPAM microgel films and their potential use as switchable cell culture substrates“, *Advanced Functional Materials*, vol. 20, no. 19, pp. 3235–3243, Oct. 2010. DOI: 10.1002/adfm.201000730.

[126] Y. Deng, B. M. La Fontaine, H. J. Levinson, and A. R. Neureuther, „Rigorous EM simulation of the influence of the structure of mask patterns on EUVL imaging“, in *Emerging Lithographic Technologies VII*, R. L. Engelstad, Ed., vol. 5037, Jun. 2003, p. 302. DOI: 10.1117/12.484986.

[127] F. Béron, M. V. P. dos Santos, P. G. de Carvalho, K. O. Moura, L. C. Arzuza, and K. R. Pirota, „How to Characterize Cylindrical Magnetic Nanowires“, in *Magnetic Materials*, InTech, Aug. 2016. DOI: 10.5772/63482.

[128] U. Tiwari, R. Ghosh, and P. Sen, „Theory of magneto-optic Kerr effects“, *Physical Review B*, vol. 49, no. 3, pp. 2159–2162, Jan. 1994. DOI: 10.1103/PhysRevB.49.2159.

[129] J. Nowak, C. Bärhold, C. Kessler, and S. Odenbach, „Gelation of a nanocomposite-hydrogel system and its dependency on mechanical loads“, *Applied Rheology*, vol. 27, no. 5, 2017. DOI: 10.3933/ApplRheol-27-52850.

[130] E. J. Lam Po Tang, A. HajiRassouliha, M. P. Nash, P. M. Nielsen, A. J. Taberner, and Y. O. Cakmak, „Non-contact Quantification of Jugular Venous Pulse Waveforms from Skin Displacements“, *Scientific Reports*, vol. 8, no. 1, p. 17 236, Dec. 2018. DOI: 10.1038/s41598-018-35483-4.

[131] S. Richardson, T. P. Babarenda Gamage, A. HajiRassouliha, T. Jackson, K. Hedges, A. Clark, A. Taberner, M. H. Tawhai, and P. M. Nielsen, „Towards a real-time full-field stereoscopic imaging system for tracking lung surface deformation under pressure controlled ventilation“, in *Computational Biomechanics for Medicine: Measurements, Models, and Predictions*, Cham: Springer International Publishing, 2018, pp. 119–130, ISBN: 9783319755892. DOI: 10.1007/978-3-319-75589-2_12.

[132] A. HajiRassouliha, A. J. Taberner, M. P. Nash, and P. M. Nielsen, „Subpixel phase-based image registration using Savitzky–Golay differentiators in gradient-correlation", *Computer Vision and Image Understanding*, vol. 170, pp. 28–39, May 2018. DOI: 10.1016/j.cviu.2017.11.003.

[133] A. Lenk, R. G. Ballas, R. Werthschützky, and G. Pfeifer, *Electromechanical Systems in Microtechnology and Mechatronics – Electrical, Mechanical and Acoustic Networks, their Interactions and Applications*, ser. Microtechnology and MEMS. Berlin, Heidelberg: Springer Berlin Heidelberg, 2011, pp. XXIV, 472, ISBN: 978-3-642-10805-1. DOI: 10.1007/978-3-642-10806-8.

[134] ANSYS, *Coupled Field Analysis Guide*, Release 19. Canonsburg, 2018.

[135] G. Müller, *FEM für Praktiker 1 Grundlagen*, 8. Renningen-Malmsheim: expert-Verlag, ISBN: 9783816926856.

[136] H. B. Callen, *Thermodynamics and Introduction to Thermostatistics*, 2nd ed. New York, NY: John wiley & sons, 1981.

[137] C. Vergari, P. Pourcelot, L. Holden, B. Ravary-Plumioën, G. Gerard, P. Laugier, D. Mitton, and N. Crevier-Denoix, „True stress and Poisson's ratio of tendons during loading", *Journal of Biomechanics*, vol. 44, no. 4, pp. 719–724, Feb. 2011. DOI: 10.1016/j.jbiomech.2010.10.038.

[138] C. W. Smith, R. J. Wootton, and K. E. Evans, „Interpretation of experimental data for Poisson's ratio of highly nonlinear materials", *Experimental Mechanics*, vol. 39, no. 4, pp. 356–362, Dec. 1999. DOI: 10.1007/BF02329817.

[139] J. Bergström, „Elasticity/Hyperelasticity", in *Mechanics of Solid Polymers*, Elsevier, 2015, pp. 209–307. DOI: 10.1016/B978-0-323-31150-2.00005-4.

[140] F. Horkay and G. B. McKenna, „Polymer Networks and Gels", in *Physical Properties of Polymers Handbook*, New York, NY: Springer New York, 2007, pp. 497–523. DOI: 10.1007/978-0-387-69002-5_29.

[141] L. Treloar, *The Physics of Rubber Elasticity*, 3rd ed. Oxford University Press, USA, 1975, p. 322, ISBN: 9780191523304.

[142] H. G. Schild, „Poly(N-isopropylacrylamide): experiment, theory and application", *Progress in Polymer Science*, vol. 17, no. 2, pp. 163–249, Jan. 1992. DOI: 10.1016/0079-6700(92)90023-R.

[143] V. Ermatchkov, L. Ninni, and G. Maurer, „Thermodynamics of phase equilibrium for systems containing N-isopropyl acrylamide hydrogels", *Fluid Phase Equilibria*, vol. 296, no. 2, pp. 140–148, Sep. 2010. DOI: 10.1016/j.fluid.2010.03.014.

[144] K. F. Arndt, B. Ferse, and N. Oelsner, „Application of photochemistry in synthesis of smart nanocomposite hydrogels", *Zeitschrift fur Physikalische Chemie*, vol. 228, no. 2-3, pp. 209–227, Jan. 2014. DOI: 10.1515/zpch-2014-0464.

[145] J. Erfkamp, M. Guenther, and G. Gerlach, „Hydrogel-based piezoresistive sensor for the detection of ethanol", *Journal of Sensors and Sensor Systems*, vol. 7, no. 1, pp. 219–226, Apr. 2018. DOI: 10.5194/jsss-7-219-2018.

[146] P. J. Mehner, M. Allerdißen, S. Haefner, A. Voigt, U. Marschner, and A. Richter, „Modeling the closing behavior of a smart hydrogel micro-valve“, *Journal of Intelligent Material Systems and Structures*, vol. 30, no. 9, pp. 1409–1418, May 2019. DOI: 10.1177/1045389X17742726.

[147] M. Bao and H. Yang, „Squeeze film air damping in MEMS“, *Sensors and Actuators, A: Physical*, vol. 136, no. 1, pp. 3–27, May 2007. DOI: 10.1016/j.sna.2007.01.008.

[148] ANSYS, *Advanced Analysis Guide*, Release 19. Canonsburg, 2018.

[149] T. Bechtold, G. Schrag, and L. Feng, *System-Level Modeling of MEMS*, T. Bechtold, G. Schrag, and L. Feng, Eds. Weinheim, Germany: Wiley-VCH Verlag GmbH & Co. KGaA, Feb. 2013, vol. 10, pp. 1–530, ISBN: 9783527647132. DOI: 10.1002/9783527647132.

[150] F. Ganji, S. Vasheghani-Farahani, and E. Vasheghani-Farahani, „Theoretical description of hydrogel swelling: A review“, *Iranian Polymer Journal (English Edition)*, vol. 19, no. 5, pp. 375–398, Mar. 2010.

[151] M. Sobczyk and T. Wallmersperger, „Modeling and simulation of chemically stimulated hydrogel layers using the multifield theory“, in *Electroactive Polymer Actuators and Devices (EAPAD) 2016*, Y. Bar-Cohen and F. Vidal, Eds., vol. 9798, Apr. 2016, p. 979 810, ISBN: 9781510600393. DOI: 10.1117/12.2217890.

[152] H. Bruus, *Theorethical Microfluids*. Oxford University Press, 2008, p. 346, ISBN: 978–0199235087.

[153] P. Lancaster and K. Šalkauskas, *Curve and surface fitting: an introduction*, 1st ed. Amsterdam, Boston: Academic Press Inc, 1986, p. 280, ISBN: 978-0124360617.

[154] U. Marschner and R. Werthschützky, *Aufgaben und Lösungen zur Schaltungsdarstellung und Simulation elektromechanischer Systeme*. Springer-Verlag, 2015, ISBN: 9783642551680. DOI: 10.1007/978-3-642-55169-7.

[155] A. Voigt, U. Marschner, and A. Richter, „Multiphysics equivalent circuit of a thermally controlled hydrogel microvalve“, *Journal of Intelligent Material Systems and Structures*, vol. 28, no. 16, pp. 2265–2274, Sep. 2017. DOI: 10.1177/1045389X16685445.

[156] L. F. Shampine, M. W. Reichelt, and J. A. Kierzenka, „Solving index-I DAEs in MATLAB and Simulink“, *SIAM Review*, vol. 41, no. 3, pp. 538–552, Jan. 1999. DOI: 10.1137/S0036144599334425X.

[157] M. J. D. Powell, *Numerical Methods for Nonlinear Programming Algebraic Equations*. New York: Gordon and Breach Science Publishers, 1970, pp. 87–144.

[158] P. J. Mehner, A. Beck, A. Voigt, U. Marschner, and A. Richter, „Dynamic finite element modelling of a hydrogel-based micro-valve with 2-way fluid structure interactions“, in *ASME 2017 Conference on Smart Materials, Adaptive Structures and Intelligent Systems, SMASIS 2017*, ser. Structural Health Monitoring, American Society of Mechanical Engineers, vol. 2, American Society of Mechanical Engineers, Sep. 2017, ISBN: 9780791858264. DOI: 10.1115/SMASIS2017-3859.

[159] Y. Cengel and J. Cimbala, *Fluid Mechanics: Fundamentals And Applications*, 4th ed. New York, NY: McGraw-Hill Education, 2017, ISBN: 978-1259921902.

[160] U. Marschner, J. Páez Chávez, A. Voigt, and A. Richter, „Equivalent circuit of the concentration transport in a fluidic channel“, in *ASME 2016 Conference on Smart Materials, Adaptive Structures and Intelligent Systems, SMASIS 2016*, vol. 2, ASME, Sep. 2016, V002T03A011, ISBN: 9780791850497. DOI: 10.1115/SMASIS2016-9118.

[161] J. Lekner, „Viscous flow through pipes of various cross-sections“, *European Journal of Physics*, vol. 28, no. 3, pp. 521–527, May 2007. DOI: 10.1088/0143-0807/28/3/014.

[162] Y. I. Ismail and E. G. Friedman, *On-Chip Inductance in High Speed Integrated Circuits*. Boston, MA: Springer US, 2001, ISBN: 978-1-4613-5677-6. DOI: 10.1007/978-1-4615-1685-9.

[163] J. L. Hudson, M. Hart, and D. Marinko, „An experimental study of multiple peak periodic and nonperiodic oscillations in the Belousov-Zhabotinskii reaction“, *The Journal of Chemical Physics*, vol. 71, no. 4, pp. 1601–1606, Aug. 1979. DOI: 10.1063/1.438487.

[164] K. Kruse and F. Jülicher, „Oscillations in cell biology“, *Current Opinion in Cell Biology*, vol. 17, no. 1, pp. 20–26, Feb. 2005. DOI: 10.1016/j.ceb.2004.12.007.

[165] J. D. Murray, *Mathematical Biology I. An introduction*, 17th ed., J. D. Murray, Ed., ser. Interdisciplinary Applied Mathematics. New York, NY: Springer New York, 2002, vol. 17, p. 551, ISBN: 978-0-387-95223-9.

[166] S. Haefner, R. Koerbitz, P. Frank, M. Elstner, and A. Richter, „High Integration of Microfluidic Circuits Based on Hydrogel Valves for MEMS Control“, *Advanced Materials Technologies*, vol. 3, no. 1, p. 1700108, Jan. 2018. DOI: 10.1002/admt.201700108.

[167] P. Frank, J. Schreiter, S. Haefner, G. Paschew, A. Voigt, and A. Richter, „Integrated microfluidic membrane transistor utilizing chemical information for on-chip flow control“, *PLoS ONE*, vol. 11, no. 8, A. Han, Ed., e0161024, Aug. 2016. DOI: 10.1371/journal.pone.0161024.

[168] R. M. Guijt, E. Baltussen, G. van der Steen, R. B. M. Schasfoort, S. Schlautmann, H. A. H. Billiet, J. Frank, G. W. K. van Dedem, and A. van den Berg, „New approaches for fabrication of microfluidic capillary electrophoresis devices with on-chip conductivity detection“, *ELECTROPHORESIS*, vol. 22, no. 2, pp. 235–241, Jan. 2001. DOI: 10.1002/1522-2683(200101)22:2<235::AID-ELPS235>3.0.CO;2-0.

[169] D. P. Bishop, L. Blanes, A. B. Wilson, T. Wilbanks, K. Killeen, R. Grimm, R. Wenzel, D. Major, M. Macka, D. Clarke, R. Schmid, N. Cole, and P. A. Doble, „Microfluidic high performance liquid chromatography-chip hyphenation to inductively coupled plasma–mass spectrometry“, *Journal of Chromatography A*, vol. 1497, pp. 64–69, May 2017. DOI: 10.1016/j.chroma.2017.03.025.

[170] Y.-H. Chang, G.-B. Lee, F.-C. Huang, Y.-Y. Chen, and J.-L. Lin, „Integrated polymerase chain reaction chips utilizing digital microfluidics“, *Biomedical Microdevices*, vol. 8, no. 3, pp. 215–225, Sep. 2006. DOI: 10.1007/s10544-006-8171-y.

[171] G. Liu and S. Quek, „FEM for Two-Dimensional Solids“, in *The Finite Element Method*, Elsevier, 2014, pp. 161–217. DOI: 10.1016/B978-0-08-098356-1.00007-2.

[172] ANSYS, *ANSYS Mechanical APDL Material Reference*, Release 19. Canonsburg, 2018.

[173] A. Ehrenhofer, G. Bingel, G. Paschew, M. Tietze, R. Schröder, A. Richter, and T. Wallmersperger, „Permeation control in hydrogel-layered patterned PET membranes with defined switchable pore geometry - Experiments and numerical simulation“, *Sensors and Actuators, B: Chemical*, vol. 232, pp. 499–505, Sep. 2016. DOI: 10.1016/j.snb.2016.03.152.

[174] A. Ehrenhofer, M. Elstner, and T. Wallmersperger, „Normalization of hydrogel swelling behavior for sensoric and actuatoric applications“, *Sensors and Actuators, B: Chemical*, vol. 255, pp. 1343–1353, Feb. 2018. DOI: 10.1016/j.snb.2017.08.120.